

The Effects of Metal Additives on Soot Formation

by

Alan S. Feitelberg

B.S., Worcester Polytechnic Institute (1984)

M.S., Chemical Engineering Practice,
Massachusetts Institute of Technology (1986)

Submitted to the
Department of Chemical Engineering
in Partial Fulfillment of the Requirements for the Degree of

Doctor of Philosophy

at the

Massachusetts Institute of Technology
September 1990

Copyright © Massachusetts Institute of Technology 1990

Signature of Author _____
Department of Chemical Engineering
July 16, 1990

Certified by _____
Professor Adel F. Sarofim
Thesis Supervisor

Certified by _____
Professor John P. Longwell
Thesis Supervisor

Accepted by _____
Professor William M. Deen
Chairman, Departmental Committee for Graduate Students
OF TECHNOLOGY

OCT 04 1990

LIBRARIES

ARCHIVES

The Effects of Metal Additives on Soot Formation

by

Alan S. Feitelberg

Submitted to the Department of Chemical Engineering, July 16, 1990,
in Partial Fulfillment of the Requirements for the Degree of
Doctor of Philosophy in Chemical Engineering

ABSTRACT

The overall objective of this thesis was to develop a better understanding of the effects of transition metal additives on soot formation. Iron and manganese were added to premixed ethylene/oxygen/nitrogen flames with fuel equivalence ratios ranging from 2.22 to 2.49. The iron concentration was 1 mole Fe/10,000 moles C in the flame, while the manganese concentration was 1 mole Mn/14,600 moles C in the flame. Light absorption and laser light scattering techniques were used to measure the soot particle size, concentration, and rate of growth. Low molecular weight, stable gas phase species concentrations were measured by gas sample withdrawal and gas chromatography. Laser induced fluorescence was used to measure relative changes in the gas phase polycyclic aromatic hydrocarbon (PAH) concentration. PAH samples were also collected for analysis using gas and liquid chromatography. A thermophoretic probe withdrew samples for transmission electron microscopy and image analysis.

The additives increased the amount of soot formed under all conditions, up to a factor of 3. Iron increased the soot volume fraction more than manganese. The iron additive also caused up to a 6-fold increase in the fluorescence coefficient, while the manganese additive had little effect on fluorescence. The fluorescence coefficient was approximately proportional to the total tar concentration. The additives did not cause a detectable change in the concentration of any of the low molecular weight, stable gas phase species up through benzene. The additives did not have a measurable effect on soot particle inception or soot particle collision rates.

Equilibrium calculations were used to predict the chemical states of the additives in the flame. At high temperatures, both iron and manganese were predicted to exist in the gas phase, predominantly as free metal atoms. As the flame temperature decreased, iron was predicted to precipitate out of the gas phase as metallic iron, while manganese was predicted to form solid MnO.

Metallic iron on the surface of the growing soot particles was hypothesized to catalyze acetylene deposition to form soot. A reaction probability between acetylene and an iron site of about 0.023 fit the measurements reasonably well. To calculate the fraction of the particle surface covered by iron, two limiting cases were investigated: infinitely slow diffusion of iron through soot, and infinitely fast diffusion of iron through soot. The experimental measurements fell between the two limiting cases. Predictions of the fraction of the particle surface covered by iron ranged from about 0.5% to 3%. Metallic iron on the surface of the soot was also hypothesized to catalyze PAH formation.

Thesis Supervisors: Professor A. F. Sarofim
Professor J. P. Longwell

ACKNOWLEDGEMENTS

As I near the end of my stay at MIT and I contemplate graduation, I realize that many people have helped me get through MIT and complete my degrees, and I gratefully say thank you to you all. Six years is far too short a time to spend among such talented and admirable people. I got to know half of you only half as well as I would have liked, and I have properly thanked half of you only half as well as you deserved. To at least partially remedy the situation, I must acknowledge:

Dino Megaridis, who helped me with the design of the thermophoretic probe;

Mike Frongillo, who helped me with the electron microscopy and image analysis;

Pedro Bolsaitis, Lenore Rainey, and Art Lafleur, who helped me with the PAH sampling and chemical analysis;

Judy Wornat, Shin-Gyoo Kang, Karl Graham, Zhiyou Du, and Jean-Charles de Hemptinne, who helped me survive life in 66-125 and 66-153;

Arun Chandavarkar, and everyone who went to Brookhaven and NL, who helped me survive Practice School;

and Tony Modestino, who helped me with almost everything.

I owe extra special thanks to:

Jim Rees, who didn't stop me from jumping out of an airplane when he had the chance;

Benjamin Pease, Melissa Ko, and Martha Morgan, who didn't quit when they had the chance;

Ann Westerheim, and everyone on the Tang Hall Residents Association Executive Committee, who didn't impeach me when they had the chance;

Greg Chamitoff, and all the other residents of apartment 6B over the years, who didn't throw me out when they had the chance;

Professors J. M. Beér and J. B. Howard, who didn't fall asleep when they had the chance;

Professors A. F. Sarofim and J. P. Longwell, who didn't fire me when they had the chance;

and of course,

my brother, Richard Feitelberg, who didn't kill me when he had the chance;

and my Mom and Dad, who had me when they had the chance.

Alan S. Feitelberg
July 16, 1990

TABLE OF CONTENTS

	<i>page</i>
ABSTRACT	2
ACKNOWLEDGEMENTS	3
TABLE OF CONTENTS	4
LIST OF SYMBOLS	7
LIST OF FIGURES	12
LIST OF TABLES	17
1. INTRODUCTION	18
1.1 Background and Motivation	18
1.2 Thesis Objectives	22
1.3 Method of Approach	24
2. LITERATURE REVIEW	25
2.1 Particle Shape and Size Distributions	25
2.2 Light Scattering Theory	32
2.2.1 Small Homogeneous Spheres	35
2.2.2 Small Coated Spheres	41
2.2.3 Small Homogeneous Spheroids	43
2.2.4 Homogeneous Spheres of Arbitrary Size	45
2.2.5 Gases	47
2.3 Laser Induced Fluorescence	48
2.4 The Refractive Index of Soot	53
2.5 Soot Formation	57
2.5.1 Soot Particle Inception	57
2.5.2 Soot Particle Collisions, Coalescence, and Coagulation	58
2.5.3 Soot Surface Growth	60
2.5.4 Soot Oxidation	62
2.6 Effects of Metal Additives on Soot Formation	63
2.6.1 Practical Combustion Systems	63
2.6.2 Laboratory-Scale Systems and Mechanisms	64

Table of Contents (continued)

3. EXPERIMENTAL APPARATUS AND TECHNIQUES	67
3.1 Premixed Flame Burner	67
3.2 Temperature Measurements	74
3.3 Absorption, Scattering, and Fluorescence Measurements	75
3.4 Gas Sample Withdrawal and Analysis	79
3.5 Thermophoretic Sampling and Analysis	85
3.6 Bulk Solid and PAH Sampling	97
4. EXPERIMENTAL RESULTS	102
4.1 Path Length Measurements	102
4.2 Absorption Measurements	104
4.3 Scattering Coefficient Measurements	104
4.4 Fluorescence Coefficient Measurements	111
4.5 Depolarization Ratio Measurements	115
4.6 Temperature Measurements	120
4.7 Low Molecular Weight Species Concentrations	125
4.8 High Molecular Weight Species Concentrations	128
4.9 Particle Size and Shape Distribution Measurements	142
5. INTERPRETATION OF EXPERIMENTAL RESULTS	149
5.1 Calculation of Residence Time	149
5.2 Interpretation of Optical Measurements	149
5.2.1 Comparison of Rayleigh Theory and Lorenz-Mie Theory	150
5.2.2 Comparison of Homogeneous Sphere and Coated Sphere Theory	152
5.2.3 The Use of a Volume Weighted Average Refractive Index	155
5.2.4 Comparison of Spheroid Theory and Particle Shape Data	159
5.3 Soot Volume Fraction	160
5.4 Geometric Mean Soot Particle Diameter	165
5.5 Soot Particle Number Density	169
5.6 Soot Particle Surface Area per Unit Volume	173
5.7 Soot Mass Addition Rate	176

Table of Contents (continued)

6. EQUILIBRIUM CALCULATIONS	180
6.1 Water-Gas Shift Equilibration	180
6.2 Acetylene-Diacetylene Equilibration	180
6.3 Chemical State of Iron and Manganese	181
6.4 Chemical State of Calcium, Barium, and Sodium	184
7. CATALYZED ACETYLENE DEPOSITION MODEL	188
7.1 Model Assumptions	188
7.2 Comparison of Measurements and Model Predictions	190
8. SUMMARY AND CONCLUSIONS	196
APPENDIX A: Calibration of Optical Pyrometer	198
APPENDIX B: Calibration and Alignment of Light Scattering Apparatus	200
APPENDIX C: Correction of Mole Fractions to Account for Water Condensation	206
APPENDIX D: Thermophoretic Sampling Probe Timing Circuit	212
APPENDIX E: Validity of Light Scattering Assumptions	215
REFERENCES	216
PRODUCTION NOTE	229

LIST OF SYMBOLS

a	core radius of a coated sphere
A	length of longest axis of a spheroid
A_f	field area (total area on screen of image analyzer)
A_N	Avogadro's number, 6.023×10^{23}
A_p	projected area of a particle resting in a stable position
b	overall radius of a coated sphere
B	breadth of projected area of a particle
B	length of shorter axis of a spheroid
c_2	Planck's second constant, 1.43847 cm K
C	length of third axis of a spheroid
\hat{C}_p	heat capacity at constant pressure per unit mass
C_{vv}	differential scattering cross-section per molecule
$C_{vv,rel}$	scattering cross-section of species i relative to N_2 , $C_{vv,i}/C_{vv,N_2}$
d	diameter
d_a	projected area diameter
d_c	perimeter diameter
d_g	geometric mean diameter
d_{mode}	modal diameter
e_s	eccentricity of an ellipse or a spheroid
E	voltage
E_r	elongation ratio (length/breadth)
f_v	volume fraction
f_v^*	ultimate soot volume fraction
f_N	ratio of sixth moment to square of third moment of diameter distribution
F	Rayleigh light scattering function for homogeneous spheres
F_c	Rayleigh light scattering function for coated sphere
G	Rayleigh light absorption function for homogeneous spheres
\dot{G}	volumetric gas flow rate
G_c	Rayleigh light absorption function for coated spheres

List of Symbols (continued)

i	square root of (-1)
I	transmitted intensity
I_c	current
I_0	incident intensity
k	imaginary part of refractive index
k_B	Boltzmann constant, R/A_N , 1.3805×10^{-23} J/K
k_c	thermal conductivity
k_{eff}	imaginary part of effective refractive index of coated sphere
k_{HW}	Harris and Weiner (1983(a),1983(b)) soot growth rate constant
k_{sg}	empirical soot surface growth rate constant
K_{ac}	equilibrium constant for the acetylene-diacetylene reaction
K_{ext}	extinction coefficient
K_{wg}	equilibrium constant for the water-gas shift reaction
l	mean free path of a gas
L	path length through an absorbing medium
L', L''	components of polarizabilities of spheroids
L_m	maximal chord length of projected area of particle
m	complex index of refraction, $n - k i$
\bar{m}	volume weighted average refractive index of a coated sphere
m_{eff}	effective refractive index of a multicomponent particle, $n_{eff} - k_{eff} i$
m_i	refractive index of core of coated sphere, $n_i - k_i i$
m_o	refractive index of outer layer of coated sphere, $n_o - k_o i$
m_{soot}	mass of soot per unit volume
m_{th}	coefficient from free-molecule coagulation theory
M	molecular weight
n	real part of refractive index
n_{eff}	real part of effective refractive index of coated sphere
N	number density (number of particles per unit volume)
n_0	real refractive index of a gas at T_0, P_0, λ_0
p	particle size distribution function

List of Symbols (continued)

P	pressure
P_c	perimeter of projected outline of a particle
Pe', Pe''	depolarization factors for oblate and prolate spheroids
P_{vp}	vapor pressure
P_0	power
q	ratio of core radius to overall radius of a coated sphere
$Q_{f\lambda} \Delta\lambda$	fluorescence coefficient
$Q_{f,h}, Q_{f,v}$	vertically and horizontally polarized components of fluorescent light
Q_w, Q_{vh}, Q_{hh}	scattering coefficients
r	radius
R	ideal gas constant, 8.314 J/mol K
R_e	electrical resistance
s	estimated standard deviation
S	total surface area per unit volume
s^2	estimated variance
s_g	estimated geometric mean standard deviation
s_g^2	estimated geometric mean variance
T	temperature
T_{br}	brightness temperature
t	time
v	velocity
V	volume
V_0	scattering volume
\bar{x}	estimated mean value of distributed variable x
x_g	estimated geometric mean value of distributed variable x
x_i	mole fraction of species i
Z	molecular collision rate

GREEK SYMBOLS

α	dimensionless particle diameter, $\pi d/\lambda$
----------	--

List of Symbols (continued)

α_{sp}	constant arising from the self-preserving size distribution
α_t	thermal diffusivity, $k_c / \rho \hat{C}_p$
α', α''	polarizabilities of oblate and prolate spheroids
α_λ	spectral absorptivity
β	dimensionless overall size of a coated sphere, $2\pi b / \lambda$
γ	reaction probability or collision efficiency
$\Delta\lambda$	integrated area of percent transmitted versus wavelength curve
ε_λ	spectral emissivity
ε	complex electrical permittivity, $\varepsilon = \varepsilon_1 - i\varepsilon_2$
ε_0	permittivity of free space, $8.854 \times 10^{-12} \text{ C}^2 / \text{N m}^2$
η	efficiency
θ	scattering angle
κ	absorption index
λ	wavelength of light
λ_e	excitation wavelength
μ	average or mean value
μ_g	geometric mean
μ_{med}	median
μ_{mode}	mode
ν	frequency
π	pi, 3.14159265359...
ρ	density
ρ_ν	depolarization ratio, $Q_{\nu h} / Q_{\nu w}$
ρ_ν^T	total depolarization ratio for a gas, including Raman lines
ρ_ν^c	depolarization ratio of central Rayleigh line of a gas
σ	standard deviation
σ^2	variance
σ_g	geometric mean standard deviation
σ_g^2	geometric mean variance
σ_0	width parameter of the zeroth order lognormal distribution

List of Symbols (continued)

τ	transmissivity
τ_d	thermophoretic probe delay time
τ_e	thermophoretic probe exposure time
τ_i	thermophoretic probe insertion time
τ_q	quench time
τ_w	thermophoretic probe withdrawal time
φ	fuel equivalence ratio
ψ', ψ''	components of polarizabilities of spheroids
Ω	solid angle

ACRONYMS

CMT	cyclopentadienyl manganese tricarbonyl
FID	flame ionization detector
GC	gas chromatography
HAB	height above burner
LC	liquid chromatography
LNSD	lognormal size distribution
MMT	methylcyclopentadienyl manganese tricarbonyl
MSD	monodisperse size distribution
NSD	normal size distribution
PAH	polycyclic aromatic hydrocarbon
PMT	photomultiplier tube
SLPM	standard liters per minute
SPSD	self-preserving size distribution
TEM	transmission electron microscope
TSP	thermophoretic sampling probe
ZOLD	zeroth order lognormal size distribution

LIST OF FIGURES

Figure	Description	<i>page</i>
1.1-1	A pictorial representation of soot formation in a premixed flame	20
2.1-1	Illustration of maximal chord length and breadth for irregularly shaped particles resting in a stable position on a plane	26
2.2-1	Geometry of light scattering and absorption	33
2.2.1-1	Surface and contour maps of the Rayleigh function $F(n, k)$	37
2.2.1-2	Surface and contour maps of the Rayleigh function $G(n, k)$	38
2.2.1-3	Dependence of characteristic diameter on refractive index	40
2.2.1-4	Dependence of number density on refractive index	40
2.2.2-1	Geometry of coated spheres	41
2.3-1	Energy level diagram for fluorescence	50
2.4-1	The refractive index of soot, as determined by four groups	55
3.1-1	The premixed flame burner and additive feed system	68
3.1-2	Comparison of the measured and expected ferrocene feed rates	71
3.1-3	Comparison of the measured and expected cyclopentadienyl manganese tricarbonyl feed rates	72
3.3-1	The light absorption apparatus	76
3.3-2	The light scattering apparatus	78
3.3-3	Transmission characteristics of laser line filters used for scattering and fluorescence measurements	80
3.4-1	The gas sampling apparatus	81
3.4-2	The water-cooled quartz probe used for gas sampling	82
3.5-1	The thermophoretic sampling probe system	89
3.5-2	Detail of the thermophoretic sampling probe	91
3.5-3	The circuit used to calibrate the motion of the thermophoretic sampling probe	92

Figure	Description	page
3.5-4	A typical trajectory of the thermophoretic sampling probe	92
3.5-5	The thermophoretic sampling probe insertion time and withdrawal time	93
3.5-6	The thermophoretic sampling probe delay time and exposure time	94
3.6-1	The bulk solid and PAH sample collection system	98
4.1-1	Profiles of premixed flame diameter	103
4.2-1	Extinction coefficient measurements in the $C/O = 0.74$ and $C/O = 0.77$ flames, both with and without additives	105
4.2-2	Extinction coefficient measurements in the $C/O = 0.80$ and $C/O = 0.83$ flames, both with and without additives	106
4.3-1	Scattering coefficient measurements in the $C/O = 0.74$ and $C/O = 0.77$ flames, both with and without additives	107
4.3-2	Scattering coefficient measurements in the $C/O = 0.80$ and $C/O = 0.83$ flames, both with and without additives	108
4.3-3	Estimated fraction of measured scattering coefficient due to scattering from gas molecules	110
4.4-1	Correction of fluorescence measurements to account for contribution from scattering	112
4.4-2	Comparison of measured and corrected fluorescence coefficients in the $C/O = 0.83$ flame	114
4.4-3	Fluorescence coefficient measurements in the $C/O = 0.77$ and the $C/O = 0.83$ flames, both with and without the iron additive	116
4.4-4	Fluorescence coefficient measurements in the $C/O = 0.80$ and $C/O = 0.80 + Mn$ flames	117
4.5-1	Depolarization ratio measurements in the $C/O = 0.74$ and $C/O = 0.77$ flames, both with and without additives	118
4.5-2	Depolarization ratio measurements in the $C/O = 0.80$ and $C/O = 0.83$ flames, both with and without additives	119
4.6-1	Temperature measurements in the $C/O = 0.74$ and $C/O = 0.77$ flames, both with and without additives	121
4.6-2	Temperature measurements in the $C/O = 0.80$ and $C/O = 0.83$ flames, both with and without additives	122

Figure	Description	page
4.6-3	Comparison of measured temperature and estimated temperature in the $C/O = 0.77$ flame	124
4.6-4	Temperature measurements in the $C/O = 0.52$ flame	126
4.7-1	Overview of the gas phase composition in the $C/O = 0.77$ flame	127
4.7-2	Methane and acetylene concentration profiles in the $C/O = 0.77$, $C/O = 0.77 + Mn$, and $C/O = 0.77 + Fe$ flames	129
4.7-3	Ethylene and ethane concentration profiles in the $C/O = 0.77$, $C/O = 0.77 + Mn$, and $C/O = 0.77 + Fe$ flames	130
4.7-4	Allene (propadiene) and methyl acetylene concentration profiles in the $C/O = 0.77$, $C/O = 0.77 + Mn$, and $C/O = 0.77 + Fe$ flames	131
4.7-5	Diacetylene and vinyl acetylene concentration profiles in the $C/O = 0.77$, $C/O = 0.77 + Mn$, and $C/O = 0.77 + Fe$ flames	132
4.7-6	Benzene and 1,3-butadiene concentration profiles in the $C/O = 0.77$, $C/O = 0.77 + Mn$, and $C/O = 0.77 + Fe$ flames	133
4.7-7	Concentration profiles of the fixed gases in the $C/O = 0.77$ and $C/O = 0.77 + Fe$ flames	134
4.7-8	Empirical correlation of mole fraction acetylene with C/O ratio and height above burner	135
4.8-1	Total tar concentrations in the $C/O = 0.83$ and $C/O = 0.83 + Fe$ flames	136
4.8-2	Correlation of fluorescence coefficient and total tar concentration	136
4.8-3	Concentrations of naphthalene and acenaphthylene in the $C/O = 0.83$ and $C/O = 0.83 + Fe$ flames	138
4.8-4	Concentrations of fluorene and phenanthrene in the $C/O = 0.83$ and $C/O = 0.83 + Fe$ flames	139
4.8-5	Concentrations of anthracene and fluoranthene in the $C/O = 0.83$ and $C/O = 0.83 + Fe$ flames	140
4.8-6	Concentration of pyrene in the $C/O = 0.83$ and $C/O = 0.83 + Fe$ flames	141
4.9-1	Typical transmission electron micrograph of soot particles collected from the $C/O = 0.77$ flame	143
4.9-2	The projected area diameter distribution in the $C/O = 0.77$ flame, 12.5 mm from the burner surface	145
4.9-3	The projected area diameter distribution in the $C/O = 0.77$ flame, 17.5 mm from the burner surface	146

Figure	Description	page
4.9-4	The elongation ratio distribution in the $C/O = 0.77$ flame	147
5.2.1-1	Comparison of particle diameters in the $C/O = 0.83$ flame, calculated using either Rayleigh theory or Lorenz-Mie theory	151
5.2.2-1	Results of coated sphere analysis of absorption measurements	154
5.2.3-1	Comparison of the volume weighted average refractive index and the effective refractive index of coated spheres containing iron and soot	157
5.2.3-2	Overlay of Figure 5.2.3-1 onto Figures 2.2.1-3 and 2.2.1-4	158
5.2.4-1	Comparison of measured depolarization ratio and the depolarization ratio calculated from thermophoretic probe shape measurements	161
5.3-1	Soot volume fraction profiles in the $C/O = 0.74$ and $C/O = 0.77$ flames, both with and without additives	163
5.3-2	Soot volume fraction profiles in the $C/O = 0.80$ and $C/O = 0.83$ flames, both with and without additives	164
5.4-1	Optically determined particle diameters in the $C/O = 0.74$ and $C/O = 0.77$ flames, both with and without additives	166
5.4-2	Optically determined particle diameters in the $C/O = 0.80$ and $C/O = 0.83$ flames, both with and without additives	167
5.4-3	Comparison of geometric mean particle diameters in the $C/O = 0.77$ flame, as determined optically and by the thermophoretic probe	168
5.5-1	Soot particle number density profiles in the $C/O = 0.74$ and $C/O = 0.77$ flames, both with and without additives	170
5.5-2	Soot particle number density profiles in the $C/O = 0.80$ and $C/O = 0.83$ flames, both with and without additives	171
5.5-3	Demonstration of the method used to determine the best-fit of number density measurements to free-molecule coagulation theory	172
5.6-1	Soot surface area per unit volume in the $C/O = 0.74$ and $C/O = 0.77$ flames, both with and without additives	174
5.6-2	Soot surface area per unit volume in the $C/O = 0.80$ and $C/O = 0.83$ flames, both with and without additives	175
5.7-1	Soot mass addition rates in the $C/O = 0.74$ and $C/O = 0.77$ flames, both with and without additives	177
5.7-2	Soot mass addition rates in the $C/O = 0.80$ and $C/O = 0.83$ flames, both with and without additives	178

Figure	Description	page
6.1-1	Comparison of gas phase composition measurements and the water-gas shift equilibrium constant	182
6.2-1	Comparison of gas phase composition measurements and the acetylene-diacetylene reaction equilibrium constant	182
6.3-1	Equilibrium prediction of the chemical state of iron in the C/O = 0.77 + Fe flame	183
6.3-2	Equilibrium prediction of the chemical state of manganese in the C/O = 0.77 + Mn flame	185
6.4-1	Equilibrium prediction of the chemical state of calcium added to the C/O = 0.74 and C/O = 0.83 flames	186
6.4-2	Equilibrium prediction of the chemical state of barium added to the C/O = 0.74 and C/O = 0.83 flames	186
6.4-3	Equilibrium prediction of the chemical state of sodium added to the C/O = 0.74 and C/O = 0.83 flames	187
7.2-1	Comparison of soot volume fraction measurements in flames with iron additives and catalyzed acetylene deposition model	191
7.2-2	Comparison of soot volume fraction measurements in flames with iron additives and catalyzed acetylene deposition model	192
7.2-3	Model predictions of the fraction of the total soot surface area covered by iron	193
A-1	The circuit used to test the calibration of the optical pyrometer	199
A-2	The variation of lamp brightness temperature with current	199
B-1	Geometry of scattering volume	203
B-2	Demonstration of the alignment of the light scattering apparatus	205
B-3	Demonstration of the alignment of the light scattering apparatus	205
C-1	Diagram of gas sampling apparatus and the mass balance system	207
C-2	Sum of the <i>in situ</i> mole fractions calculated by three different methods	210
D-1	Schematic diagram of thermophoretic sampling probe timing circuit	213
D-2	Calibration of the thermophoretic sampling probe timing circuit	214

LIST OF TABLES

Table	Description	<i>page</i>
2.2.5-1	Optical properties of some common gases	49
3.1-1	Premixed flame gas flow rates	69
3.1-2	Metal additive feed rates	69
3.4-1	Stable species found in gas samples	86
3.4-2	GC calibration standards	87
3.4-3	Stable species with known retention times, but not found in gas samples	88
3.6-1	PAH species identified using gas chromatography	100
3.6-2	PAH species identified using liquid chromatography	101
4.8-1	Range of concentrations of the PAH species identified via liquid chromatography in the $C/O = 0.83$ and $C/O = 0.83 + Fe$ flames	141
5.5-1	Results of coagulation theory best-fit calculations	172
C-1	Summary of mass balance methods and results	210

1. INTRODUCTION

1.1 Background and Motivation

The incomplete combustion of hydrocarbon fuels often results in the formation of the solid carbonaceous particles known as soot. In practical combustion systems, soot is emitted in the form of agglomerates containing up to several dozen primary particles. While the agglomerate size and shape can vary widely, the primary particles are roughly spherical in shape, with diameters ranging from about 10 to 40 nm. The composition and molecular structure of the primary particles are also variable, and depend upon the type of combustor, the time-temperature history of the particles in the combustor, and the presence or absence of inorganic matter in the fuel. In general, soot particles consist mainly of carbon and hydrogen with a mole ratio ranging from about 1:1 for the youngest isolable particles to about 8:1 for the oldest particles (Palmer and Cullis, 1965).

Soot has been recognized as a human health hazard since 1775, when Sir Percival Pott first linked soot to skin cancer in man. Later studies revealed that soot is harmful because it is a carrier of carcinogens. Polycyclic aromatic hydrocarbons (PAH) like naphthalene and fluoranthene are frequently found in soot particles (Homann and Wagner, 1967). Soot particles can be in the respirable size range ($\sim 0.1 \mu\text{m}$ to $\sim 5.0 \mu\text{m}$ in diameter), making them carriers that can introduce PAH into the body via the respiratory tract. The toxic, carcinogenic, and mutagenic properties of many PAH have been widely reported (Sax, 1984; National Cancer Institute, 1985) and are the subject of continuing research (Wornat, 1988; Lam, 1988(b)).

Although less widely publicized than the effects on human health, soot emissions have serious effects on other species. For example, in some areas of England, the common form of *Biston betularia* (also named the peppered moth because of its mottled wings) has been replaced by *Biston betularia* f. *carbonaria*, a black-winged phenotype. In these regions, soot emissions from nearby industries have killed the lichens normally growing on trees and turned the tree barks black. In a classic series of experiments, Kettlewell (1961) showed that an ordinary peppered moth is camouflaged well on a lichen-covered tree but is easily seen and eaten by birds when resting on a blackened tree trunk. A member of the black phenotype resting on a blackened tree trunk is much less likely to be seen and eaten.

The phenomenon of dark phenotypes replacing light phenotypes has been observed in 170 moth species in the United States and England (Curtis, 1979).

The frescoes in the Sistine Chapel, painted by Michelangelo in 1508, have also turned black because of soot emissions. Until the invention of the electric light, the Chapel was lit by tallow candles that deposited soot and grease on the frescoes, obscuring the true colors (Hughes, 1985; Hughes, 1987). The original colors are now being seen for the first time in centuries; a 12 year cleaning program is expected to be completed by 1992.

In addition to causing these undesirable effects when released into the environment, soot can deposit within and foul combustion devices. The increased radiative heat transfer caused by soot particles can also damage some combustors (e.g., gas turbines). However, increased radiative heat transfer and soot particle formation are useful in other systems. The production of carbon black is one combustion process in which soot (or carbon black) formation is desirable.

For these reasons, a considerable effort has been expended on trying to understand the fundamental mechanisms of soot formation, with the hope that this understanding will lead to ways of controlling soot formation and emissions. Most workers agree that soot formation can be broadly broken down into the steps shown in Figure 1.1-1, a pictorial representation of the soot formation process in a premixed flame. Although soot formation is depicted as a linear process in Figure 1.1-1, some of the steps occur simultaneously or are bypassed in systems with mixing patterns that are more complex than the mixing in a premixed flame. The details of some of the steps are poorly understood and are the subject of heated debate (Baum, 1990).

The first step of combustion shown in Figure 1.1-1, the attack and destruction of the fuel molecule, occurs in both sooting and non-sooting systems. At typical combustion temperatures (1500 to 2000 K) free radical concentrations become significant, and free radical chemistry predominates in the gas phase. If enough oxygen is fed to the system, then almost all of the fuel can be converted into CO, CO₂, H₂O, and H₂. If the amount of O₂ fed to the system is decreased (the carbon to oxygen ratio of the feed is increased), then some of the fuel can be converted into low molecular weight hydrocarbons. Free radicals can participate in both destruction and molecular weight growth reactions, and if molecular weight growth reaction rates exceed destruction reaction rates, then aromatic molecules and

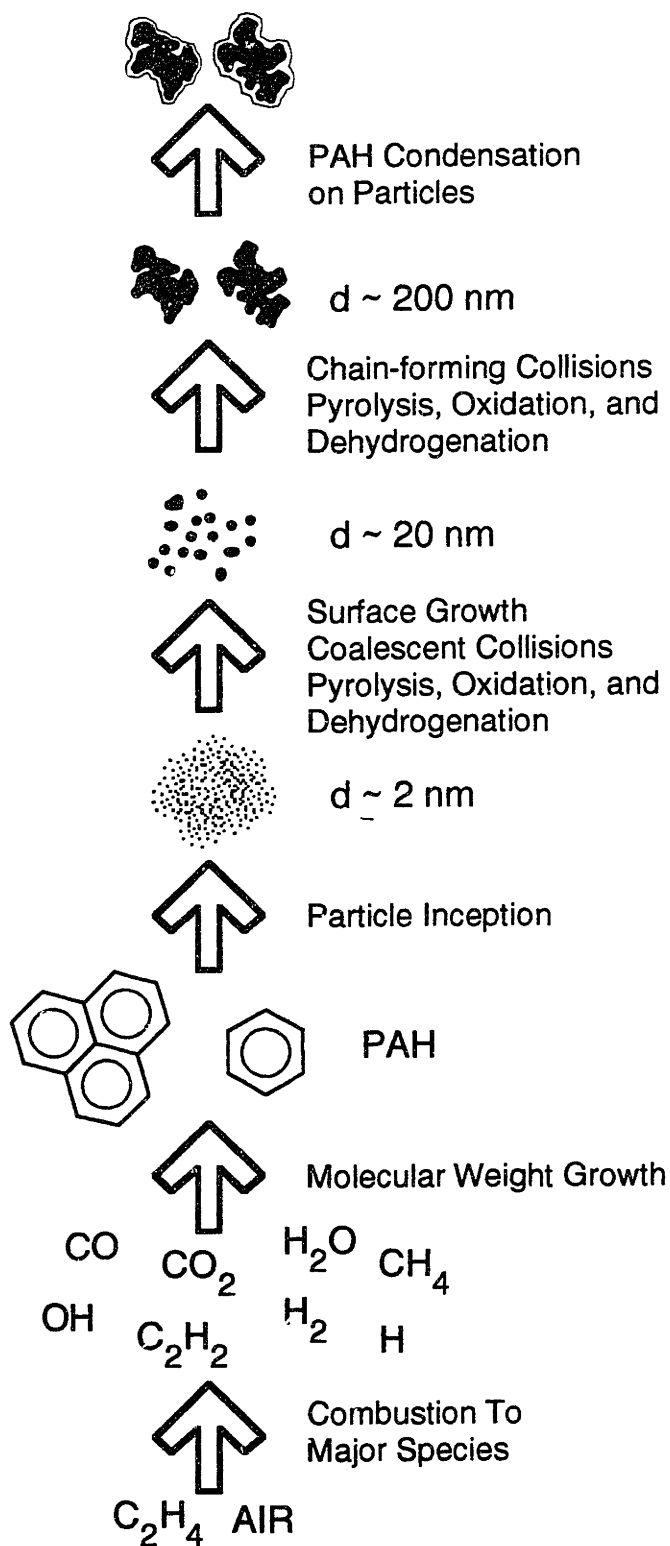


Figure 1.1-1: A pictorial representation of soot formation in a premixed flame.

PAH can form. State-of-the-art kinetic models can predict the gas phase chemistry up through the C_2 and some of the C_3 , C_4 , and higher species (Westmoreland, 1986).

If the carbon to oxygen ratio of the feed is increased even further, soot particle inception can take place. Particle inception is the formation of the first solid soot particles from the gas phase. The smallest detectable solid particles are about 1.5 nm in diameter, corresponding to a molecular weight of about 2130 amu (Wersborg, Fox, and Howard, 1975). Some believe that ions play an important role in particle inception (Wersborg, Yeung, and Howard, 1975; Calcote and Keil, 1988), while others believe that particle inception is a continuous molecular weight growth process, proceeding from low molecular species through PAH to soot (McKinnon, 1989). Another recent theory maintains that soot particle inception may proceed through "buckminsterfullerene," a C_{60} molecule with a truncated icosahedral structure (Zhang *et al.*, 1986). However, this theory has not gained widespread acceptance. In general, the theories describing particle inception are qualitative, although quantitative models are being developed (Harris *et al.*, 1986).

Once formed, soot particles begin to collide with and stick to each other. Free-molecule coagulation theory describes soot particle collision rates relatively well (Prado and Lahaye, 1981). However, the transition from coalescent collisions to chain-forming collisions is not well understood. A coalescent collision occurs when two particles collide and fuse into a single larger particle. A collision in which two particles collide and do not fuse, but retain their individual identities within an agglomerate, is a chain-forming collision.

Usually occurring simultaneously with particle collisions is surface growth, a gas-solid reaction that increases the mass of a particle. Harris and Weiner (1983(a), 1983(b)) believe that acetylene is the predominant soot growth species, while others believe that PAH may be the gas phase species that add to the particles (Lam, 1988(b)).

The soot mass growth rate observed in premixed flames is actually the net sum of surface growth reactions (which add mass) and pyrolysis, oxidation, and dehydrogenation reactions (which remove mass). Most workers agree that soot particles dehydrogenate while collisions and surface growth are taking place (Prado and Lahaye, 1981). Depending on the combustion conditions, mass loss through pyrolysis and oxidation may be significant in comparison to surface growth.

If the combustion aerosol is cooled, PAH can condense out of the gas phase onto the soot particles. This condensation differs from surface growth in that condensed PAH are physically adsorbed on the particle surface and can be removed without breaking any chemical bonds. The mass added to the particles by surface growth is chemically bonded to the particles.

One method often employed for reducing soot emissions is the use of soot-reducing fuel additives. However, the mechanisms of additive action are only qualitatively understood at best, partly due to the reported wide variations in additive effectiveness. For example, Weeks *et al.* (1959) found that an iron compound was most effective in an oil burner, followed in order by nickel, cobalt, and manganese naphthenates. In contrast, another study of naphthenates in an oil burner found the most effective to be cobalt, followed by manganese, iron, and nickel (Vaerman, 1964). In general, barium is the most effective inhibitor of soot formation among the group II metals, while manganese and iron are the most effective transition metals (Howard and Kausch, 1980). Transition metals are well known carbon oxidation catalysts (Figueiredo *et al.*, 1987). Howard and Kausch concluded that a better understanding of the mechanisms through which transition metal additives effect soot formation would be very useful.

Knowledge of the mechanisms of additive action may also aid in the understanding of soot formation during the combustion of fuels that inherently contain metals. Coal can contain compounds of silicon, aluminum, iron, calcium, magnesium, sodium, and potassium in concentrations ranging from 5 to 25% by weight (calculated as oxides). Residual fuel oils can contain nickel and vanadium, in the form of porphyrins, in concentrations up to 500 ppm (e.g., Perry and Chilton, 1973). Understanding the effects of metal additives on soot formation may also shed some light on the formation of soot from these fuels.

1.2 Thesis Objectives

The overall objective of this thesis was to develop a better understanding of how transition metal additives effect the soot formation process described in Section 1.1. The metals chosen for study were iron and manganese, the transition metals that Howard and Kausch (1980) found to be the most effective in reducing soot formation in practical systems. The questions to be answered in this thesis are how these metals affect the soot for-

mation process and become incorporated into soot particles. More specifically, the following hypotheses and questions are to be addressed:

1) Do transition metal additives influence soot particle inception?

A number of different researchers have proposed that metal additives can influence particle inception. Both increases (Ritrievi, 1984; Feugier, 1973; Feugier, 1978; Marinescu and Danescu, 1976) and decreases (Hayhurst and Jones, 1989; Bulewicz *et al.*, 1975) in soot particle inception have been reported. Most of the results that have been reported concern alkaline and alkaline earth metals.

2) Do transition metal additives influence particle collision rates?

Haynes *et al.* (1979) proposed that alkaline earth metal additives can decrease particle collision rates in premixed ethylene flames. Their hypothesis is that the additives increase the number of particles with an electrostatic charge, and that electrostatic repulsion decreases the particle collision rate. Although few studies have been conducted, transition metals have not been reported to act through this mechanism.

3) Do transition metal additives increase surface growth?

Ritrievi (1984) made this suggestion to explain increased soot mass addition rates in premixed ethylene flames. Metallic iron at the surface of a growing soot particle was believed to enhance the reaction probability between soot and the gas phase growth species. The ability of other transition metals to act through the same mechanism has not been established.

4) Do transition metal additives alter the gas phase composition?

Since soot particles grow and are oxidized through gas-solid reactions, a change in the gas phase composition may result in more or less soot. Jenkins (1972) has proposed that metals can catalytically dissociate water vapor to produce OH and H atom, thus increasing soot oxidation.

5) Do transition metal additives change the optical properties of soot?

Optical techniques have been used by many researchers to measure changes in the soot aerosol caused by metal additives. These techniques can be very sensitive to the effective refractive index of the particles, which depends upon the composition and structure of the particles.

6) Are the metals in a condensed phase or the gas phase in the flame?

The answer to this question is important to the answers of all of the other questions. For example, if a metal additive exists entirely in the vapor phase, then it can neither catalyze surface growth nor alter the effective refractive index of soot particles.

1.3 Method of Approach

To answer the questions described in Section 1.2, iron and manganese were added to premixed ethylene/oxygen/nitrogen flames with C/O ratios ranging from 0.74 to 0.83. Metals were added to the flame by saturating a nitrogen gas stream fed to the flames with a volatile organometallic compound. The iron concentration was 1 mole Fe/10,000 moles C in the flame, while the manganese concentration was 1 mole Mn/14,600 moles C in the flame. These concentrations are in the range typically used in practical systems.

To answer the first three questions listed in Section 1.2, light absorption and laser light scattering techniques were used to measure the soot particle size, concentration, and rate of growth. Flame temperatures were measured with an optical pyrometer.

To answer the fourth question, laser induced fluorescence was used to measure relative changes in the gas phase polycyclic aromatic hydrocarbon (PAH) concentration. In addition, solid samples and PAH were collected and analyzed using gas chromatography and high-performance liquid chromatography. Low molecular weight, stable gas phase species concentrations were measured by gas sample withdrawal and gas chromatography.

To answer the fifth question in Section 1.2, light scattering theory was used to develop a simple, graphical technique for evaluating the sensitivity of optically determined particle sizes and concentrations to changes in the composition and structure of the particles. In addition, a thermophoretic probe was used to withdraw soot samples for transmission electron microscopy and image analysis. To answer the sixth question, equilibrium calculations were performed to predict the chemical state of metal additives in the flames.

2. LITERATURE REVIEW

2.1 Particle Shape and Size Distributions

Soot is formed as an aerosol, a suspension of particles in a gas phase. In general, aerosol particles may be either liquid or solid, and may be either all the same size (monodisperse) or different sizes (polydisperse). The quantities typically used to characterize an aerosol include: volume fraction, f_v , defined as the total volume of particles per unit volume; number density, N , the total number of particles per unit volume; specific surface area, S , the total aerosol surface area per unit volume; and a characteristic particle dimension. For spherical particles, the characteristic particle dimension is the sphere diameter, d . For irregularly shaped particles, a single characteristic dimension may be difficult to define or measure.

Consider the projection of an irregularly shaped particle resting in a stable position on a plane, as shown in Figure 2.1-1 for a number of particle shapes. The projected area of a particle onto the stable plane will be denoted by A_p , and the perimeter of the projection will be denoted by P_c . The projected area diameter, d_a , defined as the diameter of the circle having the same area as the projected area of the particle, is one possible characteristic dimension. The projected area diameter can be calculated from measurements of A_p using

$$A_p = (\pi/4) d_a^2 \quad (2.1-1)$$

The perimeter diameter, d_c , is another possible characteristic dimension, and is defined as the diameter of the circle having the same perimeter as the projected outline of the particle. The perimeter diameter can be calculated from measurements of P_c using

$$P_c = \pi d_c \quad (2.1-2)$$

The projected area diameter and perimeter diameter are independent of the orientation of the projection, and are uniquely defined for a given projected area. Other frequently used diameters, such as Martin's diameter and Feret's diameter, depend upon the orientation of the projection, and are not uniquely defined for a given projection. Martin's diameter and Feret's diameter have meaning only when averaged over a large number of randomly oriented particles of similar shape, and will not be discussed here.

The maximal chord length, breadth, and elongation ratio are other parameters used to characterize irregularly shaped particles. A chord is a line segment connecting two points on the boundary of the projected particle area. The maximal chord length, L_m , is the longest of all possible chords for a given particle outline. The breadth, B , is the projection of the particle outline onto the normal to the maximal chord length. L_m and B are illustrated for the particles shown in Figure 2.1-1. The elongation ratio, E_r , is a measure of the circularity of the particles and is defined as

$$E_r = L_m/B \quad (2.1-3)$$

E_r is unity for spheres and greater than or equal to 1 for all other projected area shapes.

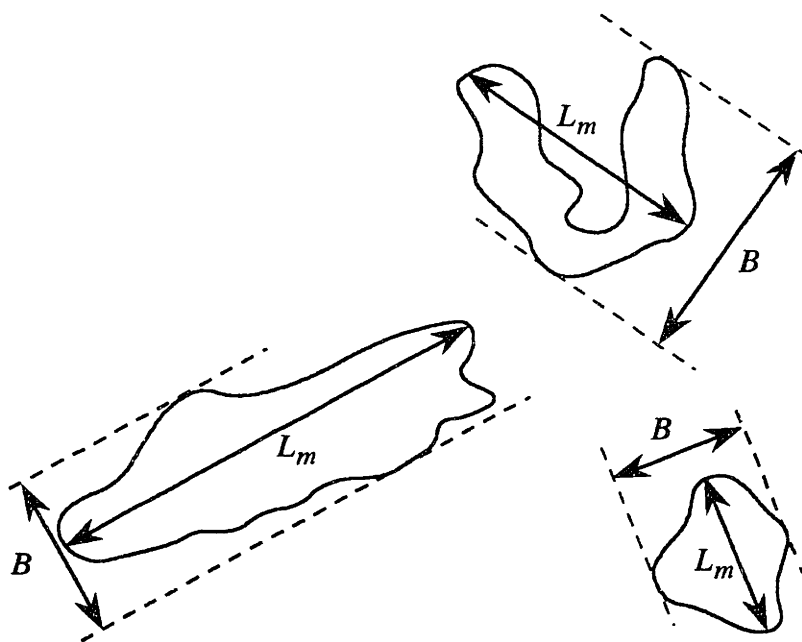


Figure 2.1-1: Illustration of maximal chord length and breadth for irregularly shaped particles resting in a stable position on a plane.

Aerosols are also characterized by their particle size distribution, $p(x)$, where x denotes a characteristic size parameter of the particles, such as diameter, surface area, or volume. If x represents the diameter, then $p(x)$ is called the diameter distribution; if x

represents the particle volume, then $p(x)$ is called the volume distribution. By definition, the fraction of particles in the size range from $x = x_1$ to $x = x_2$ is given by

$$\int_{x_1}^{x_2} p(x) dx \equiv \left\{ \begin{array}{l} \text{fraction of particles with} \\ \text{size between } x_1 \text{ and } x_2 \end{array} \right. \quad (2.1-4)$$

For all size distributions, the definition of $p(x)$ yields:

$$\int_{-\infty}^{\infty} p(x) dx \equiv 1 \quad (2.1-5)$$

Since x represents a physical dimension which cannot be negative, $p(x)$ is identically zero for $x \leq 0$ for most distributions, and in these cases the integration in Eq. 2.1-5 need be carried out only from zero to infinity. However, some distributions which have been used to describe aerosols admit negative values of x and, therefore, cannot be completely satisfactory.

Several quantities are commonly used to describe the shape of a distribution. The average or mean value of a distribution, μ , is defined as

$$\mu = \int_{-\infty}^{\infty} x p(x) dx \quad (2.1-6)$$

The geometric mean of a distribution, μ_g , is defined as

$$\ln \mu_g = \int_0^{\infty} (\ln x) p(x) dx \quad (2.1-7)$$

Thus, $\ln \mu_g$ is the average value of $\ln x$. The mode of a distribution, μ_{mode} , is the value of x at maximum frequency:

$$\left. \frac{dp}{dx} \right|_{\mu_{mode}} = 0 \quad (2.1-8)$$

The median of a distribution, μ_{med} , is the value of x below which 50% of the population falls:

$$\int_0^{\mu_{med}} p(x) dx = 0.5 \quad (2.1-9)$$

Most distributions are also characterized by a parameter which is a measure of the width or spread of the distribution. One such measure is the variance, σ^2 , defined as

$$\sigma^2 = \int_{-\infty}^{\infty} (x - \mu)^2 p(x) dx \quad (2.1-10)$$

The standard deviation of a distribution, σ , is defined as the square root of the variance. Similar to the definition of geometric mean, the geometric mean variance, σ_g^2 , is defined as:

$$\sigma_g^2 = \int_0^{\infty} (\ln x - \ln \mu_g)^2 p(x) dx \quad (2.1-11)$$

Thus, σ_g^2 is the variance of $\ln x$. The geometric mean standard deviation, σ_g , is defined as the square root of the geometric mean variance. Some authors also refer to a relative standard deviation, defined as σ/μ .

Dobbins, Santoro, and Semerjian (1983) have noted that a particular ratio of moments, which they call f_N , is a convenient measure of the width of a distribution, especially when interpreting light scattering measurements from spherical particles. The n^{th} moment of a distribution is defined as the mean value of x^n :

$$\langle x^n \rangle = \int_{-\infty}^{\infty} x^n p(x) dx \quad (2.1-12)$$

Equations 2.1-5 and 2.1-6 are actually the zeroth and first moments, respectively, of the distribution $p(x)$. For spherical particles, with $x = d$, the sphere diameter, Dobbins *et al.* define f_N as

$$f_N = \frac{\langle d^6 \rangle}{\langle d^3 \rangle^2} \quad (2.1-13)$$

In many cases, neither the aerosol particle shape nor the aerosol size distribution are known *a priori* and must be determined experimentally. The aerosol is an infinite population (in the statistical sense) from which a finite number of particle size and shape measurements can be made. If N measurements, x_1, x_2, \dots, x_N , are made of the distributed variable x , then the distribution parameters described above can only be estimated. The estimated mean, \bar{x} , and estimated geometric mean, x_g , are defined by

$$\bar{x} = \frac{1}{N} \sum_{i=1}^N x_i \quad (2.1-14)$$

$$\ln x_g = \frac{1}{N} \sum_{i=1}^N \ln x_i \quad (2.1-15)$$

The estimated variance, s^2 , estimated geometric mean variance, s_g^2 , and estimated n^{th} moment, \bar{x}^n , can be found from

$$s^2 = \frac{1}{N-1} \sum_{i=1}^N (x - \bar{x})^2 \quad (2.1-16)$$

$$s_g^2 = \frac{1}{N-1} \sum_{i=1}^N (\ln x - \ln x_g)^2 \quad (2.1-17)$$

$$\bar{x}^n = \frac{1}{N} \sum_{i=1}^N (x_i)^n \quad (2.1-18)$$

Volk (1980) lists a number of equivalent definitions for the estimated variance. The estimated standard deviation, s , and the estimated geometric mean standard deviation, s_g , are the square roots of s^2 and s_g^2 , respectively.

Several different size distributions have been used to describe soot aerosols. The simplest is the monodisperse size distribution (MSD):

$$p(x) = \begin{cases} 0, & x \neq x^* \\ 1, & x = x^* \end{cases} \quad (2.1-19)$$

where all particles have the same size, x^* . Substituting Eq. 2.1-19 into the appropriate definitions shows that $\mu = x^*$, $\sigma = 0$, and $f_N = 1$ for the MSD. All other unimodal distributions approach the MSD in the limit as $\sigma \rightarrow 0$.

Two other distributions that have been used to describe soot aerosols are the Gaussian or normal size distribution (NSD)

$$p(x) = \frac{1}{\sqrt{2\pi} \sigma} \exp \left\{ -\frac{(x - \mu)^2}{2 \sigma^2} \right\}, \quad -\infty < x < \infty \quad (2.1-20)$$

and the lognormal size distribution (LNSD)

$$p(x) = \frac{1}{\sqrt{2\pi} x \sigma_g} \exp \left\{ -\frac{(\ln x - \ln \mu_g)^2}{2 \sigma_g^2} \right\}, \quad x > 0 \quad (2.1-21)$$

Substituting Eq. 2.1-20 into the appropriate definitions shows that the mean of the NSD is μ , the variance is σ^2 , and $\mu = \mu_{med} = \mu_{mode}$. Substitution of Eq. 2.1-21 into the appropriate definitions shows that the geometric mean of the LNSD is μ_g , the geometric mean variance is σ_g^2 , $\mu_{med} = \mu_g$, and

$$f_N = \exp(9 \sigma_g^2) \quad (2.1-22)$$

$$\mu_{mode} = \mu_g \exp(-\sigma_g^2) \quad (2.1-23)$$

$$\langle x^n \rangle = \mu_g^n \exp\left(\frac{n^2 \sigma_g^2}{2}\right) \quad (2.1-24)$$

Another size distribution that has been used to describe soot aerosols is the zeroth order lognormal size distribution (ZOLD), defined as

$$p(x) = \frac{\exp\left(-\frac{1}{2} \sigma_0^2\right)}{\sqrt{2\pi} \sigma_0 \mu_{mode}} \exp\left\{-\frac{(\ln x - \ln \mu_{mode})^2}{2 \sigma_0^2}\right\}, \quad x > 0 \quad (2.1-25)$$

where σ_0 is a measure of the width and skewness of the distribution. Substitution of Eq. 2.1-25 into the appropriate definitions shows that the mode of the ZOLD is μ_{mode} and

$$f_N = \exp(9 \sigma_0^2) \quad (2.1-26)$$

$$\sigma = \mu_{mode} \left[\exp(4 \sigma_0^2) - \exp(3 \sigma_0^2) \right]^{1/2} \quad (2.1-27)$$

$$\langle x^n \rangle = \mu_{mode}^n \exp\left(\frac{n(n+2) \sigma_0^2}{2}\right) \quad (2.1-28)$$

The self-preserving size distribution (SPSD) has been developed by Friedlander and coworkers (Swift and Friedlander, 1964; Wang and Friedlander, 1967) to describe aerosols coagulating as a result of Brownian motion. The SPSP is based upon the hypothesis that aerosols coagulating through Brownian motion will approach the same reduced particle volume distribution, regardless of the initial distribution, after a sufficiently long period of time. The reduced particle volume is the particle volume V divided by the mean particle volume \bar{V} . The width of the SPSP is invariant. Graham and Robinson (1976) have compared numerical calculations of the SPSP performed by three groups, and have determined that the best estimate of the SPSP gives

$$f_N = 2.0788 \quad (2.1-29)$$

Nenniger (1986) and McMurray and Friedlander (1978) have shown that self-preserving solutions to the aerosol dynamics equations can arise even if surface growth is occurring simultaneously with Brownian-motion driven collisions and coagulation.

All of the distributions described above have been used to describe soot aerosols. D'Alessio and coworkers (D'Alessio *et al.*, 1973; D'Alessio *et al.*, 1977), Haynes and

coworkers (Haynes *et al.*, 1979; Haynes *et al.*, 1982), and Baumgärtner *et al.* (1984) assumed that the soot particles formed in premixed flames were spherical and monodisperse ($f_N = 1$). Bonczyk (1983) and Gomez *et al.* (1987) assumed that the soot particles formed in diffusion flames were spherical and monodisperse. In another study, D'Alessio *et al.* (1975) used the LNSD, with σ_g ranging from 0 to 0.3 (f_N from 1 to 2.25), to interpret light scattering measurements in premixed flames. Prado *et al.* (1981) used the LNSD, with $\sigma_g = 0.2$ ($f_N = 1.43$), to interpret optical measurements in premixed propane/oxygen flames. Bockhorn and coworkers (Bockhorn *et al.*, 1982; Bockhorn *et al.*, 1984) used the LNSD, with a relative standard deviation of 0.34, in a study of hydrocarbon/oxygen flames. Ramer *et al.* (1986) assumed the ZOLD was appropriate in a study of premixed methane/oxygen flames. Harris and Weiner (1983(a), 1983(b), 1984(a), 1984(b)) assumed the soot aerosols in premixed ethylene flames and premixed ethylene/toluene flames followed the SPSD.

The range of assumptions concerning the shape and width of the soot particle size distribution is not surprising, considering that relatively few studies have been conducted in which either the shape or the width were measured. Wersborg *et al.* (1973) measured the soot size distribution in a low pressure acetylene oxygen flame. A molecular beam sampling system, electron microscopy, and image analysis were used to measure the projected area diameter. The distribution progressed from Gaussian to lognormal, with the estimated relative standard deviation (s/\bar{d}_a) increasing from about 0.2 to 0.5. Charalampopoulos and Felske (1987) assumed that the soot aerosols formed in their premixed methane oxygen flames followed the ZOLD, and determined the width from photon correlation measurements. They found the distribution broadened with increasing height above the burner, with $f_N = 1.17$ at 6 mm and $f_N = 1.52$ at 16 mm. Megaridis (1987) measured the soot size distribution in an ethylene diffusion flame. Samples were withdrawn thermophoretically and the projected area diameter was measured using transmission electron microscopy and image analysis. The relative standard deviation (s/\bar{d}_a) of the primary particles was found to vary from 0.13 to 0.22. Additional measurements of the soot particle size distribution have been reported by Bonne *et al.* (1965) and Bockhorn *et al.* (1981).

Several workers have predicted that soot aerosols formed in premixed flames

should rapidly approach the SPSPD once particle inception ceases, even if surface growth is occurring (Harris and Kennedy, 1988; Kennedy, 1984). However, the direct experimental measurements described above have failed to verify this prediction. There are considerable experimental difficulties associated with measuring the *in situ* soot aerosol size distribution. If a sample is removed from a flame for image analysis, then the quenching must be sufficiently rapid to prevent additional collisions and surface growth during sampling. Otherwise, the measured size distribution may be more representative of processes occurring during sampling than processes occurring in the flame. The *in situ* optical technique used by Charalampopoulos and Felske avoids this problem, but the effect of non-sphericity on photon correlation measurements is unknown. Several workers have suggested that *in situ* soot particles can be non-spherical aggregates (Megaridis, 1987; Prado *et al.*, 1981), and that the deviations from sphericity may be large enough to have a significant effect on optical measurements (Dobbins and Megaridis, 1990; Kumar and Tien, 1989). Very little quantitative information is available concerning the soot particle shape distribution and its evolution as particles grow. Given the difficulty of directly measuring the soot particle size distribution, and the considerable theoretical justification for believing that soot aerosols should follow the SPSPD (at least after particle inception has ceased), soot aerosols formed in premixed flames should be assumed to follow the SPSPD.

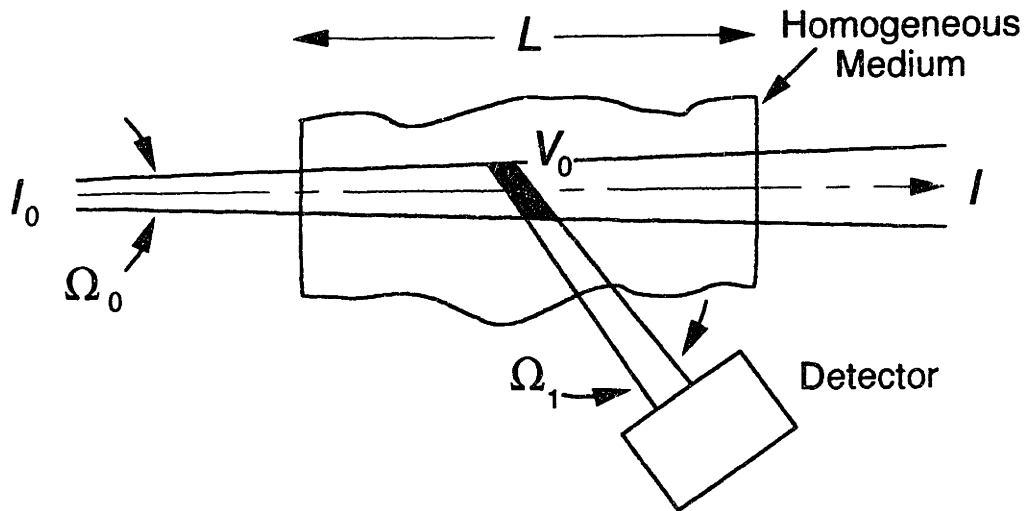
2.2 Light Scattering Theory

Consider a monochromatic beam of light passing through a homogeneous medium, as shown in Figure 2.2-1. In this context, "homogeneous" means spatially uniform, and does not necessarily mean the medium is a single phase. The power measured by a detector at some angle θ is given by

$$P_0 = \eta Q V_0 I_0 \Omega_0 \Omega_1 \quad (2.2-1)$$

where

- P_0 = detected power [energy/time],
- η = collection efficiency [dimensionless],
- Q = scattering coefficient [1/(length)(solid angle)],
- V_0 = scattering volume,
- I_0 = incident intensity [energy/(time)(area)(solid angle)],
- Ω_0 = solid angle of incident beam, and
- Ω_1 = solid angle of detected beam.



$$Q = \frac{P_0}{\eta V_0 I_0 \Omega_0 \Omega_1} \quad K_{\text{ext}} = \frac{1}{L} \ln \left(\frac{I_0}{I} \right)$$

Q = Scattering coefficient [1/(length)(solid angle)]
 K_{ext} = Extinction coefficient [1/length]

P_0 = Detected power [energy/time]
 V_0 = Scattering volume
 I = Intensity [energy/(time)(area)(solid angle)]
 L = Path length through medium
 η = Overall detection efficiency
 Ω = Solid angle

Figure 2.2-1: Geometry of light scattering and absorption. The intersecting incident and detected beams define the plane of reference. The scattering coefficient is measured point-wise, while the extinction coefficient is a line-of-sight average through the medium.

The intersecting incident and detected beams define a plane, and the polarization state of the light will be referenced to this plane. Linearly polarized light with the electric vector perpendicular to the reference plane will be called vertically polarized; if the electric vector is parallel to the reference plane, then the light will be called horizontally polarized.

In many experimental systems the incident beam is linearly polarized and the detected beam can be considered to be the sum of vertically and horizontally polarized components. If the incident beam is vertically polarized and only the vertically polarized component of the scattered beam is measured, then Q in Equation 2.2-1 becomes Q_{vv} . The first subscript indicates the polarization state of the incident beam, and the second subscript indicates which polarized component is being detected. Q_{vh} , Q_{hv} , and Q_{hh} are defined similarly to Q_{vv} . The law of reciprocity developed by Rayleigh (1900) and Krishnan (1938), and restated by Perrin (1942), requires that Q_{vh} equals Q_{hv} .

Again referring to Figure 2.2-1, the extinction coefficient is defined as

$$K_{ext} = (-1/L) \ln (I/I_0) \quad (2.2-2)$$

where K_{ext} = extinction coefficient [1/length],
 L = path length through medium,
 I = transmitted intensity [energy/(time)(area)(solid angle)], and
 I_0 = incident intensity [energy/(time)(area)(solid angle)].

Equation 2.2-2 is frequently called the Lambert-Beer Law. Notice that the scattering coefficient is a point-wise measurement, while the extinction coefficient is a line-of-sight average through the medium. If the absorbing species are thermally equilibrated, then the ratio I/I_0 is related to the spectral absorptivity, α_λ , and the spectral emissivity, ϵ_λ , through Eq. 2.2-3:

$$1 - (I/I_0) = \alpha_\lambda = \epsilon_\lambda \quad (2.2-3)$$

Equations 2.2-1 and 2.2-2 are phenomenological definitions of the scattering and extinction coefficients. In other words, Q_{vv} , Q_{vh} , Q_{hh} , and K_{ext} are defined for any homogeneous medium. However, relating these quantities to fundamental properties of the medium (particle diameter or particle concentration, for example) is not always trivial. Simplifying assumptions and approximations about the medium often have to be made in order to determine the particle diameter and concentration.

Sections 2.2.1 through 2.2.5 present different sets of assumptions that can be used

to interpret measurements of Q_w , Q_{vh} , Q_{hh} , and K_{ext} . However, the following assumptions are common to all of the following sections:

- 1) the scattering volume contains a statistically large number of randomly oriented particles. The number of particles per unit volume will be denoted by N .
- 2) each particle scatters as a separate entity, and there are no electrical interactions between particles. This assumption is reasonable if the interparticle distance is greater than 3 particle radii.
- 3) multiple scattering is negligible, or light scatters once and then leaves the system without further scattering. This assumption is reasonable if the optical mean free path is larger than the physical dimension of the system ($1/K_{ext} \gg L$).

The validity of these assumptions, at least as they apply to the measurements made in this thesis, will be discussed in Appendix E.

2.2.1 Small Homogeneous Spheres

If scattering and absorption from small, homogeneous, optically isotropic spheres are the dominant processes in the sample volume, then Rayleigh theory can be used to relate optical measurements of Q_w , Q_{hh} , and K_{ext} to physical properties of the aerosol:

$$Q_w = N \left(\frac{\lambda^2}{4\pi^2} \right) F(m) \langle \alpha^6 \rangle \quad (2.2.1-1)$$

$$Q_{vh} \equiv 0 \quad (2.2.1-2)$$

$$Q_{hh} = Q_w \cos^2 \theta \quad (2.2.1-3)$$

With the additional assumption that the spheres are strongly absorbing,

$$K_{ext} = N \left(\frac{\lambda^2}{\pi} \right) G(m) \langle \alpha^3 \rangle \quad (2.2.1-4)$$

where

$$F(m) = \left| \frac{m^2 - 1}{m^2 + 2} \right|^2 \quad (2.2.1-5)$$

$$G(m) = \text{Im} \left\{ - \frac{m^2 - 1}{m^2 + 2} \right\} \quad (2.2.1-6)$$

$$\alpha = \pi d / \lambda = \text{dimensionless sphere diameter} \quad (2.2.1-7)$$

d = sphere diameter,

$m = n - ki$ = refractive index of spheres, and

$$\text{Im}\{a + bi\} = b.$$

The assumption that m does not depend on particle size has been used to pull the functions $F(m)$ and $G(m)$ out of the integration over the particle size distribution in Equations 2.2.2-1 and 2.2.2-4. Felske *et al.* (1986) have plotted contour maps of $F(m)$ and $G(m)$ over a narrow range of refractive indices. These functions are plotted over a wider range in Figures 2.2.1-1 and 2.2.1-2.

The depolarization ratio, ρ_v , is defined as

$$\rho_v = \frac{Q_{vh}}{Q_w} \quad (2.2.1-8)$$

Rayleigh theory predicts that the depolarization ratio should be zero for spheres composed of an optically isotropic medium. In practice, however, many aerosols contain particles that are not perfectly spherical. Finite values of ρ_v can be attributed to deviations from sphericity and/or optical isotropy. A more detailed discussion of the effect of particle shape on the depolarization ratio is presented in Section 2.2.3. Notice also that Q_w and Q_{vh} are independent of the scattering angle θ , while Q_{hh} varies simply as $\cos^2\theta$.

The Rayleigh equations are an approximation to the complete Lorenz-Mie theory presented in Section 2.2.4. While the Lorenz-Mie equations are valid for homogeneous spheres of arbitrary size, the computational complexity of these equations is a strong motivation for the development of simpler approximations that are valid over limited ranges. The errors associated with using the Rayleigh approximations are small provided that $\alpha \ll 1$ and the real and imaginary parts of $m\alpha$ are much less than one.

Equations 2.2.1-1 and 2.2.1-4 can be solved simultaneously to give the number density, N , and characteristic diameter of the distribution in terms of Q_w and K_{ext} . Regardless of the type of distribution, the expression for N is

$$N = \left(\frac{K_{ext}^2}{4 \lambda^2 Q_w} \right) \left(\frac{F(m)}{[G(m)]^2} \right) f_N \quad (2.2.1-9)$$

However, the expression for the characteristic diameter depends upon the type of distribution. If the distribution is monodisperse, then

$$d = \lambda \left(\frac{4 Q_w}{\pi^2 K_{ext}} \right)^{1/3} \left(\frac{G(m)}{F(m)} \right)^{1/3} \quad (2.2.1-10)$$

If the distribution is lognormal, then the geometric mean diameter, d_g , is given by

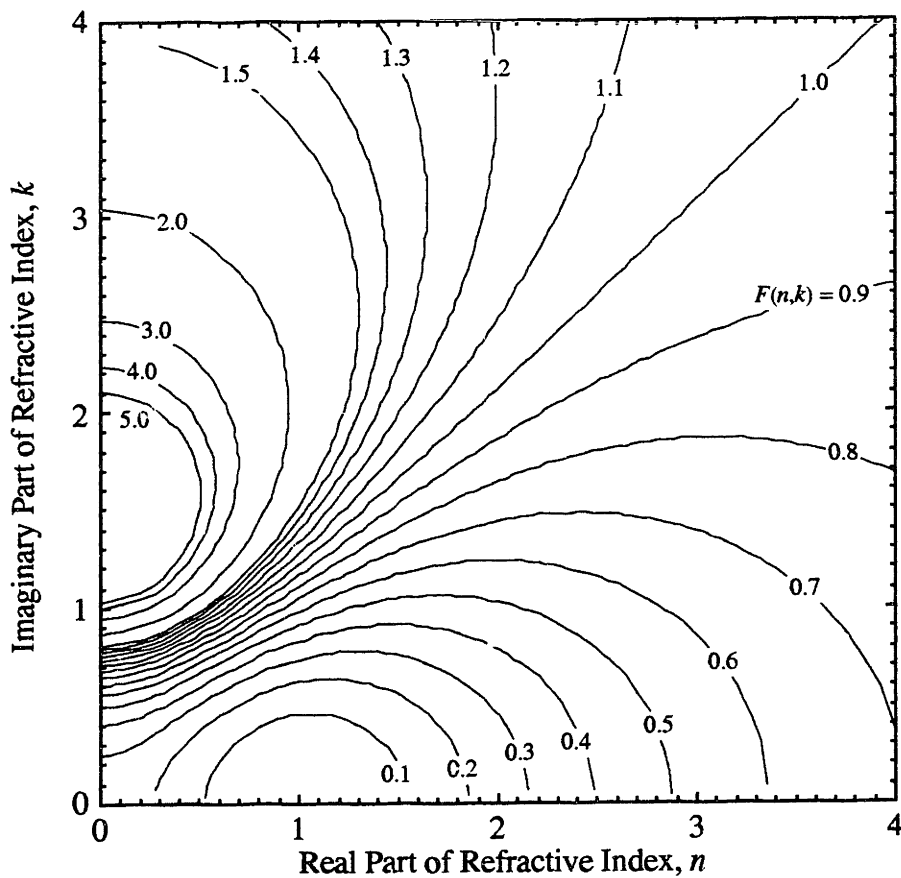
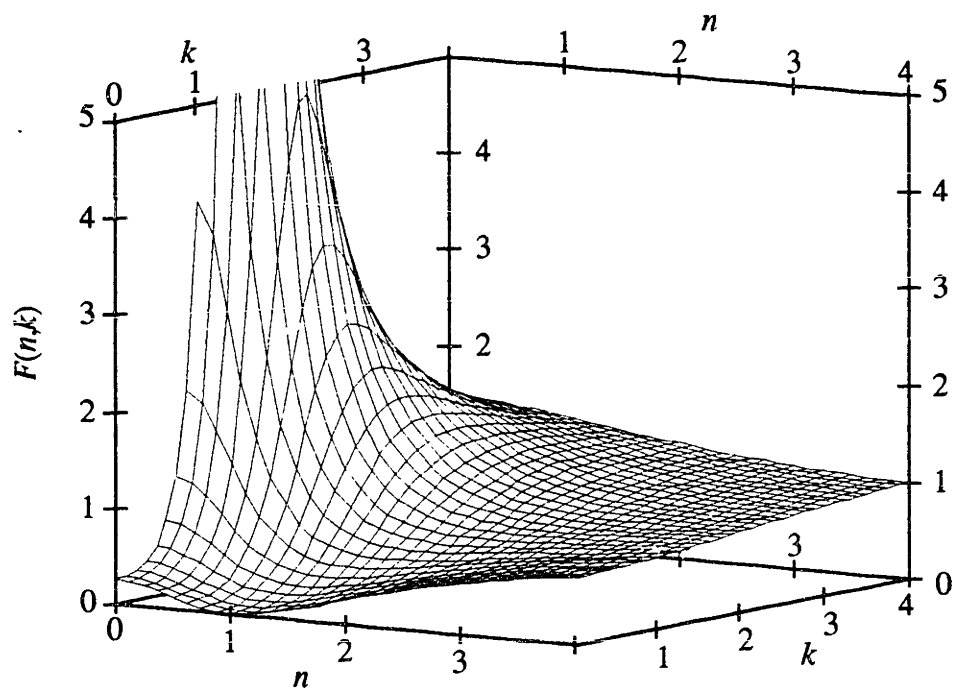


Figure 2.2.1-1: Surface and contour maps of the Rayleigh scattering function $F(n, k)$.

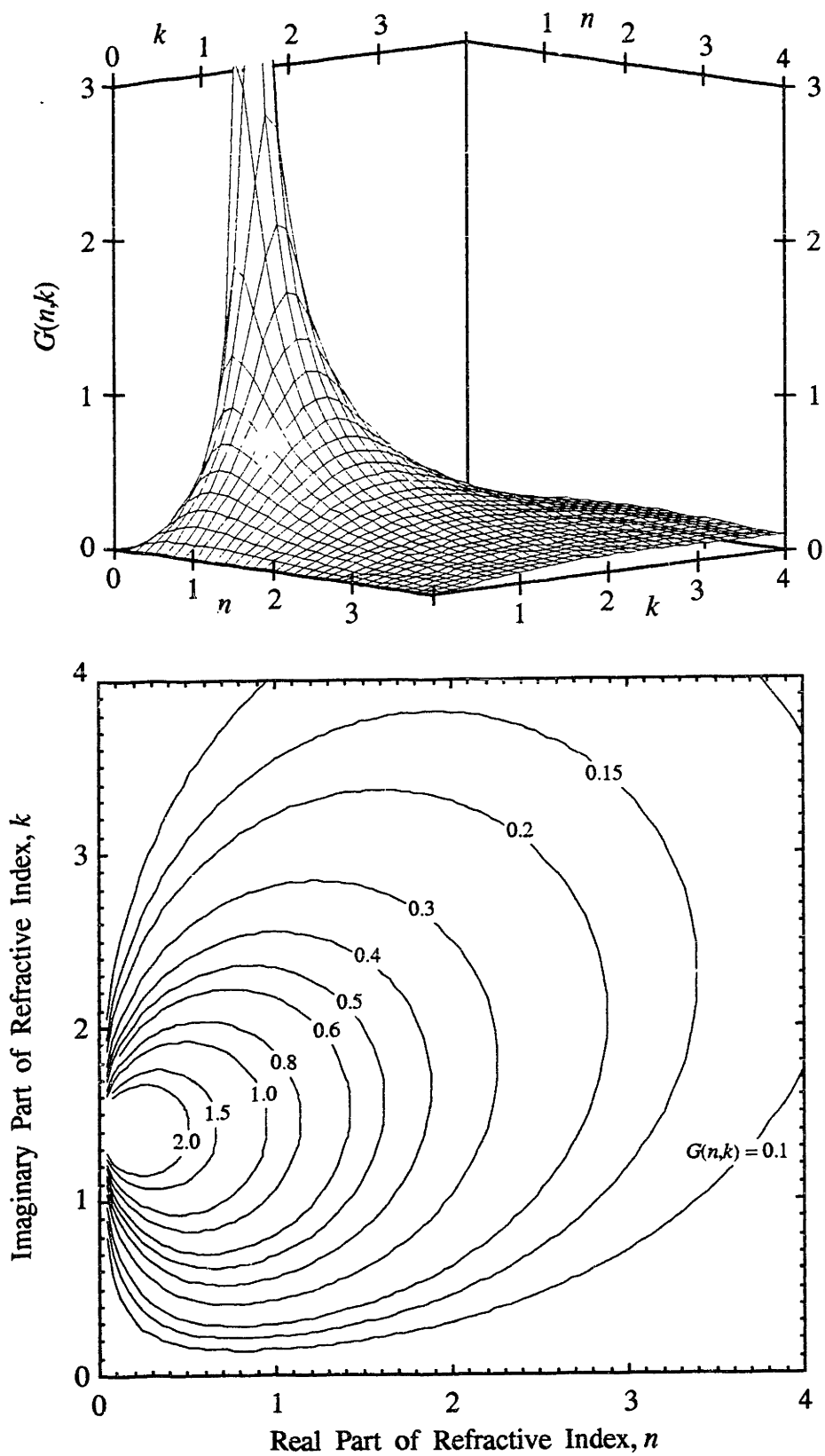


Figure 2.2.1-2: Surface and contour maps of the Rayleigh scattering function $G(n, k)$.

$$d_g = \lambda \left(\frac{4 Q_w}{\pi^2 K_{ext}} \right)^{1/3} \left(\frac{G(m)}{F(m)} \right)^{1/3} \exp \left\{ -\frac{9}{2} \sigma_g^2 \right\} \quad (2.2.1-11)$$

If the distribution follows the ZOLD, then the modal diameter is given by

$$d_{mode} = \lambda \left(\frac{4 Q_w}{\pi^2 K_{ext}} \right)^{1/3} \left(\frac{G(m)}{F(m)} \right)^{1/3} \exp \left\{ -\frac{11}{2} \sigma_0^2 \right\} \quad (2.2.1-12)$$

The volume fraction, f_v , can be determined from K_{ext} alone and does not depend on the type or width of the distribution:

$$f_v = \frac{\lambda K_{ext}}{6\pi G(m)} \quad (2.2.1-13)$$

Although not immediately apparent from Equations 2.2.1-4 and 2.2.1-13, K_{ext} and f_v do not depend upon the particle shape in the Rayleigh size regime.

Once N and d are known, all of the aerosol properties can be determined. For example, the total surface area per unit volume, S , of an aerosol is given by

$$S = \frac{\lambda^2}{\pi} N \int_0^{\infty} \alpha^2 p(\alpha) d\alpha \quad (2.2.1-14)$$

If α is lognormally distributed, then this expression simplifies to

$$S = \pi d_g^2 N \exp(2 \sigma_g^2) \quad (2.2.1-15)$$

The refractive index of the particles and the type and width of the particle size distribution must be known to use Equations 2.2.1-9 through 2.2.1-15 to calculate N , d_g , and S from measurements of Q_w and K_{ext} . The dependence of optically determined sizes and concentrations on the type and width of the distribution is given explicitly in Equations 2.2.1-9 through 2.2.1-15. The uncertainties of the type and width of the soot particle size distribution are discussed in Section 2.1.

The refractive index of soot has also been the topic of considerable research, and the literature on this subject is reviewed in Section 2.4. Independent of the type and width of the distribution, the characteristic diameter is always proportional to $[G(m)/F(m)]^{1/3}$, and the number density is always proportional to $F(m)/[G(m)]^2$. Felske *et al.* (1986) have plotted contour maps of these ratios over a narrow range of refractive indices. Contour maps of these two ratios are plotted over a wider range in Figures 2.2.1-3 and 2.2.1-4. N is much more sensitive to changes in the refractive index than is the

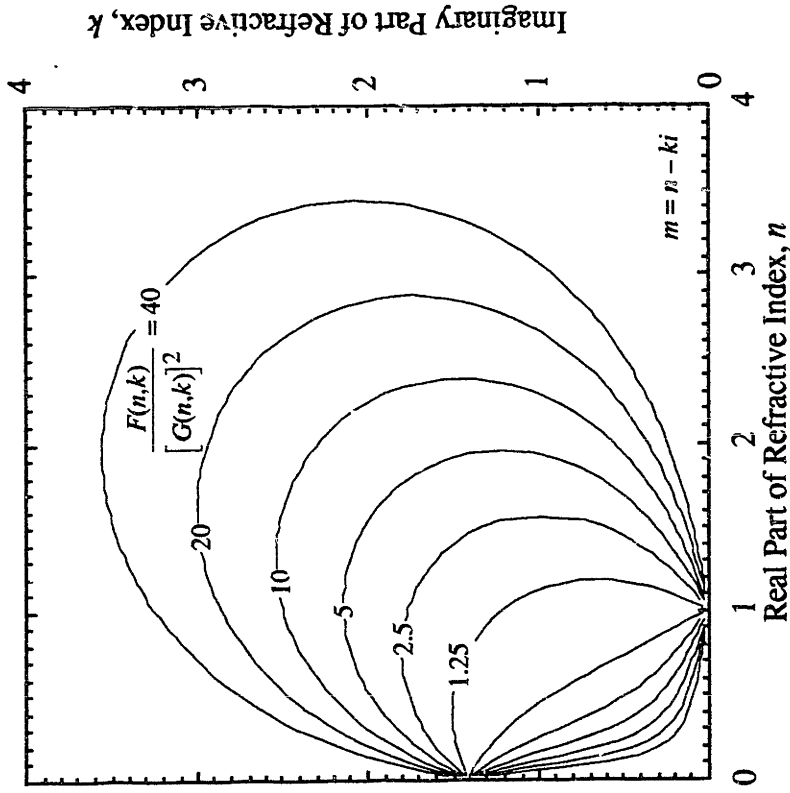


Figure 2.2.1-4: Contour map of $F(m)/[G(m)]^2$. The number density determined from scattering and extinction coefficient measurements is directly proportional to this ratio. N is much more sensitive than the characteristic diameter to uncertainties in the refractive index (compare to Figure 2.2.1-3).

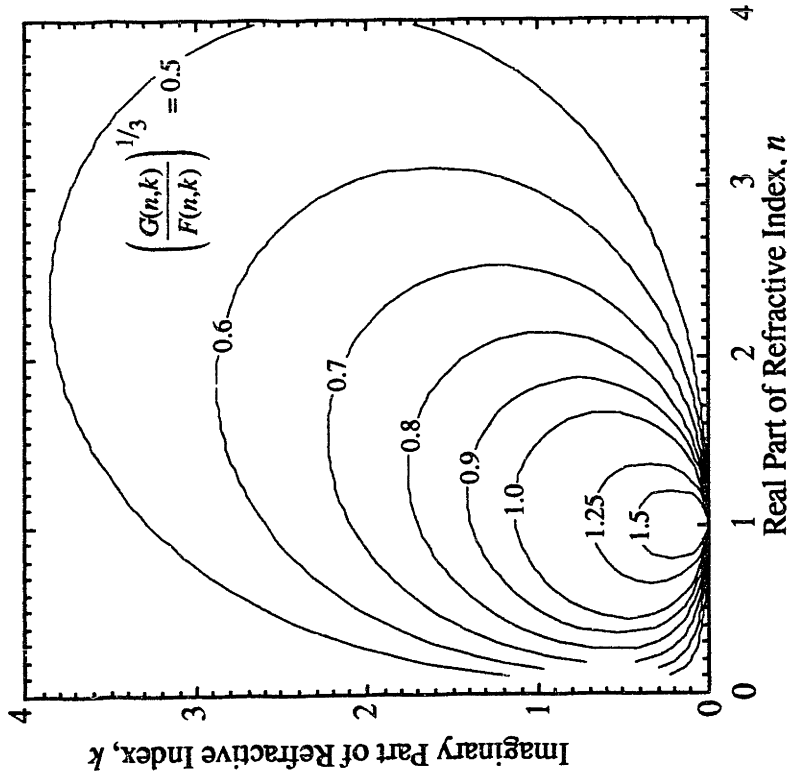


Figure 2.2.1-3: Contour map of $[G(m)/F(m)]^{1/3}$. The characteristic particle diameter determined from scattering and extinction coefficient measurements is directly proportional to this ratio in the Rayleigh size regime.

characteristic diameter. Use of these contour maps for interpreting optical measurements from coated particles is discussed in Chapter 5.

2.2.2 Small Coated Spheres

In this section, the scattering and absorption properties of small coated spheres (see Figure 2.2.2-1) will be presented. The spheres are assumed to be composed of two different media, each of which is optically isotropic. The radius of the core is a and the refractive index of the core medium is $m_i = n_i - k_i i$. The refractive index of the coating medium is $m_o = n_o - k_o i$, and the overall radius of the sphere is b . An important parameter for coated spheres is q , defined as

$$q = a/b = (\text{core radius})/(\text{total radius}) \quad (2.2.2-1)$$

$$q^3 = a^3/b^3 = (\text{core volume})/(\text{total volume}) \quad (2.2.2-2)$$

As q approaches zero, a coated sphere approaches a homogeneous sphere composed only of the coating material. As q approaches unity, a coated sphere approaches a homogeneous sphere composed only of the core material. To distinguish from the homogeneous particle equations, the overall dimensionless diameter of a coated sphere will be denoted by β , defined as

$$\beta = 2\pi b/\lambda \quad (2.2.2-3)$$

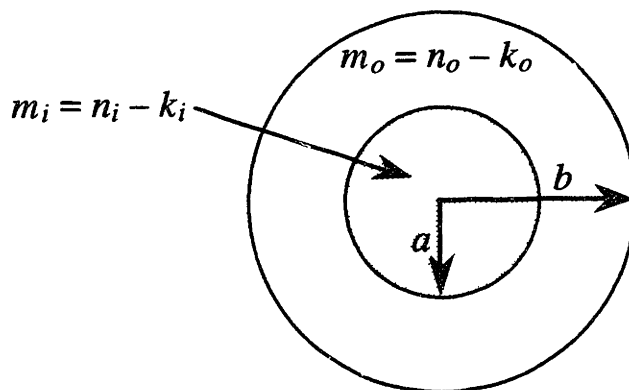


Figure 2.2.2-1: Geometry of coated spheres.

Güttler (1952) and Kerker (1969) present the scattering and absorption properties of coated spheres that are much smaller than the wavelength of light. If scattering and absorption from small coated spheres are the dominant processes occurring in the sample volume, then Q_w and K_{ext} are given by

$$Q_w = N \left(\frac{\lambda^2}{4\pi^2} \right) \int_{\beta=0}^{\infty} \int_{q=0}^1 \beta^6 F_c(m_i, m_o, q^3) p(q; \beta) dq d\beta \quad (2.2.2-4)$$

$$K_{ext} = N \left(\frac{\lambda^2}{\pi} \right) \int_{\beta=0}^{\infty} \int_{q=0}^1 \beta^3 G_c(m_i, m_o, q^3) p(q; \beta) dq d\beta \quad (2.2.2-5)$$

where

$$F_c(m_i, m_o, q^3) = \left| \frac{(m_o^2 - 1)(m_i^2 + 2m_o^2) + q^3(2m_o^2 + 1)(m_i^2 - m_o^2)}{(m_o^2 + 2)(m_i^2 + 2m_o^2) + q^3(2m_o^2 - 2)(m_i^2 - m_o^2)} \right|^2 \quad (2.2.2-6)$$

$$G_c(m_i, m_o, q^3) = \text{Im} \left[- \frac{(m_o^2 - 1)(m_i^2 + 2m_o^2) + q^3(2m_o^2 + 1)(m_i^2 - m_o^2)}{(m_o^2 + 2)(m_i^2 + 2m_o^2) + q^3(2m_o^2 - 2)(m_i^2 - m_o^2)} \right] \quad (2.2.2-7)$$

As in the case of small homogeneous particles, Q_w is independent of the scattering angle θ , Q_{hh} is related to Q_w by Equation 2.2.1-3, and Q_{vh} is zero.

In these equations, q and β are independent variables, and $p(q; \beta)$ is defined by

Equation 2.2.2-8:

$$\int_{q_1}^{q_2} \int_{\beta_1}^{\beta_2} p(q; \beta) d\beta dq = \begin{cases} \text{fraction of particles with dimensionless} \\ \text{overall diameter between } \beta_1 \text{ and } \beta_2 \text{ and} \\ \text{core radius/total radius between } q_1 \text{ and } q_2 \end{cases} \quad (2.2.2-8)$$

If q is constant for all particles of all sizes, then Equations 2.2.2-4 and 2.2.2-5 are greatly simplified:

$$Q_w = N \left(\frac{\lambda^2}{4\pi^2} \right) F_c(m_i, m_o, q^3) \langle \beta^6 \rangle \quad (2.2.2-9)$$

$$K_{ext} = N \left(\frac{\lambda^2}{\pi} \right) G_c(m_i, m_o, q^3) \langle \beta^3 \rangle \quad (2.2.2-10)$$

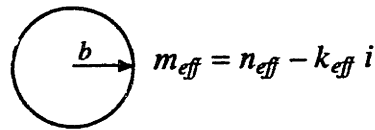
Thus, F_c and G_c are the coated sphere analogs of the functions F and G for homogeneous

spheres. Equations 2.2.2-9 and 2.2.2-10 can be solved for N and β to yield expressions very similar to Equations 2.2.1-9 through 2.2.1-15. F and G are replaced by F_c and G_c , respectively, and α is replaced by β .

A coated sphere can be treated as a homogeneous sphere of the same size by introducing the concept of an effective refractive index, $m_{eff} = n_{eff} - k_{eff}i$, of a coated sphere.



scatters and absorbs light exactly the same as this homogeneous sphere



provided that m_{eff} is chosen to satisfy

$$F(m_{eff}) = F_c(m_i, m_o, q^3) \quad (2.2.2-11)$$

$$G(m_{eff}) = G_c(m_i, m_o, q^3) \quad (2.2.2-12)$$

Solving Equations 2.2.2-11 and 2.2.2-12 simultaneously for m_{eff} can be somewhat tedious. Felske *et al.* (1986) discuss the possibility of approximating m_{eff} with the volume weighted average refractive index of a coated particle, \bar{m} , defined as

$$\bar{m} = q^3 m_i + (1 - q^3) m_o \quad (2.2.2-13)$$

A more detailed discussion of the utility of \bar{m} and m_{eff} , and how well \bar{m} approximates m_{eff} , is given in Chapter 5.

2.2.3 Small Homogeneous Spheroids

Just as a sphere composed of an anisotropic medium always scatters light more intensely than an isotropic sphere of the same volume, an ellipsoid always scatters light more intensely than a sphere of the same volume. In the former case, the increased scattering arises from optical anisotropy (the dielectric constant is a symmetric tensor) while in the latter case the increased scattering arises from geometrical anisotropy. In this section the scattering properties of small spheroids, assumed to be composed of an optically isotropic medium, will be presented.

Spheroids are ellipsoids with two axes of equal length. Consider the most general

spheroid with three axes of lengths A , B , and C , where A is always the longest axis and B is always the shortest axis. The volume V of a spheroid is

$$V = 4\pi ABC/3 \quad (2.2.3-1)$$

If the two axes of equal length are longer than the third axis ($A = C > B$), then the spheroid is oblate (a flattened sphere). If the two axes of equal length are shorter than the third axis ($A > B = C$), then the spheroid is prolate (a stretched sphere). An oblate spheroid can be generated by rotating an ellipse about its minor axis, while a prolate spheroid can be generated by rotating an ellipse about its major axis.

The eccentricity e_s of a spheroid is defined as

$$e_s = \sqrt{\frac{A^2 - B^2}{A^2}} \quad (2.2.3-2)$$

As e_s approaches unity, an oblate spheroid approaches the shape of a circular disk, while a prolate spheroid approaches the shape of a needle. Both types of spheroid approach the shape of a sphere as e_s approaches zero.

If scattering and absorption from randomly oriented spheroids that are small in comparison to the wavelength of light are the dominant processes occurring in the sample volume, then the expressions given by Kerker (1969) and Müller-Dethlefs (1979) for Q_w , Q_{vh} , and Q_{hh} can be used:

$$Q_w = \frac{3N\pi^2}{5\lambda^4} \int_0^1 \int_0^\infty V^2 [3(L')^2 + 4L'L'' \cos(\psi' - \psi'') + 8(L'')^2] p(V; e_s) dV de_s \quad (2.2.3-3)$$

$$Q_{vh} = \frac{3N\pi^2}{5\lambda^4} \int_0^1 \int_0^\infty V^2 [(L')^2 - 2L'L'' \cos(\psi' - \psi'') + (L'')^2] p(V; e_s) dV de_s \quad (2.2.3-4)$$

$$Q_{hh} = Q_w \cos^2 \theta + Q_{vh} \sin^2 \theta \quad (2.2.3-5)$$

Notice that Q_w and Q_{vh} are again independent of the scattering angle θ .

In these equations the particle volume V and eccentricity e_s are independent variables, and $p(V; e_s)$ is defined as

$$\int_{e_{s1}}^{e_{s2}} \int_{V_1}^{V_2} p(V; e_s) dV de_s = \left\{ \begin{array}{l} \text{fraction of particles with} \\ \text{volume between } V_1 \text{ and } V_2 \\ \text{and eccentricity between } e_{s1} \text{ and } e_{s2} \end{array} \right. \quad (2.2.3-6)$$

L', L'', ψ' , and ψ'' are related to the polarizabilities of the particles, α' and α'' :

$$\alpha' = \frac{3V}{4\pi} L' e^{-i\psi'} = \frac{V(m^2 - 1)}{4\pi + (m^2 - 1) Pe'} \quad (2.2.3-7)$$

$$\alpha'' = \frac{3V}{4\pi} L'' e^{-i\psi''} = \frac{V(m^2 - 1)}{4\pi + (m^2 - 1) Pe''} \quad (2.2.3-8)$$

For oblate spheroids, the depolarization factor Pe' is given by

$$Pe' = \frac{4\pi}{e_s^2} \left[1 - \left(\frac{1 - e_s^2}{e_s^2} \right)^{1/2} \arcsin e_s \right] \quad (2.2.3-9)$$

For prolate spheroids, the depolarization factor Pe' is given by

$$Pe' = 4\pi \frac{1 - e_s^2}{e_s^2} \left[\frac{1}{2e_s} \ln \left(\frac{1 + e_s}{1 - e_s} \right) - 1 \right] \quad (2.2.3-10)$$

For both oblate and prolate spheroids, the depolarization factor Pe'' is

$$Pe'' = (4\pi - Pe')/2 \quad (2.2.3-11)$$

As e_s approaches zero, Equations 2.2.3-9 through 2.2.3-11 approach the depolarization factors for spheres:

$$Pe' = Pe'' = 4\pi/3 \quad (2.2.3-12)$$

The polarizabilities depend on the spheroid volume, but L', L'', ψ' , and ψ'' depend only upon the refractive index and the eccentricity of the particle. Thus, the depolarization ratio for a small spheroid depends only upon the refractive index and eccentricity.

The extinction coefficient is still given by Equation 2.2.1-4, provided that the mean spheroid volume is substituted for the mean sphere volume:

$$K_{ext} = \frac{6N \pi G(m) \bar{V}}{\lambda} \quad (2.2.3-13)$$

2.2.4 Homogeneous Spheres of Arbitrary Size

The exact solutions to Maxwell's equations for the case of scattering of a plane electromagnetic wave by an optically isotropic sphere of arbitrary size were found independently by Mie (1908) and Lorenz (1898), and are frequently referred to as Lorenz-Mie theory. Q_w is no longer independent of scattering angle, and will now be written as $Q_w(\theta)$ to emphasize this difference. Q_{wh} and ρ_w are again zero for all scattering angles. The refractive index will again be assumed to be a constant, independent of particle size.

If scattering and absorption by homogeneous, optically isotropic spheres are the dominant processes in the sample volume, then the scattering coefficients Q_w and Q_{hh} are given by

$$Q_w(\theta) = N \left(\frac{\lambda^2}{4\pi^2} \right) \int_0^\infty i_1(m, \alpha, \theta) p(\alpha) d\alpha \quad (2.2.4-1)$$

$$Q_{hh}(\theta) = N \left(\frac{\lambda^2}{4\pi^2} \right) \int_0^\infty i_2(m, \alpha, \theta) p(\alpha) d\alpha \quad (2.2.4-2)$$

where

$$i_1(m, \alpha, \theta) = |S_1|^2 \quad (2.2.4-3)$$

$$i_2(m, \alpha, \theta) = |S_2|^2 \quad (2.2.4-4)$$

$$S_1 = \sum_{n=1}^{\infty} (-1)^{n+1} \frac{2n+1}{n(n+1)} \left\{ a_n \pi_n(\cos \theta) + b_n \tau_n(\cos \theta) \right\} \quad (2.2.4-5)$$

$$S_2 = \sum_{n=1}^{\infty} (-1)^{n+1} \frac{2n+1}{n(n+1)} \left\{ a_n \tau_n(\cos \theta) + b_n \pi_n(\cos \theta) \right\} \quad (2.2.4-6)$$

$$\pi_n(\cos \theta) = \frac{P_n^{(1)}(\cos \theta)}{\sin \theta} \quad (2.2.4-7)$$

$$\tau_n(\cos \theta) = \frac{d}{d\theta} P_n^{(1)}(\cos \theta) \quad (2.2.4-8)$$

$$a_n = \frac{\Psi_n(\alpha) \Psi'_n(m\alpha) - m \Psi_n(m\alpha) \Psi'_n(\alpha)}{\zeta_n(\alpha) \Psi'_n(m\alpha) - m \Psi_n(m\alpha) \zeta'_n(\alpha)} \quad (2.2.4-9)$$

$$b_n = \frac{m \Psi_n(\alpha) \Psi'_n(m\alpha) - \Psi_n(m\alpha) \Psi'_n(\alpha)}{m \zeta_n(\alpha) \Psi'_n(m\alpha) - \Psi_n(m\alpha) \zeta'_n(\alpha)} \quad (2.2.4-10)$$

$P_n^{(1)}(\cos \theta)$ are the associated Legendre polynomials of the first kind. $\Psi_n(z)$, $\zeta_n(z)$, $\Psi'_n(z)$, and $\zeta'_n(z)$ are the Ricatti-Bessel functions and their derivatives. The Ricatti-Bessel functions are related to the more common Bessel and Hankel functions by

$$\Psi_n(z) = \left(\frac{\pi z}{2} \right)^{\frac{1}{2}} J_{n+\frac{1}{2}}(z)$$

$$\zeta_n(z) = \left(\frac{\pi z}{2} \right)^{\frac{1}{2}} H_{n+\frac{1}{2}}(z)$$

where

$$J_{n+\frac{1}{2}}(z) = \text{half integral order Bessel function}$$

$$H_{n+\frac{1}{2}}^{(2)}(z) = \text{half integral order Hankel function of the second kind}$$

The extinction coefficient is given by

$$K_{ext} = N \int_0^{\infty} C_{ext}(m, \alpha) p(\alpha) d\alpha \quad (2.2.4-11)$$

where

$$C_{ext} = \frac{\lambda^2}{2\pi} \sum_{n=1}^{\infty} (2n+1) \{\text{Re}(a_n + b_n)\} \quad (2.2.4-12)$$

Converting measurements of Q_w and K_{ext} into particle sizes and concentrations in the Lorenz-Mie size regime requires an iterative solution of the equations listed above.

Bohren and Huffman (1983) give an efficient and robust computer code for evaluating i_1 , i_2 , and C_{ext} .

2.2.5 Gases

In this section, the scattering properties of transparent gases ($m = \text{real number}$) will be presented. Bridge and Buckingham (1966), Rudder and Bach (1968), and Rowell *et al.* (1971) provide a more detailed discussion than will be presented here.

Consider the sample volume to contain a transparent gas at temperature T and pressure P . Q_w is related to the fundamental properties of the gas by

$$Q_w = N C_{vw} \quad (2.2.5-1)$$

where C_{vw} is the differential scattering cross-section per molecule and N is the number of molecules per unit volume. For an ideal gas,

$$N = P/k_B T \quad (2.2.5-2)$$

where k_B is the Boltzmann constant. Graham *et al.* (1974) report the temperature variation of C_{vw} is small in comparison to the $1/T$ dependence of N , so that C_{vw} can be assumed to be independent of temperature.

At $T = T_0$ and $P = P_0$, C_{vw} is given by

$$C_w = \frac{4\pi^2(n_0 - 1)^2}{N_0^2 \lambda_0^4} \left(\frac{3}{3 - 4\rho_v^c} \right) \quad (2.2.5-3)$$

where

$n_0 = \text{real refractive index of gas at } T_0, P_0, \lambda_0$

$\lambda_0 = \text{wavelength of light}$

$N_0 = P_0/k_B T_0 = \text{number of molecules per unit volume}$

$\rho_v^c = \text{depolarization ratio of the central Rayleigh line}$

The depolarization ratio is written as ρ_v^c to emphasize the exclusion of the frequency-shifted rotational Raman lines. The Raman effect gives rise to Stokes and anti-Stokes lines, with a depolarization ratio of 3/4, shifted about 2 to 5 nm away from the central Rayleigh line. If the Raman lines are included in measurements of Q_{vv} and Q_{vh} , then ρ_v^c becomes ρ_v^T . Rowell *et al.* report that for diatomic and linear polyatomic molecules, $\rho_v^T/\rho_v^c \approx 4$, and for angular symmetric top molecules (molecules in which two of the three rotational moments of inertia are equal, and the third is nonzero), $\rho_v^T/\rho_v^c \approx 3$. The distinction between ρ_v^c and ρ_v^T has not always been made clear in the literature, in part due to the difficulty of completely separating the central Rayleigh line from the Raman lines. More than one worker has inadvertently used ρ_v^T when ρ_v^c should have been used (e.g., Neoh, 1980; D'Alessio, 1981). This mistake is frequently overlooked because the error is usually small. For example, if ρ_v^T is used instead of ρ_v^c in Equation 2.2.5-3, then the C_{vv} calculated for N_2 is increased by ~1%, and the C_{vv} calculated for CO_2 is increased by ~4%.

Table 2.2.5-1 gives values for n_0 and C_{vv} for some common gases at $T_0 = 273$ K, $P_0 = 1$ atm, and $\lambda_0 = 514.5$ nm. C_{vv} was calculated using Eq. 2.2.5-3, and can be considered to be independent of temperature. The refractive indices at 514.5 nm have been interpolated from data at different wavelengths in the Landolt-Börnstein tables (1962).

Data on ρ_v^c is from a variety of sources at 488.0 nm. However, Rowell *et al.* report ρ_v^c is approximately independent of λ in the range 488.0 to 632.8 nm. Also listed in Table 2.2.5-1 is $C_{vv,rel}$ for each species i , defined as

$$C_{w,rel} = \frac{C_{w,i}}{C_{w,N_2}} \quad (2.2.5-4)$$

2.3 Laser Induced Fluorescence

There are many references which discuss the theory and practice of fluorescence (e.g., Berlman, 1971; D'Alessio, 1981). Only a brief review of the phenomenon and observations made in flames will be presented here.

Figure 2.3-1 (adapted from Berlman, 1971) is an energy-level diagram which depicts the process of a molecule absorbing energy and subsequently returning to the ground state by several different pathways. When a molecule absorbs a quantum of light,

Species	$(n_0 - 1) \times 10^6$	$100 \rho_v^c$	$C_{vv} \times 10^{28}$ (cm ² /sr)	$C_{vv, rel}$
N ₂	300.5	0.31 (a)	7.07	1
O ₂	273.4	0.78 (a)	5.89	0.833
H ₂	140.2	0.25 (a)	1.54	0.218
H ₂ O	253.6	0.40 (b)	5.04	0.713
CO	337.5	0.18 (a)	8.90	1.26
CO ₂	451.9	1.01 (a)	16.13	2.28
CH ₄	445.2	0.01 (c)	15.45	2.19
C ₂ H ₄	731.1	0.30 (d)	41.83	5.92

Table 2.2.5-1: Optical properties of some common gases. All refractive indices are at $P = 1$ atm, $T = 273$ K, and were interpolated from Landolt-Börnstein (1962) at a wavelength of 514.5 nm. Depolarization ratios were compiled from a variety of sources:

- (a) Rowell *et al.* (1971);
- (b) Müller-Dethlefs and Weinberg (1978);
- (c) Bridge and Buckingham (1966);
- (d) Rudder and Bach (1968).

All of the depolarization ratio data is at wavelength of 488.0 nm. However, Rowell *et al.* report that the depolarization ratio does not depend on wavelength in the range 488.0 to 632.8 nm. Differential scattering cross-sections were computed using the data in this Table and Eq. 2.2.5-3. These cross-sections are for a wavelength of 514.5 nm, $P = 1$ atm, and $T = 273$ K. Graham *et al.* (1974) report that the differential cross-section can be considered independent of temperature up to 2000 K.

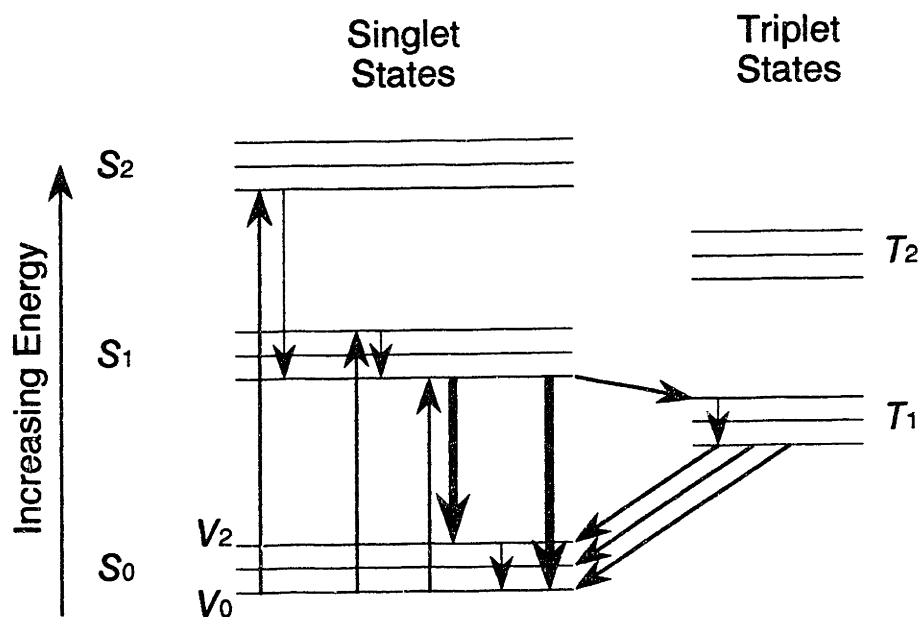


Figure 2.3-1: Energy level diagram for fluorescence (adapted from Berlman, 1971). S , T , and V represent singlet, triplet, and vibrational states of a molecule. Each electronic level is made up of many vibrational and rotational levels. The arrows pointing upward depict absorption of a quantum of light. The thick arrows pointing straight down indicate possible fluorescent transitions. The thin arrows pointing straight down represent internal conversion of energy without the emission of a photon. The arrow pointing to the right represents intersystem crossing, the transition from an excited singlet state to a triplet state. The arrows pointing the left indicate possible phosphorescent transitions.

an electron in the molecule can be promoted from the ground state to an excited singlet state (depicted by the arrows pointing upwards in Figure 2.3-1). The life of the excited singlet state is very short (of the order 10^{-11} seconds) and the excited electron quickly drops to the lowest energy excited singlet state, as shown by some of the thin arrows pointing downward. The process of this excited molecule returning to the ground state by emitting a photon is called fluorescence (the thick arrows pointing straight down in Figure 2.3-1). Since the energy of the emitted photon is usually less than the energy of the absorbed photon, the fluorescence wavelength is usually longer than the excitation wavelength.

Fluorescence is sometimes referred to as inelastic scattering because the emitted light has a different frequency (therefore different energy) than the incident light. In contrast, Rayleigh and Lorenz-Mie scattering are referred to as elastic scattering, because the emitted light has the same frequency as the incident light.

The lifetime of an excited gas phase molecule is usually longer than its rotational frequency, resulting in completely unpolarized fluorescence (Müller-Dethlefs, 1979). In addition, the lifetime of the excited molecule can be long enough for it to return to the ground state, without emitting a photon, through a number of different pathways. Collisional quenching occurs when the excited molecule returns to the ground state by colliding and exchanging energy with another molecule. Intersystem crossing occurs when the molecule transitions from a singlet state to a triplet state, as shown by the arrow pointing to the right in Figure 2.3-1. The process of a molecule returning to the ground state from the triplet state by emitting a photon is termed phosphorescence, and is shown by the arrows pointing to the left in Figure 2.3-1. The triplet state can be metastable; the molecule may remain in this state for as long as several seconds, providing considerable time for collisional quenching to occur. Therefore, the observed fluorescence is a competition between radiative and non-radiative transitions (due to collisions involving either singlet or triplet states) to the ground state.

Consider once more a monochromatic beam of light (wavelength λ_e) passing through a homogeneous medium, as shown in Figure 2.2-1. The detector need not observe at λ_e ; let the center of the observation wavelength range be denoted by λ , and the integrated area under the fraction detected versus wavelength curve of the detector be de-

noted $\Delta\lambda$. The fluorescence coefficient, $Q_{f\lambda}\Delta\lambda$, is given by

$$P_0 = \eta(Q_{f\lambda}\Delta\lambda)V_0 I_0 \Omega_0 \Omega_1 \quad (2.3-1)$$

where the notation is the same as in Equation 2.2-1. The fluorescence coefficient has the same dimensions as the scattering coefficient, $1/[(\text{length})(\text{solid angle})]$. Like the definition of the scattering coefficient, the definition of $Q_{f\lambda}\Delta\lambda$ is a phenomenological one, and can be properly attributed to fluorescence only if fluorescence is the dominant process generating light in the observation wavelength range. The fluorescence coefficient is a strong function of λ_e , the excitation wavelength, and the observation wavelength range.

Several investigators have detected fluorescence from combustion systems excited with visible light (e.g., D'Alessio *et al.*, 1977; Haynes *et al.*, 1980; Di Lorenzo *et al.*, 1981; Prado *et al.*, 1984; Petarca and Marconi, 1989). When the excitation wavelength is 488.0 nm or 514.5 nm (the operating wavelengths of argon ion lasers), the fluorescence spectrum is generally broad and featureless, extending from 400 nm to almost 700 nm. The peak in fluorescence intensity is shifted towards longer wavelengths, as expected. Almost all workers agree that the fluorescence observed in flames is due to polycyclic aromatic hydrocarbons (PAH) in the gas phase. There is some disagreement, however, concerning the individual species responsible for the fluorescence. One theory proposes that the fluorescence is due to predominantly acenaphthylene (Coe *et al.*, 1981), while another theory holds that very high molecular weight PAH are responsible for the fluorescence (Müller-Dethlefs, 1979; Barbella *et al.*, 1990).

Coe *et al.* (1981) suggested that acenaphthylene is the dominant fluorescing species, based on the similarity between the fluorescence spectra of a methane/air diffusion flame and a non-sooting ethylene/air diffusion flame containing injected acenaphthylene. Based on room temperature spectra, acenaphthylene would not be expected to fluoresce at 488.0 nm. Only very large PAH (for example: rubicene, $M = 326$ g/mole; circumanthrene, $M = 448$ g/mole) can be expected to absorb at this wavelength. Coe *et al.* believe that the fluorescence can be attributed to acenaphthylene because it possesses a "hidden transition," and the excitation spectrum shifts to the red as temperature increases.

Barbella *et al.* (1990) withdrew soot and PAH samples from a vertical spray flame obtained by atomizing a commercial fuel oil. The samples were separated into several fractions, including fractions that contained mono-ring aromatics, two-ring aromatics,

three to seven ring aromatics, and polar compounds. Barbella *et al.* systematically compared *in situ* fluorescence spectra with the room temperature absorption and fluorescence spectra of the different fractions. They concluded that the *in situ* fluorescence does not correlate with the acenaphthylene concentration, but is mainly due to high molecular weight polycyclic aromatic compounds and polar compounds. Müller-Dethlefs (1979) supports this view, proposing that the broad band fluorescence observed in premixed and diffusion flames (with $\lambda_e = 488$ nm) is caused by PAH with 10 or more rings.

Identifying the individual PAH species responsible for the *in situ* fluorescence is a formidable task. More than one hundred different PAH species can be found in typical combustion environments (Lam, 1988(b)) and only a fraction of these have been positively identified. Analytical techniques that can separate and identify individual PAH species are still being developed (Wornat, 1988). In comparison to optical probes, sampling probes have low spatial resolution, and secondary reactions may occur in a probe if quenching is not rapid, further confounding attempts to compare *in situ* fluorescence measurements to sampling measurements. There are also differences between the *in situ* fluorescence of PAH in the vapor phase at combustion temperatures and the fluorescence of PAH in solution at lower temperatures. Correlating PAH concentration and/or composition with *in situ* fluorescence coefficient measurements may be a topic of active research for several more years.

2.4 The Refractive Index of Soot

The equation for a wave propagating in an absorbing medium (e.g., Gray, 1972) is:

$$E = E_0 \exp\left[\frac{-2\pi k x}{\lambda_0}\right] \exp\left[-2\pi i \left(\frac{n x}{\lambda_0} - \nu t\right)\right] \quad (2.4-1)$$

where E_0 = amplitude of wave at $x = 0$ in the medium,
 E = instantaneous value of the electric vector at distance x and time t ,
 ν = frequency of source,
 λ_0 = wavelength of light in vacuum, and
 n, k = components of complex index of refraction, $m = n - k i$

The real part of the refractive index, n , is the ratio of the phase velocity of light in vacuum to the phase velocity of light in the absorbing medium. The imaginary part of the re-

fractive index, k , is related to the exponential decay of the wave as it passes through the medium, and leads to attenuation of the amplitude of the electric vector. In older literature, the refractive index is sometimes written as

$$m = n (1 - \kappa i) \quad (2.4-2)$$

where κ is called the absorption index. The refractive index is also related to the complex electrical permittivity, $\epsilon = \epsilon_1 - \epsilon_2 i$, through Equation 2.4-3:

$$\epsilon / \epsilon_0 = m^2 \quad (2.4-3)$$

where $\epsilon_0 =$ permittivity of free space $= 8.854 \times 10^{-12} \text{ C}^2/\text{N m}^2$.

An accurate value for the *in situ* refractive index of soot is required to convert light scattering measurements into particle sizes and concentrations (see Section 2.2). Some of the reported values of m are presented in Figure 2.4-1. The data appearing in Figure 2.4-1 is not comprehensive. Rather, the purpose of this figure is to include data taken with the principal techniques used for measuring m , and to compare the range of values reported.

Dalzell and Sarofim (1969) determined the refractive index of soot in the wavelength range $435.8 \text{ nm} \leq \lambda \leq 10 \text{ }\mu\text{m}$. Soot samples were collected from acetylene or propane diffusion flames, compressed into pellets, and the reflectance was measured. Their results for propane soot are shown in Figure 2.4-1.

Felske *et al.* (1984) used the same technique as Dalzell and Sarofim, taking into account the void space in the compressed pellets. The real and imaginary parts of the particle refractive index were, respectively, 12% and 21% greater than the real and imaginary parts of the compressed powder refractive index. Their results were significantly dependent upon the void fraction near the surface of the pellet, which was not the same as the bulk void fraction. As shown in Figure 2.4-1, their analysis also predicts a somewhat different relationship between m and λ .

Lee and Tien (1981) used *in situ* measurements of ϵ_λ taken in the visible of polystyrene and plexiglass flames to determine m in the range $300 \text{ nm} \leq \lambda \leq 20 \text{ }\mu\text{m}$. Their results are also shown in Figure 2.4-1. Lee and Tien report that m is not a strong function of T at flame temperatures, although there may be significant difference between the optical constants at flame temperature and room temperature. However, their technique is marred by the low sensitivity of m on λ in such a narrow wavelength range.

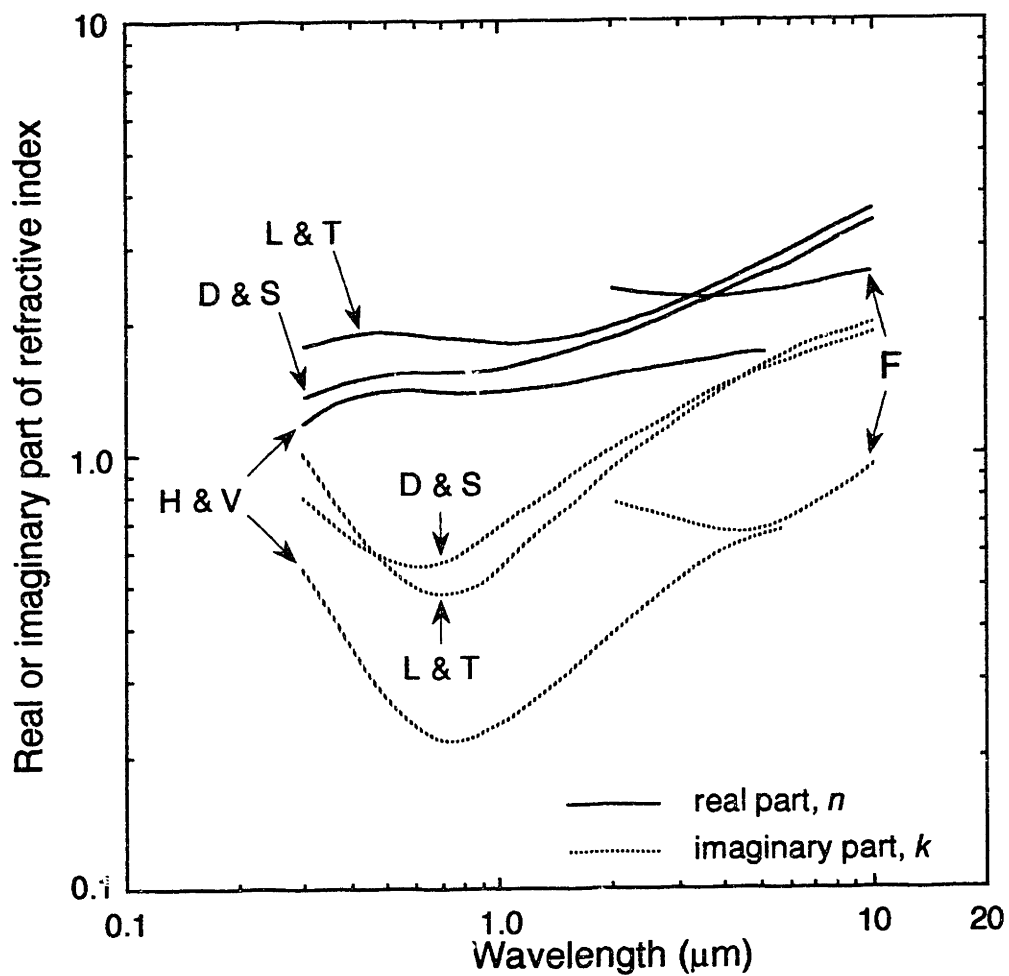


Figure 2.4-1: The refractive index of soot, as determined by four groups: D & S = Dalzell & Sarofim, (1969); L & T = Lee and Tien, (1981); F = Felske et al., (1984); H & V = Habib and Vervisch, (1987).

Habib and Vervisch (1987) combined diffusion broadening spectroscopy and multiple wavelength measurements of the spectral emissivity to determine m in the range $400 \text{ nm} \leq \lambda \leq 5.0 \text{ }\mu\text{m}$. Their reported real and imaginary parts of m are significantly lower than most other reported results (see Figure 2.4-1). The assumption of a monodisperse size distribution may have contributed to the low values of n and k that they found.

Recently Charalampopoulos and Felske (1987) measured the refractive index of soot in a premixed methane/oxygen flame at a single wavelength (488.0 nm) by combining dynamic light scattering measurements (which determined the particle size distribution independently of m) with measurements of K_{ext} and Q_w . They found the refractive index increased with increasing height above the burner, from about $1.4 - 0.4 i$ to about $1.7 - 0.7 i$. The increase in the refractive index was attributed to dehydrogenation of the soot particle as they aged. The average refractive index for all heights in the flame was $1.6 - 0.59 i$.

Given the difficulty of collecting soot samples that are representative of the *in situ* particles, and the dependence of m on particle temperature, *in situ* measurement techniques are preferred over other techniques. The results of Charalampopoulos and Felske are the most accurate *in situ* data available, since the soot particle size distribution is taken into account, and the measurements are not extrapolated over a wide wavelength range. In premixed methane flames, their variable refractive index should be used. For other premixed flames, there is still not enough data to warrant the use of a variable refractive index. Other factors (such as geometrical and/or optical anisotropy, the uncertainty of the particle size distribution, and the different C/H ratios of soot particles formed in different flames) are potentially greater sources of error than the use of a constant refractive index. The average value of m that Charalampopoulos and Felske found, $m = 1.6 - 0.59 i$, should be used in other premixed flames. Figures 2.2.1-3 and 2.2.1-4 show that the maximum possible error incurred by using a constant refractive index instead of a variable refractive index is small. Using $m = 1.4 - 0.4 i$ instead of $1.6 - 0.59 i$ would increase the optically determined diameter by 16% and decrease the optically determined number density by 21% in the Rayleigh size regime. Using $m = 1.7 - 0.7 i$ instead of $1.6 - 0.59 i$ would decrease \bar{d} by 6% and increase N by 12%.

2.5 Soot Formation

The literature on soot formation is extensive; approximately 200 papers have been published concerning soot every year for the last ten years (McKinnon, 1989). In addition to studies conducted in practical combustion devices, laboratory studies have been conducted in a variety of different systems (e.g., shock tubes, diffusion flames, atmospheric pressure and low pressure premixed flames, well-stirred reactors, and liquid spray flames) with a range of different gaseous and liquid fuels and number of different measurement techniques (e.g., optical diagnostics, molecular beam/mass spectrometry, and thermophoretic probing/image analysis). Fortunately, an overview of the historical development of the field can be obtained by consulting several review papers (Street and Thomas, 1955; Palmer and Cullis, 1965; Haynes and Wagner, 1980).

In the following sections, the literature on the overall soot formation process (see Figure 1.1-1) will be reviewed and divided into four stages: particle inception, particle collisions and coagulation, surface growth, and soot oxidation. This division is conceptual; in many systems these steps are neither temporally nor spatially separate. The current understanding of soot formation will be given more emphasis than older theories. The literature on soot formation from gaseous fuels burned in flames is most applicable to this thesis, and will be given special attention.

2.5.1 Soot Particle Inception

Soot particle inception, as the term will be used here, is the name given to the chemical and physical processes that generate the first solid soot particles from the gas phase. Particle inception is probably the least well understood step in the soot formation process, in part because little experimental data is available. Extremely high spatial resolution is required to probe the soot particle inception zone, which lasts for only about 2.5 ms in an atmospheric pressure premixed ethylene flame (Harris *et al.*, 1986). Sampling measurements are difficult in the inception zone because temperature and concentration gradients are steep. The interpretation of optical measurements in the inception is complicated by the low soot volume fraction and small soot particle diameter, making scatter and absorption from gas phase species significant in comparison to scatter and absorption from particles. For these reasons, soot particle inception is most often

studied in low-pressure systems, in which the inception zone is expanded.

Wersborg *et al.* (1973) investigated particle inception in a low pressure acetylene-oxygen flame with a molecular beam sampling system. The smallest detectable solid particles were about 1.5 nm in diameter, corresponding to a molecular weight of about 2130 amu, or about 175 carbon atoms. Other experimental studies of particle inception in flames have been conducted by D'Alessio *et al.* (1977), Bittner (1981), and Harris *et al.* (1986). Nevertheless, there is little data on the species that bridge the gap between large gas-phase molecules and small solid particles.

The lack of critical data has led to considerable speculation concerning the mechanism of soot particle inception. Some have suggested that ions play an important role in particle inception (e.g., Wersborg, Yeung, and Howard, 1975; Calcote and Keil, 1988). Others believe that particle inception is a continuous molecular weight growth process, proceeding from low molecular species through PAH to soot (e.g., Frenklach *et al.*, 1984; Harris *et al.*, 1986; McKinnon, 1989). Another recent theory maintains that soot particle inception may proceed through "buckminsterfullerene," a C₆₀ molecule with a truncated icosahedral structure (Zhang *et al.*, 1986). However, this theory has not gained widespread acceptance (Baum, 1990). In general, even the best theories describing particle inception are in only qualitative agreement with experimental observations.

2.5.2 Soot Particle Collisions, Coalescence, and Coagulation

Consider an aerosol consisting of particles with diameters that are much smaller than the mean free path of the surrounding gas molecules. The mean free path of a gas, l , is given by

$$l = \frac{\mu}{\rho} \left(\frac{\pi M}{2 k_B T} \right)^{\frac{1}{2}} \quad (2.5.2-1)$$

where μ is the gas viscosity, ρ is the gas density, and M is the gas molecular weight (see Friedlander, 1977). Aerosols in this size range are said to be in the free-molecule regime, because particle collision rates are driven by the thermal motion, and small particles can be treated simply as large molecules. If every particle-particle collision is a sticking collision, then the change in the particle number density solely due to collisions is given by

$$-\frac{dN}{dt} = \frac{1}{2} \left(\frac{3}{4\pi} \right)^{1/6} \left(\frac{6k_B T(t)}{\rho} \right)^{1/2} \alpha(t) f_v^{1/6}(t) N^{11/6}(t) \quad (2.5.2-2)$$

where ρ is the density of the particulate phase, $f_v(t)$ is the instantaneous particle volume fraction, and $\alpha(t)$ is a factor which depends upon the shape of the particle size distribution (Graham and Robinson, 1976).

Under certain conditions the aerosol size distribution approaches the self-preserving size distribution (see Section 2.1); in these cases $\alpha(t)$ is no longer time dependent, and can be replaced by a constant, α_{sp} . Graham and Robinson report the best estimate of α_{sp} is

$$\alpha_{sp} = 6.554 \quad (2.5.2-3)$$

The factor $\alpha(t)$ is a weak function of the shape of the particle size distribution; for a monodispersion, $\alpha(t) = 4\sqrt{2} \approx 5.657$ (Haynes and Wagner, 1980). Integration of Eq. 2.5.2-2 then gives

$$N^{-5/6}(t) = N_0^{-5/6} + \frac{5}{12} \alpha_{sp} \left(\frac{3}{4\pi} \right)^{1/6} \left(\frac{6k_B}{\rho} \right)^{1/2} \int_{t_0}^t T^{1/2}(t) f_v^{1/6}(t) dt \quad (2.5.2-4)$$

Therefore, a plot of $N^{-5/6}(t)$ versus the integral in Eq. 2.5.2-4 should be a straight line, with slope m_{th} of

$$m_{th} = \frac{5}{12} \alpha_{sp} \left(\frac{3}{4\pi} \right)^{1/6} \left(\frac{6k_B}{\rho} \right)^{1/2} \quad (2.5.2-5)$$

Optical measurements of soot aerosols have shown that the slope of this line is 2 to 4 times greater than the theoretical prediction (Bockhorn *et al.*, 1982; Woods, 1988). Kennedy (1987) and Harris and Kennedy (1988) have shown that interparticle van der Waals forces can be expected to increase the collision rate (and, therefore, the slope of the line) by about a factor of 2. The remaining difference between the measurements and theory is within the error of the optical measurements (see Sections 2.2 and 2.4). Marlow and Slatest (1984) have discussed in some detail the theory of aerosol coagulation and the effect of van der Waals forces on particle collision rates.

Although soot particle collision rates are modeled well by free-molecule coagulation theory, the factors which govern the transition from coalescent collisions to chain-forming collisions are not well understood. In a coalescent collision, two particles fuse to

form a single, spherical particle. A chain-forming collision occurs when two particles collide and do not fuse, but retain their individual identities while remaining held together at a single point of contact. Prado and Lahaye (1981) and Smith (1982) have suggested that changing particle viscosity controls the transition from coalescent to chain-forming behavior. In contrast, Howard and Longwell (1983) suggested that soot particle collisions may never be truly coalescent. Surface growth rates early in a flame may be rapid enough to fill intraparticle voids within an agglomerate, making chain-forming collisions appear to be coalescent collisions. As the agglomerate size increases, the intraparticle void volume also increases, making the non-coalescent behavior more apparent, especially when combined with the decreasing surface growth rate observed in premixed flames (see Section 2.5.3).

Experiments have failed to prove conclusively that soot particle collisions are either exclusively coalescent or exclusively chain-forming. In a shock flow study, Graham (1977) showed that particles up to almost 40 nm in diameter can coalesce on collision. Haynes *et al.* (1980) have found evidence that soot particles in premixed flames coalesce on collision at short residence times. In contrast, Jones and Wong (1975) have presented optical results that suggest some chain-forming collisions occur within the flame itself. Generally, the *in situ* morphology of soot particles in premixed flames is not known. Most researchers have assumed soot particles are spheres because there is little data concerning the particle shape, and because of the simplicity afforded by this assumption.

Distinguishing between the two types of collisions using sampling probes is difficult. Much of the agglomeration seen in samples withdrawn from flames using conventional probes may have occurred during the sampling process, and may not be representative of the *in situ* particle morphology. The two theories described above highlight the need for rapid sample quenching. Dobbins and Megaridis (1987) have recently developed a thermophoretic sampling probe which may be useful in quantifying the evolution of the fractal-like nature of soot aggregates.

2.5.3 Soot Surface Growth

Surface growth is the name given to the gas-solid reaction that eventually accounts for 90% or more of the total amount of soot formed in a flame. Many studies in both at-

atmospheric pressure and low pressure premixed flames have shown that the surface growth reaction is initially very rapid and decreases with time until the surface growth reaction ceases. Haynes and Wagner (1982) suggested that soot surface growth in premixed flames be described empirically by an expression of the form

$$\frac{df_v}{dt} = k_{sg} (f_v^* - f_v) \quad (2.5.3-1)$$

where f_v^* = ultimate soot volume fraction, and

k_{sg} = empirically determined surface growth constant.

While f_v^* is a strong function of the fuel, the fuel equivalence ratio, the flame temperature, and the flame pressure, Haynes and Wagner found that k_{sg} depends only on temperature, and has an apparent "activation energy" of 40-50 kcal/mole. Although this approach can empirically fit soot growth curves, it provides little insight into the mechanism of surface growth.

Harris and Weiner (1983(a), 1983(b)) have proposed a mechanistic model for surface growth:

$$\frac{df_v}{dt} = \frac{1}{\rho_{soot}} k_{HW} S [C_2H_2] \quad (2.5.3-2)$$

In this approach, surface growth is simply a first order elementary reaction between soot and acetylene. However, Harris and Weiner found that their rate constant, k_{HW} , is not constant in premixed flames. Since df_v/dt decays to zero, S is approximately constant, and $[C_2H_2]$ decreases by only about 50%, k_{HW} must decrease by an order of magnitude within a flame. Harris and Weiner attribute the decline in k_{HW} to decreasing soot surface reactivity with time. Dasch (1985) formalized this concept, and showed how the k_{sg} and k_{HW} constants are related. Woods (1988) has extended Harris and Weiner approach even further, postulating that the C_2H_2 - soot reaction takes place only at specific active sites (likely to be radical in nature) on the soot particle surface, and that these sites are conserved in the growth reaction. According to Woods, the decline in the soot growth rate in the flame is due to the loss of active sites from the surface, caused by a combination of the decreasing flame temperature and the decreasing radical concentration of the flame.

Lam *et al.* (1988) have recently shown that the possibility of PAH being a significant part of the surface growth reaction cannot be excluded. If acetylene is the predominant surface growth species, then the reaction probability γ between soot and C_2H_2 is

about 5×10^{-4} . If PAH are the dominant soot growth species, then γ between soot and PAH is about 0.5.

2.5.4 Soot Oxidation

The catalyzed and non-catalyzed oxidation of soot removed from flames (and other forms of carbon) has been studied extensively (e.g., Wright, 1975; Baker, 1979; Floess, 1985; Figueiredo *et al.*, 1987; Du, 1990). The most active carbon gasification catalysts are the alkali and alkaline earth salts, and transition metals of the iron and platinum groups (McKee, 1980). The majority of this work is motivated by the need to understand processes occurring in the production of fuels and synthesis gases. The temperatures are much lower than are typically found in flames, and the gas phase composition is different from the flame gas composition. The mechanisms of carbon oxidation in these low-temperature studies are different from the mechanism of soot oxidation in flames. However, this low-temperature work is important for understanding the oxidation of soot particles once they leave the flame.

Soot oxidation in flames has been investigated by Millikan (1962), Fenimore and Jones (1967), Page and Ates (1978) and Neoh (1980). All of these workers have concluded that OH is the species principally responsible for soot oxidation in flames. Fenimore and Jones used a double burner/premixed ethylene flame apparatus and concluded that the reaction probability, γ , between soot and OH was ~ 0.1 . Page and Ates, also investigating ethylene flames, found γ to be about 0.25.

Neoh completed a thorough study of soot oxidation in premixed flames. After considering O_2 , O, OH, H_2O , and CO_2 as possible oxidants, Neoh concluded that OH was the principal oxidant of soot in flames with $1575 \text{ K} < T < 1865 \text{ K}$ and $10^{-5} < \text{mole fraction } O_2 < 0.05$. If the soot particles were assumed to be non-porous spheres, and every reactive collision was assumed to remove one carbon atom, then the reaction probability between soot and OH was found to be 0.28, independent of temperature. Neoh also found some evidence for internal burning within the soot particles. Neoh's soot oxidation mechanism is the best available model for soot oxidation in flames, and is preferable over the empirical model for pyrographite oxidation developed by Nagle and Strickland-Constable (1962).

2.6 Effects of Metal Additives on Soot Formation

The effects of metal additives on soot formation have been studied in many practical and laboratory-scale combustion systems. Investigations have been conducted in domestic and utility boilers (e.g., Weeks *et al.*, 1959; Kukin, 1973), gas turbines (e.g., Giovanni *et al.*, 1972), diesel engines (e.g., Golothan, 1967), diffusion flames (e.g., Jenkins, 1972; Bonczyk, 1988), and premixed flames (e.g., Ritrievi, 1984; Hayhurst and Jones, 1989). While tests in practical systems are required to establish additive effectiveness, such tests frequently yield little or no information on the mechanisms of additive action. Since the objective of this thesis is to develop a better understanding of the mechanisms through which metal additives effect soot formation, only a brief description of some of the work in practical systems will be given in Section 2.6.1. Emphasis will be given to tests that used iron and manganese, the two metals studied in this thesis. Investigations in laboratory scale systems and the proposed mechanisms of additive action will be discussed in Section 2.6.2.

2.6.1 Practical Combustion Systems

Perhaps the first study of the effects of metal additives on soot formation was conducted by Bartholomé and Sachsse (1949). Salt solutions of many metals were found to reduce soot formation and produce particles of a smaller size. Weeks *et al.* (1959) tested iron (in the form of ferrocene) and other metals (as naphthenates) in an oil heating combustor. Weeks *et al.* found the order of effectiveness of metal additives in reducing soot formation was

Fe Ni Co Mn Pb Mg
—————→
decreasing effectiveness

Changing the organic substituent had little observable effect. In another oil burner study, Vaerman (1964) also demonstrated that the metals, and not the organic substituents, were the active components in the additives. However, Vaerman found the order of effectiveness in reducing soot to be

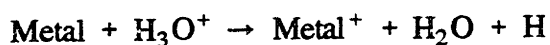
Cu Co Mn Fe Ni Pb K Ba
—————→
decreasing effectiveness

The effects of iron and manganese on soot formation have been studied in several practical systems. A soot-reducing fuel additive containing manganese (MMT, methylcyclopentadienyl manganese tricarbonyl) was sold by Ethyl Corporation for several years as Combustion Improver No. 2 (Howard and Kausch, 1980). (CMT, cyclopentadienyl manganese tricarbonyl, was selected for this thesis instead of MMT because CMT is a solid at room temperature, while MMT is a liquid.) Martin *et al.* (1971) tested 206 commercial additives, and found ferrocene and MMT to have the greatest effect on reducing particle emissions. Although 14 different metals were represented in the 206 compounds studied, only additives containing iron, manganese, or cobalt significantly reduced particle emissions. Toone (1968) found that adding ferrocene did not reduce carbon formation in a Rolls Royce Dart engine. Friswell (1972) added ferrocene and MMT (among other compounds) to an aviation kerosene. When burned under conditions simulating gas-turbine combustion, iron and manganese had almost the same effect. Under certain conditions, manganese reduced carbon formation by 73%. Giovanni *et al.* (1972) have tested MMT in model gas turbines burning a jet fuel. They found an increase in the particulate mass which they attributed to solid phase manganese oxides.

The different results from these studies illustrate the difficulty in drawing even qualitative conclusions from studies in practical systems. Howard and Kausch (1980) reviewed the metal additive literature on both practical and laboratory-scale systems through 1980 and concluded that the most effective soot-reducing fuel additives are ones which contain manganese, iron, or barium.

2.6.2 Laboratory-Scale Systems and Mechanisms

In their review of the metal additive literature, Howard and Kausch (1980) outlined three broad mechanisms of additive action. Mechanism I is an ionic mechanism based upon the observations of Haynes *et al.* (1979) in premixed flames and Bulewicz *et al.* (1975) in diffusion flames. Both groups observed a shift to smaller soot particle sizes when alkali metal were added to the flame. Several authors agree (e.g., Calcote, 1972) that alkali metals, unlike other metals, can ionize extensively in flames and participate in charge transfer reactions of the type



Calcote then speculates that the reduction in natural flame ions will reduce soot formation because metal ions are less efficient soot nuclei than natural flame ions. Hayhurst and Jones (1989) also support this hypothesis. Haynes *et al.* proposed that the alkali metals promote charging of the soot particles, thereby reducing the coagulation rate and the particle size. Between one and three charges per particle would explain the order of magnitude decrease in the particle coagulation rate that they observed.

Mechanism II is based on the observations of Cotton *et al.* (1971) on the effects of alkaline earth metals in propane diffusion flames. Alkaline earth metals have been observed to reduce soot formation under both fuel rich and fuel lean conditions. Alkaline earth hydroxides are believed to form in the flames and reduce soot formation by catalyzing the decomposition of water vapor into hydrogen and hydroxyl radicals. The increased hydroxyl radical concentration then results in an increased oxidation rate of soot and/or soot precursors. Jenkins (1972) also supported this view. Using saturated laser induced fluorescence, Bonczyk (1987) has inferred OH concentrations in diffusion flames containing alkaline earth metals. Bonczyk found that calcium, strontium, and barium actually decrease the OH concentration, apparently disproving this hypothesis.

Mechanism III, as described by Howard and Kausch, applies to transition metals and is believed to function only in regions where soot oxidation occurs. Transition metal oxides occluded in soot particles are suggested as being capable of accelerating soot burnout. Since there is no soot oxidation zone in premixed flames, observation of this mechanism is unlikely in this study. Howard and Kausch concluded that a better understanding of the mechanisms through which transition metal additives effect soot formation would be very useful.

Laboratory-scale investigations of the effects of iron and manganese on soot formation have been conducted by Ritrievi (1984), who added ferrocene vapor to premixed ethylene/oxygen/nitrogen flames, and Hayhurst and Jones (1989), who added a 0.002 M aqueous manganese chloride solution to premixed $C_2H_2/O_2/Ar$ flames. Ritrievi found that iron increased the amount of soot under all conditions. Ritrievi proposed that iron oxide homogeneously nucleated in the gas phase before soot particle inception occurred. The FeO particles were proposed to act as seed particles on which soot could deposit, increasing particle inception. Once within the soot particles, FeO was further assumed to

be reduced to metallic iron. The metallic iron then diffused to the particle surface, where it catalyzed soot surface growth.

Hayhurst and Jones (1989) found that manganese had no effect on the soot particle size and number density. Sodium and strontium, when added in the same concentration as manganese, noticeably reduced the particle size. Padley and Sugden (1959) observed the emission spectra of H_2 flames containing added manganese. The two major species present were free Mn atoms (~75% of the manganese) and MnO (~25%). A trace amount of $MnOH$ (<1%) was detected.

The conflicting results from the studies in practical systems show that combustion temperature, time, and mixing can influence soot formation and the effects of metal additives on soot formation. The results from the studies in laboratory systems (in which these variables can be controlled) show the soot aerosol and the gas phase composition must be characterized in detail to discriminate between the possible mechanisms of additive action. In particular, changes in the soot particle size and concentration must be measured; changes in the gas phase composition must be measured; and the chemical state of the additive must be determined. Mechanism III, proposed by Howard and Kausch, suggests that the spatial distribution of transition metals within the soot particles may also be important. A transition metal would have to be at the surface of a soot particle to catalyze soot oxidation.

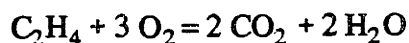
3. EXPERIMENTAL APPARATUS AND TECHNIQUES

3.1 Premixed Flame Burner

The burner used to generate premixed ethylene flames is shown in Figure 3.1-1. The flow rates of ethylene, oxygen, nitrogen, and air were regulated by setting the pressure drop through calibrated critical flow orifices. After passing through the critical flow orifices, the gases were mixed in a long chamber (length/diameter = 10) packed with stainless steel wool and sent to the burner. Two sintered stainless steel disks within the burner straightened the gas velocity profile. The flame holder was a 48 mm (1.9 in) diameter cylinder of Corning Celcor, a ceramic honeycomb with 400 cells per square inch. An annulus of nitrogen surrounded the flame and shielded it from the atmosphere. A water-cooled plate was mounted 38 mm (1.5 in) above the burner surface to stabilize the flame. To examine different regions of the flame, the burner could be translated vertically with a positioning accuracy of ± 0.1 mm and horizontally with a positioning accuracy of ± 0.25 mm.

Two slightly different stabilization plates were used. Both plates were water-cooled, and both were perforated with holes to allow most of the combustion products to rise into an exhaust hood. One of the plates had many small holes of varying sizes, and this plate was used in almost all experiments. However, in order to withdraw gas and soot samples, a probe was inserted down through the plate and into the flame. A second plate, with only two large holes, was used in order to accommodate the large diameter probes needed for some of the sampling experiments.

The flow rates used to generate each flame are listed in Table 3.1-1. Each flame will be referred to by the mole ratio of carbon to oxygen in the feed gas (e.g., 'the C/O = 0.77 flame'). The fuel equivalence ratio, ϕ , is defined as the actual C/O ratio divided by the C/O ratio for a stoichiometric reaction, assuming complete combustion to CO₂ and H₂O. For ethylene, the stoichiometric reaction is



so that ϕ equals three times the actual C/O ratio. The C/O = 0.52 flame was the only non-sooting flame. Table 3.1-1 also shows that the percent N₂ in the feed gas was varied

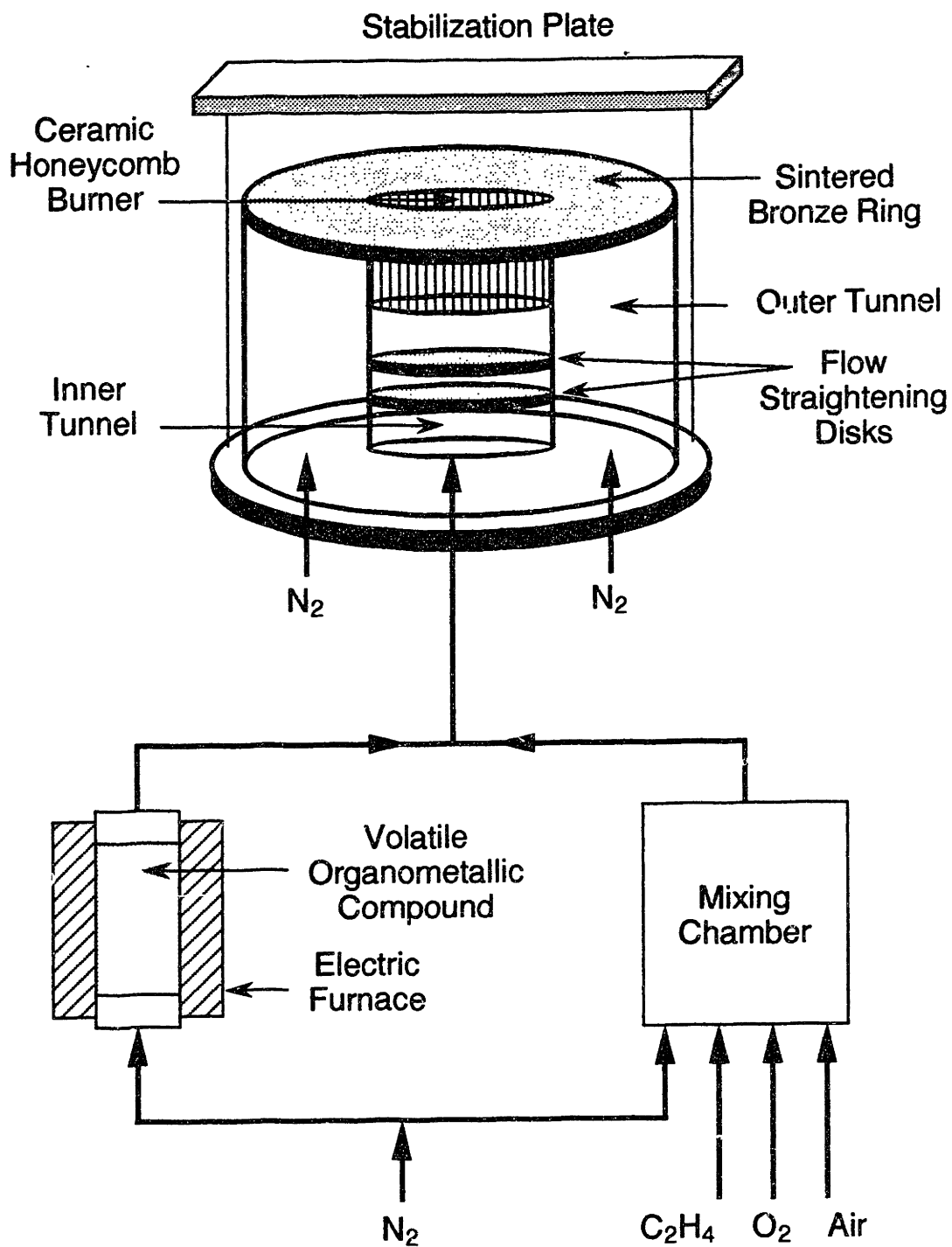


Figure 3.1-1: The premixed flame burner and additive feed system. The volatile organometallic compound was either ferrocene or cyclopentadienyl manganese tricarbonyl.

C/O Ratio	ϕ	GAS FLOW RATE (standard liters per minute)					Percent N ₂
		N ₂	O ₂	Air	C ₂ H ₄	Total	
0.52	1.56	3.63	0	16.34	1.77	21.74	76.1
0.74	2.22	3.63	1.17	5.59	1.73	12.12	66.4
0.77	2.31	3.63	1.19	5.03	1.73	11.58	65.7
0.80	2.40	3.63	1.20	4.53	1.73	11.09	65.0
0.83	2.49	3.63	1.24	4.03	1.73	10.63	64.1

Table 3.1-1: Premixed flame gas flow rates. Standard conditions are 1 atm and 20°C. Each flame will be referred to by the C/O ratio, e.g., 'the C/O = 0.74 flame.' The total gas flow rate and percent nitrogen were varied between flames so that each flame was flat and stable.

Metal	Volatile Compound	ADDITIVE FEED RATE		Metal/Carbon Mole Ratio in Flame
		mg/min	μ moles/min	
Iron	Fe (C ₅ H ₅) ₂	2.77	14.4	1/10,000
Manganese	C ₅ H ₅ Mn (CO) ₃	2.01	9.85	1/14,600

Table 3.1-2: Metal additive feed rates. Each flame will be referred to by the C/O ratio and the presence or absence of a metal. For example, 'the C/O = 0.77 flame' contains no additive, while 'the C/O = 0.77 + Mn flame' contains the manganese additive in the concentration listed in this table.

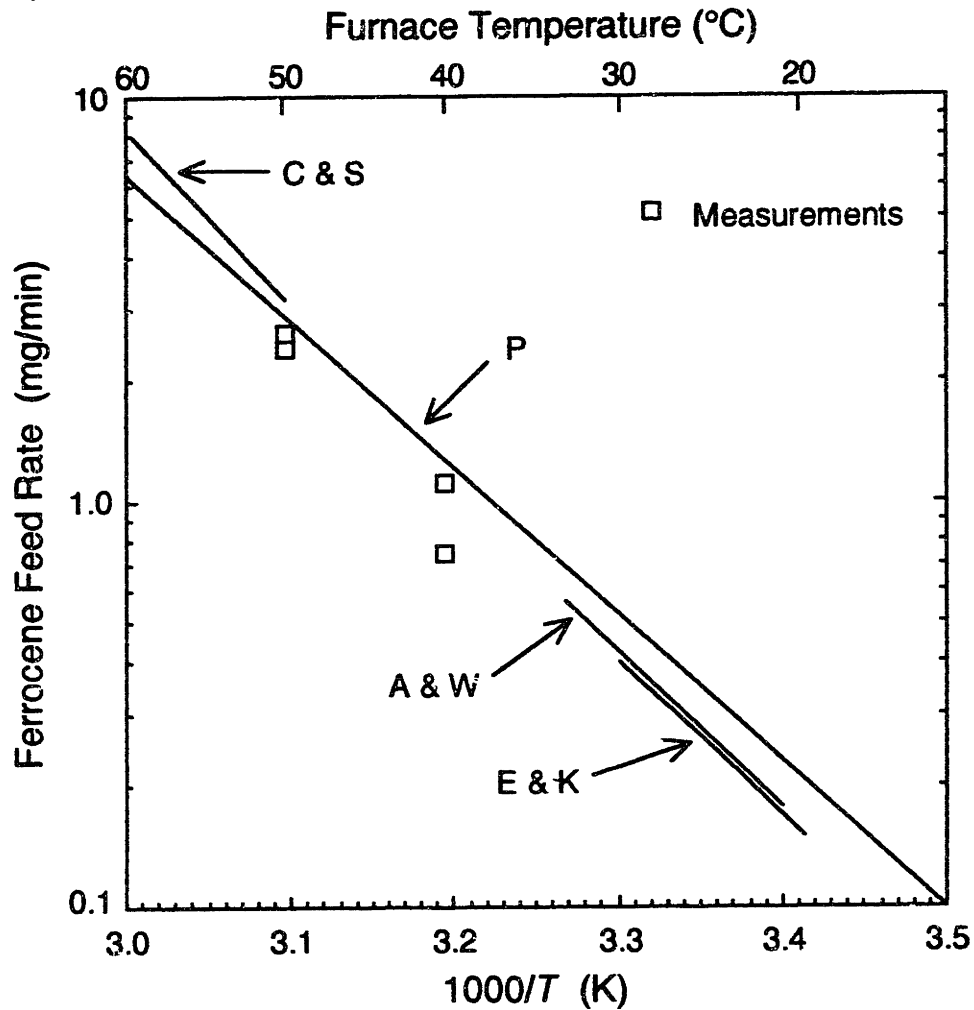
only slightly between sooting flames, while the total gas flow rate dropped by about 12% from the $C/O = 0.74$ flame to the $C/O = 0.83$ flame. The total gas flow and percent N_2 were varied between flames so that each flame was flat and stable. The same N_2 flow rate was used in all flames (3.63 standard liters per minute) to facilitate calibration of the metal additive feed system.

To introduce metal additives into the flame, the nitrogen flow was diverted from the mixing chamber to a glass tube packed with a volatile organometallic compound, as shown in Figure 3.1-1. The nitrogen gas and volatile compound were heated by an electric furnace surrounding the tube, and the nitrogen left the tube saturated with vapor. The furnace temperature was regulated to within $\pm 0.1^\circ\text{C}$ of the desired temperature with a proportional temperature controller. Once saturated, the additive-laden nitrogen was then combined with the other gases and fed to the burner. All gas lines between the furnace and the burner were kept 15°C above the furnace temperature with heating tapes to prevent precipitation of the additive. Thermocouples were placed at several locations to monitor the gas line temperatures.

The calibration of the additive feed system was accomplished by establishing the actual gas flow rates that would be used for a flame, and sending the feed gases through a liquid nitrogen cooled trap, rather than the burner. The additive feed rate was determined from the mass gained by the trap and the elapsed time.

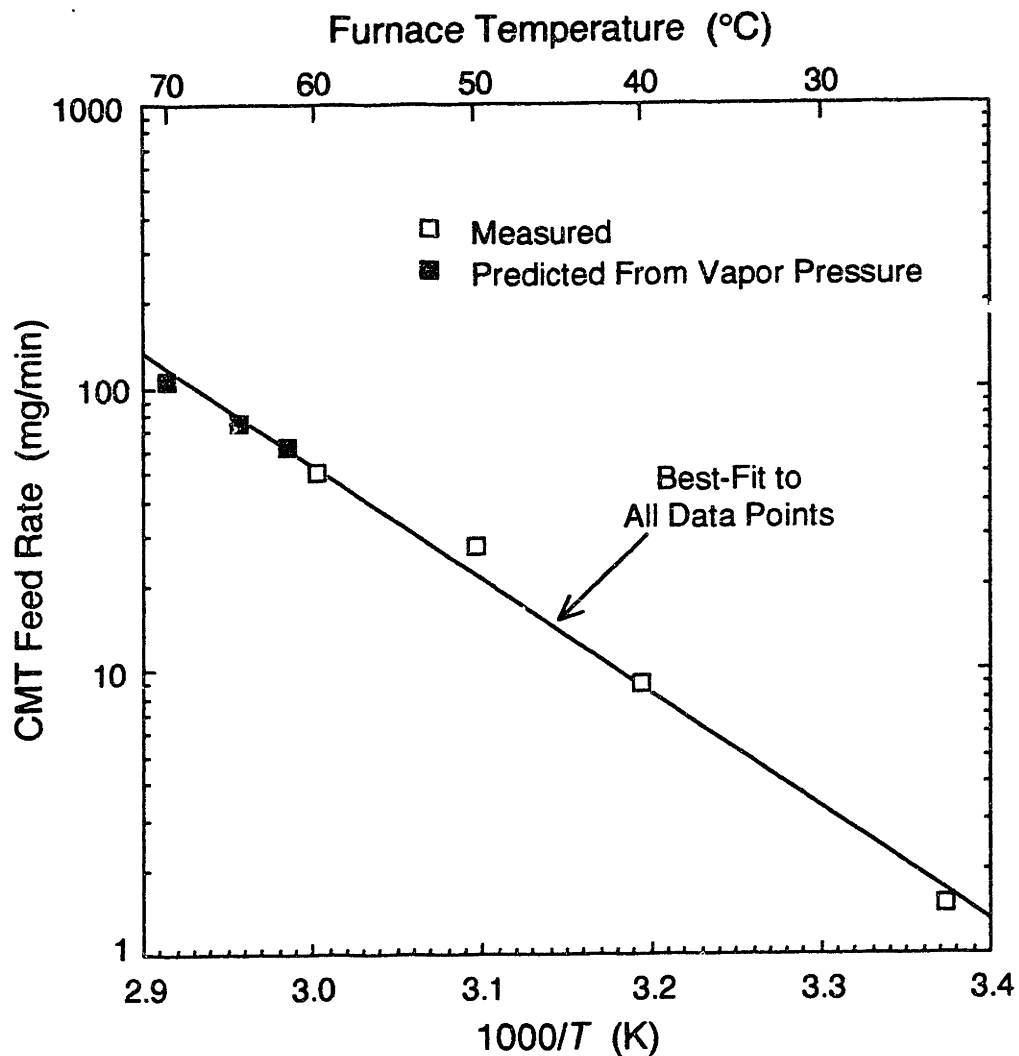
Figure 3.1-2 compares the experimentally measured $\text{Fe}(\text{C}_5\text{H}_5)_2$ (dicyclopentadienyl iron, or ferrocene) feed rate to the expected feed rate, assuming the nitrogen leaving the furnace was saturated at the furnace temperature, and the partial pressure of the additive was equal to its vapor pressure, P_{vp} . Several expected feed rates are shown, because the vapor pressure of ferrocene has been reported several times in the literature (Cordes and Schreiner, 1959; Edwards and Kington, 1962; Andrews and Westrum, 1969; Pelino *et al.*, 1981). The measurements of Pelino *et al.* are the most accurate and extend over the widest temperature range. The agreement between the predictions, assuming saturation, and the measurements is quite good. For this reason, the nitrogen gas stream was assumed to be saturated with ferrocene, and the vapor pressure measurements of Pelino *et al.* were used to calculate the ferrocene feed rate.

Figure 3.1-3 compares the experimentally measured $\text{C}_5\text{H}_5\text{Mn}(\text{CO})_3$ (cyclopentadi-



$$\text{Feed Rate (mg/min)} = 1.669 \times 10^{(12 - 3805/T(K))}$$

Figure 3.1-2: Comparison of the measured ferrocene feed rate and the expected feed rate, assuming saturation. The expected feed rate, based on the vapor pressure data from four groups, is shown in this figure: C & S = Cordes and Schreiner, 1959; P = Pelino *et al.*, 1981; A & W = Andrews and Westrum, 1969; E & K = Edwards and Kington, 1962. The vapor pressure data of Pelino *et al.* is the most accurate; the equation shown is the expected feed rate based on their data.



$$\text{Feed Rate (mg/min)} = 5.830 \times 10^{(13 - 4013/T(K))}$$

Figure 3.1-3: Comparison of the measured cyclopentadienyl manganese tricarbonyl (CMT) feed rate and the predicted feed rate, assuming saturation. The vapor pressure data of Cordes and Schreiner (1959) was used to predict the feed rate. The best-fit line was calculated using both the measured feed rates and the feed rates predicted from the vapor pressure.

enyl manganese tricarbonyl, or CMT) feed rate to the expected feed rate, based on the vapor pressure of CMT (Cordes and Schreiner, 1959). The best-fit line in this figure has been calculated using the data from the cold trap experiments and the data from Cordes and Schreiner. Although the P_{vp} data of Cordes and Schreiner is over a limited temperature range, the agreement between the two sets of measurements is encouraging. Therefore, the best-fit line shown in Figure 3.1-3 was used to calculate the CMT feed rate.

The metal additive feed rates are listed in Table 3.1-2. For flames containing ferrocene, the furnace temperature was set to 50°C, which corresponds to a ferrocene feed rate of 2.77 mg/min (14.4 μ moles/min). Since the ethylene feed rate was the same in all of the sooting flames (1.73 SLPM, or 0.0720 moles/min), the mole ratio of iron to carbon was the same in all flames, 1 mole Fe/10,000 moles C. For flames containing CMT the additive bed was maintained at room temperature, 25°C, which corresponds to a CMT feed rate of 2.01 mg/min (9.85 μ moles/min). The mole ratio of manganese to carbon was 1 mole Mn/14,600 moles C. Each flame containing a metal additive will be referred to by the C/O ratio and the additive, e.g., 'the C/O = 0.77 + Mn flame.'

The additives had a negligible effect on the flame C/O ratio. For example, the C_5H_5 groups added to the flame as part of the ferrocene additive increased the C/O ratio of the 0.74 flame to 0.741.

When burning flames without additives, no visible deposits were formed on the ceramic flame holder after up to 100 hours of operation. However, flames with metal additives generated deposits that visibly discolored the flame holder after one or two hours. After 10 to 15 hours of operation (not necessarily continuous), the deposit became so heavy that a stable flame could not be sustained — the flame front would descend below the top of the flame holder. The transition from a flame holder that could support a flame to one that could not support a flame was rapid. In other words, for the first 10 to 15 hours the flame was stable and no changes in the flame could be measured. At some point in time, however, a noticeable change could be observed in the scattering or absorption signal. A red glow would appear in the center of the ceramic honeycomb at this time. Within about 10 minutes of first noticing a change in the signal, the red glow would spread out to the edges of the flame holder and the flame front would descend into

the burner. The flame was usually extinguished (by turning off the feed gases) long before the flame descended into the burner, since O-rings within the burner would melt. Measurements ceased as soon as the red glow and signal change were observed.

Some of the burner deposit could be removed by washing the ceramic in concentrated hydrochloric acid. However, even when washing was continued until the HCl wash was colorless, a cleaned burner plug could not support a stable flame for more than a few minutes. Sanding down the burner plug to remove the contaminated end, removing a depth of several millimeters, proved to be a very successful method for restoring a burner plug. After such a treatment a burner plug would generally support flames with additives for another 10 to 15 hours, as expected for an uncontaminated plug.

3.2 Temperature Measurements

An optical pyrometer (Pyrometer Instrument Model No. 95) was used to measure flame brightness temperatures, T_{br} , at 655 nm. The pyrometer was mounted on a tripod approximately 1.5 m from the flame and focused on the center of the flame. The calibration of the optical pyrometer was verified by measuring brightness temperatures from a tungsten filament lamp calibrated by the National Bureau of Standards (NBS). Details of the calibration test and results are given in Appendix A.

The brightness temperature of the flame was converted into the actual flame temperature using the Wien equation

$$\exp\left(\frac{-c_2}{\lambda T_{br}}\right) = \epsilon_\lambda \exp\left(\frac{-c_2}{\lambda T}\right) \quad (3.2-1)$$

where $c_2 = \text{Planck's second constant} = 1.43847 \text{ cm K}$,

$T_{br} = \text{brightness temperature}$,

$T = \text{gas temperature}$,

$\epsilon_\lambda = \text{spectral emissivity at wavelength } \lambda$, and

$\lambda = \text{wavelength of emissivity and brightness temperature measurements}$.

When solved for T , Equation 3.2-1 becomes

$$T = \frac{c_2 T_{br}}{c_2 + \lambda T_{br} \ln \epsilon_\lambda} \quad (3.2-2)$$

Equation 3.2-2 requires ϵ_λ and T_{br} at the same wavelength. However, T_{br} was measured at 655 nm (the operating wavelength of the pyrometer) while the spectral emissivi-

ty was measured at 514.5 nm. The wavelength of the ϵ_λ measurements was chosen to match the wavelength of the scattering measurements, described in Section 3.3. The scattering measurements were taken with an argon ion laser which operates at only certain wavelengths.

The emissivity at one wavelength, λ_1 , can be used to estimate the emissivity at a second wavelength, λ_2 , if the refractive index is assumed to be constant over the wavelength range from λ_1 to λ_2 . With this assumption, Equation 2.2.1-13 shows

$$\lambda_1 K_{ext,1} = \lambda_2 K_{ext,2} \quad (3.2-3)$$

or

$$\lambda_1 \ln(1 - \epsilon_{\lambda_1}) = \lambda_2 \ln(1 - \epsilon_{\lambda_2}) \quad (3.2-4)$$

Solving Eq. 3.2-4 for the emissivity at the second wavelength gives

$$\ln(\epsilon_{\lambda_2}) = \ln \left[1 - (1 - \epsilon_{\lambda_1})^{\lambda_1/\lambda_2} \right] \quad (3.2-5)$$

Substituting this result into Eq. 3.2-2 gives

$$T = \frac{c_2 T_{br}}{c_2 + \lambda_2 T_{br} \ln \left[1 - (1 - \epsilon_{\lambda_1})^{\lambda_1/\lambda_2} \right]} \quad (3.2-6)$$

which is the equation that was used to calculate flame temperatures from T_{br} measured at $\lambda_2 = 655$ nm and ϵ_λ measured at $\lambda_1 = 514.5$ nm. Figure 2.4-1 shows that the refractive index can be assumed constant over the narrow range $514.5 \text{ nm} < \lambda < 655 \text{ nm}$.

3.3 Absorption, Scattering, and Fluorescence Measurements

Measurements of the flame ϵ_λ were made with the apparatus shown in Figure 3.3-1. The light source was a tungsten filament lamp (General Electric #20AT24/2) powered by a highly stable DC source (Hewlett-Packard 6268B) operated in load voltage regulation mode. The light beam was chopped at 400 Hz by a variable speed chopper (Laser Precision CTX-534) which also supplied a reference signal to a lock-in amplifier (EG&G 128A). The lock-in amplifier filtered out signals that were not synchronized with the reference signal frequency, thereby rejecting light from the flame and other sources.

An image of the filament was focused on a point above the center of the burner with a 15 cm focal length lens. A second 15 cm focal length lens collected the transmitted light and created an image of the filament on a photomultiplier tube (Hamamatsu R928). The photomultiplier tube (PMT) was mounted in an insulated housing (Pacific

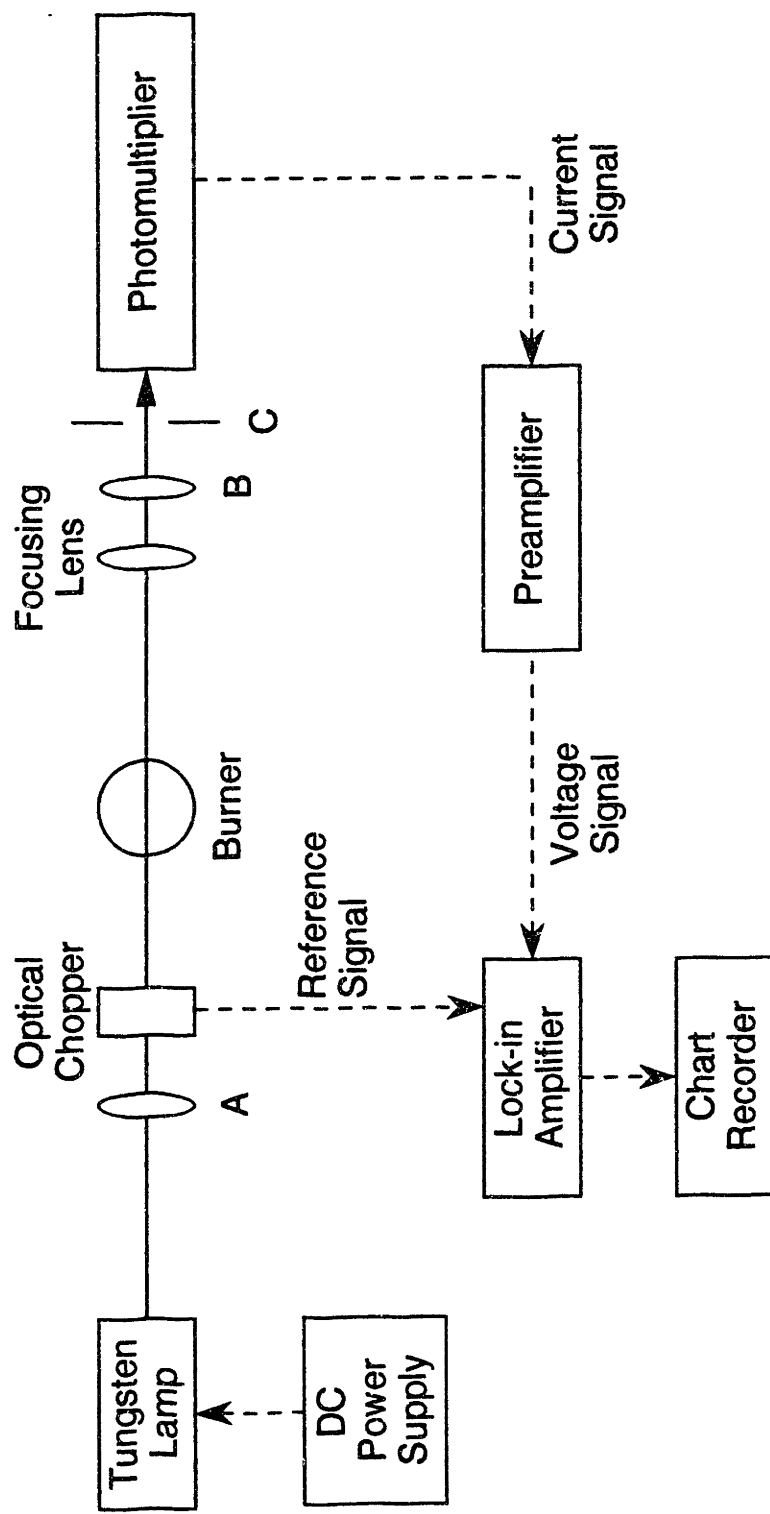


Figure 3.3-1: The light absorption apparatus. A = focusing lens; B = narrow band interference filter; C = adjustable apertures used to determine sample volume.

Instruments 3461) and cooled to $-10.0 \pm 0.1^\circ\text{C}$ (Pacific Instruments Model 33). A high voltage power supply (Pacific Instruments Model 204) was used to set the total potential drop through the PMT. A 514.5 nm narrow band interference filter (1.0 nm bandwidth) was mounted on the PMT housing, and selected the wavelength for the emissivity measurements.

The sample volume in the flame was set by a fixed diameter aperture on the PMT focusing lens and two slits mounted behind the interference filter. These slits created an aperture that was 2.0 mm wide and 0.12 mm high. The current signal from the PMT was converted into a voltage signal by a current sensitive preamplifier (EG&G Model 181) and sent to the lock-in amplifier. The output voltage signal from the lock-in amplifier was monitored with a chart recorder (Soltec 1242). A zero suppression, scale expansion feature of the lock-in amplifier was used to measure the spectral emissivity, $(I_o - I)/I_o$ (see Eq. 2.2-3), down to values as low as 0.005, which corresponds to a 0.5% change in the intensity of the light reaching the PMT.

In addition to the emissivity, the path length, L , through the flame was needed to calculate the extinction coefficient. The luminous yellow diameter of the flame was taken as the path length, and was measured from color photographs. Since the flame flickers, three photographs were taken of each flame, and average path lengths were used. The metal additives did not cause a significant change in the path length.

Measurements of the scattering coefficient and the fluorescence coefficient were made with the apparatus shown in Figure 3.3-2. For scattering measurements, the light source was an argon ion laser (Coherent Innova 90) operated at 514.5 nm in light regulation mode. The laser beam power was usually set to about 0.6 W. Higher beam powers were used for some flames with low soot volume fractions, and lower beam powers were used for some flames with high soot concentrations. The vertically polarized beam was focused in the center of the flame with a 30 cm focal length lens, and chopped at 500 Hz with a variable speed chopper (Rofin Model 7500). An adjustable width slit and a variable aperture diaphragm were positioned along the beam path between the chopper and the burner to prevent stray beams of laser light from reaching the flame.

The PMT focusing lens, interference filter, slits, and PMT housing were all mounted on a rotating arm that could pivot about the center of the burner. The arm could be ro-

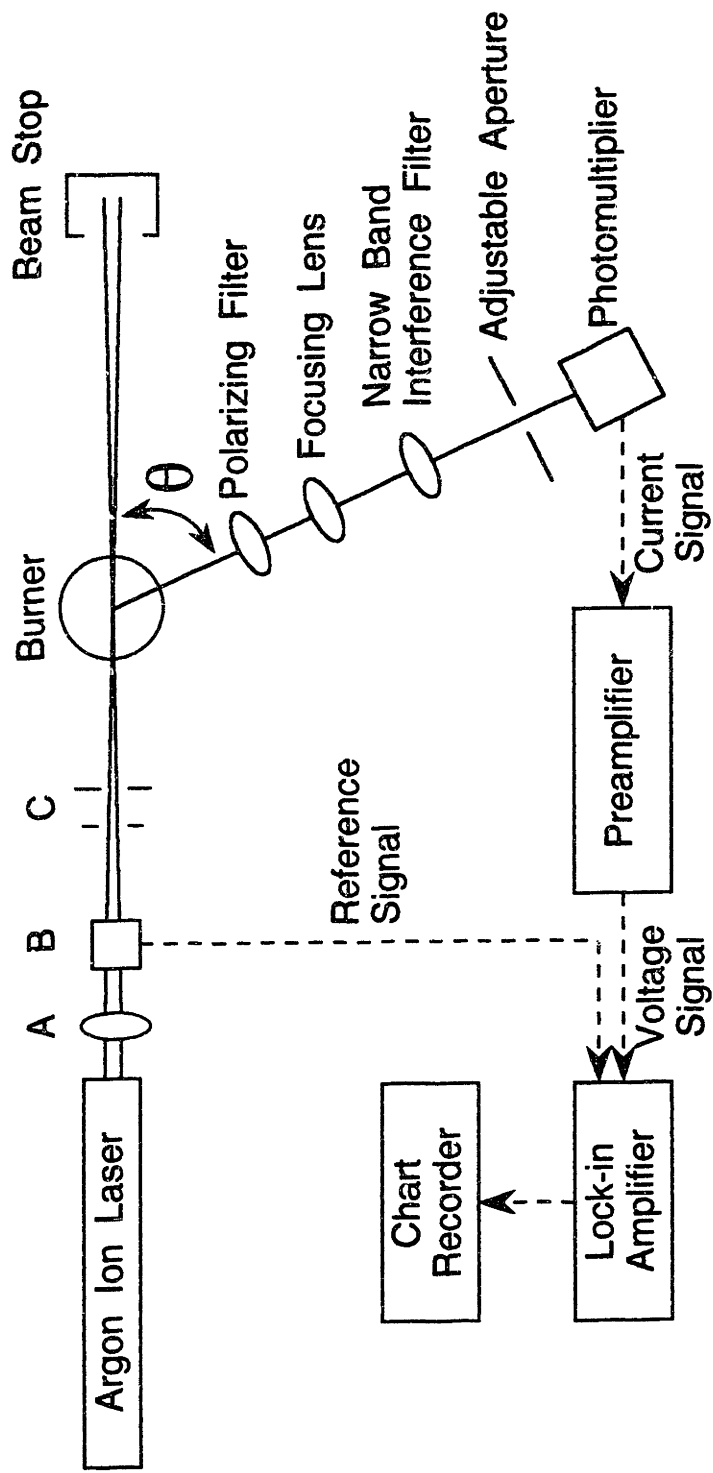


Figure 3.3-2: The light scattering apparatus. **A** = focusing lens; **B** = optical chopper; **C** = light stops; θ = scattering angle. Unless otherwise noted, the scattering angle θ was always set to 45° .

tated to any angle θ from -15° to 135° (see Figure 3.3-2) with an accuracy of $\pm 0.5^\circ$, and allowed the equipment mounted on it to be used for both extinction coefficient and scattering coefficient measurements without alteration. A linear polarizing filter in a rotating mount was placed in front of the light collection lens for scattering measurements. In all other respects, the light collection system and signal detection equipment were the same for both scattering and extinction coefficient measurements. Unless otherwise noted, all scattering and fluorescence measurements were made at a scattering angle of $\theta = 45^\circ$.

Calibration of the scattering signal was accomplished by measuring the scattering signal from nitrogen. The alignment of the rotating arm was checked by measuring scattering from nitrogen and carbon dioxide at angles between 30° and 130° . The calibration measurement was performed before each run, while the alignment was checked every few months. The details of the calibration and alignment are discussed in Appendix B.

For fluorescence measurements, the argon ion laser was tuned to the 488.0 nm beam line. The observation wavelength was maintained at 514.5 nm. In order to improve the signal-to-noise ratio, the laser power was increased to a level as high as possible (while still maintaining light regulation mode) and the 1.0 nm bandwidth filter was replaced with a 10.0 nm bandwidth filter. The transmission characteristics of the two filters are compared in Figure 3.3-3 (data supplied by the manufacturer). In particular, the ratio of the areas under the curves is $5.0744/0.4378 = 11.59$.

3.4 Gas Sample Withdrawal and Analysis

Gas samples were withdrawn for light hydrocarbon analysis using the apparatus shown in Figure 3.4-1. A metal bellows gas sampling pump (Metal Bellows MB-158) drew combustion products isokinetically through a water cooled quartz probe with a 1.1 mm (0.045 inch) internal diameter at the tip (see Figure 3.4-2). The sampled gas passed through a particle filter (Nupro 60 μm in-line filter), mass flow meter (Emerson Electric 5831-1), and metering valve before entering the metal bellows pump. Gas samples were collected in 125 ml glass sampling bulbs (Supelco 2-2161) fitted with non-greased teflon stopcocks. Samples for gas chromatography (GC) analysis were withdrawn by a needle inserted through a rubber septum on the bulb. A new rubber septum was used for each sample.

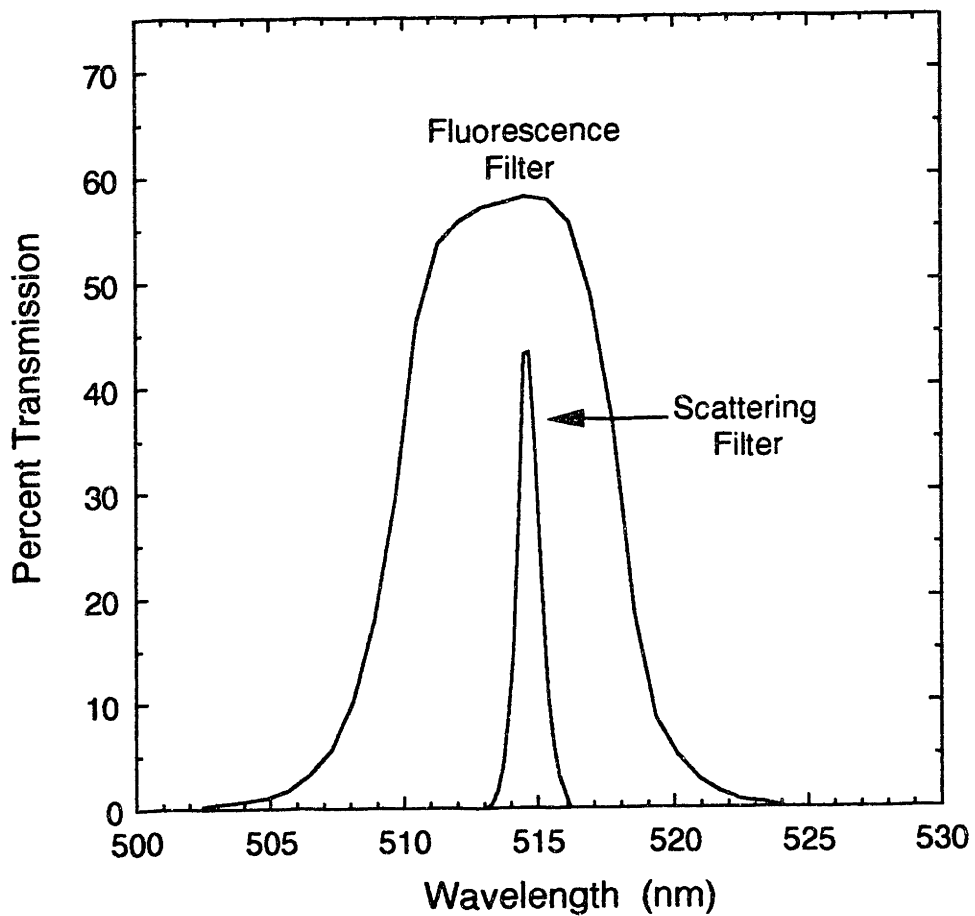


Figure 3.3-3: Transmission characteristics of laser line filters used for scattering and fluorescence measurements. The ratio of the area under the curves is $5.0744/0.4378 = 11.59$. The data was supplied by the manufacturer.

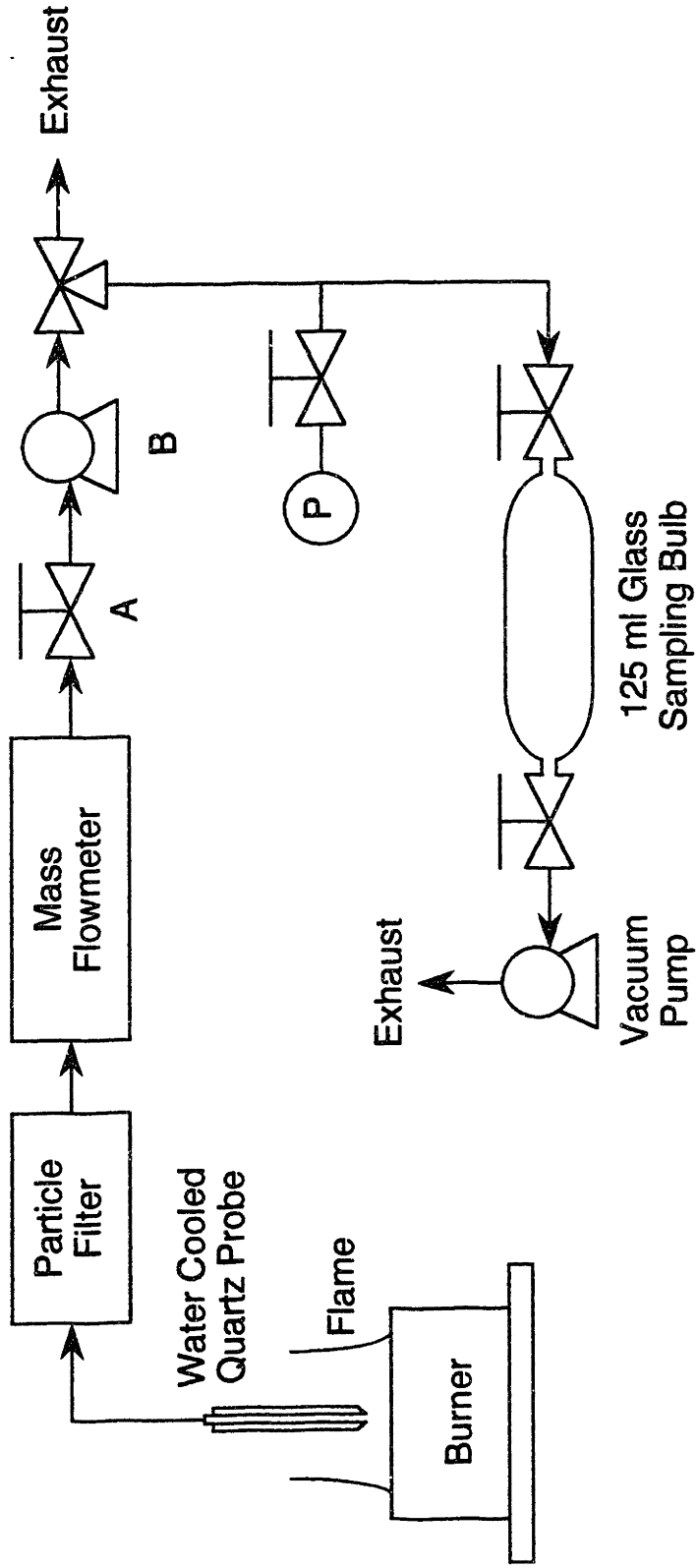


Figure 3.4-1: The gas sampling apparatus. **A** = metering valve; **B** = metal bellows gas sampling pump.

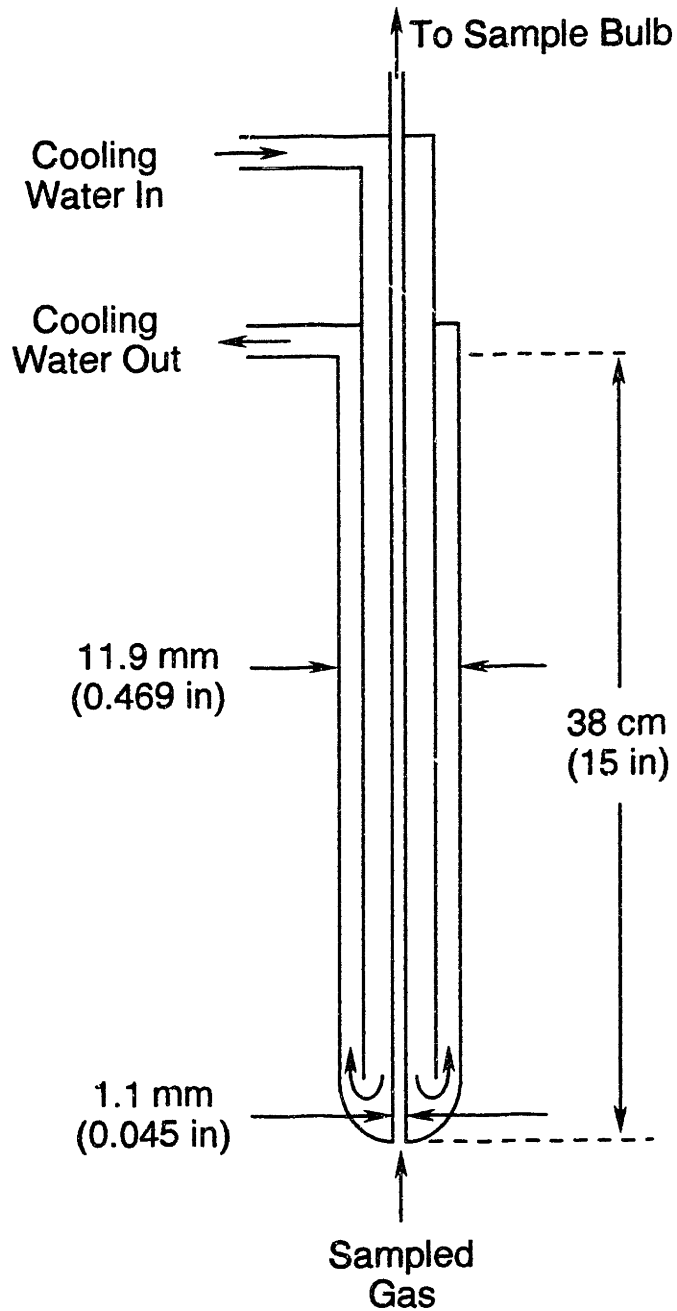


Figure 3.4-2: The water-cooled quartz probe used for gas sampling. The internal diameter of the probe was 1.1 mm at the tip. Gas samples were withdrawn isokinetically.

Quenching of the sampled gas was relatively fast. The characteristic quench time, τ_q , is the time required for the centerline gas temperature to reach 90% of its final value. Eckert and Drake (1959) show that τ_q can be calculated using

$$\frac{\alpha_t \tau_q}{r^2} = 1.0 \quad (3.4-1)$$

where

$$\alpha_t = \text{thermal diffusivity} = \frac{k_c}{\rho \widehat{C}_p} \quad (3.4-2)$$

and k_c = gas thermal conductivity, r = probe radius, ρ = gas density, and \widehat{C}_p = heat capacity at constant pressure per unit mass. Using Eq. 3.4-1, the characteristic quench time was estimated to be 0.4 ms, which is adequate quenching in the post-flame zone of a pre-mixed flame where gas phase species concentrations are changing relatively slowly. Taylor (1984) gives a more detailed discussion of sample gas quenching in water cooled probes.

The procedure for filling a sample bulb was straightforward. First, the probe was positioned at the desired height above the burner. Second, the sampling flow rate was set and the bulb was evacuated with a vacuum pump (Welch Scientific Model 1400) to a pressure less than 1 torr. The sampled gas was diverted to the exhaust hood whenever the bulb was being evacuated. Next, the flame was ignited and sample collection was begun. When the pressure in the bulb reached 1.0 atm, the flow was again diverted to the exhaust hood and the bulb was again evacuated. The sample bulb was filled to 1.0 atm and subsequently evacuated 9 times. The bulb was filled and evacuated many times because the probe and sample line were not evacuated. On the tenth and final fill, the bulb was pressurized to about 1.2 atm and set aside for GC analysis.

Collecting a sample using this procedure often took over 2 hours. During this time the tip of the sampling probe would occasionally clog with soot. Clogging of the probe tip was detected by observing a decrease in the mass flow rate of the sampled gas. When the probe tip became clogged, the sampled gas was temporarily diverted to the exhaust hood and a small stainless steel pin was used to scrape the soot off of the probe. After two minutes, the sampled gas flow was again sent to the sample bulb.

Since the probe was water cooled, and the pressure in the probe was 1.0 atm, water in the sampled gas was expected to condense in the probe. Water condensation was not

observed in the sample bulbs. Therefore, the gas leaving the probe and entering the sample system was most probably saturated with H₂O at the cooling water temperature, 16°C. Details of the correction applied to the measured mole fractions to allow for water condensation are given in Appendix C.

Concentrations of fixed gases (CO, CO₂, and H₂) were determined using a Perkin-Elmer Sigma II gas chromatograph and a hot wire detector. Separations were achieved using a Porapak Q column operated isothermally at -85°C for H₂ and CO, and at 25°C for CO₂. The carrier gas was helium. The analysis scheme for H₂ and CO was also capable of detecting oxygen, and O₂ mole fractions of about 1.0×10^{-3} to 2.0×10^{-3} were detected. However, it is difficult to inject samples without allowing a small amount of air into the GC. In addition, even a tiny leak in the sample system or sample bulb could account for a significant amount of the detected oxygen. Although these measurements could reflect the in situ oxygen concentration, the experimental work required to eliminate the above possibilities was not performed, and the oxygen measurements are not considered quantitative.

Concentrations of stable C₁ through C₄ hydrocarbon species were determined chromatographically using a Hewlett-Packard 5830 and a flame ionization detector (FID). For C₁ and C₂ hydrocarbons, the separation was achieved using two columns in series, a 0.19% picric acid on Graphpac column followed by a Porapak T column. The columns were operated isothermally at 65°C. For stable C₃ and C₄ hydrocarbons, the separation was achieved using only the Graphpac column operated isothermally at 50°C. Argon was the carrier gas in both cases.

Benzene concentrations were determined using a Perkin-Elmer Sigma I and an FID. A 30 m methyl-phenyl (5%) silicone capillary column (J&W Scientific DB-5) was used to achieve the separation, and helium was used as the carrier gas. A temperature program was used to hold the column at -50°C for 2 minutes and then to heat the column to 150°C at the rate of 20°C per minute.

Table 3.4-1 lists the stable gas phase species that were detected in the flame gas samples. Also listed in this Table are the standard gas mixtures that were used to determine the calibration line for each species. The calibration line relates the integrated area of a peak to the concentration of a species. The composition of each standard is given in

Table 3.4-2. Two or three different standards were available for each species except propadiene and benzene.

A peak that appeared in the chromatographs with a retention time that corresponded to propylene was attributed to propadiene, C_3H_4 (Lam, 1988(a)). Two peaks also appeared in the flame gas chromatographs at retention times that did not correspond to any of the calibration gases. These peaks were attributed to vinyl acetylene, C_4H_4 , and diacetylene, C_4H_2 (Lam, 1988(a)). Lam identified these peaks based on both his own work (Lam, 1988(b)) and GC/mass spectrometry measurements of Vaughn (1988). The diacetylene peak was not completely separated from another small, unidentified peak that eluted after diacetylene. The integrator could not separate these two peaks, so their areas were combined and attributed to diacetylene.

No standards were available that contained propadiene, vinyl acetylene, or diacetylene. The calibration line for propylene was used to convert peak areas into mole fractions for propadiene, while the calibration line for 1,3-butadiene was used for vinyl acetylene and diacetylene.

Ethyl acetylene (1-butyne, C_4H_6) was detected in very low concentrations in some, but not all, gas samples. When ethyl acetylene was detected, its concentration was approximately 1 ppm (by volume), or a mole fraction of 10^{-6} . From these measurements the lower detection limit of the GC was established. Many C_3 and C_4 species were not detected, and therefore were concluded to have mole fractions below 10^{-6} . Table 3.4-3 lists species whose retention times were known from the standard gas mixtures but were not found in the flame gas samples.

3.5 Thermophoretic Sampling and Analysis

A thermophoretic sampling probe (TSP) was used to withdraw soot particle samples for analysis. A diagram of the thermophoretic sampling system is shown in Figure 3.5-1, and is similar to the system developed by Dobbins and Megaridis (1987). A precise timing circuit was used to energize an air operated, 4 way solenoid valve (MAC Valves 912-A-PM-57 1 BA). A schematic diagram of the timer circuit is shown in Appendix D. The circuit and valve were powered by a 12 V, 5.0 Amp hr rechargeable battery (Powersonic PS-1245). When a switch on the timer was depressed, the valve was

<u>Species</u>	<u>Formula</u>	<u>Standards</u>
hydrogen	H ₂	4, 5
oxygen	O ₂	4, 5
carbon dioxide	CO ₂	4, 5
carbon monoxide	CO	4, 5
methane	CH ₄	1, 2, 3
ethane	C ₂ H ₆	1, 2, 3
ethylene	C ₂ H ₄	1, 2, 3
acetylene	C ₂ H ₂	2, 3, 6
propadiene	C ₃ H ₄	2 [†]
methyl acetylene	C ₃ H ₄	2, 6
ethyl acetylene	C ₄ H ₆	6, 7
1,3-butadiene	C ₄ H ₆	7, 8
vinyl acetylene	C ₄ H ₄	7, 8*
diacetylene	C ₄ H ₂	7, 8*
benzene	C ₆ H ₆	9

Table 3.4-1: Stable species found in gas samples. The composition of each standard used for calibration is listed in Table 3.4-2.

[†] Propadiene (allene) concentrations were determined using the calibration line for propylene.

* Concentrations for these species were calculated using the calibration line for 1,3-butadiene.

STANDARD #1
Scott Specialty Gases Can Mix 216

<u>Species</u>	<u>% by volume in N₂</u>
methane	0.9998
ethylene	0.9982
ethane	0.9991
acetylene	0.9988
carbon monoxide	0.9993
carbon dioxide	0.9991

STANDARD #2
Scott Specialty Gases Can Mix 54

<u>Species</u>	<u>ppm (by volume) in N₂</u>
methane	20.64
ethane	17.14
ethylene	21.20
acetylene	15.86
propane	17.0
propylene	15.01
n-butane	19.08
methyl acetylene	14.76

STANDARD #3
Matheson Gas Products

<u>Species</u>	<u>% by volume in N₂</u>
methane	0.304
ethane	0.010
ethylene	0.120
acetylene	3.0

STANDARD #4
Scott Specialty Gases Can Mix 218

<u>Species</u>	<u>% by volume in N₂</u>
methane	0.997
carbon monoxide	0.999
carbon dioxide	0.999
hydrogen	0.999
oxygen	1.002

STANDARD #5
Scott Specialty Gases Can Mix 234

<u>Species</u>	<u>% by volume in He</u>
carbon monoxide	4.998
hydrogen	4.001
carbon dioxide	5.037
nitrogen	4.998
oxygen	4.998

STANDARD #6
Scott Specialty Gases Can Mix 30

<u>Species</u>	<u>ppm (by volume) in N₂</u>
acetylene	14.5
methyl acetylene	15.1
ethyl acetylene	14.1
2-butyne	16.6

STANDARD #7
Scott Specialty Gases Can Mix 55

<u>Species</u>	<u>ppm (by volume) in N₂</u>
n-butane	16.45
isobutane	17.38
1-butene	17.14
isobutylene	16.49
cis-2-butene	16.0
trans-2-butene	15.58
ethyl acetylene	24.56
1,3-butadiene	14.77

STANDARD #8
Matheson Gas Products

<u>Species</u>	<u>ppm (by volume) in N₂</u>
1,3-butadiene	96

STANDARD #9
Scott Specialty Gases Can Mix 242

<u>Species</u>	<u>ppm (by volume) in air</u>
benzene	105.8

Table 3.4-2: GC calibration standards.

<u>Species</u>	<u>Formula</u>
propane	C_3H_8
propylene	C_3H_6
n-butane	C_4H_{10}
isobutane	C_4H_{10}
1-butene	C_4H_8
isobutylene	C_4H_8
cis-2-butene	C_4H_8
trans-2-butene	C_4H_8
2-butyne	C_4H_6

Table 3.4-3: Stable species with known retention times, but not found in gas samples. These species must have mole fractions less than 10^{-6} . A peak that appeared at the retention time that corresponded to propylene was attributed to propadiene, C_3H_4 .

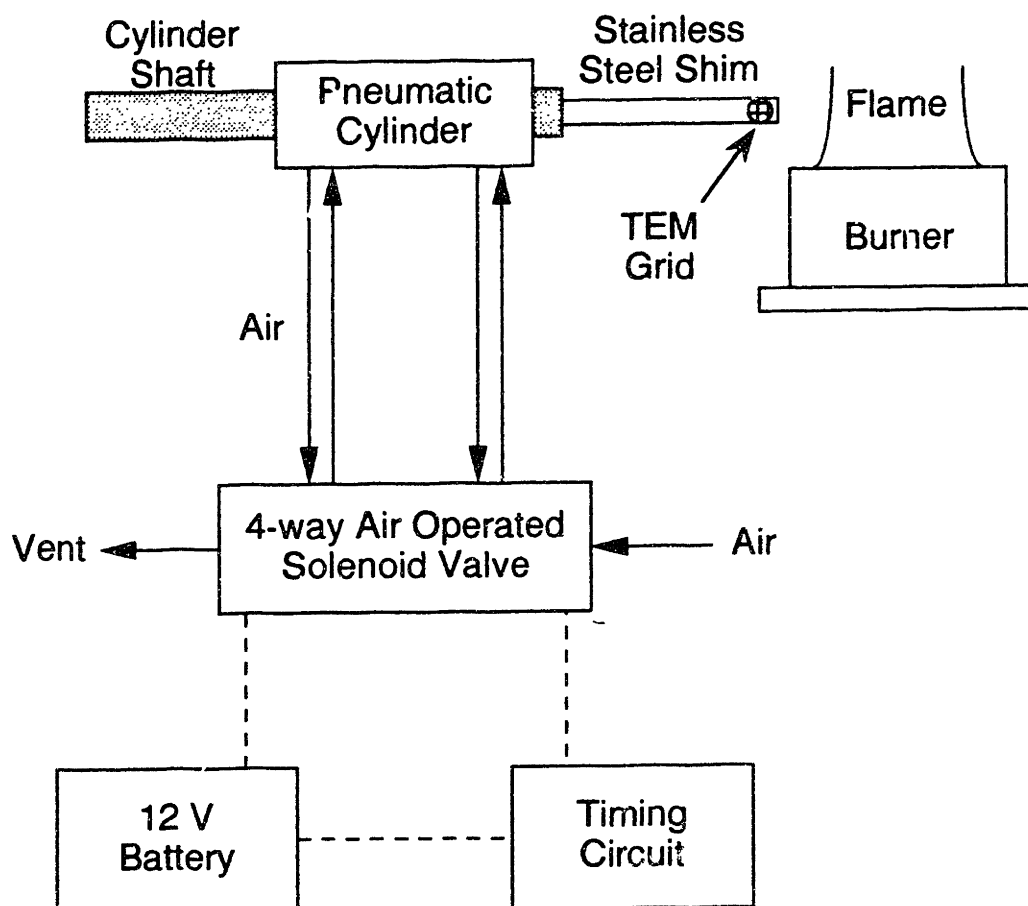


Figure 3.5-1: The thermophoretic sampling probe system. When a switch on the timing circuit was depressed, the valve was energized for a preset time interval and the cylinder shaft and shim moved forward into the flame. The cylinder shaft and shim are shown in the fully withdrawn position.

energized, and a 19 mm (3/4 in) bore, 76 mm (3 in) stroke pneumatic cylinder (Bimba 043-DXDE) was actuated. As the cylinder shaft moved forward, a 0.38 mm (0.015 in) thick stainless steel shim attached to the shaft was inserted into the flame (see Figure 3.5-2). Soot particles deposited thermophoretically on a room temperature transmission electron microscope (TEM) grid attached with epoxy to the end of the shim. The shim and TEM grid were oriented parallel to the flame streamlines. At the end of the timing cycle, the 4 way valve was de-energized, and the shim and TEM grid were withdrawn from the flame.

The circuit shown in Figure 3.5-3 was used to calibrate the movement of the TSP. A linear motion transducer (Waters Manufacturing LRT-S-100B) was attached to the rear end of the pneumatic cylinder shaft. As the shaft moved forward and backward, the change in voltage in the circuit was measured with a digitizing oscilloscope (Tektronix 5223). The voltage was used to calculate the extension of the piston, assuming that the resistance of the transducer varied linearly with distance. A typical trajectory of the TSP is shown in Figure 3.5-4. The time scale in Figure 3.5-4 was arbitrarily set to zero at the instant the timer begins the output voltage pulse. After a significant time delay, τ_d , the probe begins to move forward into the flame. The probe moves with a nearly constant velocity of approximately 2.4 m/s (5.4 miles/hour) during the insertion time, τ_i . The probe remains stationary, in the center of the flame, for a period of time denoted τ_e , the exposure time. Finally, the timer pulse ends and the probe begins to move backwards. The time for withdrawal is denoted τ_w .

Figures 3.5-5 and 3.5-6 show that τ_d , τ_i , and τ_w are nearly independent of the timer pulse width. The exposure time, however, is a strong function of the pulse width, as shown in Figure 3.5-6. Using the calibration curve shown in this figure,

$$\tau_e \text{ (ms)} = 0.972 \text{ (Pulse Width, ms)} - 29.9 \quad (3.5-1)$$

τ_e could be set between 50 and 170 ms. Because the motion of the probe was reproducible and predictable, the linear motion transducer and digitizing oscilloscope were not used to time the TSP once the calibration was complete.

The TEM grids used were 400 mesh, carbon coated circular grids, 3.05 mm in diameter (Ernest F. Fullam, No. 14560). The grid was made of copper bars nominally 25 μm in diameter, arranged to create square cells nominally 37 μm on a side. The nomi-

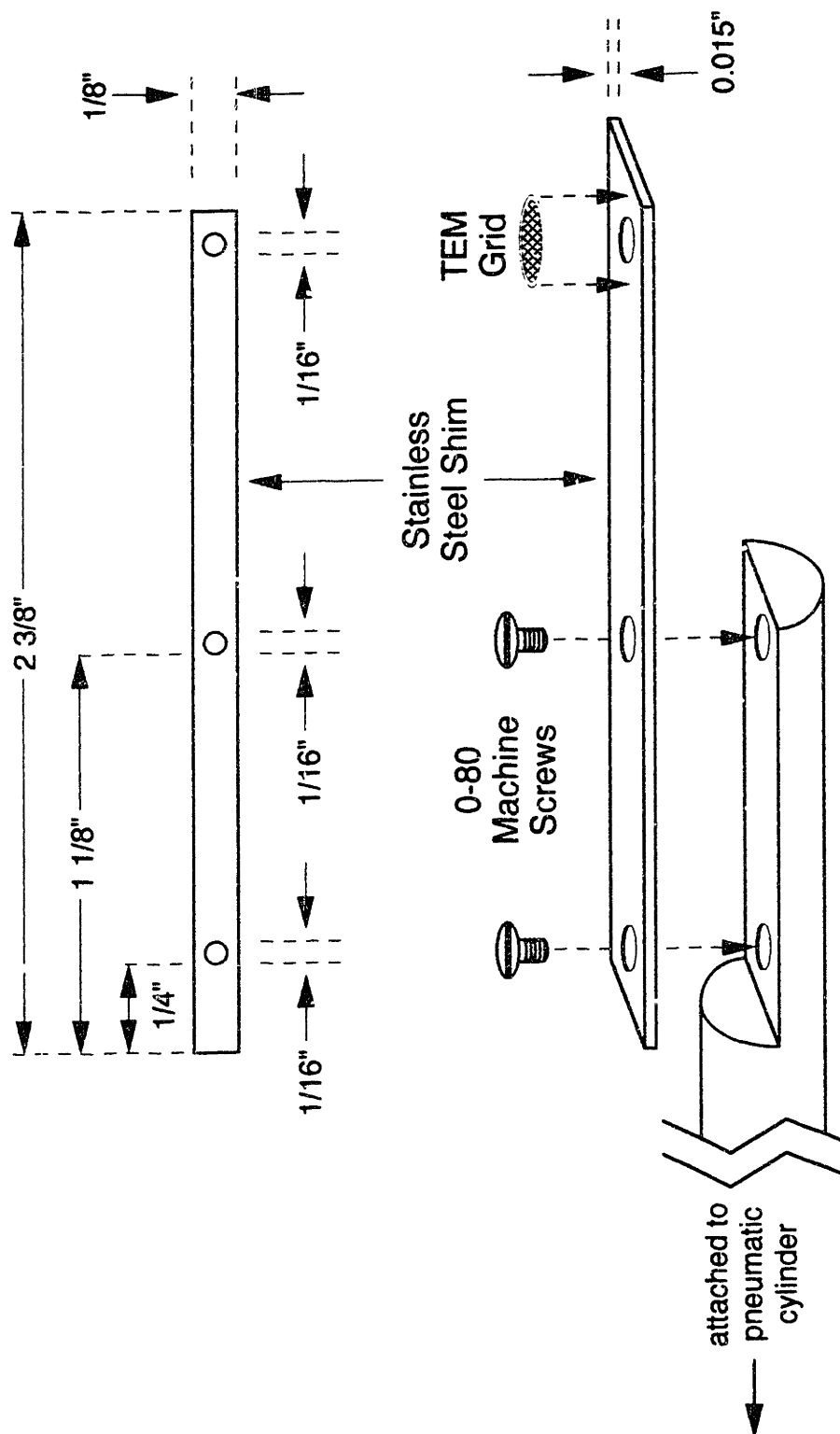


Figure 3.5-2: Detail of the thermophoretic sampling probe. The TEM grid was attached to the stainless steel shim with epoxy. The shim and TEM grid were oriented parallel to the flame streamlines. After insertion, the end of the shim with the TEM grid was cut off, and the rest of the shim was discarded.

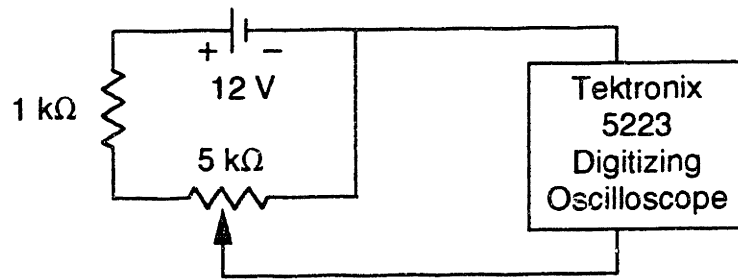


Figure 3.5-3: The circuit used to calibrate the motion of the thermophoretic sampling probe. The variable resistor was a LIN-R-TRAN ZB 8828 linear motion transducer, and was attached to the end of the thermophoretic sampling probe cylinder shaft (see Figure 3.5-1).

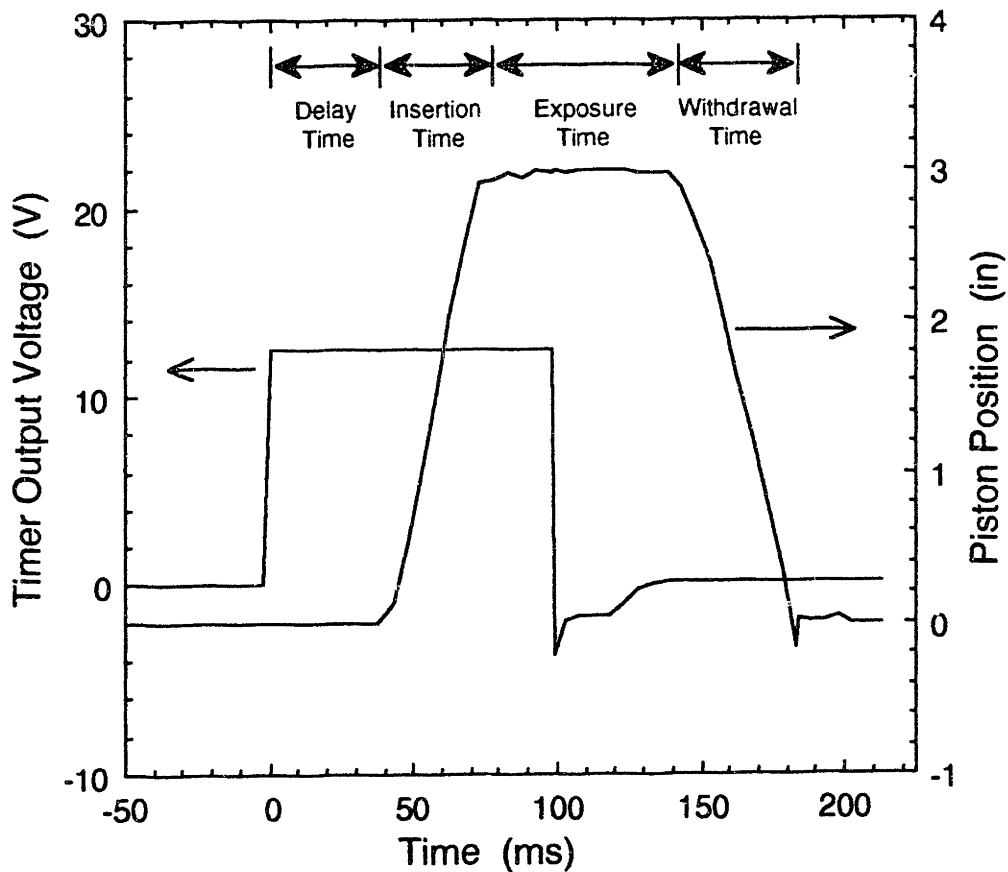


Figure 3.5-4: A typical trajectory of the thermophoretic sampling probe. The time scale was arbitrarily set to zero at the instant the timer begins the output voltage pulse.

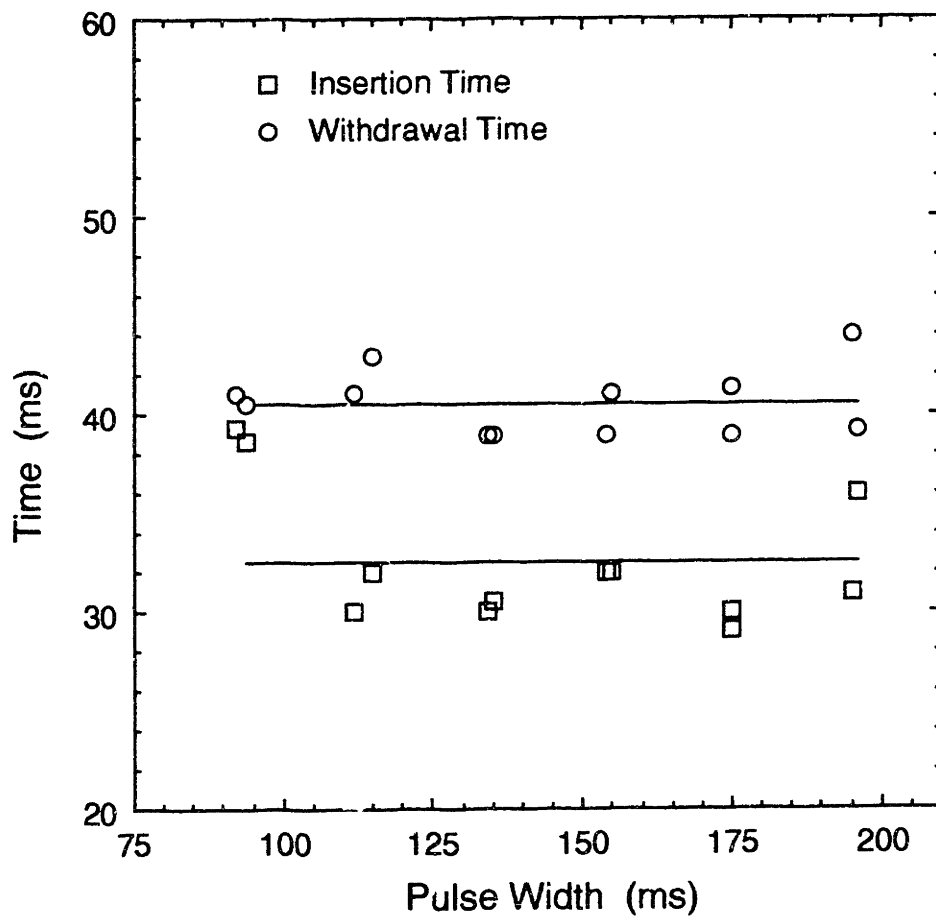
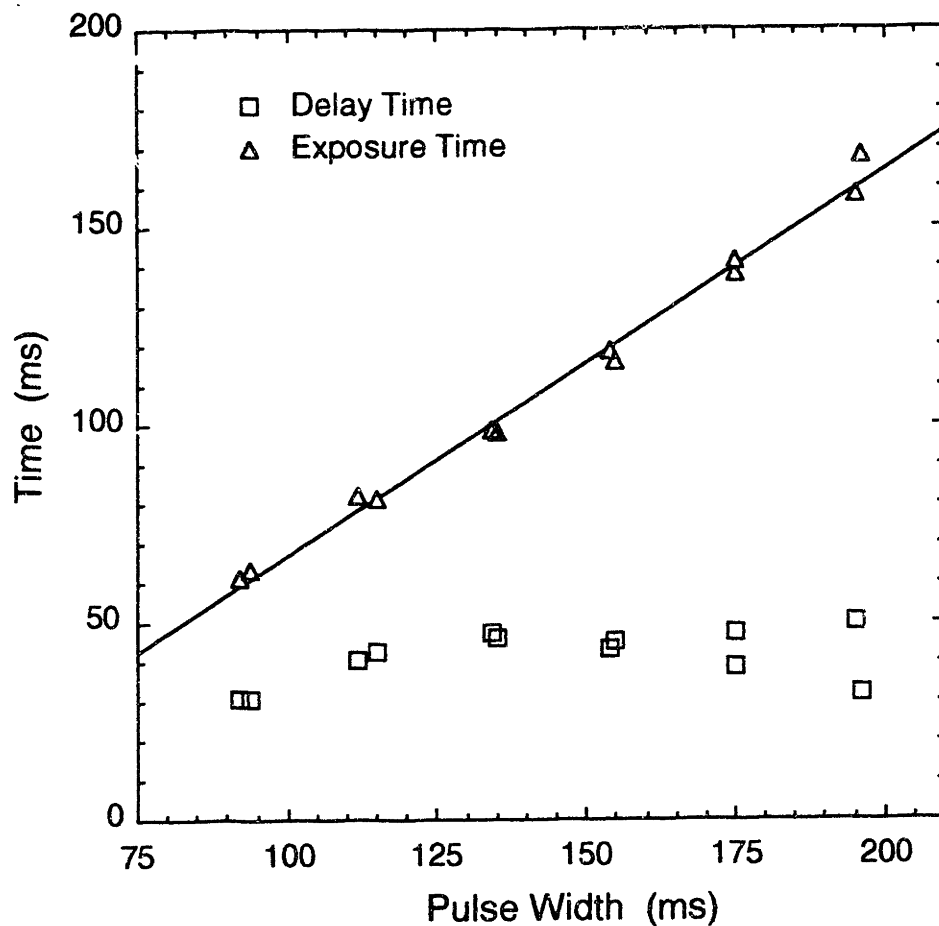


Figure 3.5-5: The thermophoretic sampling probe insertion time and withdrawal time. The horizontal lines indicate the average values.



$$\tau_e \text{ (ms)} = 0.972 \text{ (Pulse Width, ms)} - 29.9 \quad R^2 = 0.992$$

Figure 3.5-6: The thermophoretic sampling probe delay time and exposure time. The delay time is approximately constant, while the exposure time is given by the best-fit line.

nal thickness of the vapor deposited amorphous carbon film was 20 nm. The carbon films were highly stable under the electron beam and had a fine but uniform structure. A thermal radiation shield (a heavy piece of paper) was placed between the TEM grid and the flame in order to prevent significant heating of the grid before insertion. The radiation shield was removed approximately 2 seconds before the grid was inserted into the flame and replaced about 2 seconds after the grid was withdrawn from the flame. Dobbins and Megaridis (1987) reported that inserting a room temperature TEM grid into a 1900 K environment for 65 ms heated the grid to 380 K.

The characteristic quench time of the thermophoretic probe, τ_q , is the time required for a soot particle to leave the bulk gas and strike the cold TEM grid. Using the methods of Dobbins and Megaridis (1987), τ_q was estimated to be about 4 ms.

Micrographs of the thermophoretic samples were taken with either a Philips EM 400 or a JEOL JEM-200CX transmission electron microscope. However, the 200CX provided more uniform illumination and higher resolution than the EM 400, so only 200CX micrographs were subjected to image analysis. The JEOL 200CX has a point-to-point resolution of up to 0.45 nm in bright field mode, an accelerating voltage of up to 200 kV, and is capable of magnifications up to 330,000 times. The deposited particles were highly stable under the electron beam; there were no observable changes or deformations of the particles, even at the highest magnifications.

The 0.015 inch thick stainless steel shim was, of course, completely opaque to the electron beam. Since the grid was attached over a hole in the shim (see Figure 3.5-2), the grid did not have to be removed from the shim before being placed in the sample holder of the TEM. However, the sample holders of the electron microscopes were not large enough to accommodate the entire 60 mm long shim. Before a specimen could be placed in the holder, the bulk of the shim had to be cut off and discarded. The hole in the shim also allowed particles to deposit on both sides of the TEM grid. If particles were on both sides of the film, then they were visible and in focus at the same time. In other words, TEM micrographs could not be used to determine the side of the film on which a particle had deposited.

TEM negatives were subjected to image analysis with a Joyce-Loebl Magiscan 2. A negative was placed on a light table and a video camera produced a 2 to 2.5 times en-

larged image of the negative on the Magiscan 2 screen. The resolution on the screen depended on the magnification of the negative and the enlargement on the screen; a resolution of about 1.3 nm/pixel on the Magiscan screen was typical for TEM negatives taken at a magnification of 100,000 times.

The Magiscan 2 hardware and software support 64 levels of gray-scale, a variety of image-enhancing transformations, interactive image editing, and automatic feature identification and sizing. However, the TEM negatives were of extremely low contrast, since the samples were essentially 5 to 50 nm amorphous carbon particles on a 20 nm thick amorphous carbon film. Even after using a number of image-enhancing transformations, completely automatic particle identification and sizing was not possible. Features that were not part of a particle were mistakenly identified as such, and some features which were part of particles were not identified. For this reason, each particle was drawn by hand on the Magiscan 2 screen using a light pen. The human eye has a much greater dynamic range than the 64 gray levels available to the Magiscan 2, and aided by direct examination of the TEM negative, particle identification was generally unambiguous. Drawing 100 particles took about 3 hours.

In each negative, all particles that were completely within the field of view were drawn. No attempt was made to separately draw particles that may have been overlapping because they were either on opposite sides of the grid or because they were lying on top of one another. In most cases, identifying these types of features was highly subjective.

The Magiscan 2 automatically calculated the area, A_p , maximal chord length, L_m , breadth, B , and perimeter, P_c , of each drawn feature. The area measured by the Magiscan 2 is the total area of the feature outline, and corresponds to the projected area of the particle resting in a stable position. These quantities are independent of the orientation of the feature on the screen, and are illustrated in Figure 2.1-1 for a variety of projected particle shapes.

The total area on the screen of the Magiscan 2 was called the field area, A_f . The percent coverage of the grid was defined as the total area of all the particles divided by the field area. In order to minimize the two problems mentioned above, the sample times were adjusted to keep the percent coverage below 10%. The percent coverage of the

TEM grid can be estimated from the exposure time using approximate equations developed by Dobbins and Megaridis (1987).

3.6 Bulk Solid and PAH Sampling

Bulk solid samples and PAH were collected with the apparatus shown in Figure 3.6-1. A vacuum pump (Metal Bellows MB-158) drew combustion products isokinetically through a water-cooled stainless steel probe with a 3.2 mm (1/8 in) diameter at the tip. The solid particles were collected on a 0.1 μm pore polyvinylidene difluoride hydrophilic membrane filter (Millipore Durapore) while the sampled gas continued through the sampling system. The sampled gas passed through two dichloromethane (methylene dichloride, CH_2Cl_2) traps held at 0°C by an ice water bath, a mass flowmeter (Emerson Electric 5831-1), and a metering valve before being exhausted. The sampled gas passed through only metal or teflon tubing which was cleaned with dichloromethane after each sample was collected.

The dichloromethane traps were 250 ml gas wash bottles filled with approximately 125 ml (0.5 lb) of 6 mm glass beads. Dichloromethane was added to each trap to just cover the beads. The glass beads were used to break up the gas bubbles and improve gas/liquid contacting. The purpose of the dichloromethane traps was to capture gas-phase PAH that passed the filter. The soot on the filter did contain a large amount of PAH. As much as 15% of the dry mass collected on the filter was CH_2Cl_2 soluble. Some soot samples were collected for surface area measurements; for these samples only the soot on the filter was needed, and the CH_2Cl_2 traps were not used.

The quenching of the samples withdrawn with the stainless steel probe was not as fast as the quenching of the samples withdrawn with the quartz glass probe, because the stainless steel probe had a larger diameter. The characteristic quench time of samples withdrawn with the stainless steel probe was estimated using Eq. 3.4-1 to be 12 ms.

The sampling procedure was relatively simple. After the probe was positioned at the desired height above the burner, the flame was ignited, and the vacuum pump was turned on. Sample times as long as 6 or 8 hours were used in order to collect up to 40 to 60 mg of material on the filter. However, as much as 50% of the mass on the filter was water that condensed from the gas phase.

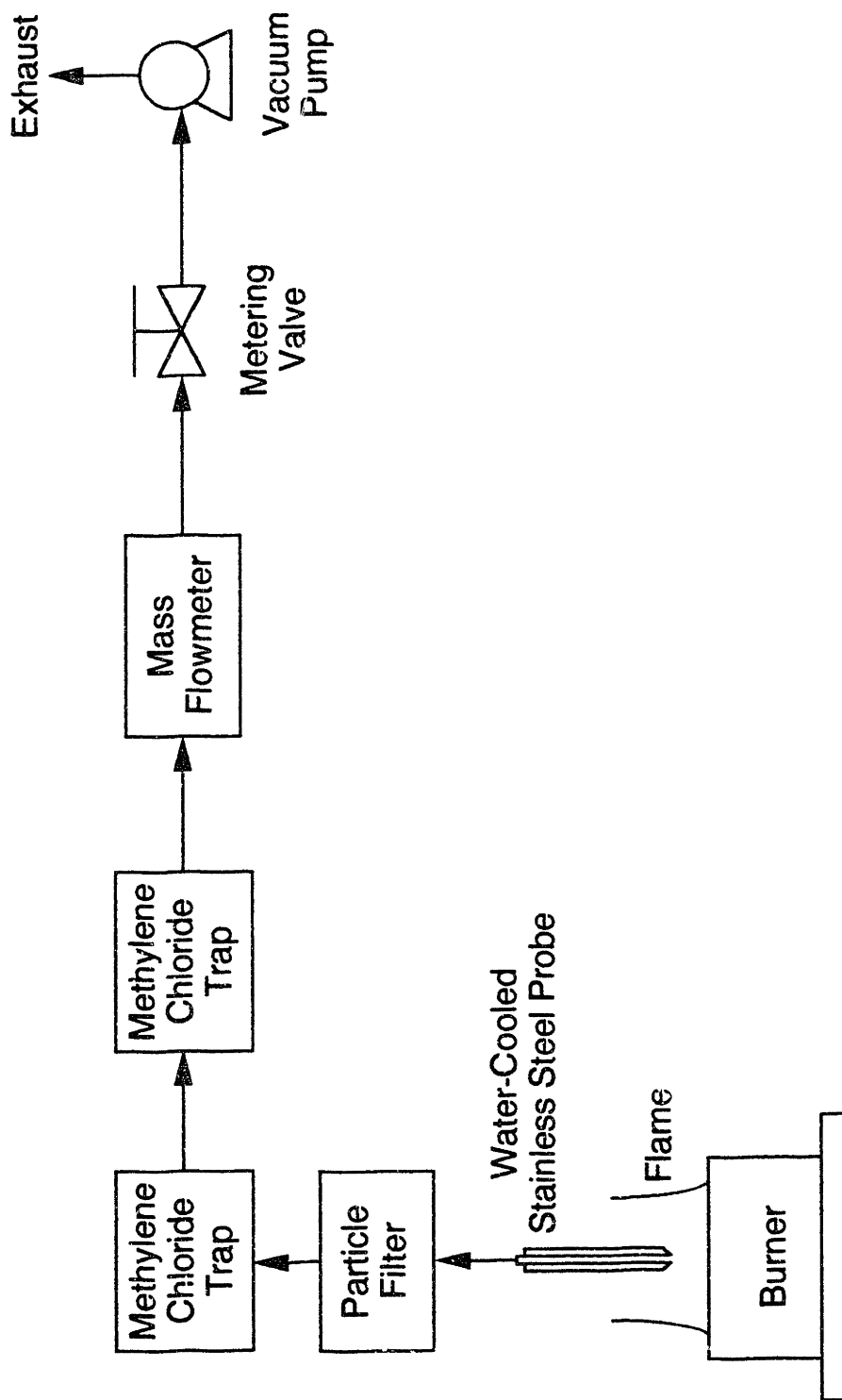


Figure 3.6-1: The bulk solid and PAH sample collection system. The internal diameter of the probe was 3.2 mm (1/8 in) at the tip.

Like the quartz glass probe, the tip of the stainless steel probe would occasionally clog with soot. Clogging of the probe tip was detected by observing a decrease in the mass flow rate of the sampled gas. When the probe tip became clogged, a small stainless steel pin was used to scrape the soot off of the probe.

By definition, the CH_2Cl_2 soluble fraction of the sample was tar, and the CH_2Cl_2 insoluble fraction was soot. After collection, all of the solid was scraped off of the filters and added to the dichloromethane in the traps. The filter was also extracted with CH_2Cl_2 , and the extract was added to the CH_2Cl_2 from the traps. A complete sample consisted of approximately 400 ml of dichloromethane, containing soot and PAH. The samples were filtered to determine the total amount of soot, and then concentrated to a volume of about 8 ml using a Kuderna-Danish evaporative concentrator.

The term "tar" is used to emphasize the difference between the CH_2Cl_2 soluble material and PAH. PAH species with molecular weights greater than about 1000 g/mole are generally insoluble in CH_2Cl_2 (Lam, 1988(b)). In other words, all of the species in the tar are PAH, but not all of the PAH present in the flame are in the tar.

Total tar concentrations were determined using a technique developed by Lafleur *et al.* (1986). A 100 μl aliquot of the concentrated CH_2Cl_2 solution was evaporated at room temperature for 5 minutes on a 12 mm diameter aluminum foil pan. The mass of the residue was determined using a Cahn 21 Microbalance. The concentrated solutions were also analyzed with a gas chromatograph (HP 5890) and a liquid chromatograph (HP 1090). The GC was equipped with an FID and a 25 meter, 5% methyl-phenyl column that was ramped from 40°C to 500°C. Helium was used as the carrier gas, and the injection volume was typically 3 μl . Some GC samples were concentrated to one-half or one-third of their original volume before injection. The LC was equipped with a reverse-phase Vidac column, and the injection volume was typically 25 μl . Interpretation of the chromatographs and identification of individual species were performed using calibration data supplied by Lafleur (1990). Table 3.6-1 lists the PAH species that were identified in the gas chromatographs; the PAH species identified in the liquid chromatographs are listed in Table 3.6-2.



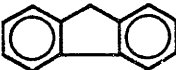
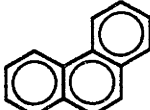
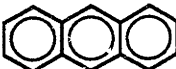
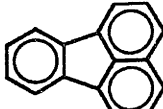

Species	Formula	<i>M</i> (g/mole)	Structure
Naphthalene	C ₁₀ H ₈	128	
Acenaphthylene	C ₁₂ H ₈	152	
Fluorene	C ₁₃ H ₁₀	166	
Phenanthrene	C ₁₄ H ₁₀	178	
Anthracene	C ₁₄ H ₁₀	178	
Fluoranthene	C ₁₆ H ₁₀	202	
Pyrene	C ₁₆ H ₁₀	202	

Table 3.6-1: PAH species identified in flame samples using gas chromatography. Many peaks which appeared in the chromatographs were not identified. Pyrene and fluoranthene were also detected using liquid chromatography.

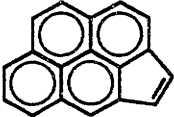
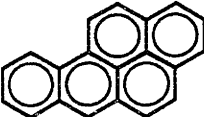
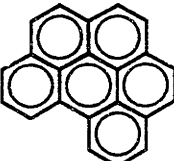
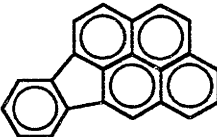
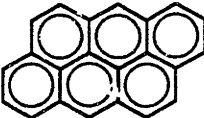
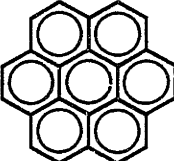
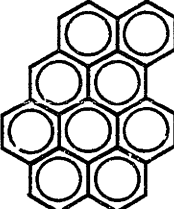
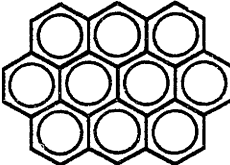
Species	Formula	<i>M</i> (g/mole)	Structure
Cyclopenta(<i>cd</i>)pyrene	C ₁₈ H ₁₀	226	
Benzo(<i>a</i>)pyrene	C ₂₀ H ₁₂	252	
Benzo(<i>ghi</i>)perylene	C ₂₂ H ₁₂	276	
Indeno(1,2,3- <i>cd</i>)pyrene	C ₂₂ H ₁₂	276	
Anthanthrene	C ₂₂ H ₁₂	276	
Coronene	C ₂₄ H ₁₂	300	
Naphtho(8,1,2- <i>abc</i>)coronene	C ₃₀ H ₁₄	374	
Ovalene	C ₃₂ H ₁₄	398	

Table 3.6-2: PAH species identified in flame samples using liquid chromatography. Pyrene and fluoranthene, which were also detected by gas chromatography, are not listed in this table. Many peaks which appeared in the chromatographs were not identified.

4. EXPERIMENTAL RESULTS

4.1 Path Length Measurements

As shown in Section 2.2, both the flame emissivity, ϵ_λ , and the path length through the flame, L , are needed to calculate the extinction coefficient, K_{ext} . The path length (the flame diameter) was measured from color photographs using the technique described in Section 3.3. Figure 4.1-1 shows the flame diameters of the $C/O = 0.74$, $C/O = 0.77$, $C/O = 0.80$, and $C/O = 0.83$ flames. The flame diameter initially decreases with increasing distance from the burner because the flame temperature is decreasing. About 20 mm from the burner, the flame diameter starts to increase as the streamlines are deflected by the stabilization plate mounted 38 mm above the burner surface (see Figure 3.1-1). The flame diameter decreases with increasing C/O ratio because the total gas flow rate and the flame temperature decrease with increasing C/O ratio (see Table 3.1-1 and Section 4.6).

Less than about 2.5 mm from the burner surface, the flame was not luminous enough to appear distinct in the photographs. The flame diameter was extrapolated back to the burner surface by assuming L was constant from 0 to 2.5 mm above the burner surface. The dashed portions of the curves in Figure 4.1-1 indicate the regions where the flame diameter was extrapolated. The flame did not extend to the edge of the ceramic honeycomb in part because of edge effects, and in part because the ceramic honeycomb was glued into a stainless steel ring. The glue filled in and blocked the outermost cells of the honeycomb, reducing the effective diameter of the honeycomb by about 2 mm.

The additives did not have a significant effect on the path length. Measurements of L in the $C/O = 0.74$ and $C/O = 0.74 + \text{Fe}$ flames revealed that the iron additive caused at most a 2% change in the path length. The average change in path length, over the range 2.5 to 25 mm from the burner surface, was 0.9%. This difference is within the precision of the path length measurements. Therefore, all flames with additives were assumed to have the same diameter as the corresponding flame without an additive.

The emissivity measurements are not presented here; however, the extinction coefficient measurements are presented in Section 4.2. The inquisitive reader can use the extinction coefficient, the flame diameter, and Equation 2.2-2 to determine the emissivity.

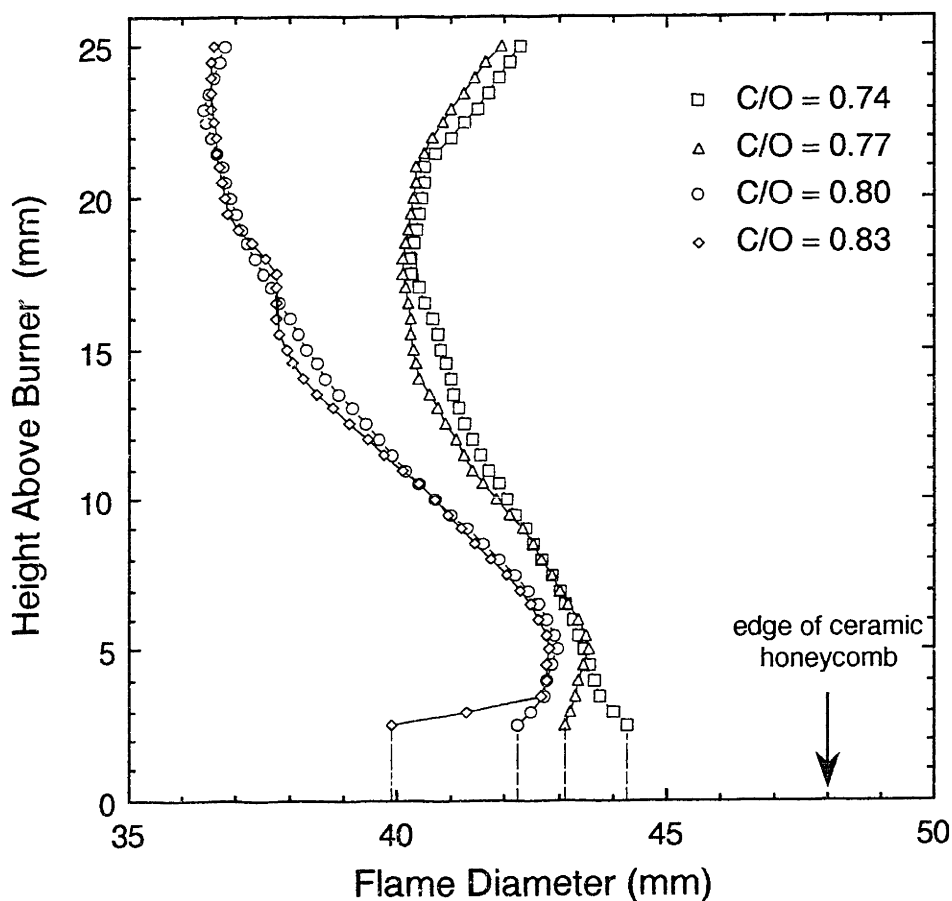


Figure 4.1-1: Profiles of path length, L , through the premixed flames. The dashed sections of the curves indicate extrapolations where the flame edge was not visible in the photographs. The general decrease in the flame diameter, from about 5 mm to about 20 mm above the burner, is caused by the decreasing flame temperature. The flame diameter subsequently starts to increase as the flame streamlines are deflected by the stabilization plate mounted 38 mm above the burner surface. As indicated by the arrow, the ceramic honeycomb flame holder was 48 mm in diameter.

4.2 Absorption Measurements

Profiles of K_{ext} (measured at $\lambda = 514.5$ nm) in the premixed flames with and without additives are shown in Figures 4.2-1 and 4.2-2. The apparatus and techniques used to measure K_{ext} are described in Section 3.3.

The additives increased the extinction coefficient in every flame, and the iron additive always increased K_{ext} more than the manganese additive. Flames containing additives initially have about the same K_{ext} as the corresponding flame without an additive, but the K_{ext} curves diverge with increasing distance from the burner. The manganese additive increased K_{ext} by as much as 50%, while the iron additive increased K_{ext} by as much as 300% (see Figure 4.2-1, the K_{ext} profiles in the C/O = 0.74, C/O = 0.74 + Mn, and C/O = 0.74 + Fe flames). Further interpretation of the K_{ext} measurements is given in Chapter 5.

For some flames, the K_{ext} profile was measured two or three times. In these cases, the average value of K_{ext} measured at any height above the burner is shown in Figures 4.2-1 and 4.2-2. The average value was also used for all subsequent calculations.

4.3 Scattering Coefficient Measurements

Profiles of the scattering coefficient Q_w (measured at $\lambda = 514.5$ nm and $\theta = 45^\circ$) are shown in Figure 4.3-1 for the C/O = 0.74 and C/O = 0.77 flames, both with and without additives. Also shown in Figure 4.3-1 are Q_w measurements in the non-sooting C/O = 0.52 flame. Q_w measurements in the C/O = 0.80 and C/O = 0.83 flames, both with and without additives, are shown in Figure 4.3-2. The apparatus and techniques described in Section 3.3 were used to measure Q_w and Q_{vh} . Depolarization ratio ($\rho_v = Q_{vh}/Q_w$) measurements are presented in Section 4.5.

For some flames, the Q_w profile was measured two or three times. In these cases, the average value of Q_w at any height above the burner is shown in Figures 4.3-1 and 4.3-2. The average value was also used for all subsequent calculations.

The additives always increased Q_w , and the iron additive always increased Q_w more than the manganese additive. Flames with additives initially have about the same scattering coefficient as the corresponding flames without additives, but the Q_w curves diverge with increasing distance from the burner. The iron additive increased the scatter-

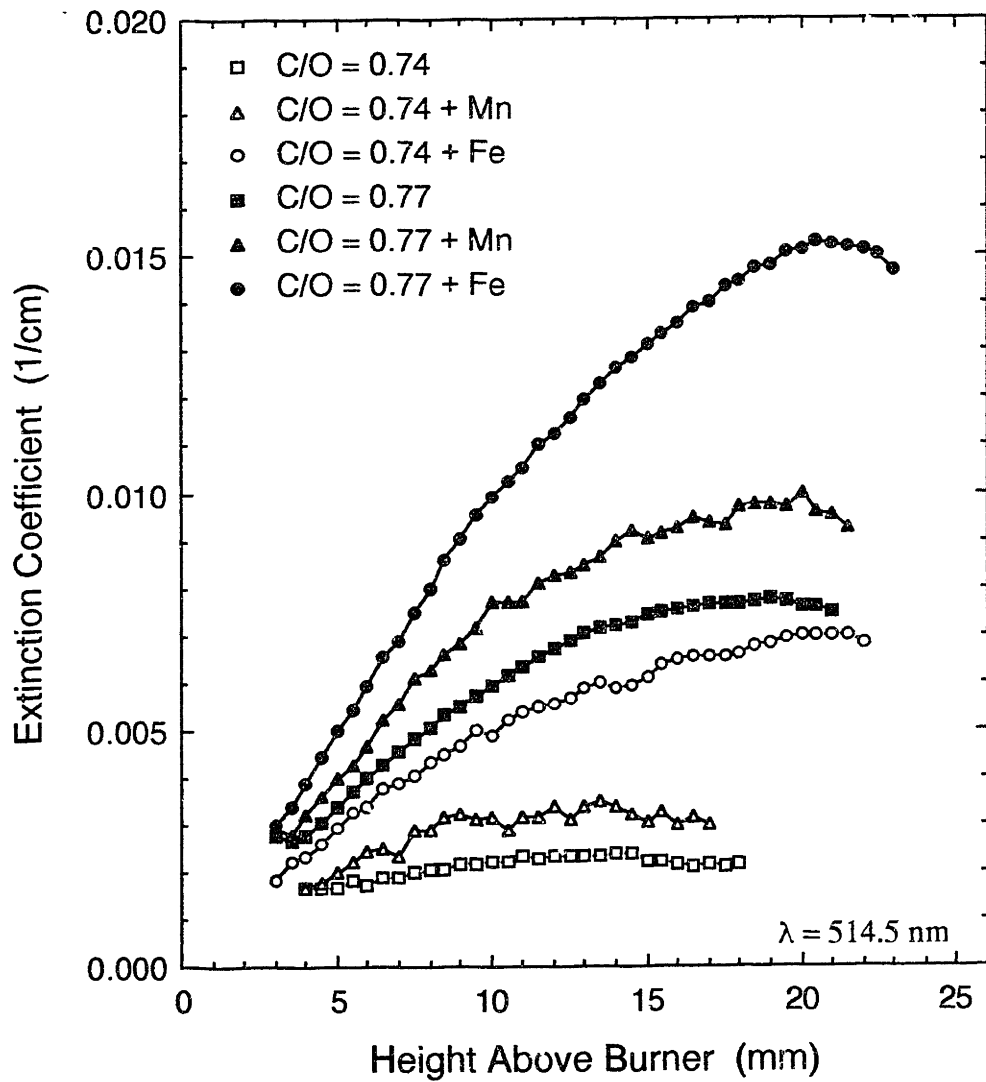


Figure 4.2-1: Extinction coefficient measurements in the C/O = 0.74 and C/O = 0.77 flames, both with and without additives.

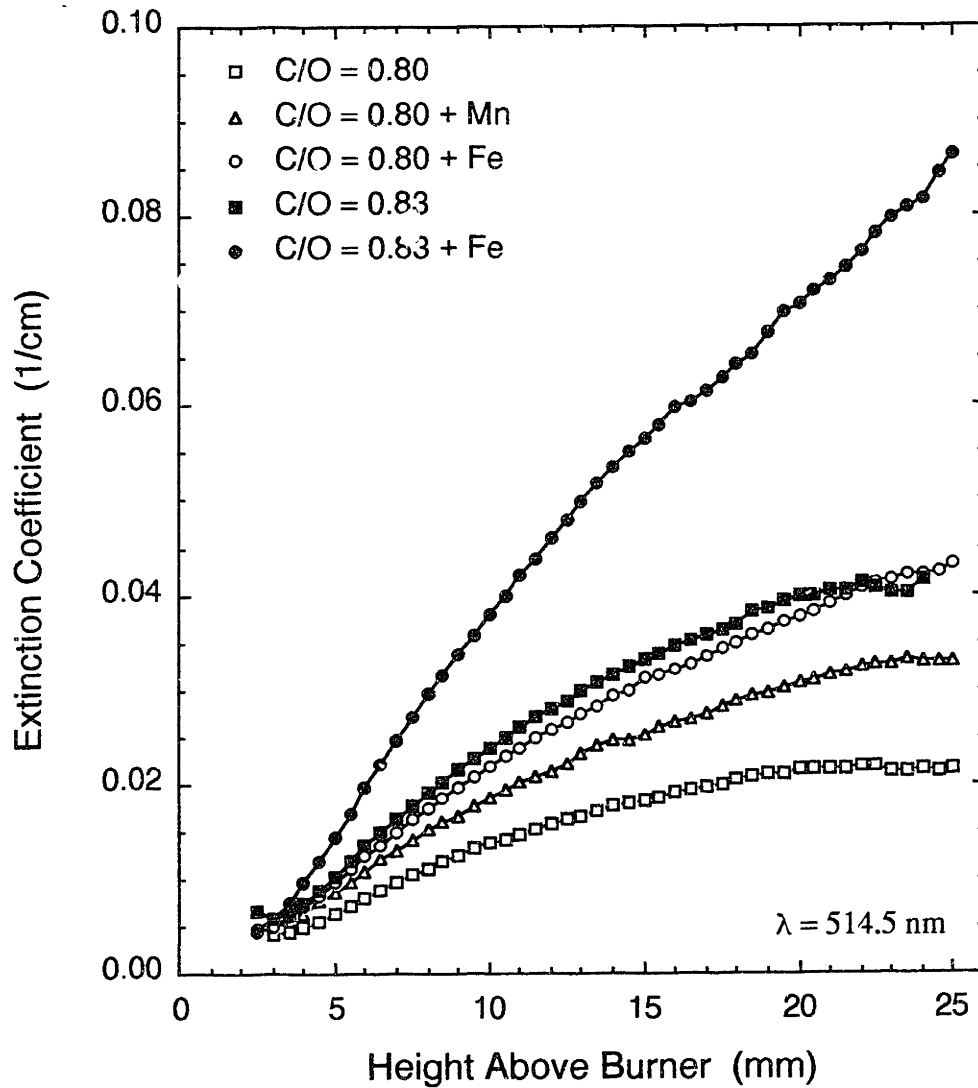


Figure 4.2-2: Extinction coefficient measurements in the C/O = 0.80 and C/O = 0.83 flames, both with and without additives.

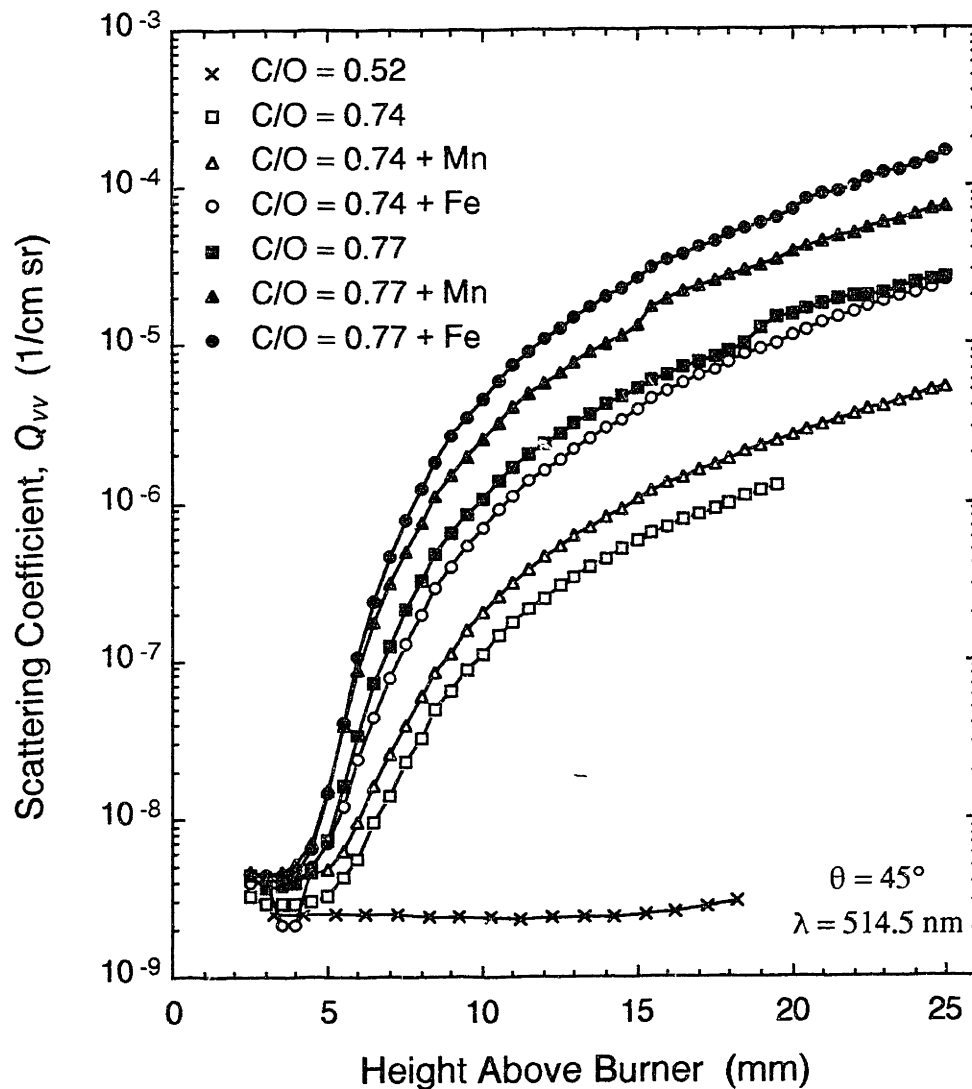


Figure 4.3-1: Scattering coefficient measurements in the C/O = 0.74 and C/O = 0.77 flames, both with and without additives. The scattering coefficient measurements in the C/O = 0.52 flame are also shown. The C/O = 0.52 flame was a non-sooting flame.

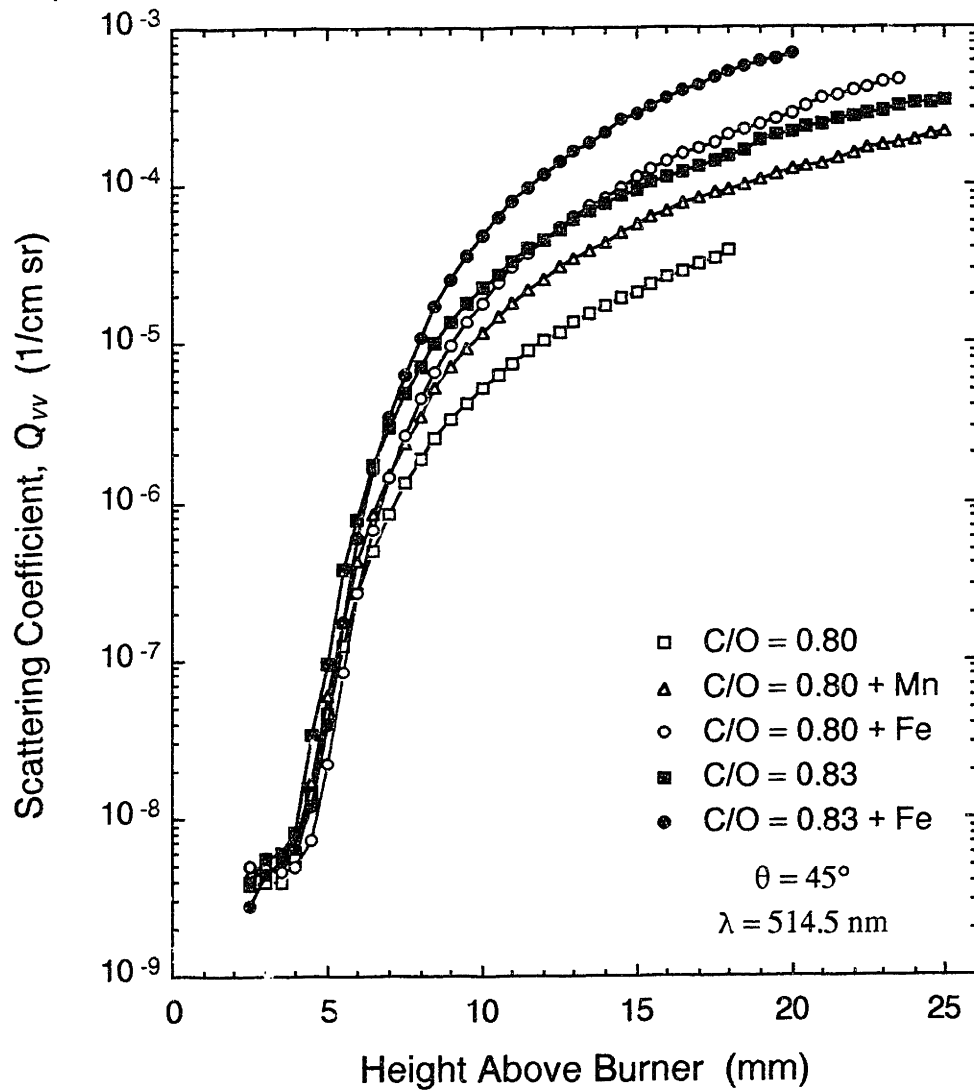


Figure 4.3-2: Scattering coefficient measurements in the C/O = 0.80 and C/O = 0.83 flames, both with and without additives.

ing coefficient by as much as a factor of 10, while the manganese additive had a smaller effect (see, for example, the $C/O = 0.74$, $C/O = 0.74 + Fe$, and $C/O = 0.74 + Mn$ flames in Figure 4.3-1).

Comparison of the Q_w measurements in the sooting flames to the Q_w measurements in the $C/O = 0.52$ flame (which was non-sooting) shows that scattering from gas-phase species is a significant fraction of the measured Q_w close to the burner surface. The fraction of the measured Q_w due to gas phase scatter was estimated as Q_w in the non-sooting $C/O = 0.52$ flame divided by Q_w in the flame of interest. This estimate is good, assuming that the differences in temperature and gas phase composition between the sooting flames and the non-sooting flame had a negligible effect on the gas phase scatter. The sooting flames are at lower temperatures than the non-sooting $C/O = 0.52$ flame, tending to increase Q_w of the gas phase in the sooting flames. However, the sooting flames have higher concentrations of species with smaller differential scattering cross-sections (CO_2 and H_2O concentrations decrease, while CO and H_2 mole fractions increase), tending to decrease the Q_w of the gas phase in the sooting flames. The two effects oppose each other, making the scattering coefficient measurements in the $C/O = 0.52$ flame a good estimate of gas phase scatter in the sooting flames. Harris (1986) has made similar arguments in his study of premixed ethylene/air flames.

An alternative method of estimating the fraction of the measured Q_w due to gas phase scatter is to calculate Q_w of the gas from composition and temperature measurements. Both techniques involve the use of experimental measurements which contain some uncertainty.

Figure 4.3-3 shows that scattering from gas phase species could account for as much as 80% of the measured Q_w close to the burner surface. The contribution from fluorescence was negligible, never accounting for more than 10% of the measured Q_w (see Section 4.4). The contributions due to gas phase scattering were subtracted from the measured scattering coefficients before attempting to convert Q_w and K_{ext} measurements into soot particle sizes and concentrations. Nevertheless, because of the approximate nature of the corrections, no attempt was made to convert Q_w measurements into soot particle sizes and concentrations until scattering from soot accounted for at least 50% of the measured Q_w . There was no procedure to correct K_{ext} measurements for absorption due

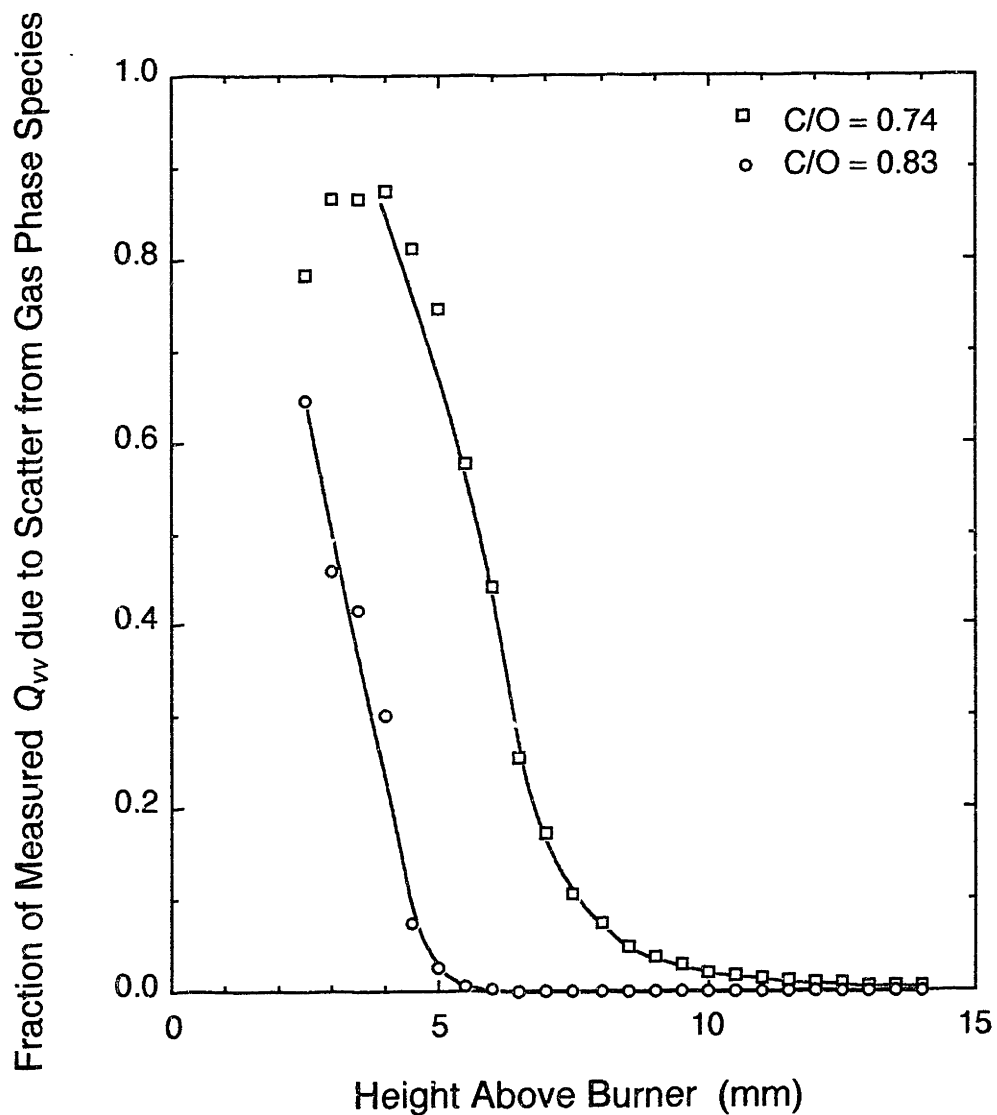


Figure 4.3-3: Estimated fraction of measured Q_{vv} due to scattering from gas molecules. The fraction of the scattering due to gas phase molecules is estimated as Q_{vv} in the non-sooting $C/O = 0.52$ flame divided by Q_{vv} in the flame of interest. Scattering from gas phase species is only significant very close to the burner surface.

to gas phase PAH close to the burner surface, another reason to use caution when interpreting measurements close to the burner surface.

4.4 Fluorescence Coefficient Measurements

The apparatus and techniques used to measure $Q_{f\lambda}\Delta\lambda$ are described in Section 3.3. In brief, the excitation wavelength for fluorescence measurements was $\lambda_e = 488.0$ nm and the observation wavelength range was centered on 514.5 nm. An interference filter, with $\Delta\lambda = 5.07$ nm, was used to set the observation wavelength range. Fluorescence in flames has been widely attributed to gas phase PAH (see Section 2.3). The correlation of these fluorescence measurements with the PAH concentration is presented in Section 4.8.

To compare the magnitude of the fluorescence coefficient to the scattering coefficient, which was measured with a filter having $\Delta\lambda = 0.44$ nm, the fluorescence coefficient was multiplied by the $\Delta\lambda$ ratio of the two filters, $0.44/5.07 = 0.086$ (see Figure 3.3-3). This provides an estimate of the magnitude of the fluorescence coefficient had the $\Delta\lambda = 0.44$ nm filter been used, assuming the fluorescence intensity is constant over the narrow range of observation. The $\Delta\lambda = 5.07$ nm was used for the fluorescence measurements instead of the $\Delta\lambda = 0.44$ nm filter to improve the signal-to-noise ratio.

Fluorescence measurements were complicated by the intense scattering from soot, which is several orders of magnitude larger than PAH fluorescence in these flames. Figure 4.4-1 shows that measured $Q_{f\lambda}\Delta\lambda$ in the C/O = 0.83 flame was not completely unpolarized. A polarizing filter was placed in front of the detector, and the vertically ($Q_{fv}\Delta\lambda$) and horizontally ($Q_{fh}\Delta\lambda$) polarized components of the fluorescent light were measured separately. The ratio Q_{fh}/Q_{fv} is initially unity, as expected, but decreases to about 0.6 with increasing distance from the burner. Fluorescence from gas phase PAH is expected to be completely unpolarized (Müller-Dethlefs, 1979), indicating that polarized light from another source was being measured along with the fluorescent emissions.

Scattering from soot is a strong source of polarized light in these flames. A small fraction of the light scattered at 488.0 nm from soot probably leaked through the interference filter used to set the observation wavelength range. The fluorescence measurements were corrected to eliminate the contribution of polarized scattering from soot, as explained below.

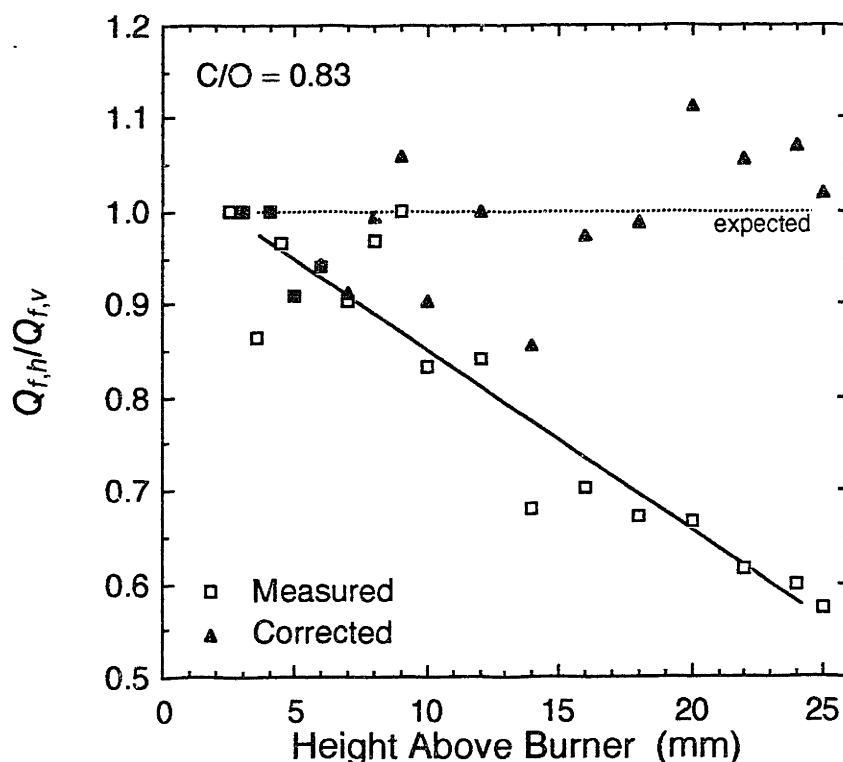


Figure 4.4-1: Correction of fluorescence measurements to account for contribution from scattering. Fluorescent emissions from gas phase PAH are expected to be completely unpolarized, $Q_{f,h}/Q_{f,v} = 1$, as shown by the dashed horizontal line. However, the measurements shown here (the square symbols), from the C/O = 0.83 flame, were not completely unpolarized, indicating light from another source was being measured along with fluorescence.

The fluorescence excitation wavelength was 488.0 nm, and an interference filter was used to center the observation wavelength range on 514.5 nm. Scattering from soot (both horizontally and vertically polarized) is several orders of magnitude more intense than fluorescence, and a small fraction of the light scattered at 488.0 nm probably leaked through the filter.

If the transmissivity of the interference filter at 488.0 nm was τ , then a small fraction of the light, τ , scattered by soot at 488.0 nm leaked through the filter. A value of $\tau = 2.2 \times 10^{-6}$ results in corrected fluorescence measurements that are completely unpolarized, as shown by the triangles in this figure. In other words, if the filter was 99.9998% opaque at 488.0 nm, then light scattered from soot that leaked through the filter would account for the polarized fluorescence measurements.

Other fluorescence measurements were corrected to eliminate the contribution of polarized scattered light from the fluorescence measurements.

Assume that the transmissivity τ of the interference filter was slightly greater than zero at 488.0 nm. Then a small fraction, τ , of the light scattered from soot (at 488.0 nm) leaked through the interference filter (centered on 514.5 nm), and the measured fluorescence coefficients are greater than the actual fluorescence coefficients by

$$(Q_{fv} \Delta\lambda)_{measured} = (Q_{fv} \Delta\lambda)_{actual} + \tau Q_w \quad (4.4-1)$$

$$(Q_{fh} \Delta\lambda)_{measured} = (Q_{fh} \Delta\lambda)_{actual} + \tau Q_{vh} \quad (4.4-2)$$

and the total fluorescence coefficient is

$$(Q_{f\lambda} \Delta\lambda)_{measured} = (Q_{f\lambda} \Delta\lambda)_{actual} + \tau(Q_{vv} + Q_{vh}) \quad (4.4-3)$$

Equations 4.4-1 and 4.4-2 were used to calculate the best-fit value of τ from Q_{vv} , Q_{vh} , $(Q_{fv} \Delta\lambda)_{measured}$, and $(Q_{fh} \Delta\lambda)_{measured}$ in the C/O = 0.83 flame. An additional constraint was required, namely that $(Q_{fv} \Delta\lambda)_{actual} = (Q_{fh} \Delta\lambda)_{actual}$, or that the actual fluorescence be unpolarized.

Figure 4.4-1 shows the corrected Q_{fh}/Q_{fv} ratio is unity, within the precision of the measurements, provided τ is about 2.2×10^{-6} . The transmissivity of the interference filter was 60% at 514.5 nm, and about 2% at 505 nm (see Figure 3.3-3). A transmissivity of 0.0002% at 488.0 nm is consistent with a Gaussian extrapolation of the transmissivity curve in Figure 3.3-3. All of the measured fluorescence coefficients were converted into the actual $Q_{f\lambda} \Delta\lambda$ using Equation 4.4-3, the measurements of Q_{vv} and Q_{vh} in each flame, and a value of $\tau = 2.2 \times 10^{-6}$.

Figure 4.4-2 compares the measured $Q_{f\lambda} \Delta\lambda$ to the corrected $Q_{f\lambda} \Delta\lambda$ in the C/O = 0.83 flame. The correction is small close to the burner surface, where scattering from soot is low, and increases with increasing distance from the burner surface. The correction never amounts to more than a 20% decrease in $Q_{f\lambda} \Delta\lambda$.

The assumption that the polarized light being measured along with the fluorescent light is due to scattering from soot can be checked by using a horizontally polarized incident beam, and measuring the polarization of the fluorescent light at a number of different angles. Although Q_{vv} is independent of θ , Q_{hh} varies with $\cos^2 \theta$ in the Rayleigh size regime. If scattering is the source of the polarized light, and a vertically polarized incident beam is used, then $Q_{fv} \Delta\lambda$ and $Q_{fh} \Delta\lambda$ should be independent of θ . If the incident beam is horizontally polarized, then $Q_{fv} \Delta\lambda$ should be independent of θ and $Q_{fh} \Delta\lambda$ should vary in a known manner with scattering angle.

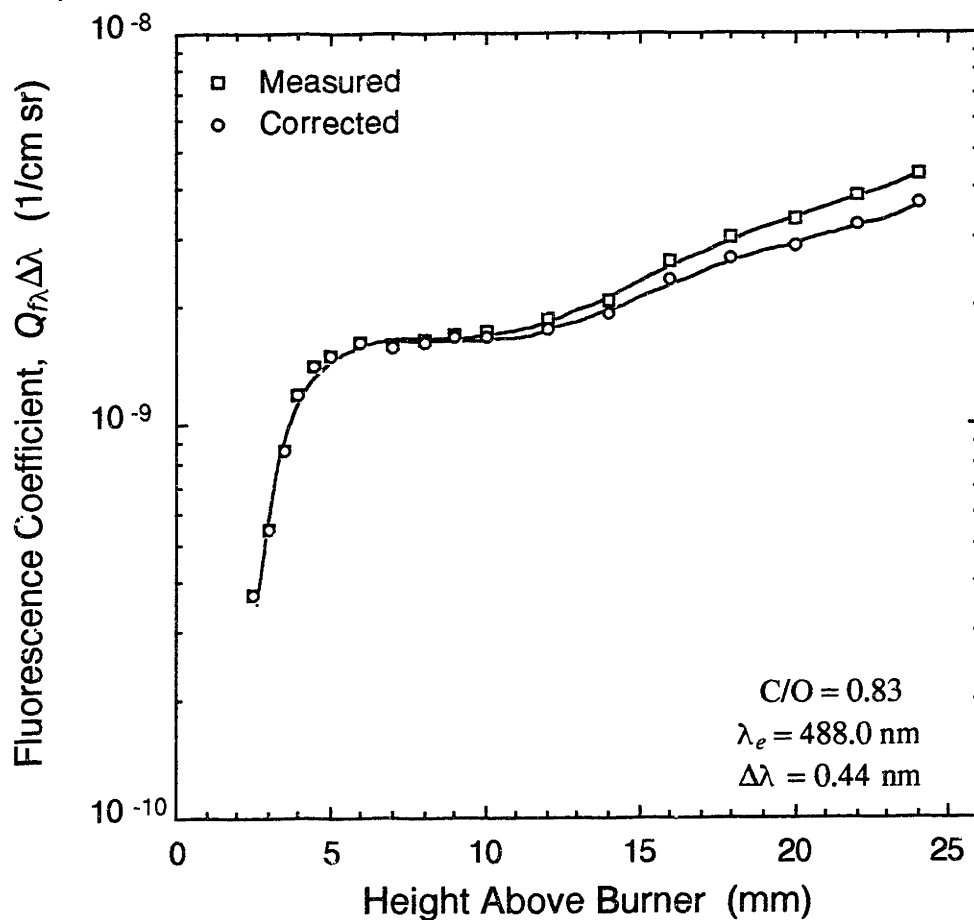


Figure 4.4-2: Comparison of measured and corrected fluorescence coefficients in the $C/O = 0.83$ flame. The “correction” consists of subtracting the polarized scattered light (Rayleigh scatter from soot) that was detected along with the unpolarized fluorescent emissions (see the explanation in the text). The correction only becomes significant far from the burner surface, where scattering from soot is becoming more and more intense, and never amounts to more than a 20% decrease in the fluorescence coefficient.

Figures 4.4-3 and 4.4-4 compare the fluorescence coefficient measurements in the flames with and without additives. The iron additive had a large effect on the fluorescence coefficient, increasing $Q_{f\lambda}\Delta\lambda$ by up to a factor of 6 in the $C/O = 0.77$ flame. In the $C/O = 0.83$ flame, the iron additive increased $Q_{f\lambda}\Delta\lambda$ by up to a factor of 3. In contrast, the manganese additive had almost no effect on $Q_{f\lambda}\Delta\lambda$ in the $C/O = 0.80$ flame. Again, the measurements in these figures have been converted to $\Delta\lambda = 0.44$ and have been corrected using Equation 4.4-3.

The fraction of the measured Q_w in the sooting flames due to fluorescence from PAH was estimated to be $(0.5)(Q_{f\lambda}\Delta\lambda)_{actual}/Q_w$, where $\Delta\lambda = 0.44$. This estimate is good, assuming that the fluorescence spectrum does not change when the excitation wavelength changes from 488.0 nm to 514.5 nm. Comparison of the $Q_{f\lambda}\Delta\lambda$ measurements to the Q_w measurements in Figures 4.3-1 and 4.3-2 shows that the contribution of fluorescence to scattering was negligible, never accounting for more than 10% of the measured Q_w .

4.5 Depolarization Ratio Measurements

Depolarization ratio ($\rho_v = Q_{vh}/Q_w$) measurements in the $C/O = 0.74$ and $C/O = 0.77$ flames, both with and without additives, are shown in Figure 4.5-1; ρ_v measurements in the $C/O = 0.80$ and $C/O = 0.83$ flames are shown in Figure 4.5-2. The apparatus and techniques used to measure ρ_v are described in Section 3.3. All ρ_v measurements were made at $\theta = 45^\circ$ and $\lambda = 514.5$ nm.

The ρ_v profiles in all of the flames are nearly identical. Close to the burner, ρ_v is relatively large, about 0.1. The depolarization ratio rapidly decreases until $\rho_v \approx 0.01$ about 5 to 10 mm from the burner surface, and then slowly decreases until $\rho_v \approx 0.005$ about 25 mm from the burner. The iron and manganese additives had no measurable effect on the depolarization ratio.

Rayleigh theory predicts $\rho_v \approx 0$ for spherical particles composed of an optically isotropic medium. Close to the burner surface, scattering from gas phase species (see Section 4.3) and unpolarized fluorescent emissions (see Section 4.4) contribute significantly to the measured Q_w and Q_{vh} . Finite values of ρ_v more than about 5 to 7 mm above the burner surface can be attributed to geometrical and/or optical anisotropy of the soot (see Section 2.2.3). Whether the depolarized component of the scattered light arises

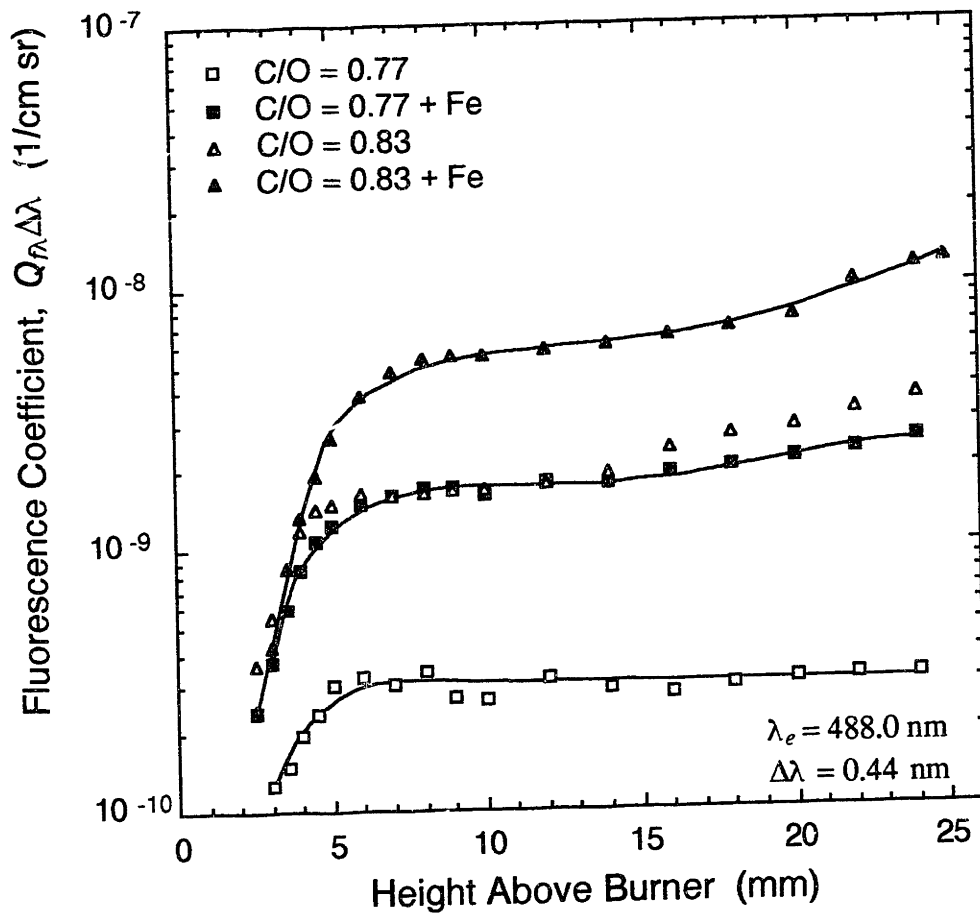


Figure 4.4-3: Fluorescence coefficient measurements in the $C/O = 0.77$ and $C/O = 0.83$ flames, both with and without the iron additive. The iron additive increased the fluorescence coefficient by up to factor of 6 in the $C/O = 0.77$ flame and by up to a factor of 3 in the $C/O = 0.83$ flame. In contrast, the manganese additive had almost no effect on the fluorescence coefficient (see Figure 4.4-4).

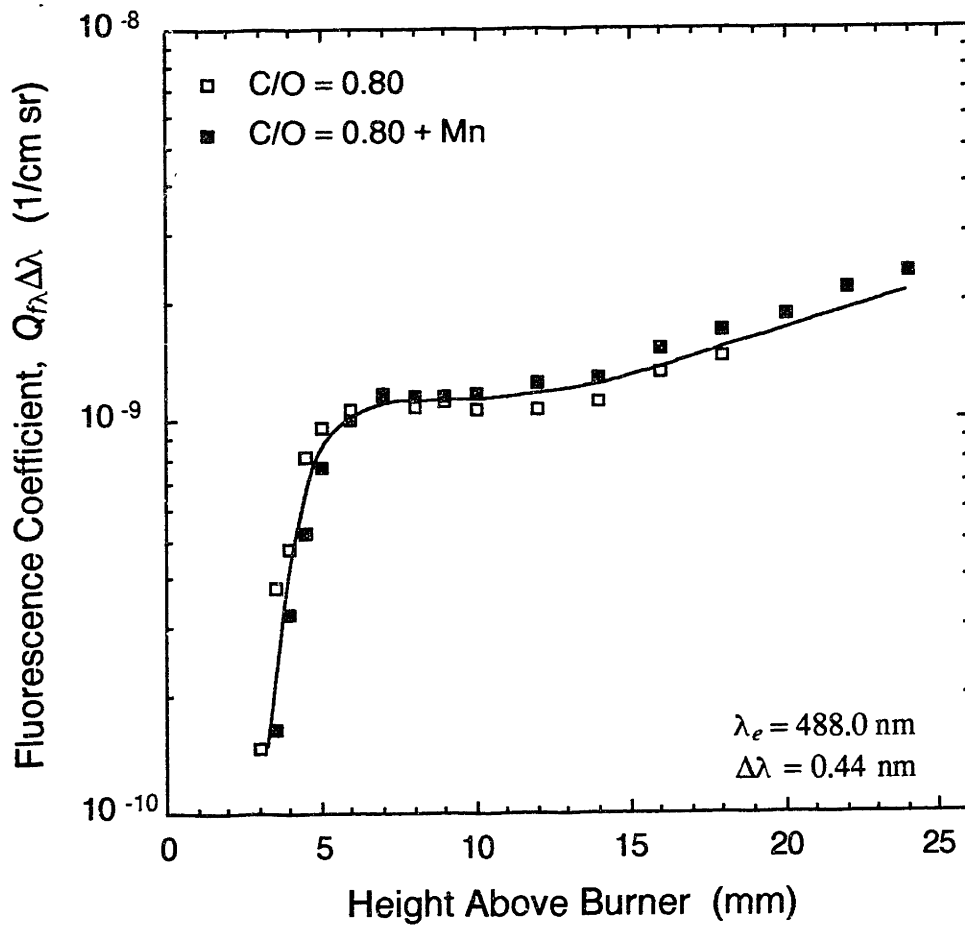


Figure 4.4-4: Fluorescence coefficient measurements in the C/O = 0.80 and C/O = 0.80 + Mn flames. The manganese additive had almost no effect on the fluorescence coefficient.

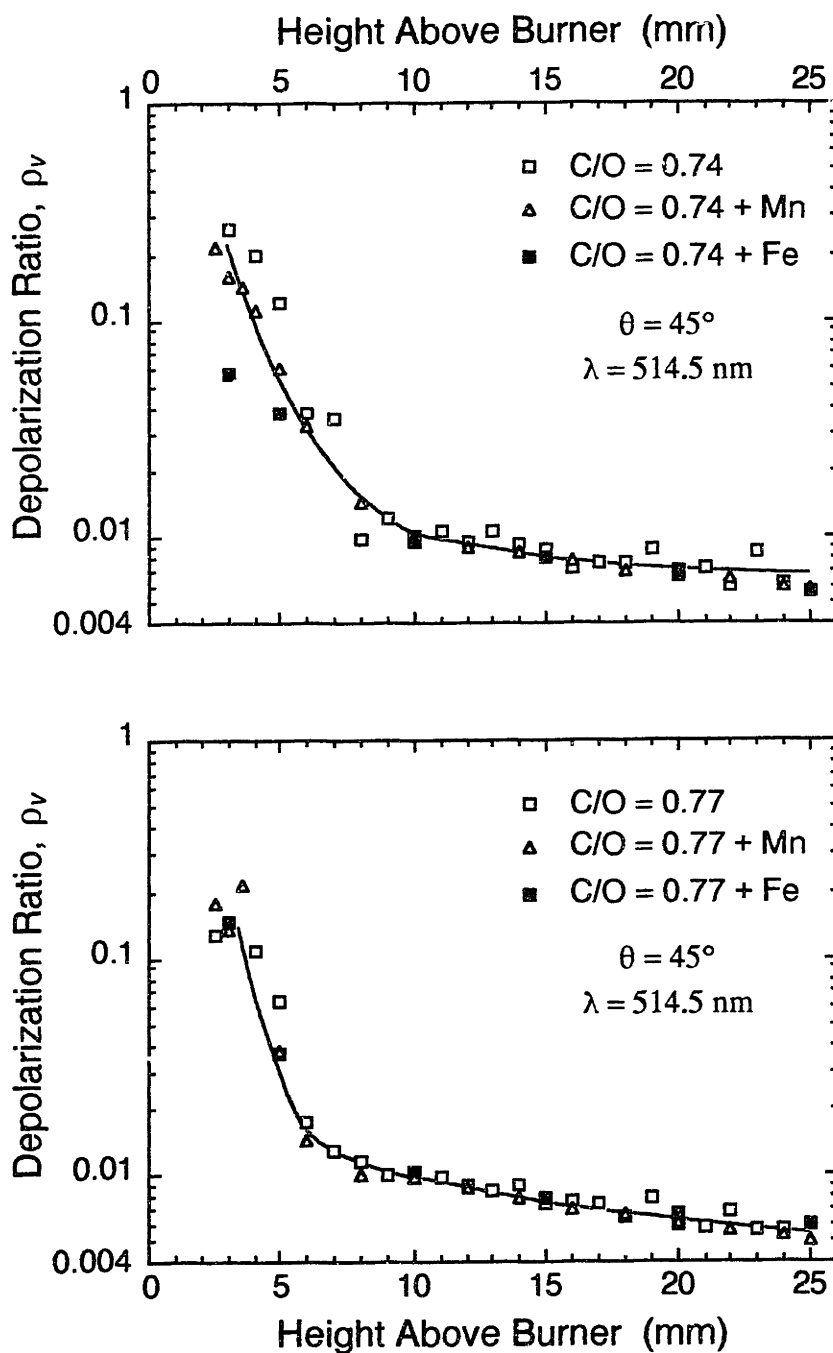


Figure 4.5-1: Depolarization ratio measurements in the C/O = 0.74 and C/O = 0.77 flames, both with and without additives. The additives had no effect on the depolarization ratio.

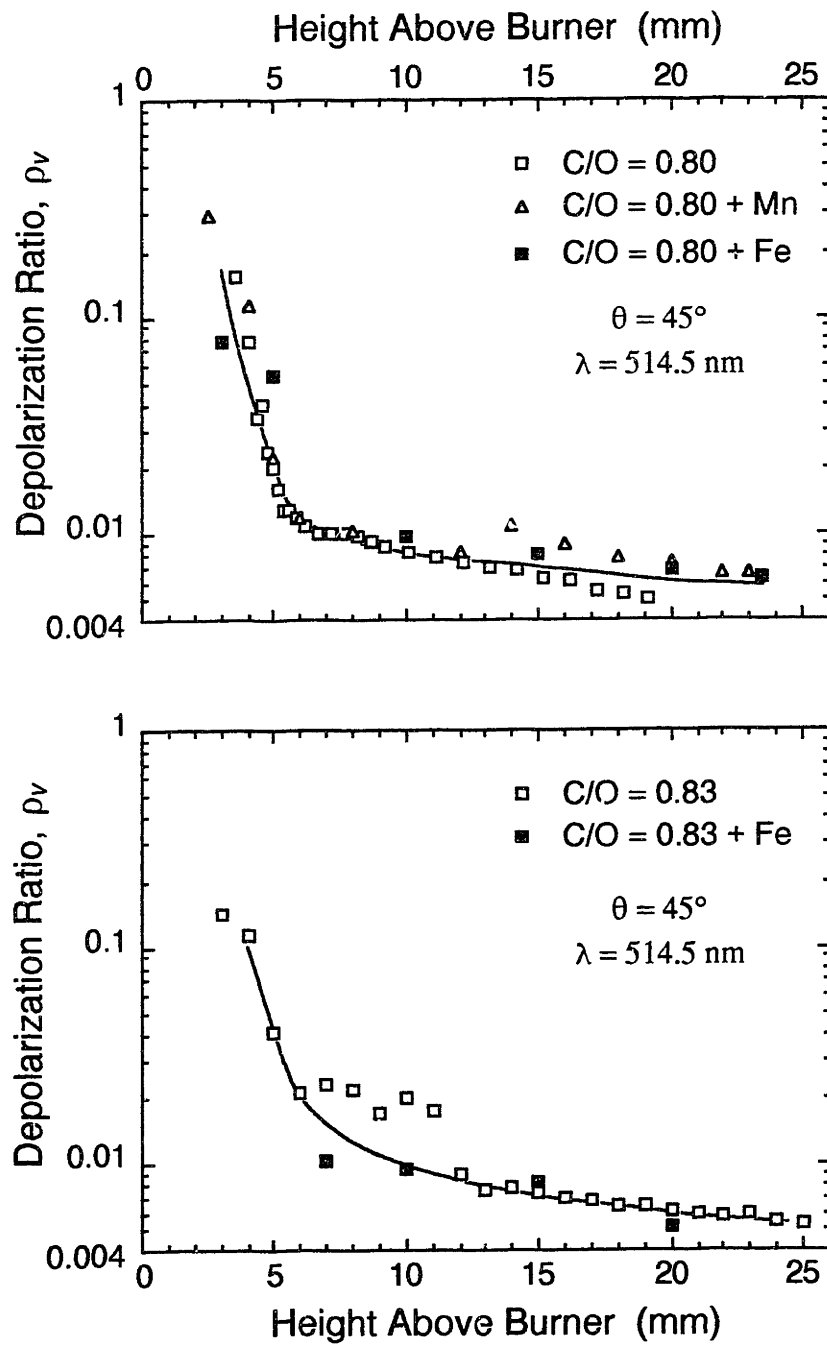


Figure 4.5-2: Depolarization ratio measurements in the C/O = 0.80 and C/O = 0.83 flames, both with and without additives. The additives had no effect on the depolarization ratio.

from geometrical or optical anisotropy is unknown. However, a change in particle shape would have to be matched by an offsetting change in the optical isotropy of the particles for the depolarization ratio to be constant. Since a fortuitous cancellation of effects is unlikely, the additives probably did not change the particle shape. Measurements of the soot particle shape distribution are presented in Section 4.9. Additional interpretation of the depolarization ratio data is given in Chapter 5.

4.6 Temperature Measurements

Premixed flame temperature measurements are shown in Figures 4.6-1 and 4.6-2. These flame temperatures were calculated from the brightness temperature (measured at 655 nm), the emissivity (measured at 514.5 nm), and Equation 3.2-6. Brightness temperatures were measured using the apparatus described in Section 3.2, and ϵ_λ was measured using the apparatus described in Section 3.3. For some flames, the brightness temperature profile (and/or the emissivity profile) was measured two or three times. In these cases, the average brightness temperature at any height above burner (and/or the average emissivity at any height above burner) was substituted into Eq. 3.2-6. Because the particles are small, the soot and the surrounding gas are at the same temperature.

Also shown in Figures 4.6-1 and 4.6-2 is the adiabatic flame temperature for each flame. Adiabatic flame temperatures were calculated assuming complete combustion to the equilibrium composition, using the computer program developed by Gordon and McBride (1976).

Close to the burner surface, the flame temperature approaches the adiabatic flame temperature. The flame temperature drops with increasing distance from the burner because the soot particles (and CO_2 and H_2O) radiate heat to the surroundings. All of the flames containing additives are at lower temperatures than the corresponding flames without additives because there is more soot in the flames containing additives; flames with more soot radiate more heat to the surroundings. The $\text{C/O} = 0.74$ flame was nearly isothermal, with a temperature decrease of about 20 K, while the temperature in the $\text{C/O} = 0.83$ decreased by almost 200 K.

These flames are at slightly higher temperatures than similar premixed flames studied by Harris and Weiner (1983(a)). The ceramic honeycomb flame support used here re-

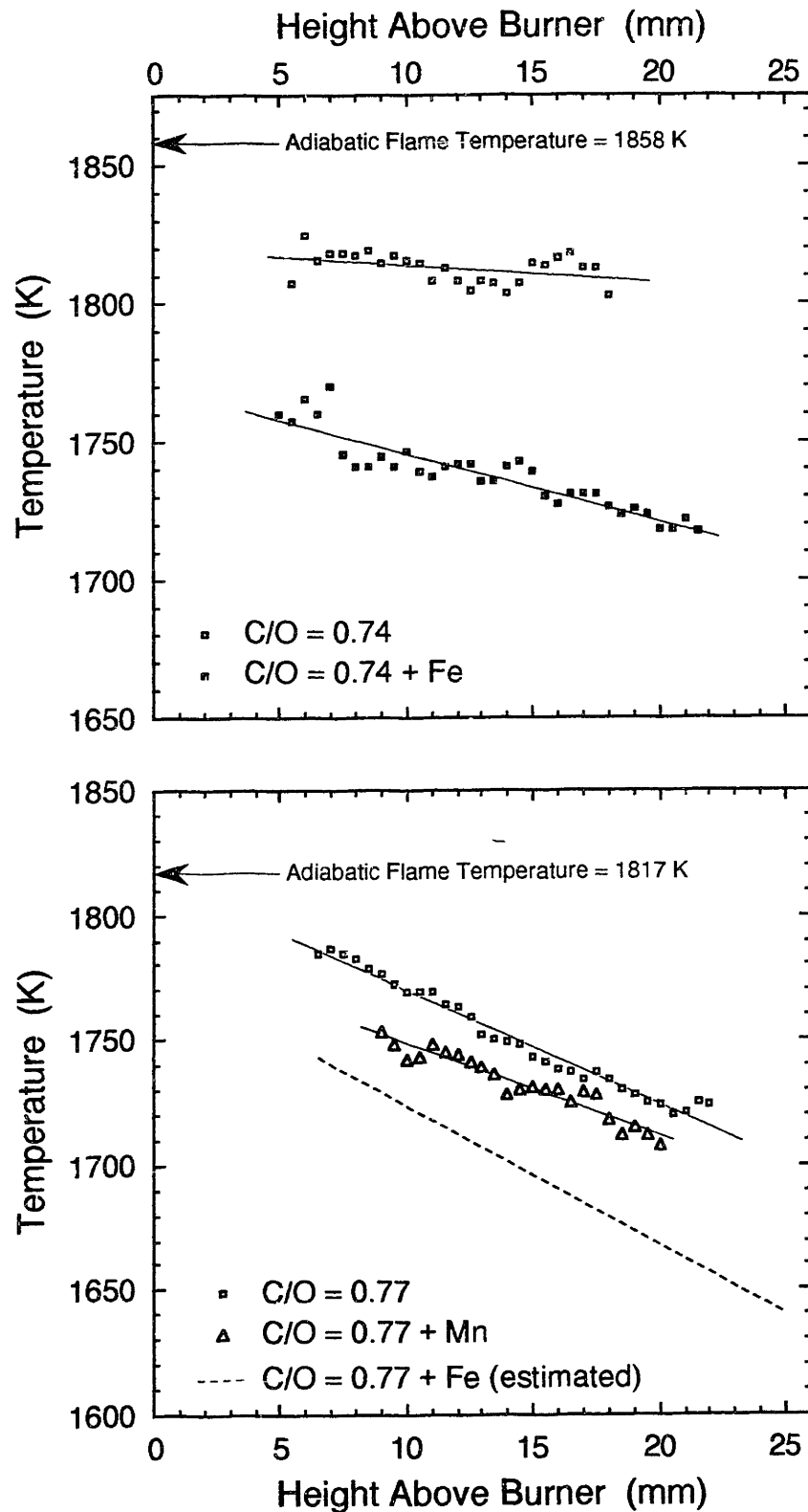


Figure 4.6-1: Temperature measurements in the $C/O = 0.74$ and $C/O = 0.77$ flames, both with and without additives. The solid straight lines are best-fits to the data. The $C/O = 0.77 + Fe$ flame temperature was estimated (see text).

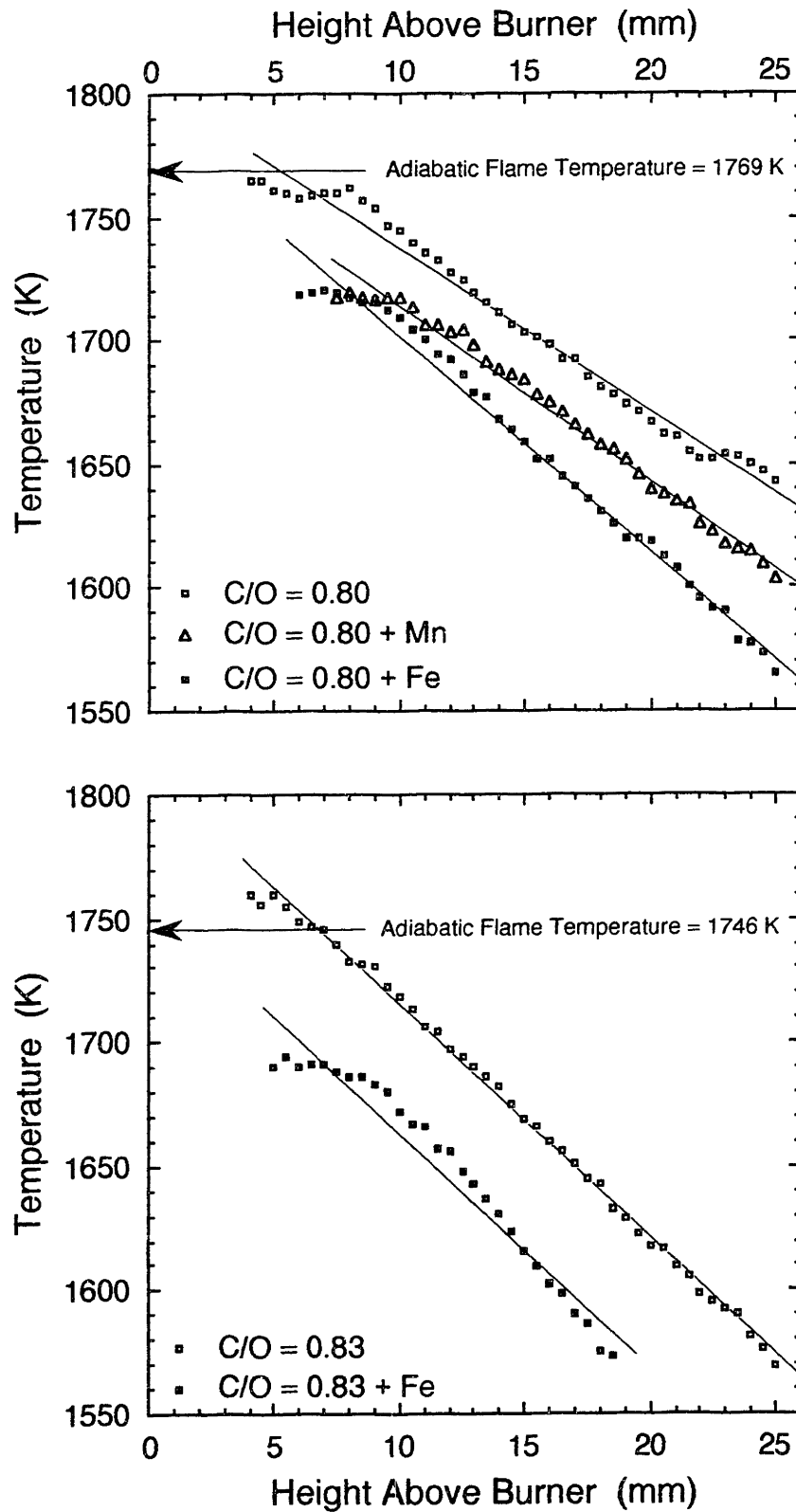
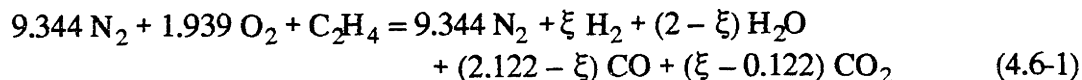


Figure 4.6-2: Temperature measurements in the $C/O = 0.80$ and $C/O = 0.83$ flames, both with and without additives. The straight lines are best-fits to the data.

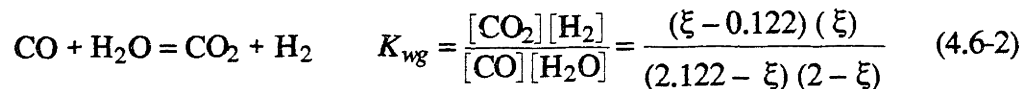
mains hotter and provides less of a heat sink than the water-cooled flame support used by Harris and Weiner (and many other researchers studying premixed flames).

The temperature in the $C/O = 0.77 + Fe$ flame was not measured. However, the temperature profile in this flame can be estimated quite accurately from the temperature measurements in the $C/O = 0.74 + Fe$ flames and the $C/O = 0.80 + Fe$ flames. As an illustration of the estimation technique, compare the temperature measurements in the $C/O = 0.74$, $C/O = 0.77$, and $C/O = 0.80$ flames, shown in Figure 4.6-3. The solid lines in Figure 4.6-3 are best-fits to the temperature measurements in the $C/O = 0.74$ and $C/O = 0.83$ flames. The dashed line in Figure 4.6-3 is an estimate of the temperature in the $C/O = 0.77$ flame, obtained by averaging the temperatures predicted by the curve fits of the other two flames at any height above burner. The agreement between the estimated temperature and the measured temperature in the $C/O = 0.77$ flame is quite good. This interpolation technique was used to estimate the temperature in the $C/O = 0.77 + Fe$ flame (the dashed line in Figure 4.6-1) from the temperature measurements in the $C/O = 0.74 + Fe$ and the $C/O = 0.80 + Fe$ flames.

As a check on the scattering measurements, the gas temperature in the non-sooting $C/O = 0.52$ flame was calculated from the Q_w measurements in that flame. Three assumptions were made to calculate the gas temperature from the Q_w measurements. First, complete combustion to CO , CO_2 , H_2O , and H_2 was assumed. From the gas feed rates given in Table 3.1-1 and conservation of mass, the stoichiometry of the reaction is then



The stoichiometric coefficient ξ cannot be determined from a mass balance alone. The second assumption was that the water-gas shift reaction was equilibrated:



$$\log_{10}[K_{wg}] = \frac{1400}{T} - 1.35, \quad 1500 < T < 2500 \text{ K} \quad (4.6-3)$$

Equations 4.6-2 and 4.6-3 can be combined to yield one equation with two unknowns, ξ and T .

The third assumption was that the differential scattering cross-section (C_w) of each species was independent of temperature in the range $273 < T < 2250$ K. With this as-

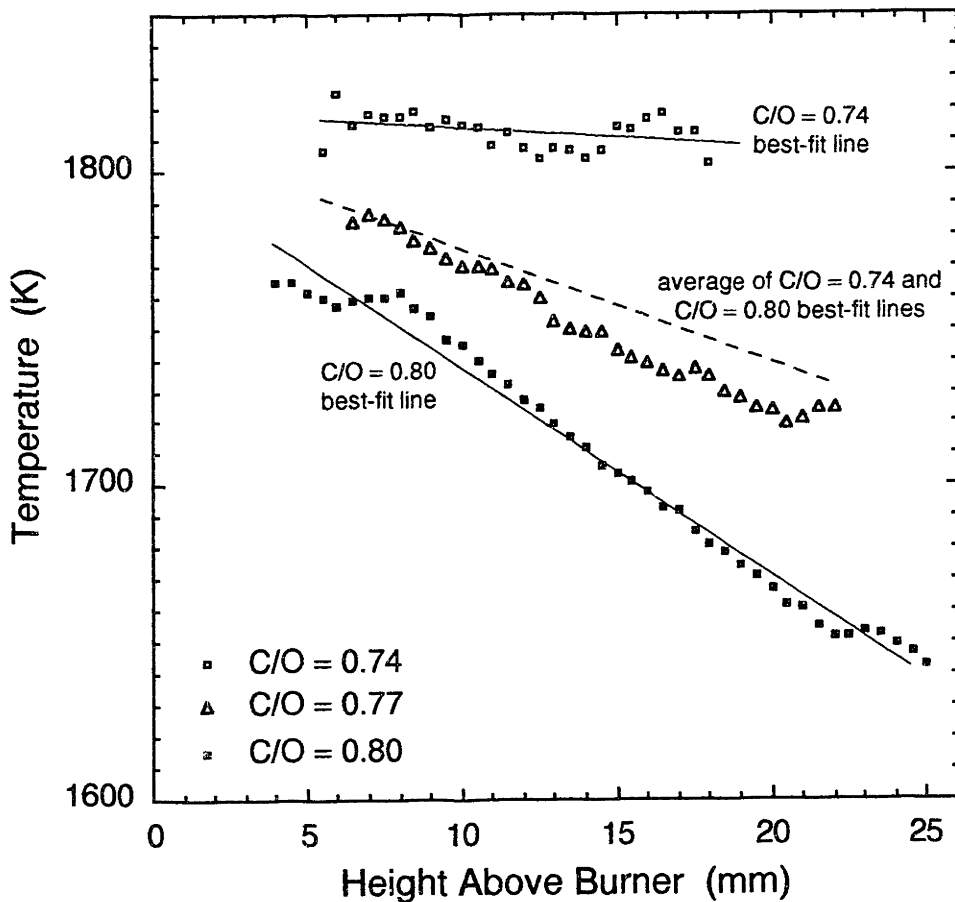


Figure 4.6-3: Comparison of measured temperature and estimated temperature in the $C/O = 0.77$ flame. The symbols are the measured temperatures. The solid lines are best-fits to the data in the $C/O = 0.74$ and $C/O = 0.80$ flames. The dashed line is an estimate of the temperature in the $C/O = 0.77$ flame, obtained by averaging the temperatures predicted by the curve fits of the other two flames at any height above the burner.

The agreement between the estimated temperature and the measured temperature in the $C/O = 0.77$ flame is good. This technique was used to estimate the temperature in the $C/O = 0.77 + Fe$ flame from temperature measurements in the $C/O = 0.74 + Fe$ flame and the $C/O = 0.80 + Fe$ flame.

sumption, the $C_{w,i}$ data in Table 2.2.5-1 can be used to calculate Q_w . Combining Equations 2.2.5-1 through 2.2.5-3 shows that Q_w is given by

$$Q_w = \frac{P}{k_B T} \sum_{i=1}^5 x_i C_{w,i} \quad (4.6-4)$$

The summation in Equation 4.6-4 is over five gas phase species: N_2 , CO , CO_2 , H_2O , and H_2 . Using Equation 4.6-1, the mole fractions x_i can be expressed solely in terms of the variable ξ . Therefore, Equation 4.6-4 is a second independent equation involving the two unknowns, ξ and T . The $C/O = 0.52$ flame temperature was calculated from the Q_w measurements shown in Figure 4.3-1 and by combining Equations 4.6-1 through 4.6-4.

The calculated temperatures in the $C/O = 0.52$ flame are shown in Figure 4.6-4. Also shown in Figure 4.6-4 is the adiabatic temperature for this flame, 1925 K. The calculated temperature and the adiabatic flame temperature differ by a maximum of 16%, and the average difference over all heights above the burner is just 10%. This agreement is good, considering the precision of the scattering measurements and the possible errors associated with the three assumption listed above. The good agreement indicates that the scattering coefficient measurements are accurate and can be accepted with confidence.

4.7 Low Molecular Weight Species Concentrations

Low molecular weight, stable gas phase species concentrations were measured using the sampling system and analytical techniques described in Section 3.4. The measured mole fractions were corrected to account for water condensation in the sampling probe, as described in Appendix C; the concentration measurements presented in this section are the corrected, *in situ* mole fractions.

Figure 4.7-1 presents an overview of the gas phase composition in the $C/O = 0.77$ flame (for clarity, some of the detected species are not shown). Acetylene and methane are the most abundant hydrocarbons, with mole fractions of about 0.03 and 0.006, respectively. Among the detectable light hydrocarbons, ethane was present in the lowest concentration, with a mole fraction of about 4×10^{-6} . Species which could have been detected, had their mole fractions been greater than 10^{-6} , are listed in Table 3.4-3.

Even with rapid quenching ($\tau_q = 0.4$ ms for these samples), several factors (such as radical recombination) can make the composition of the samples different from the com-

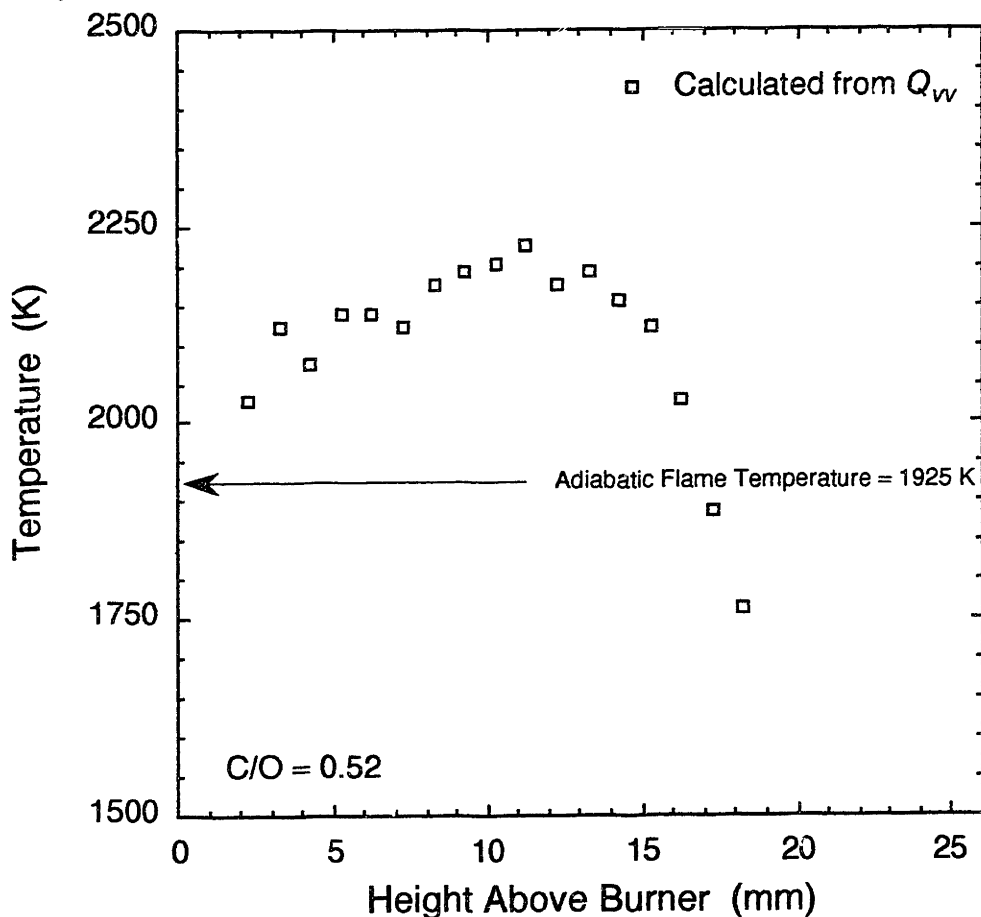


Figure 4.6-4: Temperature measurements in the $C/O = 0.52$ flame. The temperature was calculated from the measured scattering coefficient (see Figure 4.3-1) and the following assumptions:

- complete combustion to CO , CO_2 , H_2O , and H_2
- the water-gas shift reaction is equilibrated
- the differential scattering cross-sections are independent of T

The calculated temperature is at most 16% greater than the adiabatic flame temperature. This agreement is good, considering the precision of the scattering measurements and the possible errors associated with the three assumptions listed above.

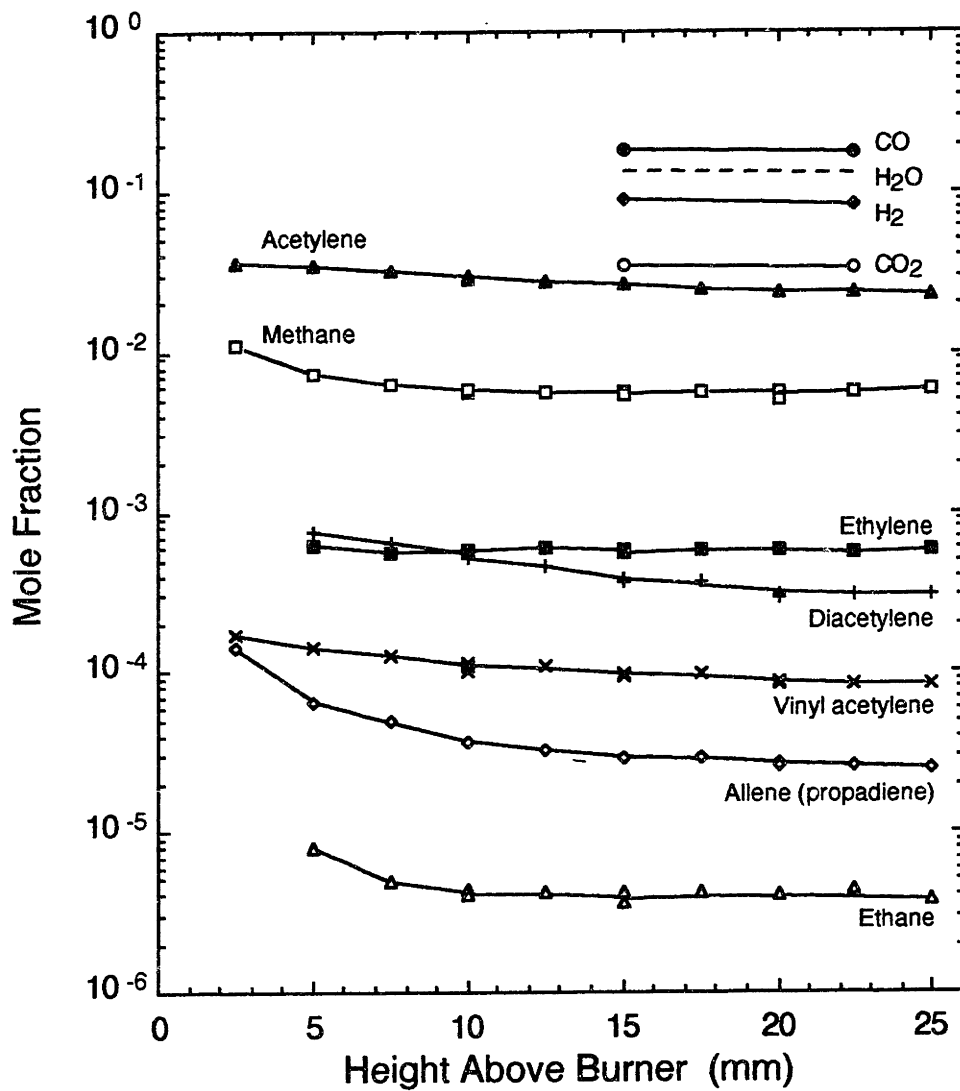


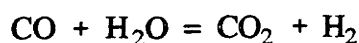
Figure 4.7-1: Overview of the gas phase composition in the C/O = 0.77 flame. The mole fraction of water was calculated from a mass balance (see Appendix C).

position of the flame. Taylor (1984) and Vaughn (1988) discuss these factors and how they may influence the concentration of some species.

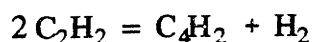
Figures 4.7-2 through 4.7-6 show that the the iron and manganese additives had no measurable effect on the concentration of any of the stable, low molecular weight hydrocarbons in the $C/O = 0.77$ flame. Figure 4.7-7 shows that the additives had no effect on the concentration of the major products of combustion, CO , CO_2 , H_2O , and H_2 .

An empirical correlation (similar to one used by Harris and Weiner, 1983(b)) was developed to estimate the acetylene mole fraction in the $C/O = 0.74$, $C/O = 0.80$, and $C/O = 0.83$ flames. Figure 4.7-8 compares the acetylene concentration profiles in the $C/O = 0.77$ and $C/O = 0.80$ flames. The solid line in Figure 4.7-8 is a third-order polynomial fit to the data from the $C/O = 0.77$ flame. The correlation coefficient for this curve fit was $R^2 = 0.992$. The dashed line in Figure 4.7-8 is the acetylene concentration predicted for the $C/O = 0.80$ flame by the empirical correlation given in the figure. The agreement between the data for the $C/O = 0.80$ flame and the correlation is good. This correlation was used to estimate the acetylene concentration in the $C/O = 0.74$ and $C/O = 0.83$ flames. Since the additives had no effect on the acetylene concentration in the $C/O = 0.77$ flame, this correlation was also used to estimate the acetylene concentration in other flames containing additives.

A discussion of the degree of equilibration of the water gas shift reaction



and the acetylene-diacetylene reaction



is given in Chapter 6.

4.8 High Molecular Weight Species Concentrations

Total tar concentration measurements in the $C/O = 0.83$ and $C/O = 0.83 + Fe$ flame are shown in Figure 4.8-1. By definition, "tar" is the CH_2Cl_2 soluble material collected with the PAH sampling system described in Section 3.6. The tar includes most, but not all, of the PAH species in the flame; PAH with molecular weights greater than approximately 1000 g/mole are generally insoluble in CH_2Cl_2 (Lam, 1988(b)). Figure 4.8-1 shows that the the iron additive increased the total tar concentration in the $C/O = 0.83$

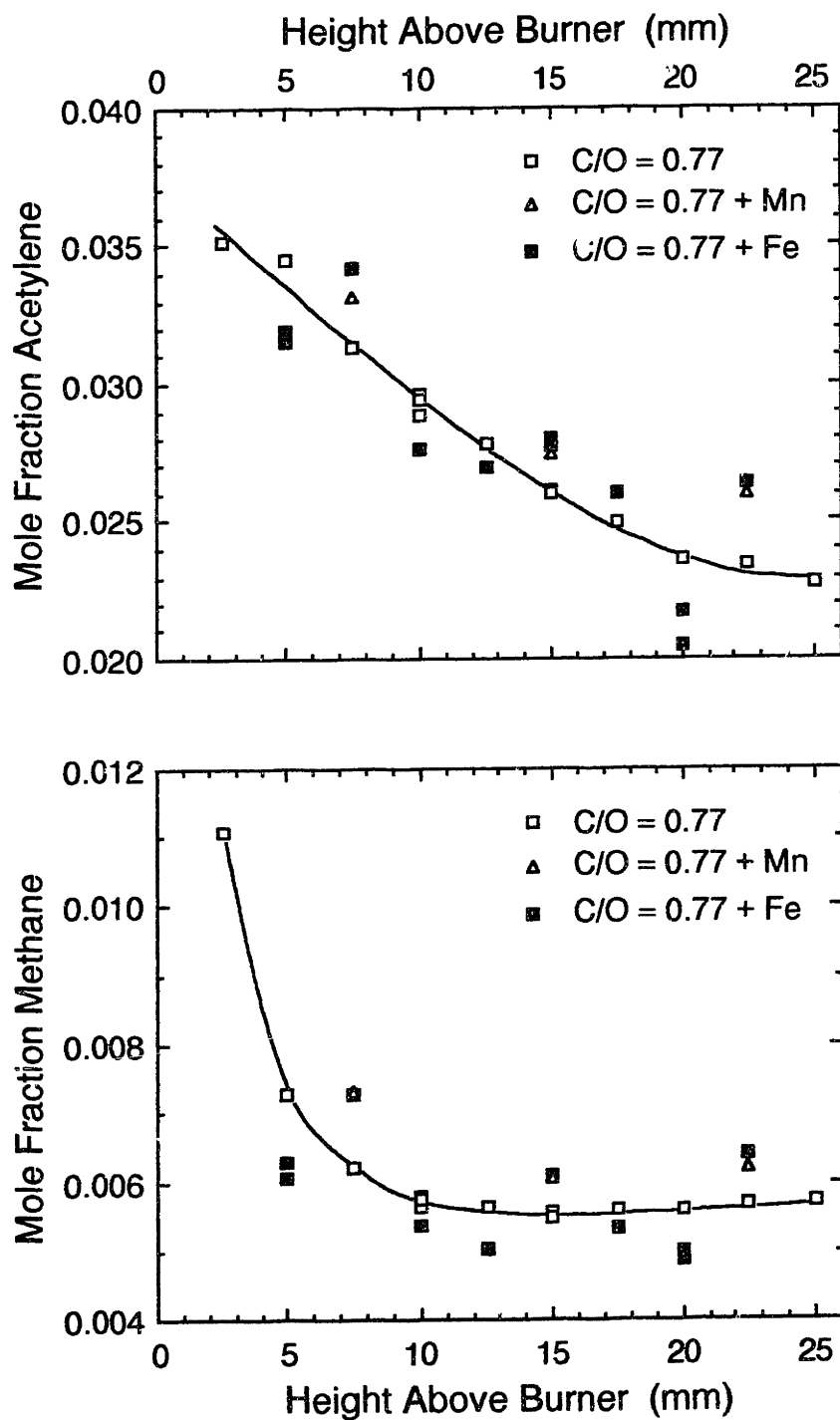


Figure 4.7-2: Methane and acetylene concentration profiles in the $C/O = 0.77$, $C/O = 0.77 + Mn$, and $C/O = 0.77 + Fe$ flames. The additives had no effect on the concentration of any of the stable, low molecular weight hydrocarbons.

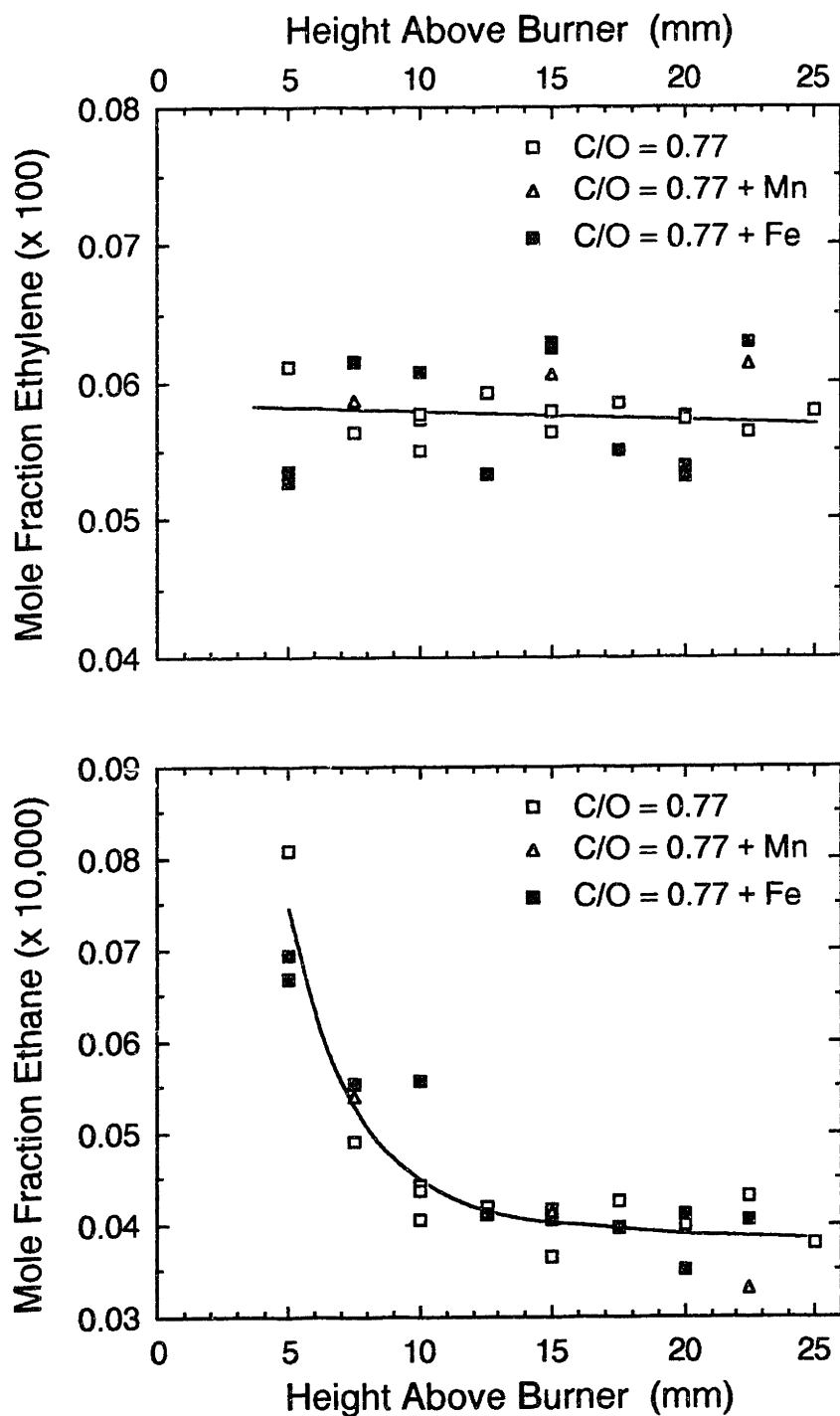


Figure 4.7-3: Ethylene and ethane concentration profiles in the $C/O = 0.77$, $C/O = 0.77 + Mn$, and $C/O = 0.77 + Fe$ flames. The additives had no effect on the concentration of any of the stable, low molecular weight hydrocarbons.

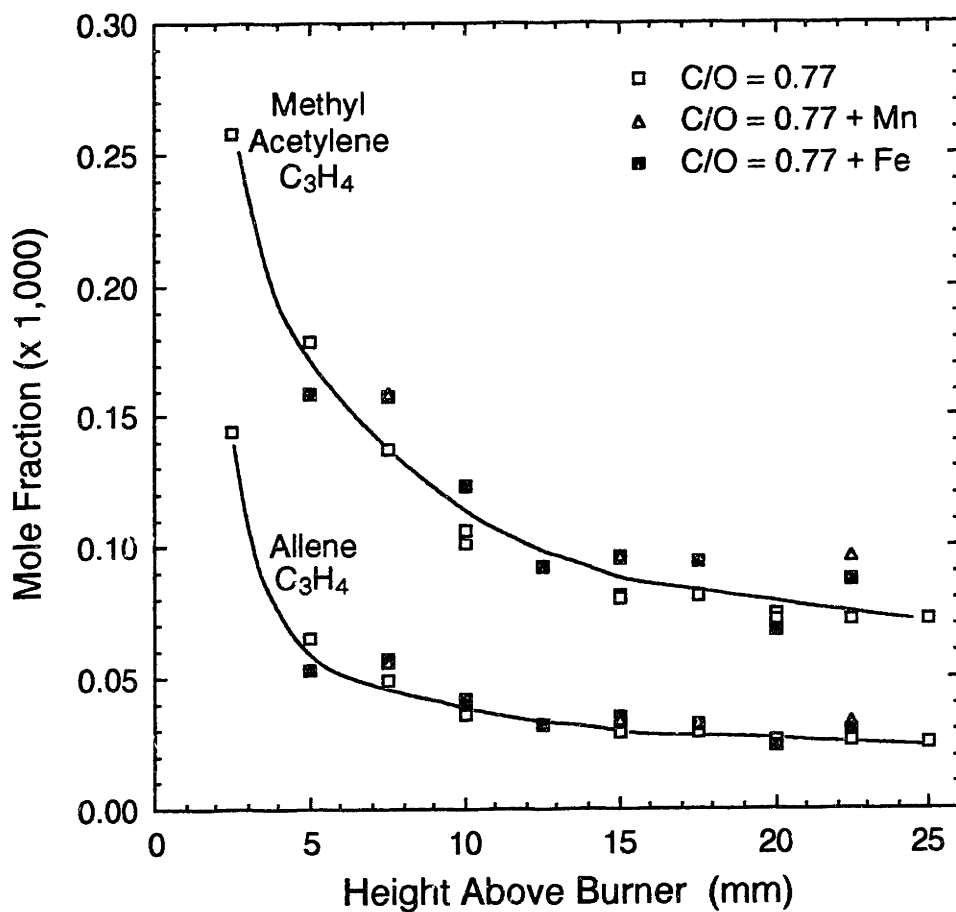


Figure 4.7-4: Allene (propadiene) and methyl acetylene concentration profiles in the $C/O = 0.77$, $C/O = 0.77 + Mn$, and $C/O = 0.77 + Fe$ flames. The additives had no effect on the concentration of any of the stable, low molecular weight hydrocarbons.

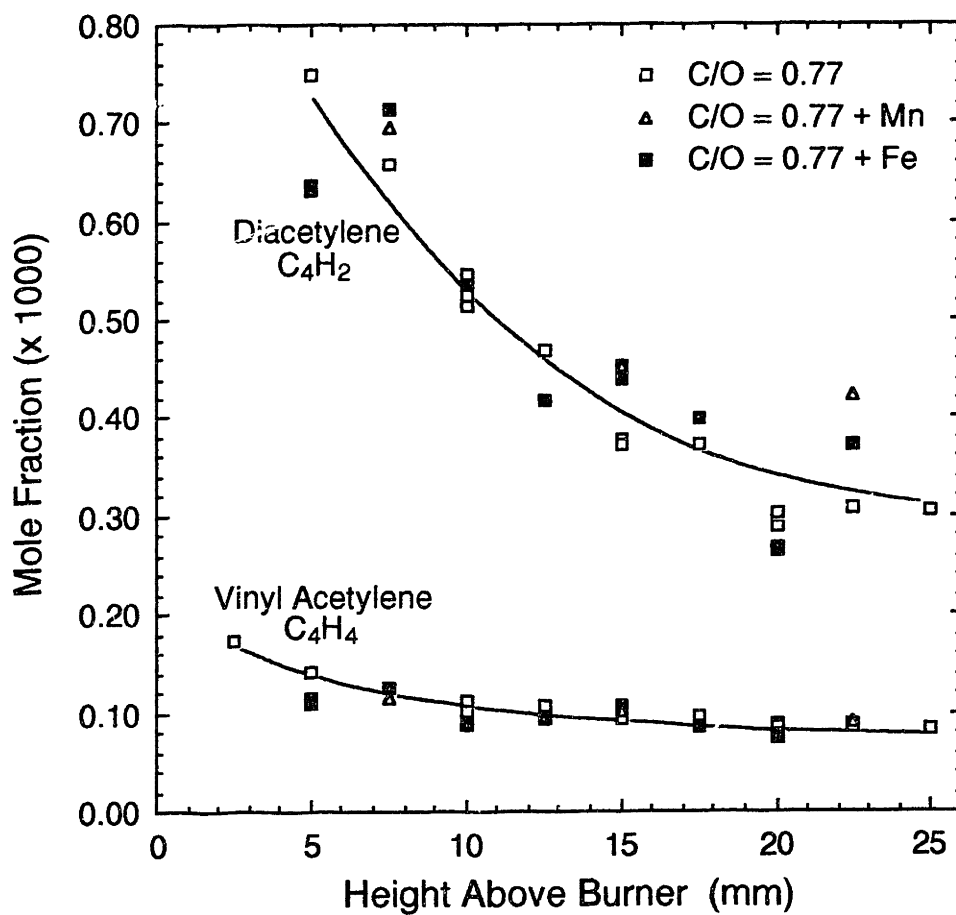


Figure 4.7-5: Diacetylene and vinyl acetylene concentration profiles in the $C/O = 0.77$, $C/O = 0.77 + Mn$, and $C/O = 0.77 + Fe$ flames. The additives had no effect on the concentration of any of the stable, low molecular weight hydrocarbons.

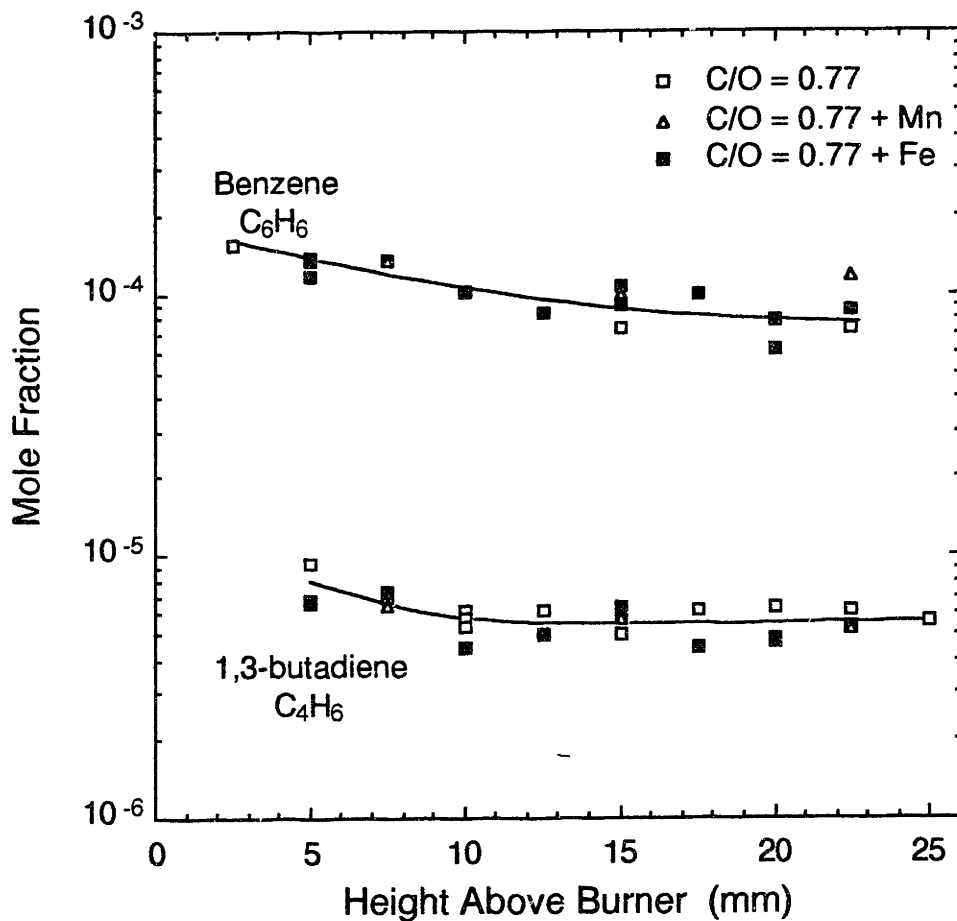


Figure 4.7-6: Benzene and 1,3-butadiene concentration profiles in the $C/O = 0.77$, $C/O = 0.77 + Mn$, and $C/O = 0.77 + Fe$ flames. The additives had no effect on the concentration of any of the stable, low molecular weight hydrocarbons.

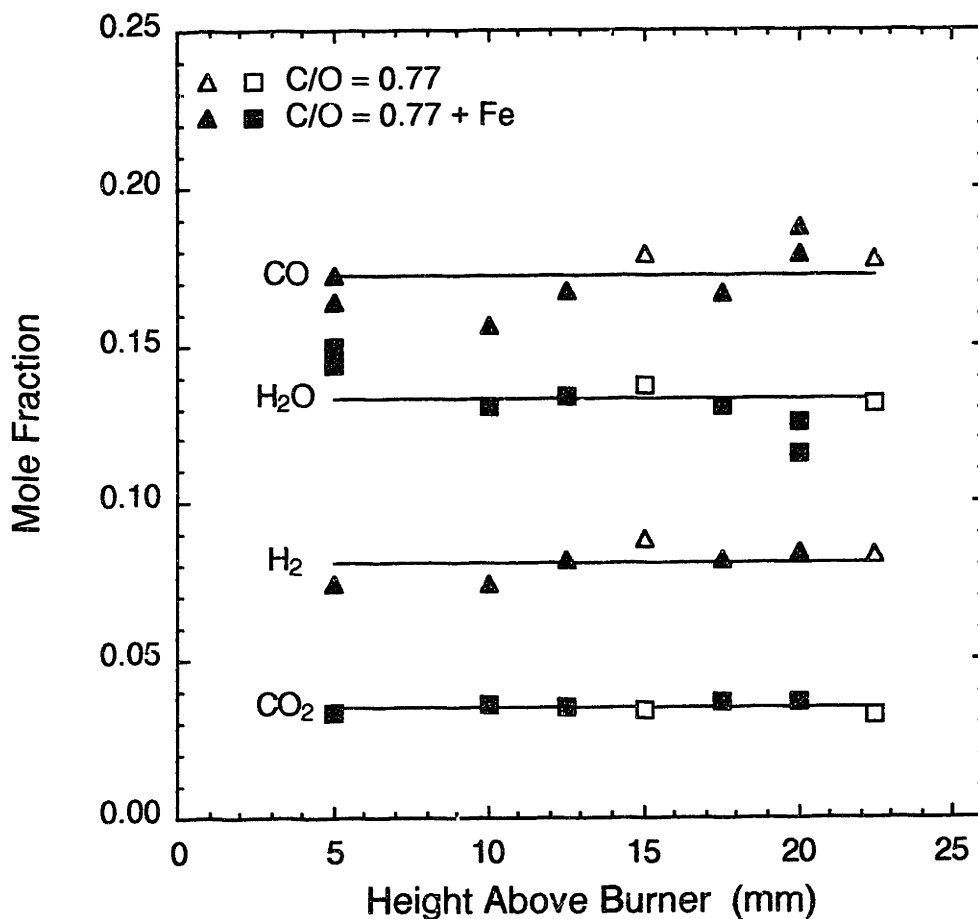


Figure 4.7-7: Concentration profiles of the fixed gases (carbon dioxide, carbon monoxide, hydrogen, and water) in the $C/O = 0.77$ and $C/O = 0.77 + Fe$ flames. The iron additive did not have a measurable effect on the concentration of any of the fixed gases. The horizontal lines are the average mole fractions. The water concentration was calculated using a mass balance (see Appendix C).

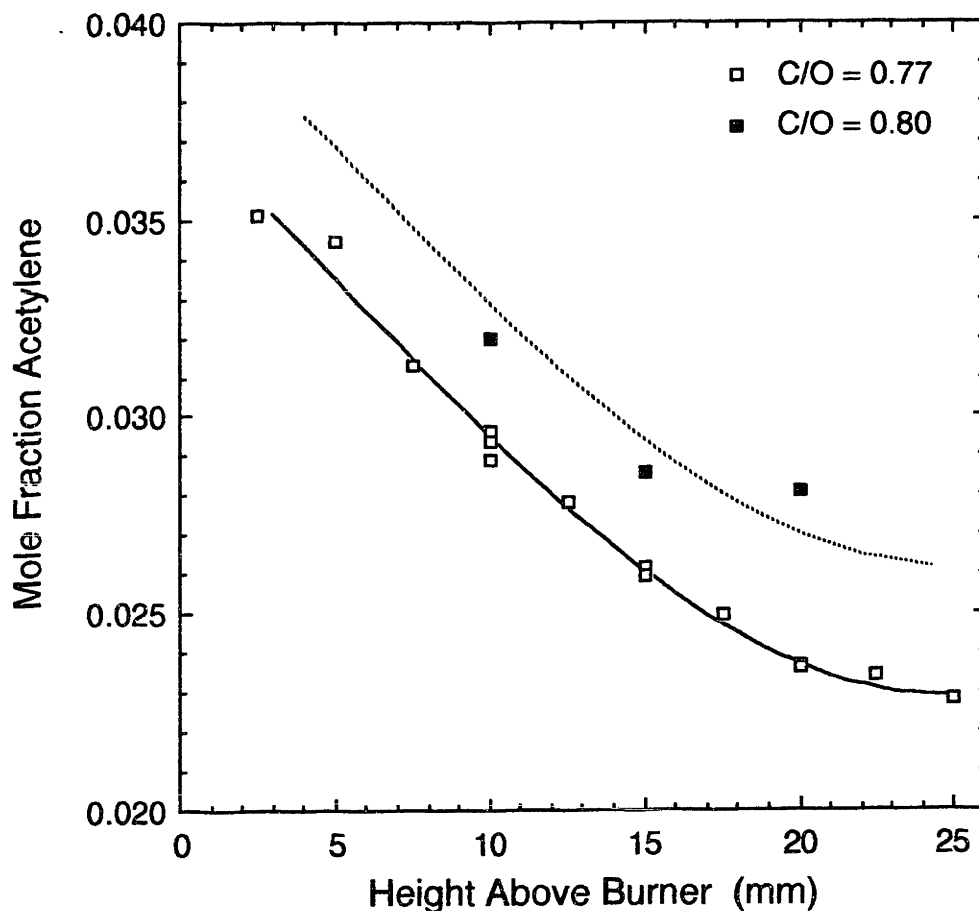


Figure 4.7-8: Empirical correlation of mole fraction acetylene with C/O ratio and height above burner (HAB). The data in the C/O = 0.77 flame was fit to a third-order polynomial

$$x_{C_2H_2} = 0.037566 - 7.829 \times 10^{-4} (HAB) - 9.087 \times 10^{-6} (HAB)^2 + 6.819 \times 10^{-7} (HAB)^3$$

$$R^2 = 0.992$$

shown by the solid line. In other flames, the acetylene concentration was estimated to be

$$x_{C_2H_2} = 0.037566 - 7.829 \times 10^{-4} (HAB) - 9.087 \times 10^{-6} (HAB)^2 + 6.819 \times 10^{-7} (HAB)^3 + 0.111 [(C/O \text{ ratio}) - 0.77]$$

The dashed line plots this correlation for the C/O = 0.80 flame. The agreement between the data for the C/O = 0.80 flame and the correlation is good. The correlation was also used to estimate the acetylene concentration in the C/O = 0.74 and C/O = 0.83 flames, for which there is no data for comparison.

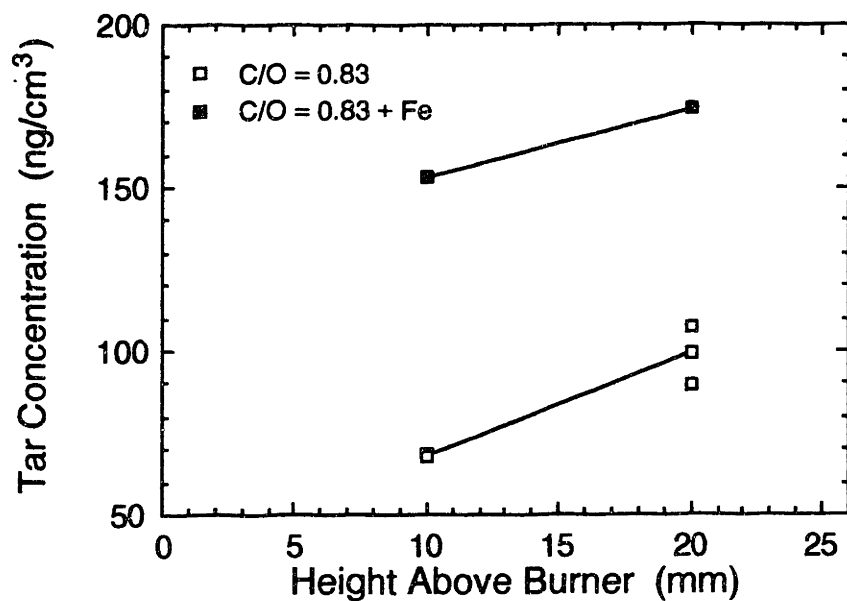


Figure 4.8-1: Total tar concentrations in the $C/O = 0.83$ and $C/O = 0.83 + Fe$ flames.

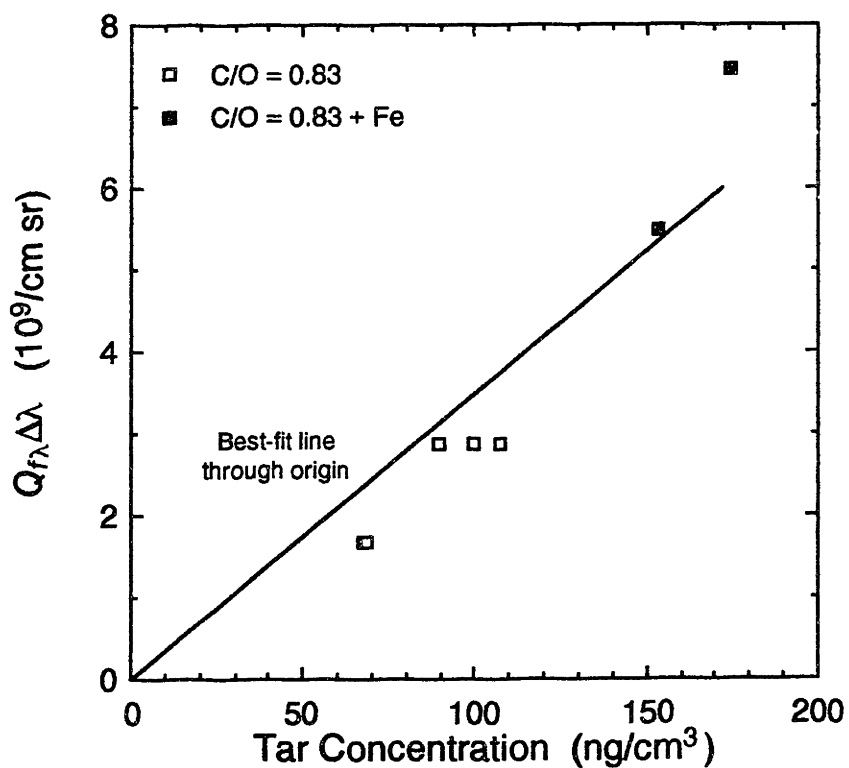


Figure 4.8-2: Correlation of fluorescence coefficient and total tar concentration.

flame, as suggested by the fluorescence coefficient measurements in Section 4.6. The total tar concentration also increases with increasing residence time, as expected from the fluorescence measurements.

Figure 4.8-2 shows that the fluorescence coefficient is roughly proportional to the total tar concentration. Care must be used when comparing $Q_{f\lambda}\Delta\lambda$ measurements and total tar concentration measurements. The fluorescence coefficient was measured *in situ* with relatively good spatial resolution (± 1 ms). In contrast, the tar samples were withdrawn with a sample probe that had a characteristic quench time of about 12 ms. The high molecular weight PAH that are CH_2Cl_2 insoluble (and are not included in the total tar concentration) are probably in the gas phase in the flame, and may contribute to the observed fluorescence. Considering these difficulties, the correlation between $Q_{f\lambda}\Delta\lambda$ and the total tar concentration is relatively good. The best-fit line (constrained to pass through the origin) is

$$Q_{f\lambda}\Delta\lambda = (3.483 \times 10^{-11}) (\text{tar concentration}) \quad R^2 = 0.85 \quad (4.8-1)$$

where the tar concentration has units of ng/cm^3 and the fluorescence coefficient has units of $1/\text{cm sr}$. Equation 4.8-1 can be used to estimate the total tar concentration from the fluorescence coefficient measurements in Section 4.4.

One of the advantages of sample withdrawal and analysis over *in situ* fluorescence measurements is the ability to obtain detailed information on the chemical composition of the PAH. Using gas and liquid chromatography 15 PAH species, with molecular weights between 128 and 398 g/mole, were identified in the tar samples (see Tables 3.6-1 and 3.6-2). Many peaks which appeared in the chromatographs were not identified. Figures 4.8-3 through 4.8-6 show that the iron additive increased the concentration of each of the 7 species identified via GC. The LC concentration measurements had greater uncertainty than the GC concentration measurements. The range of concentrations seen for each of the species identified via LC is given in Table 4.8-1. The iron additive also increased the concentration of these species.

The 15 species identified via GC and LC accounted for about 65 to 75% of the total mass of the tar. Assuming that the identifiable species are representative of the unknown species, the mean molecular weight of the tar (averaged over all the samples) was 198 g/mole. The mean molecular weight increased slightly with increasing distance from

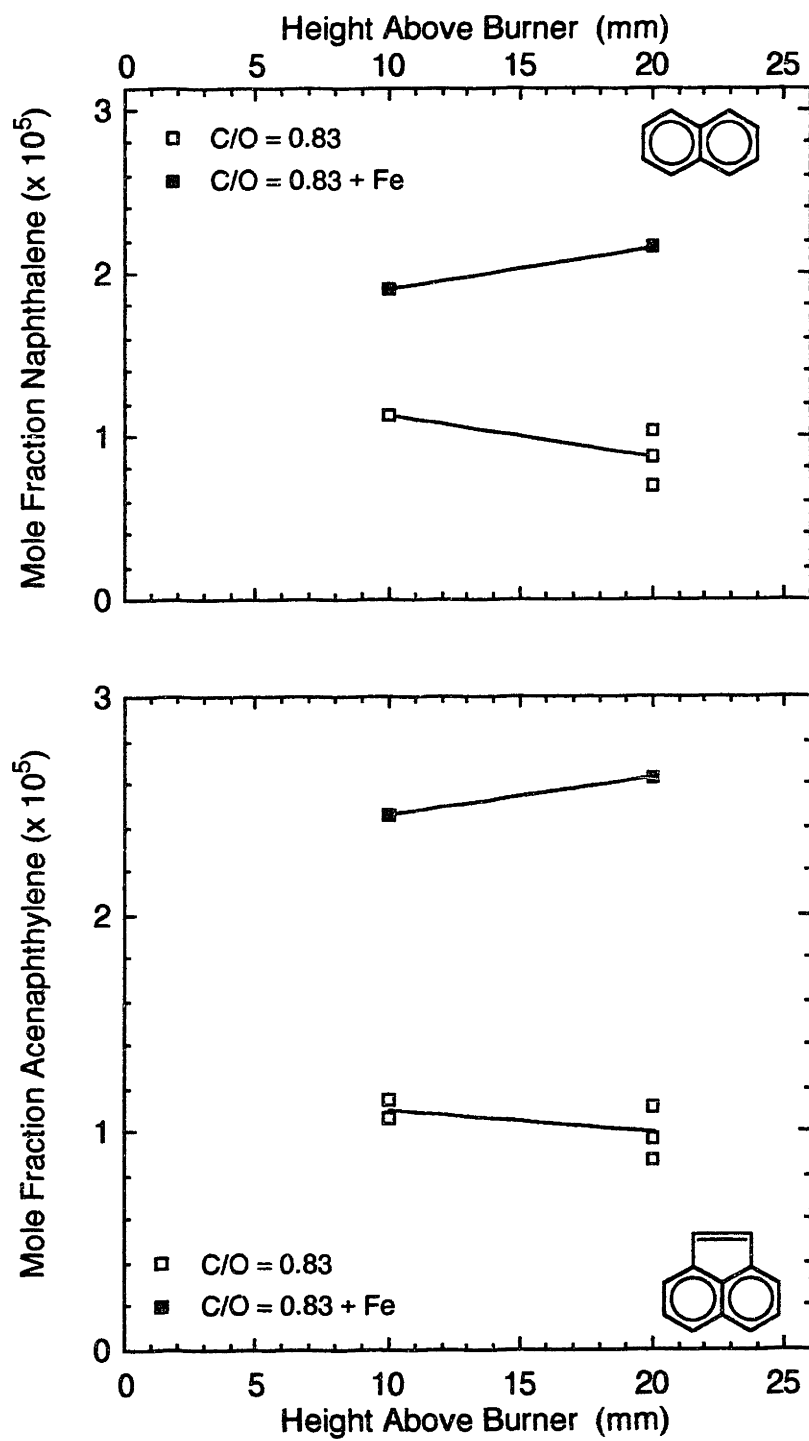


Figure 4.8-3: Concentrations of naphthalene and acenaphthylene in the C/O = 0.83 and C/O = 0.83 + Fe flames.

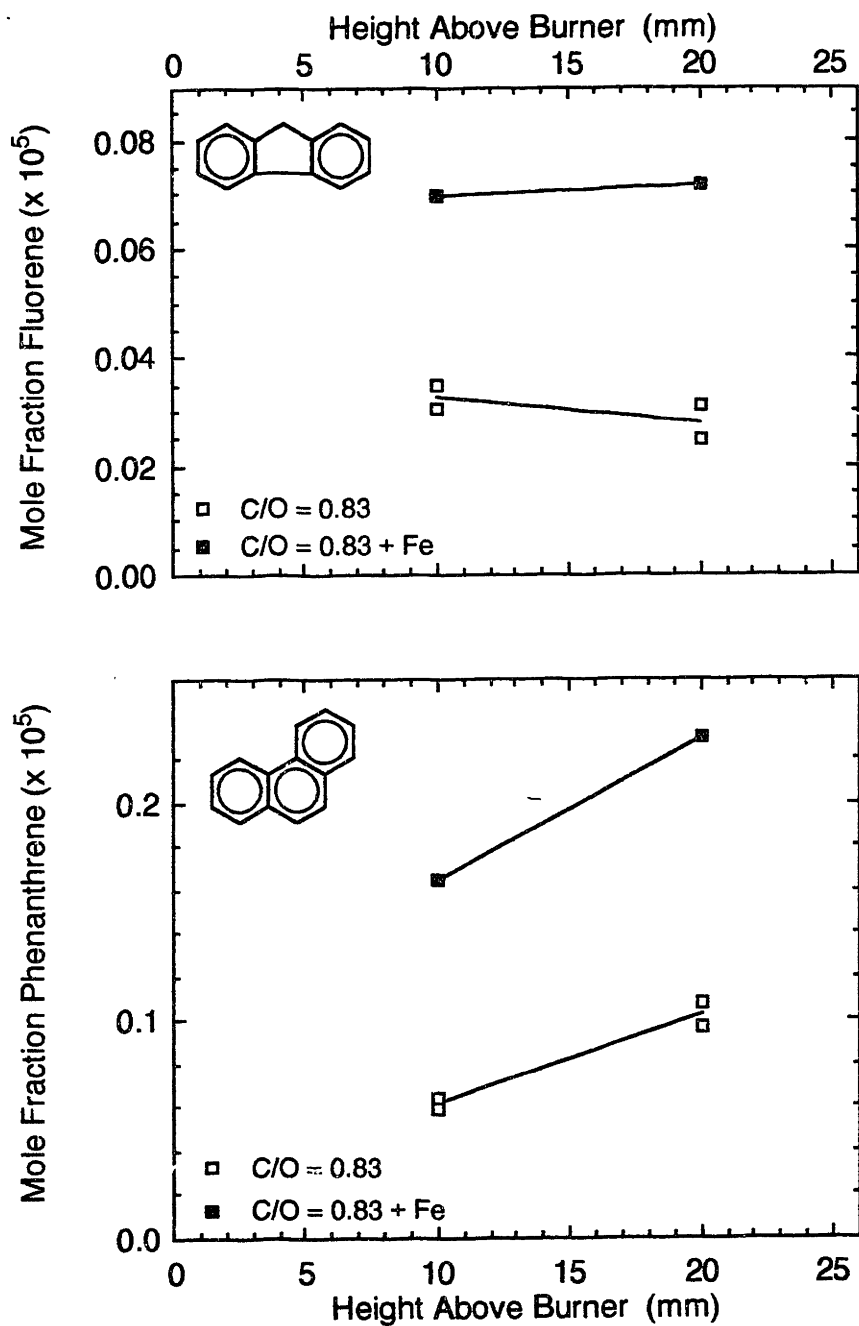


Figure 4.8-4: Concentrations of fluorene and phenanthrene in the C/O = 0.83 and C/O = 0.83 + Fe flames.

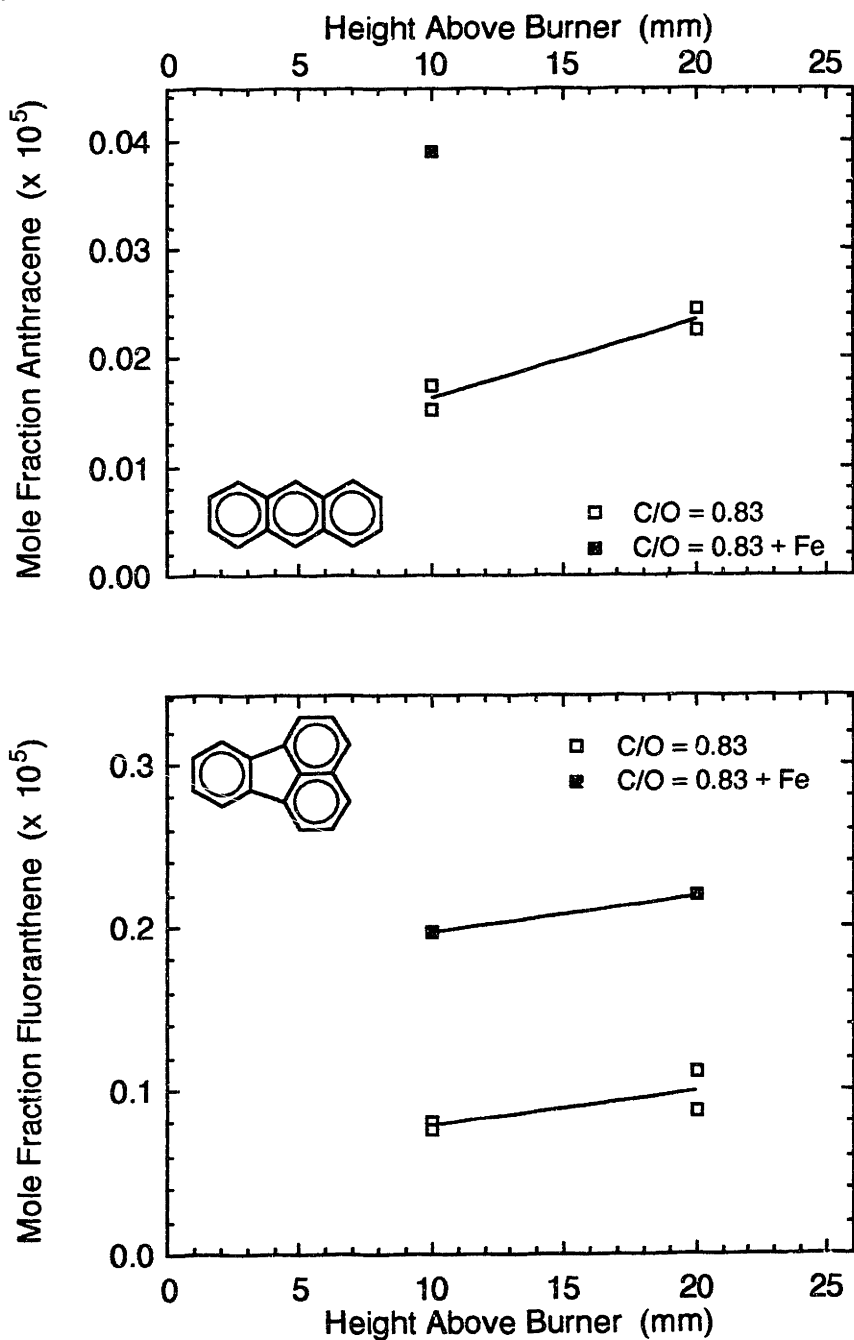


Figure 4.8-5: Concentrations of anthracene and fluoranthene in the C/O = 0.83 and C/O = 0.83 + Fe flames.

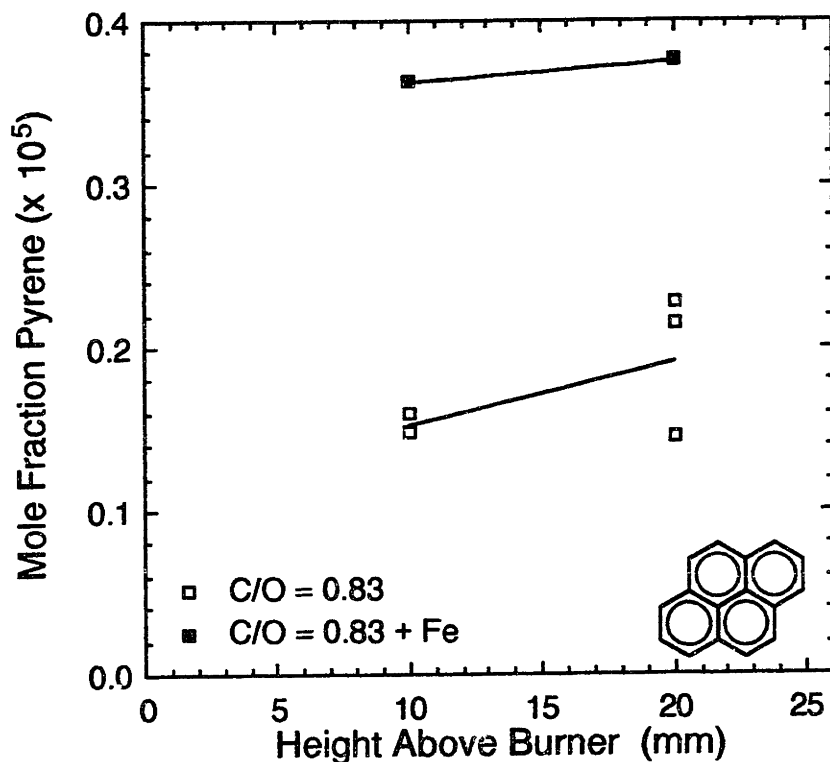


Figure 4.8-6: Concentration of pyrene in the $C/O = 0.83$ and $C/O = 0.83 + Fe$ flames.

Species	Formula	Mole Fraction ($\times 10^5$)
Cyclopenta(<i>cd</i>)pyrene	$C_{18}H_{10}$	0.4 to 2.5
Benzo(<i>a</i>)pyrene	$C_{26}H_{12}$	0.03 to 0.3
Benzo(<i>ghi</i>)perylene	$C_{22}H_{12}$	0.06 to 0.4
Indeno(1,2,3- <i>cd</i>)pyrene	$C_{22}H_{12}$	0.04 to 0.2
Anthanthrene	$C_{22}H_{12}$	0.04 to 0.3
Coronene	$C_{24}H_{12}$	0.05 to 0.3
Naphtho(8,1,2- <i>abc</i>)coronene	$C_{30}H_{14}$	0.03 to 0.09
Ovalene	$C_{32}H_{14}$	0.02 to 0.06

Table 4.8-1: Range of concentrations of the PAH species identified via liquid chromatography in the $C/O = 0.83$ and $C/O = 0.83 + Fe$ flames. The iron additive increased the concentration of all of the LC species.

the burner, from 190 g/mole at 10 mm, to 214 g/mole at 20 mm. The iron additive did not significantly change the mean molecular weight of the tar.

Given that iron had no effect on the concentration of any of the low molecular weight species, the increase in the PAH concentration (as shown by the sampling measurements and the fluorescence coefficient measurements) is somewhat surprising. These results suggest a certain amount of decoupling between the chemistry of the low molecular weight species and the PAH. Bonczyk (1987) has shown that some metal additives can decrease the OH concentration in flames. PAH are being formed and destroyed at almost equal rates (Lam, 1988(b)); a decrease in the OH concentration would decrease the PAH destruction rate and result in a net increase in the PAH concentration. However, the concentrations of (at least some of) the lower molecular weight species would also be expected to increase, and this was not observed.

An alternative explanation for the increase in the PAH concentration is that metallic iron on the surface of the particles catalyzed reactions that form PAH. Using this hypothesis, manganese then had a smaller effect on the PAH concentration because there is much less manganese in the solid phase (see Chapter 6). Of course, both of these explanations are highly speculative.

4.9 Particle Size and Shape Distribution Measurements

The thermophoretic probe described in Section 3.5 was used to collect two soot samples from the $C/O = 0.77$ flame. For one sample, a TEM grid was inserted into the flame 12.5 mm above the burner surface; for the other sample, a TEM grid was inserted 17.5 mm above the burner surface. The subsequent electron microscopy and image analysis are described in Section 3.5.

A typical transmission electron micrograph of the soot particles collected from the $C/O = 0.77$ flame is shown in Figure 4.9-1. The grainy background in this micrograph is the fine but uniform structure of the 20 nm thick amorphous carbon film coating the TEM grid. The variation in illumination is due to the inexperience of the microscopist (the author). The soot particles are the irregularly shaped, slightly darker objects in the image. Some of the particles are clearly agglomerates, consisting of several smaller, roughly spherical units. Other particles appear to be single, non-agglomerated spheres. The out-

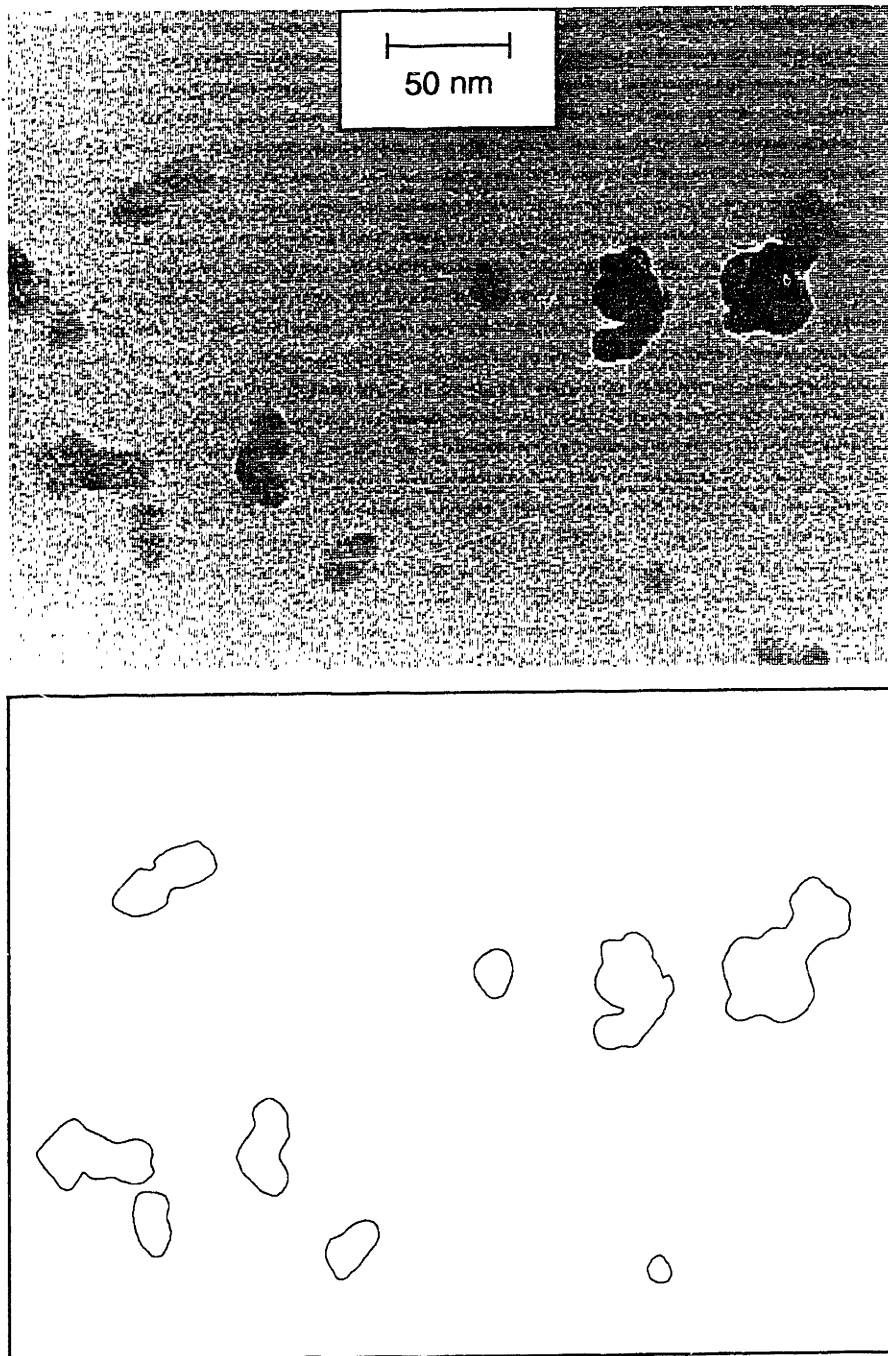


Figure 4.9-1: A typical transmission electron micrograph of soot particles collected from the $C/O = 0.77$ flame, 12.5 mm from the burner surface, using the thermophoretic probe. The upper illustration is the electron micrograph. The lower figure shows the particle outlines as they might have been drawn on the screen of the Magiscan 2 image analyzer (particles only partially within the field of view have not been outlined). The grainy background is the fine but uniform structure of the 20 nm thick amorphous carbon film coating the TEM grid. The actual image analysis was performed directly from TEM negatives.

lines of these particles, as they might have been drawn on the screen of the image analyzer, are also shown in this figure. The actual image analysis was performed directly from TEM negatives.

The projected area diameter (d_a) distribution is shown in Figures 4.9-2 and 4.9-3 for the samples collected 12.5 mm and 17.5 mm, respectively, from the burner surface. For the 12.5 mm sample, the distribution is the result of imaging a total of 748 particles from 29 micrographs. For the 17.5 mm sample, a total of 474 particles were imaged from 24 micrographs. Probability plots of the projected area diameter measurements showed that d_a could be fit well by the lognormal size distribution (see Equation 2.1-21). The best-fit to the lognormal size distribution is shown in both figures.

The geometric mean d_a was almost the same in both samples, increasing from 25.9 nm to 26.1 nm as the distance from the burner increased from 12.5 mm to 17.5 mm. The geometric mean standard deviation of the d_a distribution increased from $\sigma_g = 0.56$ to $\sigma_g = 0.72$. Substituting these widths into Equation 2.1-22 gives $f_N = 17$ and $f_N = 106$, respectively. The width of the d_a distribution is substantially greater than the width predicted by the self-preserving by the size distribution, $f_N = 2.08$ (see Equation 2.1-29).

The perimeter diameter (d_c) distribution was slightly broader than the projected area diameter distribution, and the geometric mean d_c was slightly larger than the geometric mean d_a . At a distance of 12.5 mm from the burner surface, the geometric mean d_c was 30.8 nm, with $\sigma_g = 0.64$; 17.5 mm from the burner, the geometric mean d_c was 33.5 nm, with $\sigma_g = 0.84$.

The elongation ratio distribution of these two samples is shown in Figure 4.9-4. The average elongation ratio increased from 1.49 to 1.57 as the distance from the burner increased from 12.5 mm to 17.5 mm. In contrast, the depolarization ratio decreased with increasing distance from the burner (see Figure 4.5-1). These results suggest that the depolarization of the scattered light arises more from optical anisotropy than from geometrical anisotropy. Although the soot particles become less spherical with time, they also dehydrogenate and pyrolyze. The internal molecular changes caused by the dehydrogenation and pyrolysis reaction may make the particles more optically isotropic.

The extremely broad soot particle size distribution is a cause for concern, and casts doubt on the accuracy of the thermophoretic probe measurements. The particle sizes and

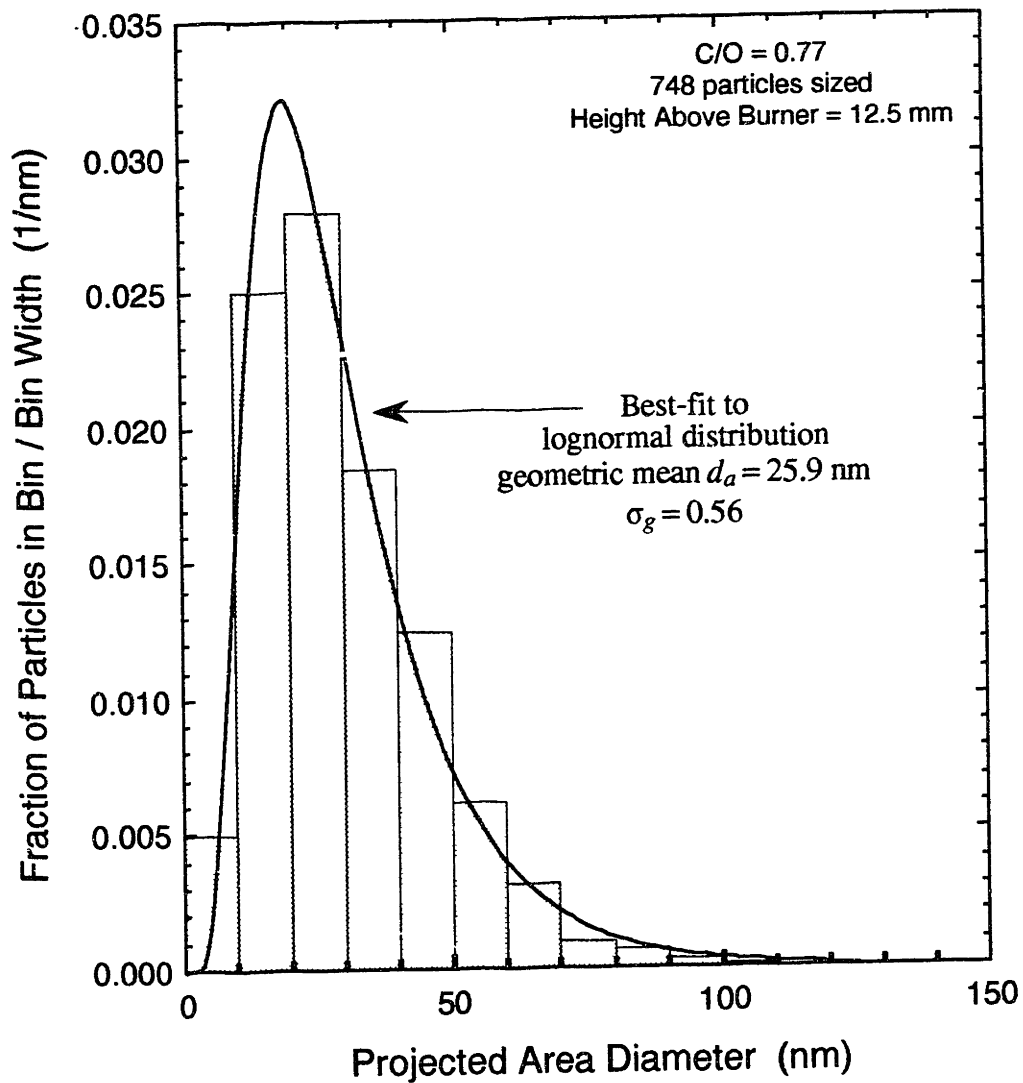


Figure 4.9-2: The projected area diameter distribution in the C/O = 0.77 flame, 12.5 mm above the burner, as determined by the thermophoretic probe and TEM image analysis. The best-fit to the lognormal size distribution (Equation 2.1-21) is shown. The ordinate of this plot is actually $p(x)$, where $x = d_a$, the projected area diameter, using the notation in Section 2.1.

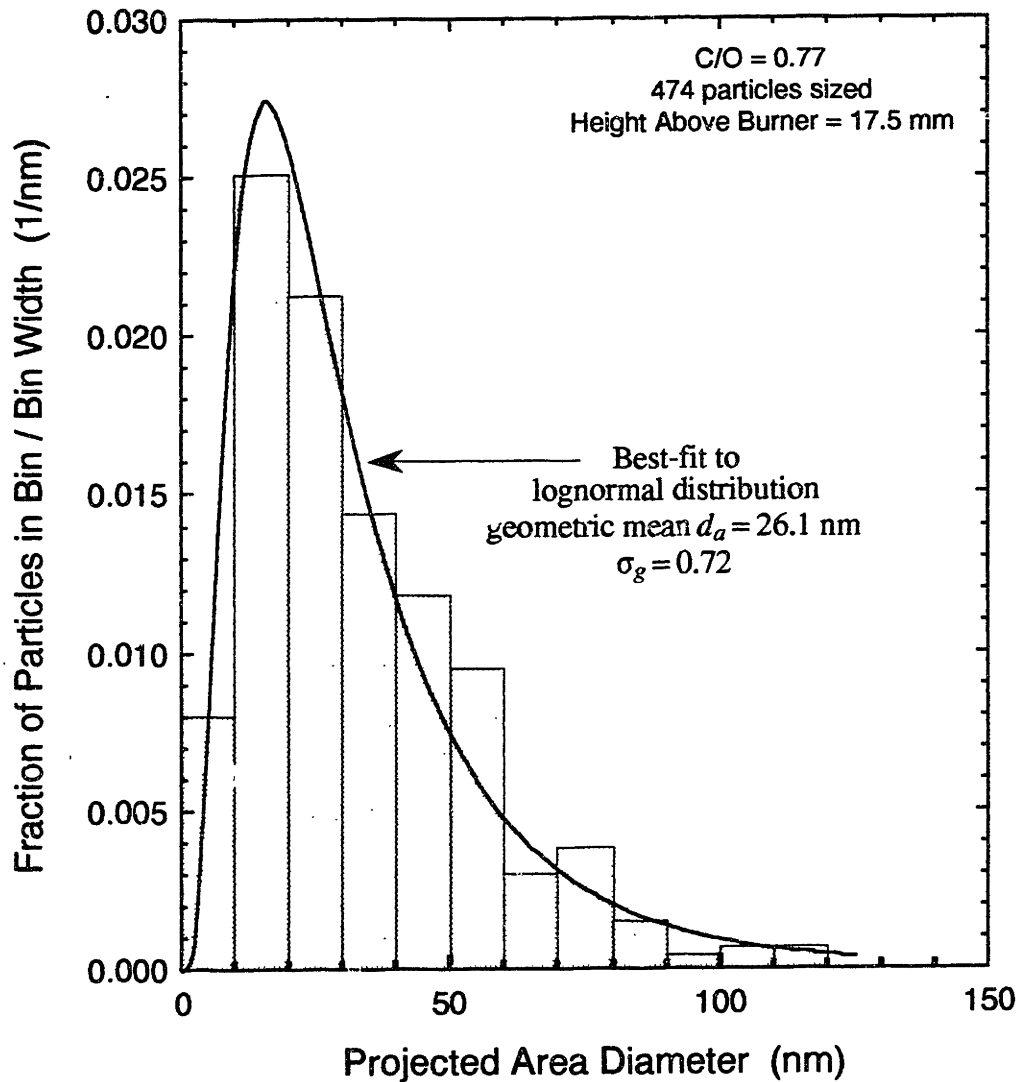


Figure 4.9-3: The projected area diameter distribution in the $C/O = 0.77$ flame, 17.5 mm above the burner, as determined by the thermophoretic probe and TEM image analysis. The best-fit to the lognormal size distribution (Equation 2.1-21) is shown. The ordinate of this plot is actually $p(x)$, where $x = d_a$, the projected area diameter, using the notation in Section 2.1.

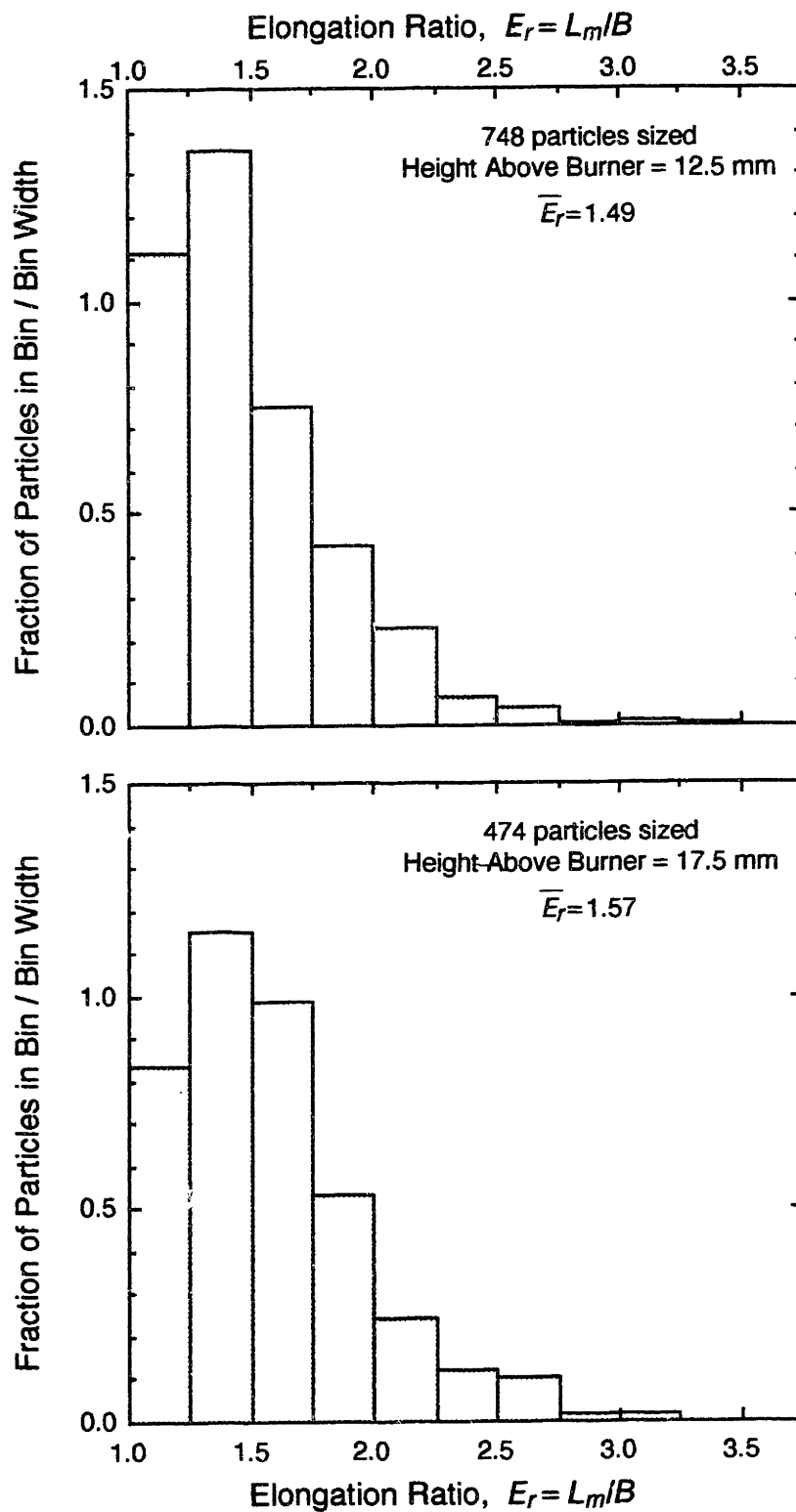


Figure 4.9-4: The elongation ratio distribution in the $C/O = 0.77$ flame, as determined by the thermophoretic probe and TEM image analysis. The soot particles become slightly less spherical with increasing distance from the burner.

shapes reported in this section may not be representative of the *in situ* particle size and shape. There are several possible sources of error in the thermophoretic sampling results. First, the motion of the probe may induce bulk flow disturbances in the flame that effect the sampling. Second, the rapid acceleration and deceleration of the probe may cause the TEM grid at the end of the probe to vibrate from side to side in the flame. The effect of such vibrations on thermophoretic sampling depends on the amplitude and frequency of the vibrations. The motion of the probe was too rapid for either bulk flow disturbances or vibrations of the TEM grid to be observed with the unaided eye. High speed cameras should be able to determine if these phenomena are occurring.

A third possibility is that the agglomeration seen in these samples may have taken place as the soot particles crossed the thermal boundary layer surrounding the probe. The characteristic quench time (the time required for a soot particle to leave the bulk gas and strike the cold TEM grid) of the thermophoretic probe was about 4 ms. Although the collision rate decreases as the temperature decreases, the coalescence time (if soot particle collisions are coalescent) increases with decreasing temperature. A detailed model of particle collisions in the thermal boundary layer of the thermophoretic probe might determine if the agglomerates exist *in situ* or are artifacts caused by poor quenching.

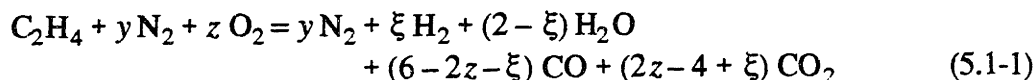
Additional comparisons between the thermophoretic sampling shape and size measurements and the optical measurements are presented in Chapter 5.

5. INTERPRETATION OF EXPERIMENTAL RESULTS

5.1 Calculation of Residence Time

The path length through the flame (see Section 4.1) and the burned gas volumetric flow rate (\dot{G}) were used to calculate the gas velocity $v(x)$ at any distance from the burner x . The volumetric gas flow rate was calculated from the total mole change upon reaction (assuming complete combustion to CO, CO₂, H₂O, and H₂) and the measured flame temperature (see Section 4.6). The velocity profile was then integrated to determine the soot particle residence time t in the flame.

To determine the total mole change upon reaction, Equation 4.6-1 (written for the C/O = 0.52 flame) was generalized to apply to any of the premixed flames:



The stoichiometric coefficients y and z are determined by the gas feed rates given in Table 3.1-1. Using this basis, the total number of moles after combustion is $(4 + y)$ moles. The total molar flow rate increased by 23% (from 0.504 to 0.622 moles/min) in the C/O = 0.74 flame, and by 29% (from 0.442 to 0.571 moles/min) in the C/O = 0.83 flame. The volumetric gas flow rate at any distance from the burner was then calculated from the flame temperature and the ideal gas law. The gas velocity v is then

$$v(x) = \frac{\text{volumetric flow rate}}{\text{cross-sectional area}} = \frac{\dot{G}}{\pi L^2/4} \quad (5.1-2)$$

where L is the flame diameter.

The calculated gas velocity actually changes very little with C/O ratio or increasing distance from the burner. Although Equation 5.1-2 was used to calculate the gas velocity at any distance from burner, a good approximation is to assume $v = 1.05$ mm/ms, $\pm 15\%$, in any flame.

The residence time t in the flame at any distance from the burner x is

$$t(x) = \int_{x=0}^x \frac{dx}{v(x)} \quad (5.1-3)$$

Equation 5.1-3 arbitrarily sets the residence time to $t = 0$ at $x = 0$, the burner surface.

Since the temperature and path length were not measured close to the burner surface, the gas velocity was assumed to be constant from $x = 0$ to 2.5 mm. This assumption is equivalent to assuming the cross-sectional area, temperature, and molar flow rate are constant from $x = 0$ to 2.5 mm. The latter two assumptions are poor, since the reaction zone in these flames is about 1 mm above the burner surface. Although an error is introduced into the residence time calculations from the assumption of a constant gas velocity close to the burner surface, two important observations should be made. First, the magnitude of the error is about the same in all of the flames. Second, the choice of zero residence time is arbitrary, so a constant additive error in all of the residence times is unimportant.

5.2 Interpretation of Optical Measurements

In the following sections, the light scattering and absorption measurements presented in Chapter 4 will be interpreted using the four different sets of assumptions presented in Sections 2.2.1 through 2.2.4. The purpose of this section is to show that Rayleigh theory for small, spherical, homogeneous particles (described in Section 2.2.1) can be used to interpret the optical measurements.

5.2.1 Comparison of Rayleigh Theory and Lorenz-Mie Theory

The Rayleigh equations presented in Section 2.2.1 are an approximation to the complete Lorenz-Mie theory presented in Section 2.2.4. The Rayleigh approximation is good for small particles ($\pi d/\lambda \ll 1$) and becomes poorer as the particle size increases. To compare Rayleigh theory and Lorenz-Mie theory in these flames, the soot particle diameter in the $C/O = 0.83$ flame was calculated from the K_{ext} and Q_{vv} measurements using both theories. The Rayleigh diameter was calculated using Equation 2.2.1-10. The Lorenz-Mie diameter was calculated by finding the diameter d which, when substituted into Equations 2.2.4-1 through 2.2.4-12, yielded the measured value of Q_w/K_{ext} . A computer program, based on the BHMIE subroutine developed by Bohren and Huffman (1983), was used to perform the necessary calculations for the Lorenz-Mie case. For both the Rayleigh theory and Lorenz-Mie theory calculations a monodisperse particle diameter distribution was assumed, and the refractive index of soot was taken as $m = 1.6 - 0.59i$.

Figure 5.2.1-1 shows that Rayleigh theory is an excellent approximation to Lorenz-

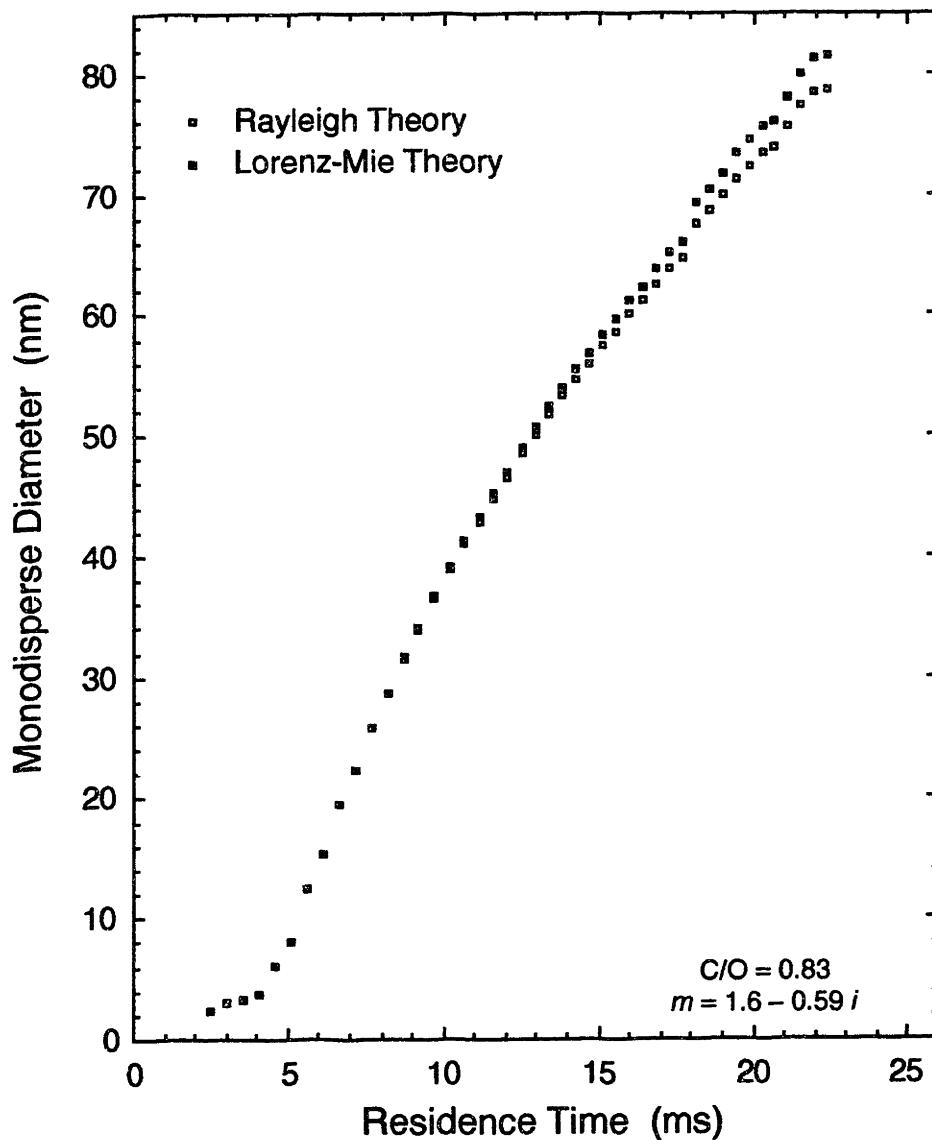


Figure 5.2.1-1: Comparison of the particle diameters in the $C/O = 0.83$ flame, calculated from light scattering measurements using either Rayleigh theory or Lorenz-Mie theory. A monodisperse size distribution and a constant refractive index, $m = 1.6 - 0.59i$, were assumed in both cases. At the largest particle diameters, Rayleigh theory underestimates the particle diameter by only 3.5%, indicating that Rayleigh theory is an adequate approximation to Lorenz-Mie theory in these flames.

Mie theory in the C/O = 0.83 flame. For particles up to 50 nm in diameter, Rayleigh theory underestimates the Lorenz-Mie monodisperse diameter by 1% or less. At the largest particle diameters, Rayleigh theory underestimates the particle diameter by only 3.5%. Since the C/O = 0.83 flame is the flame (without an additive) in which the soot particles attain the largest size, the maximum error associated with using Rayleigh theory to calculate the particle diameter instead of Lorenz-Mie theory is 3.5%.

5.2.2 Comparison of Homogeneous Sphere and Coated Sphere Theory

As will be shown in Chapter 6, thermodynamic equilibrium predicts iron and manganese will be in the solid phase (at least under some conditions) in these flames. Therefore, the soot particles are expected to contain two components, soot and an inorganic compound (either metallic iron or MnO). The extent to which the presence of metallic iron within the soot particles could influence the interpretation of the optical measurements will be investigated in this section.

To determine the effect the iron additive could have on the optical measurements, the aerosol particles were modeled as small coated spheres with the geometry shown in Figure 2.2.2-1. The soot and iron phases were assumed to be completely separate and immiscible. The particles probably did not have this idealized structure; however, the coated sphere geometry is one of the few multicomponent geometries for which rigorous solutions to the light scattering problem have been developed. Both iron core/soot coating and soot core/iron coating particles were considered. In addition to assuming the particles were coated spheres, the following assumptions were made:

- 1) all of the added iron was in the solid phase as metallic iron. Although thermodynamic equilibrium does not predict that all the iron should be in the solid phase, using this assumption determined the maximum effect iron could have on the interpretation of the optical measurements. The refractive index of metallic iron was taken as $m = 3.07 - 3.55 i$.
- 2) at any residence time, all particles of all sizes had the same percentage (by volume) of core material, or q^3 was a constant at any residence time.

The total particle volume fraction predicted by the coated sphere analysis will be compared to the soot particle volume fraction predicted by a homogeneous sphere analysis. The comparison will be performed using the absorption measurements from the C/O = 0.77 + Fe flame.

The first assumption given above allows the volume fraction of metallic iron ($f_{v, Fe}$) to be calculated from the molar feed rates of the iron additive and the feed gases. The density of iron was taken as 7.5 g/cm³. Assuming complete combustion to CO, CO₂, H₂O, and H₂, the volume fraction of metallic iron in the C/O = 0.77 + Fe flame is

$$f_{v, Fe} = (2.26 \times 10^{-6}) / T \quad (5.2.2-1)$$

where T is the flame temperature (K). The local temperature in the C/O = 0.77 + Fe flame was used to calculate $f_{v, Fe}$ at any residence time.

The total solid volume fraction is the sum of the soot and iron volume fractions:

$$f_{v, total} = f_{v, Fe} + f_{v, soot} \quad (5.2.2-2)$$

The second assumption listed above allows the total volume fraction to be determined from K_{ext} measurements:

$$f_{v, total} = f_{v, Fe} + f_{v, soot} = \frac{\lambda K_{ext}}{6 \pi G_c(m_i, m_o, q^3)} \quad (5.2.2-3)$$

The function $G_c(m_i, m_o, q^3)$ is defined in Equation 2.2.2-7. If soot forms the core and iron forms the coating, then $m_i = 1.6 - 0.59 i$, $m_o = 3.07 - 3.55 i$, and

$$q^3 = f_{v, soot} / f_{v, Fe} \quad (5.2.2-4)$$

If iron forms the core and soot forms the coating, then $m_i = 3.07 - 3.55 i$, $m_o = 1.6 - 0.59 i$, and

$$q^3 = f_{v, Fe} / f_{v, soot} \quad (5.2.2-5)$$

If the particles are homogeneous soot particles, then f_v is given by Equation 2.2.1-13.

Equations 5.2.2-3 and either 5.2.2-4 or 5.2.2-5 form a set of two equations with two unknowns: $f_{v, soot}$ and q^3 . Both sets were solved simultaneously for $f_{v, soot}$ and q^3 , using the K_{ext} measurements in the C/O = 0.77 + Fe flame.

Figure 5.2.2-1 compares the soot volume fractions calculated from the K_{ext} measurements in the C/O = 0.77 + Fe flame. The percent iron (by volume) of the solid phase is also shown. Even if all of the iron were in the solid phase, the particles would never be more than about 5% iron by volume. Figure 5.2.2-1 shows that the differences between assuming soot core/iron coating particles and iron core/soot coating particles are small. At short residence times, when the solid phase contains the greatest amount of iron, the soot core/iron coating and iron core/soot coating assumptions yield volume fractions that differ by 17%. As the amount of soot increases, the difference between the two assump-

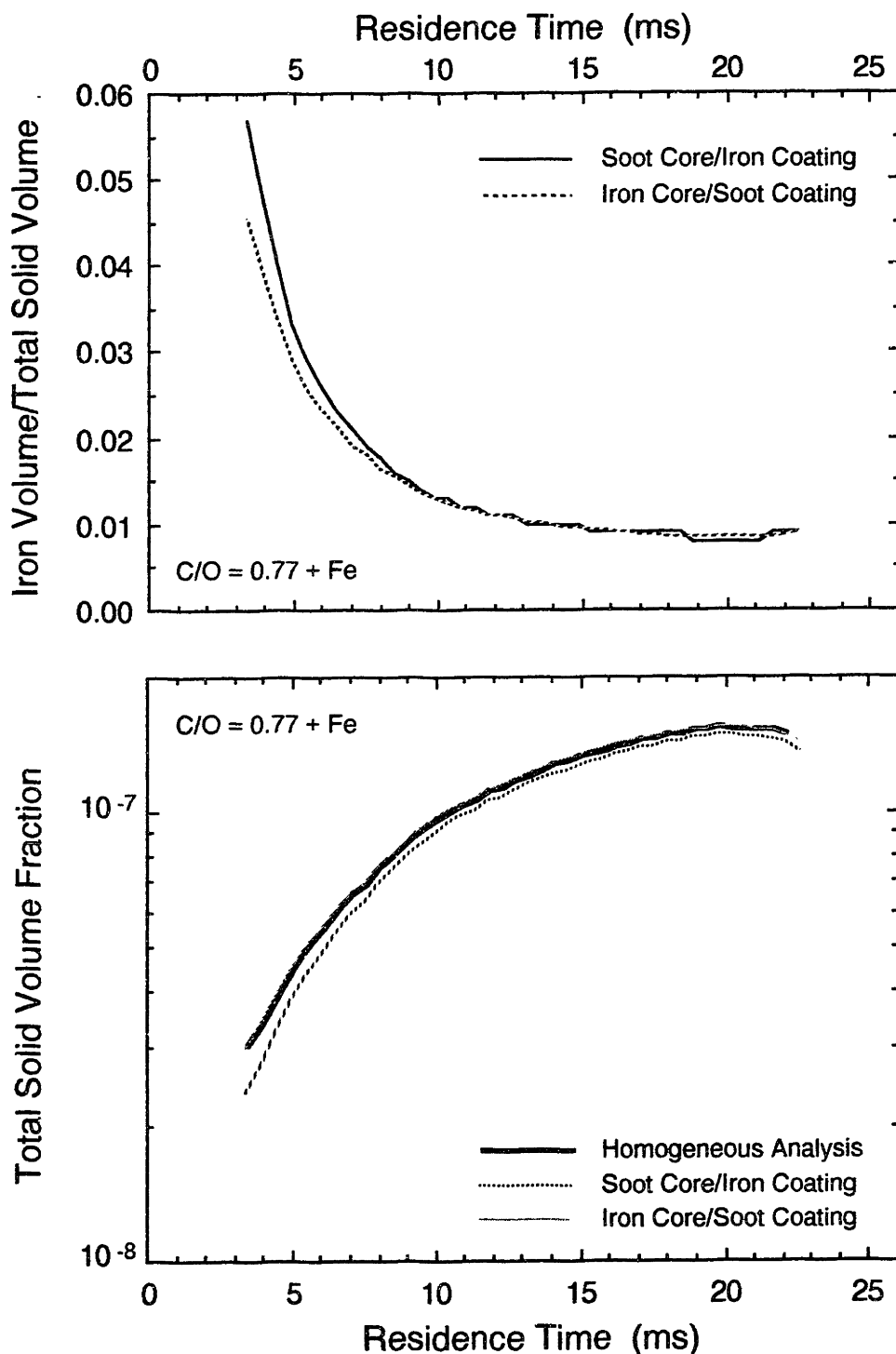


Figure 5.2.2-1: Results of coated sphere analysis of absorption measurements. For these calculations, all of the added iron was presumed to be in the solid metallic phase, in either the core of the particle or the coating, as indicated. These figures show the maximum effect the iron could have on the interpretation of the optical measurements. The difference between the homogeneous analysis (assuming the particles are pure soot) and the coated sphere analysis is negligible.

tions decreases, until the volume fractions differ by only 3% at a residence time of 20 ms. The homogeneous sphere volume fraction falls between the coated sphere volume fractions.

The soot volume fractions in the $C/O = 0.80 + Fe$ and $C/O = 0.83 + Fe$ flames are greater than the soot volume fraction in the $C/O = 0.77 + Fe$ flame (see Section 5.3). Therefore, the percent by volume of iron in the solid phase, and the differences between the two coated sphere models and the homogeneous model, will be smaller in these flames. In addition, these calculations have been performed assuming that all of the iron is in the solid phase. If the amount of iron in the solid phase is smaller (as predicted by the equilibrium calculations in Chapter 6), then the differences between the homogeneous sphere model and the coated sphere models will be smaller. For these reasons, Rayleigh light scattering theory for homogeneous particles is an adequate model for these flames.

5.2.3 The Use of a Volume Weighted Average Refractive Index

The calculations in Section 5.2.2 show that Rayleigh theory for homogeneous spheres is a good approximation to coated sphere theory for these flames, even if all of the added iron is present in the soot particles in the metallic state. In other words, the optical properties of the soot particles are not changed significantly by the presence of a trace amount (5% by volume) of metallic iron. However, situations may arise in which particles contain more than a trace amount of a second component. In these cases, homogeneous Rayleigh theory may be an inadequate description of the scattering and absorption properties of the particles. In addition, the particle structure (which of the two materials is in the core, and which is in the coating) and composition (the relative amount of each material in the particle) may be unknown. For these reasons, a simple graphical technique was developed to determine the sensitivity of optically determined particle sizes and concentrations to uncertainties in the particle structure and composition. The graphical technique uses Figures 2.2.1-3 and 2.2.1-4, which are contour maps of the homogeneous Rayleigh scattering functions $[G(m)/F(m)]^{1/3}$ and $F(m)/[G(m)]^2$.

Consider once more small coated particles with the geometry shown in Figure 2.2.2-1. As in Section 2.2.2, the ratio of the core volume to the overall particle volume will be denoted by q^3 . Several researchers have suggested using \bar{m} , the volume weighted

average refractive index of a coated sphere, as an approximation to m_{eff} , the effective refractive index of a coated sphere (see Section 2.2.2). Figure 5.2.3-1 illustrates the differences between \bar{m} and m_{eff} for coated spheres containing soot, $m = 1.6 - 0.59 i$, and iron, $m = 3.07 - 3.55 i$. Equations 2.2.2-11 and 2.2.2-12 were solved simultaneously to determine m_{eff} , while \bar{m} was calculated from Equation 2.2.2-13. Both iron core/soot coating and soot core/iron coating particles are considered in Figure 5.2.3-1. The curves in Figure 5.2.3-1 are parametrized by q^3 , as indicated.

Figure 5.2.3-1 shows that m_{eff} depends upon the structure of the particle, while \bar{m} is independent of the structure. For example, the imaginary part of the effective refractive index of a particle that is 50% iron and 50% soot is either 1.41 or 2.21, depending upon whether iron or soot is in the core. The real part of the effective refractive index is slightly less sensitive to the particle structure. The real and imaginary parts of both \bar{m} and m_{eff} are strong functions of the particle composition.

Given the refractive indices of the core and coating materials, and the relative amounts of each, two different solutions for m_{eff} can usually be found from the simultaneous solution of Equations 2.2.2-11 and 2.2.2-12. Figure 5.2.3-1 shows the physically realistic solutions for iron/soot particles. The second set of solutions generates a similar figure, but the real part of the effective refractive index is between 0 and 0.6 and the imaginary part of the effective refractive index is between 0.4 and 0.7.

Figure 5.2.3-1 shows that \bar{m} can be a poor approximation of the real and imaginary parts of m_{eff} for particles that contain more than a trace amount of a second component. However, how well the real and imaginary parts of \bar{m} approximate the real and imaginary parts of m_{eff} is not important. In a practical situation, the refractive index will be used to calculate particle diameters and concentrations from measurements of Q_w and K_{ext} . What is important is how well $[G(\bar{m})/F(\bar{m})]^{1/3}$ approximates $[G(m_{eff})/F(m_{eff})]^{1/3}$, and how well $F(\bar{m})/[G(\bar{m})]^2$ approximates $F(m_{eff})/[G(m_{eff})]^2$. As shown in Section 2.2.1, the characteristic particle diameter and the number density determined from scattering and absorption measurements are proportional to these two ratios.

Figure 5.2.3-2 overlays \bar{m} and m_{eff} (for the case of iron/soot particles) on the contour maps of $[G(m)/F(m)]^{1/3}$ and $F(m)/[G(m)]^2$. Even though \bar{m} is a poor approximation for m_{eff} , when substituted into these functions, \bar{m} and m_{eff} yield about the same results.

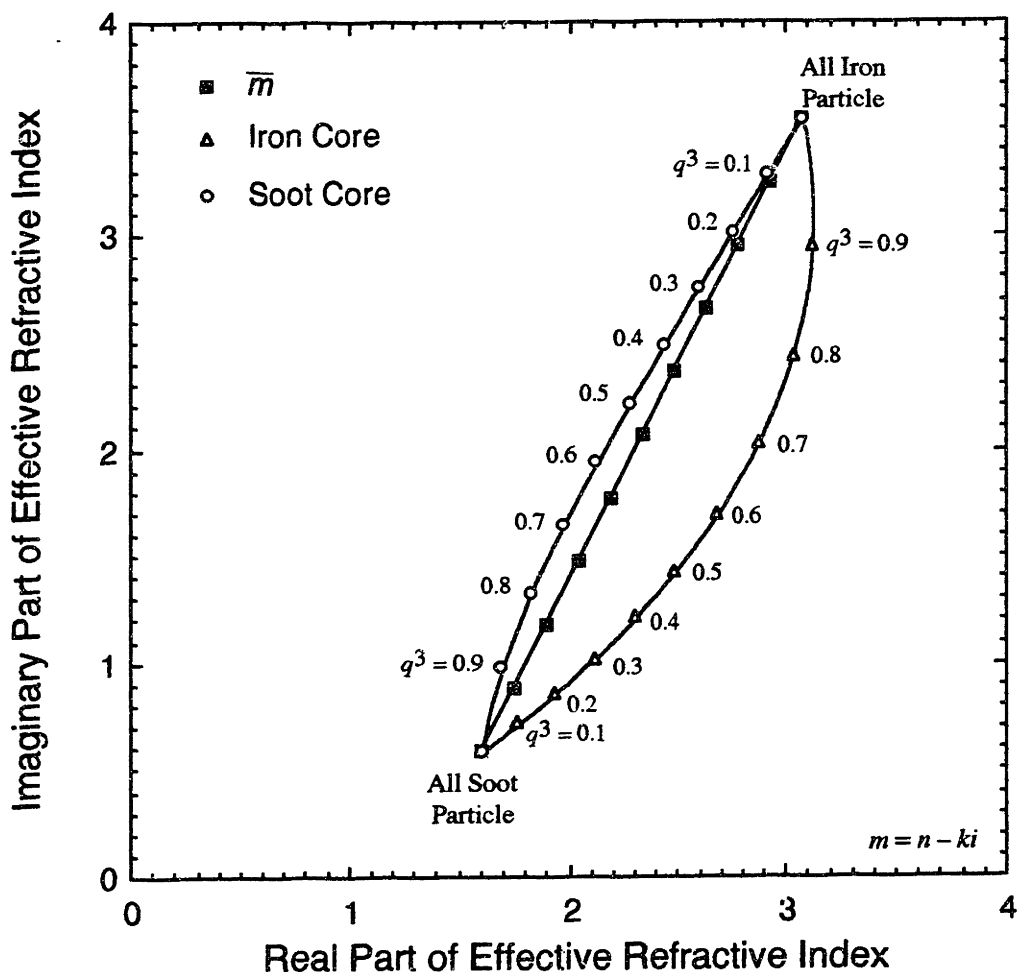


Figure 5.2.3-1: Comparison of \bar{m} and m_{eff} of coated spheres containing iron and soot. The refractive index of soot was taken as $m = 1.6 - 0.59i$, while the refractive index of iron was taken as $m = 3.07 - 3.55i$. The straight line is \bar{m} , with the solid squares indicating 0.1 increments in q^3 , the ratio of the core volume to the total particle volume. The upper curve represents the effective refractive index of particles with a soot core and an iron coating; the lower curve represents the effective refractive index of particles with an iron core and a soot coating. Both curves are parametrized by q^3 , as indicated.

Two observations are immediately apparent from this figure. First, notice that m_{eff} is very sensitive to which of the two materials is in the core, while \bar{m} is not. For example, the imaginary part of the effective refractive index of a particle which is 50% iron and 50% soot is either 1.43 or 2.21, depending upon whether iron or soot is in the core. Second, notice that \bar{m} is a poor approximation to m_{eff} for particles that contain more than a trace amount of the second material. However, as will be shown in Figure 5.2.3-2, when \bar{m} and m_{eff} are substituted into the homogeneous light scattering functions, they give about the same results.

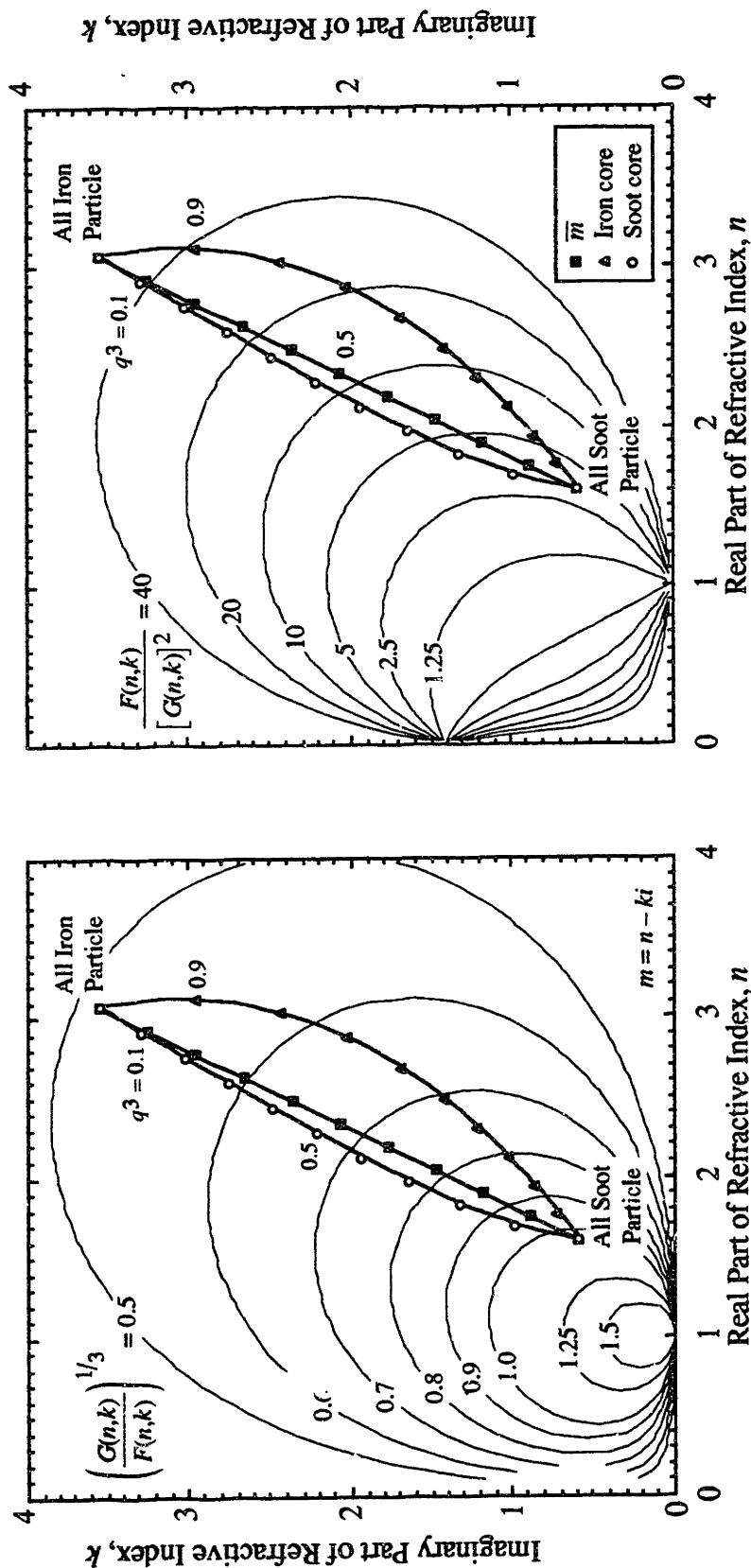


Figure 5.2.3-2: This figure is an overlay of Figure 5.2.3-1 onto Figures 2.2.1-3 and 2.2.1-4. Even though \bar{m} is a poor approximation for m_{eff} , this figure shows that both \bar{m} and m_{eff} give about the same results when substituted into the homogeneous Rayleigh scattering functions. Recall that the characteristic particle diameter determined from scattering and absorption measurements is proportional to $[G(m)/F(m)]^{1/3}$, and the particle number density is proportional to $F(m)/[G(m)]^2$ in the Rayleigh size regime. This figure shows that \bar{m} can be used to approximate m_{eff} in light scattering calculations. This figure also shows that knowledge of the relative amounts of each material in the particle is more important than knowledge of which material is in the core and which is in the coating.

Therefore, \bar{m} can be used in place of m_{eff} to calculate particle diameters and concentrations. This figure also shows that knowledge of the relative amounts of each material within the particle is much more important than knowledge of the particle structure.

The utility of Figures 2.2.1-3 and 2.2.1-4 for determining the sensitivity of optically determined sizes and concentrations to changes in the particle composition is now clear. By simply locating the refractive indices of the core and coating materials on these figures, and connecting the two points with a straight line, the lever rule can be used to locate \bar{m} . The values of $[G(\bar{m})/F(\bar{m})]^{1/3}$ and $F(\bar{m})/[G(\bar{m})]^2$ can be read directly from the figures, and are good approximations for $[G(m_{eff})/F(m_{eff})]^{1/3}$ and $F(m_{eff})/[G(m_{eff})]^2$. If the composition of the particle is uncertain, then Figures 2.2.1-3 and 2.2.1-4 allow for the quick estimation of the error introduced into the calculated diameter and concentration.

5.2.4 Comparison of Spheroid Theory and Particle Shape Data

To compare the depolarization ratio measurements to the particle shape measurements presented in Section 4.9, the soot particles were modeled as oblate and prolate spheroids. For both models the maximal chord length, L_m , was taken as the length of the major axis, and the breadth B was taken as the length of the minor axis. The volume and eccentricity of each particle were then calculated from Equations 2.2.3-1 and 2.2.3-2, respectively. The depolarization ratio of the soot aerosol was calculated according to Equations 2.2.3-3 through 2.2.3-12. For the sample withdrawn 12.5 mm above the burner (residence time = 12.6 ms), the prolate spheroid model yielded $\rho_v = 0.00483$, while for the 17.5 mm sample (residence time = 17.1 ms), the prolate spheroid model yielded $\rho_v = 0.00822$. The calculated ρ_v increases with increasing residence time because, as shown in Section 4.9, the thermophoretic probe shape measurements indicate the particles are becoming less spherical with time. The oblate spheroid model yielded depolarization ratios that were about 3% smaller than the prolate spheroid model depolarization ratios.

The oblate and prolate spheroid models are only approximations of the true particle shape (see Figure 4.9-1). Modeling the particles as polydisperse fractal aggregates containing spheres of a nearly uniform diameter might be a better approach. Dobbins and Megaridis (1990) have discussed methods of calculating the optical properties of such

materials. However, their technique requires the number of primary particles within an aggregate, and this quantity could not be determined from the TEM negatives with any degree of certainty. Identification of the individual particles within an aggregate was highly subjective. Simple tests were conducted, in which different observers were asked to count the number of individual spheres within an aggregate. For a given aggregate, different observers produced estimates of the number of individual spheres that differed by as much as a factor of 2. For this reason, a fractal analysis was not attempted.

Figure 5.2.4-1 compares the depolarization ratios measured in the $C/O = 0.77$ flame to the depolarization ratios calculated from the particle shape measurements. The agreement between the calculations and the measurements is encouraging. However, the optically measured ρ_v is always decreasing, while the calculated ρ_v is increasing.

If the oblate and prolate spheroid model depolarization ratios had been much larger than the optically measured ρ_v , then that would have indicated the agglomerates seen in the TEM negatives do not exist *in situ*. However, the ρ_v of the particles in the TEM pictures is about the same as or less than the optically measured ρ_v , so the possibility that these agglomerates exist *in situ* cannot be excluded. An *in situ* ρ_v higher than the ρ_v calculated from the TEM pictures can be attributed to optical anisotropy of the soot. The fundamental questions posed in Section 4.9 remain unanswered: Are the thermophoretic probe size and shape measurements representative of the *in situ* particles, or are they affected by sampling? Do the agglomerates seen in the TEM pictures exist *in situ*, or do the particles exist as spheres in the flame? Until these questions are answered, the degree to which the depolarization of the scattered light is due to geometrical and/or optical anisotropy will remain unknown.

5.3 Soot Volume Fraction

As demonstrated in Section 5.2, Rayleigh light scattering theory for homogeneous, spherical particles can be used to interpret the optical measurements presented in Chapter 4. Therefore, Equation 2.2.1-13 was used to calculate f_v from the measurements of K_{ext} in each flame. The refractive index of soot was taken as $m = 1.6 - 0.59i$ (see Section 2.4). Residence times were calculated as described in Section 5.1.

Soot volume fraction profiles in the $C/O = 0.74$ and $C/O = 0.77$ flames, both with

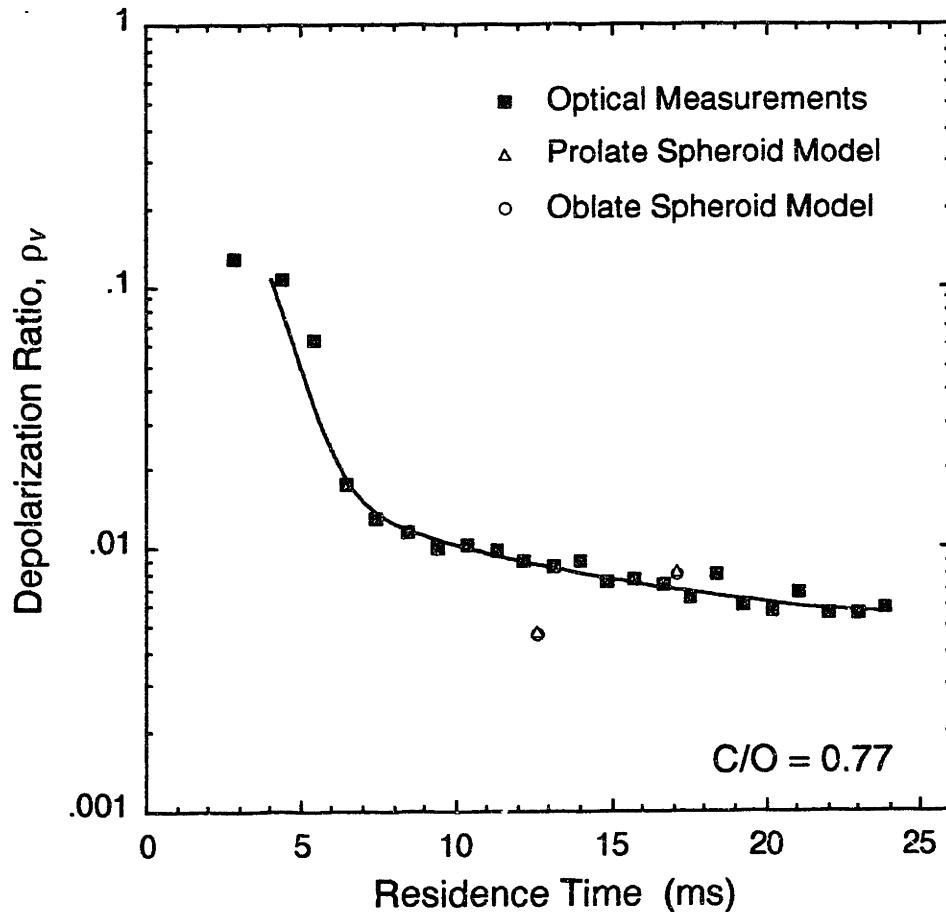


Figure 5.2.4-1: Comparison of the optically measured depolarization ratio and the depolarization ratio calculated from the thermophoretic sampling probe shape measurements. The soot particles were modeled as oblate and prolate spheroids. The measured maximal chord length was taken as the length of the major axis, and the measured breadth was taken as the length of the minor axis.

and without additives, are shown in Figure 5.3-1. Volume fraction profiles in the $C/O = 0.80$ and $C/O = 0.83$ flames, both with and without additives, are shown in Figure 5.3-2. The range of soot volume fractions spans almost 2 orders of magnitude, from about 1.5×10^{-8} at 5 ms in the $C/O = 0.74$ flame, to about 9×10^{-6} in the $C/O = 0.83 + \text{Fe}$ flame.

Perhaps the most noticeable feature in these figures is that the iron and manganese additives increased the soot volume fraction in every flame. Iron always increased the soot volume fraction more than the manganese additive. Initially, the volume fraction in each flame with an additive is about the same as the volume fraction in the corresponding flame without an additive. However, the volume fraction curves diverge with increasing residence time. In the $C/O = 0.74$ flame, the manganese additive ultimately increased f_v by about 50%, while the iron additive increased f_v by about 300%. The relative amount of the increase in the volume fraction decreased with increasing C/O ratio. In the $C/O = 0.83$ flame, the iron additive ultimately increased f_v by about 96%.

Since the volume fractions are initially the same but diverge with increasing residence time, soot mass growth rates are greater in flames with additives than in flames without additives. The derivatives of the f_v curves were used to calculate the soot mass growth rate in each flame. Soot mass growth rates are presented in Section 5.7.

Given that these metals reduce soot emissions from practical systems, the increase in f_v caused by the additives is surprising. One explanation for the increase in the amount of soot is that these metals catalyze the decomposition of acetylene to form amorphous carbon (soot). Many workers (e.g., Baker, 1979) have observed that transition metals can catalyze the decomposition of acetylene into different forms of carbon. As will be shown in Chapter 6, equilibrium predicts the iron additive is continuously precipitating out of the gas phase as metallic iron. The continuous precipitation of the iron could then create sites at which acetylene decomposition is catalyzed. A model which uses this hypothesis to explain the increase in soot volume fraction is presented in Chapter 7.

An explanation for the decrease in soot emissions seen in practical systems is that these metals, once incorporated into the soot particles, can catalyze soot burnout. Transition metals are well known to be carbon oxidation catalysts (e.g., McKee, 1980; also see Section 2.5.4). In practical systems in which these additives are used as soot-re-

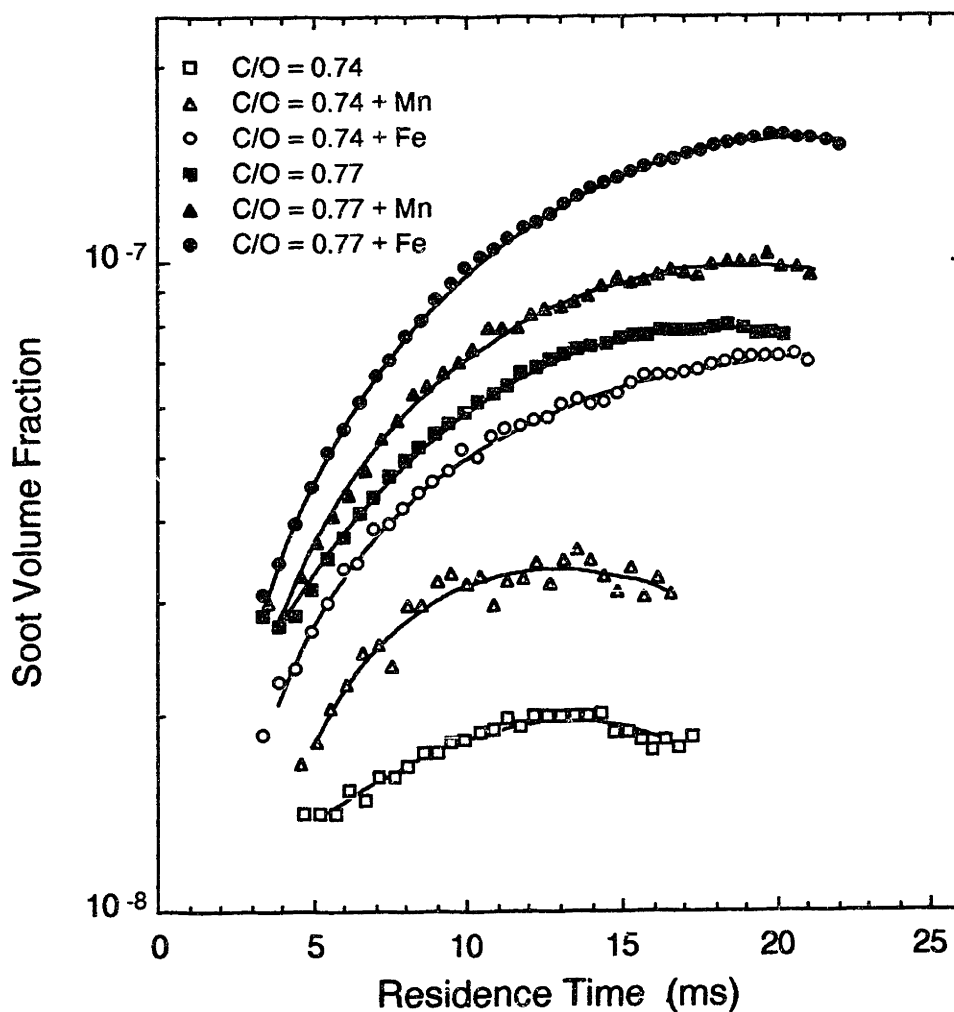


Figure 5.3-1: Soot volume fraction profiles in the $C/O = 0.74$ and $C/O = 0.77$ flames, both with and without additives. The additives increased the soot volume fraction in all of the flames. The iron additive increased the soot volume fraction more than the manganese additive.

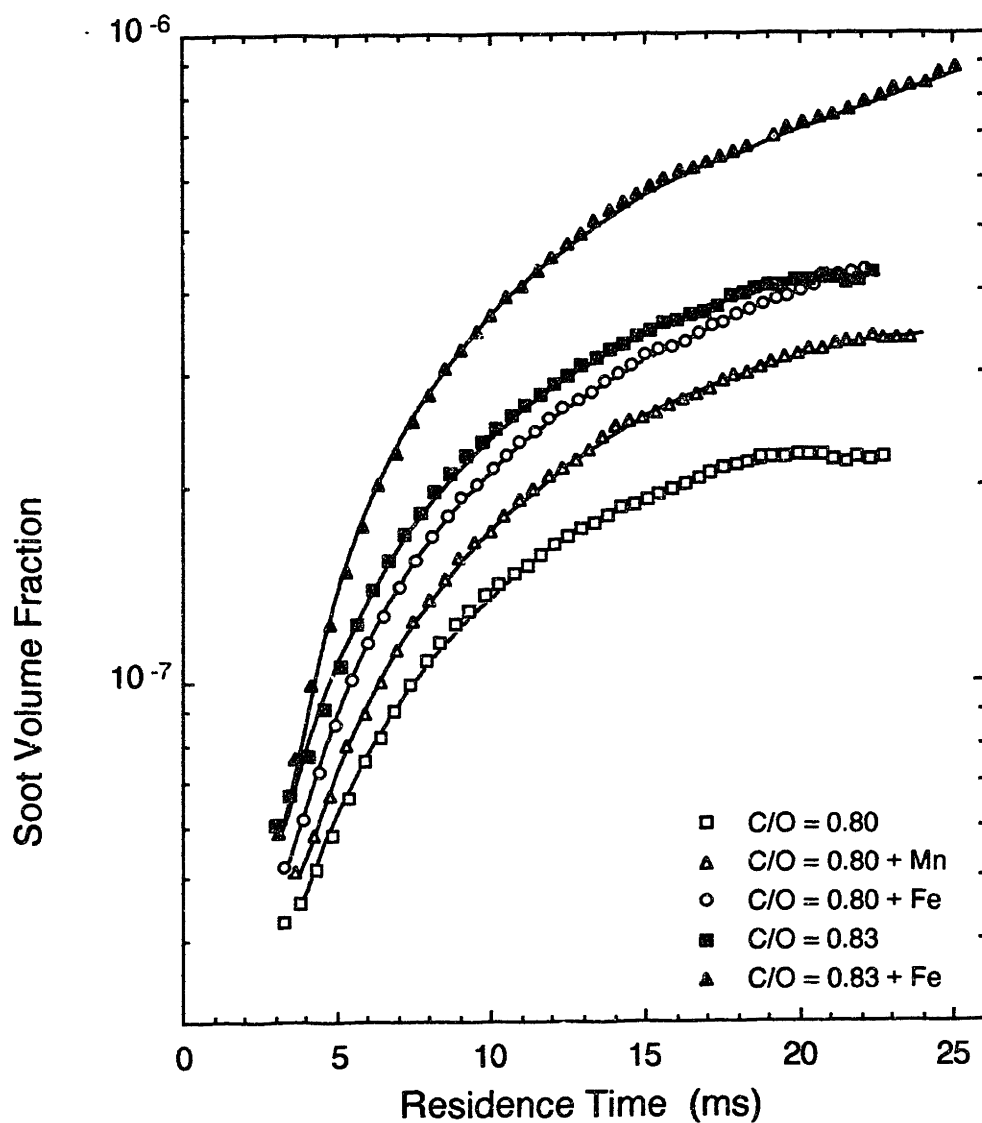


Figure 5.3-2: Soot volume fraction profiles in the C/O = 0.80 and C/O = 0.83 flames, both with and without additives.

ducing agents, the metals may initially increase the amount of soot, but then greatly increase the rate of soot burnout. If this hypothesis is correct, then the most effective method of using these metals might be to add them to a combustor after soot growth is complete, but before soot burnout has occurred. This type of scheme could be used, for example, in a staged combustor.

5.4 Geometric Mean Soot Particle Diameter

The scattering and absorption measurements presented in Sections 4.2 and 4.3 were used to calculate the geometric mean soot particle diameters (d_g) shown in Figures 5.4-1 and 5.4-2. Equation 2.2.1-11 (representing Rayleigh scattering theory for homogeneous spheres) was used to calculate d_g , with $m = 1.6 - 0.59 i$ and $\sigma_g = 0.28515$ ($f_N = 2.0788$). The geometric mean particle diameter is initially about 2 nm in all of the flames, and increases linearly with increasing residence time. The increase in particle diameter is due to both mass growth, as shown in Section 5.4, and particle collisions (see Section 5.5).

The metal additives increased the geometric mean particle diameters in all of the flames. The soot particle diameters in flames with additives are initially about the same as the diameters in the corresponding flames without an additive. However, in flames with additives the diameter increases more rapidly than in flames without additives. For example, in the $C/O = 0.80$ flame, $d_g = 33$ nm at $t = 17$ ms; the manganese additive increased d_g to 39 nm at 17 ms, and the iron additive increased d_g to 48 nm at 17 ms. The increase in diameter caused by the additive is entirely due to the increase in the soot volume fraction. As will be shown in Section 5.5, the additives had no effect on the soot particle number density.

Figure 5.4-3 compares the geometric mean particle diameter determined by the thermophoretic probe measurements (see Section 4.9) and the optical measurements. The agreement between the two techniques is encouraging. The thermophoretic probe d_g brackets the optical d_g , and differs from the optical d_g by no more than 30%. However, the thermophoretic probe measurements indicate d_g is essentially constant, while the optical measurements predict quite different behavior. Part of the difference may be attributed to the (comparatively) low spatial resolution of the thermophoretic probe. The optical measurements are non-invasive *in situ* measurements, while the quench time of

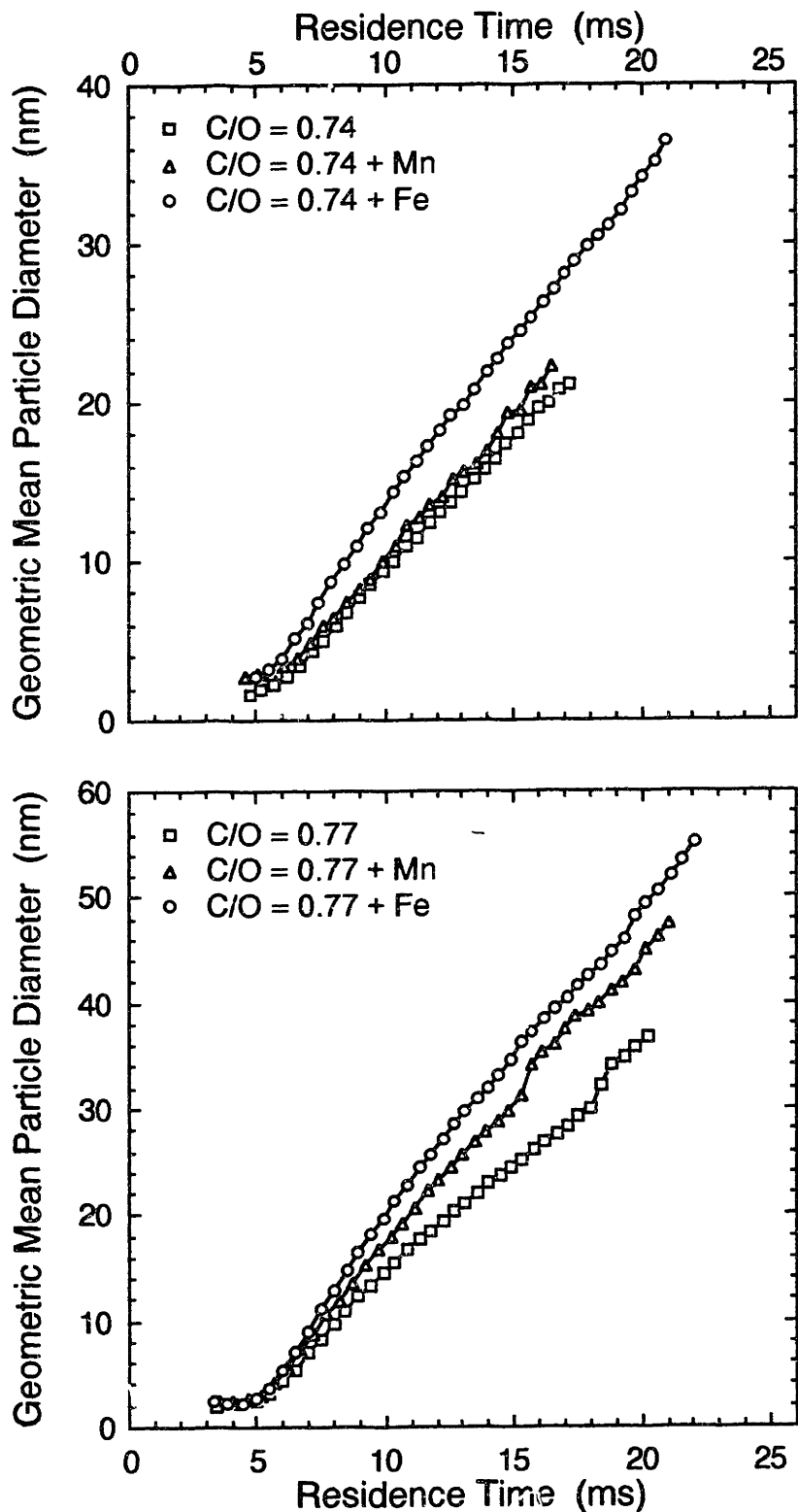


Figure 5.4-1: Optically determined particle diameters in the C/O = 0.74 and C/O = 0.77 flames, both with and without additives.

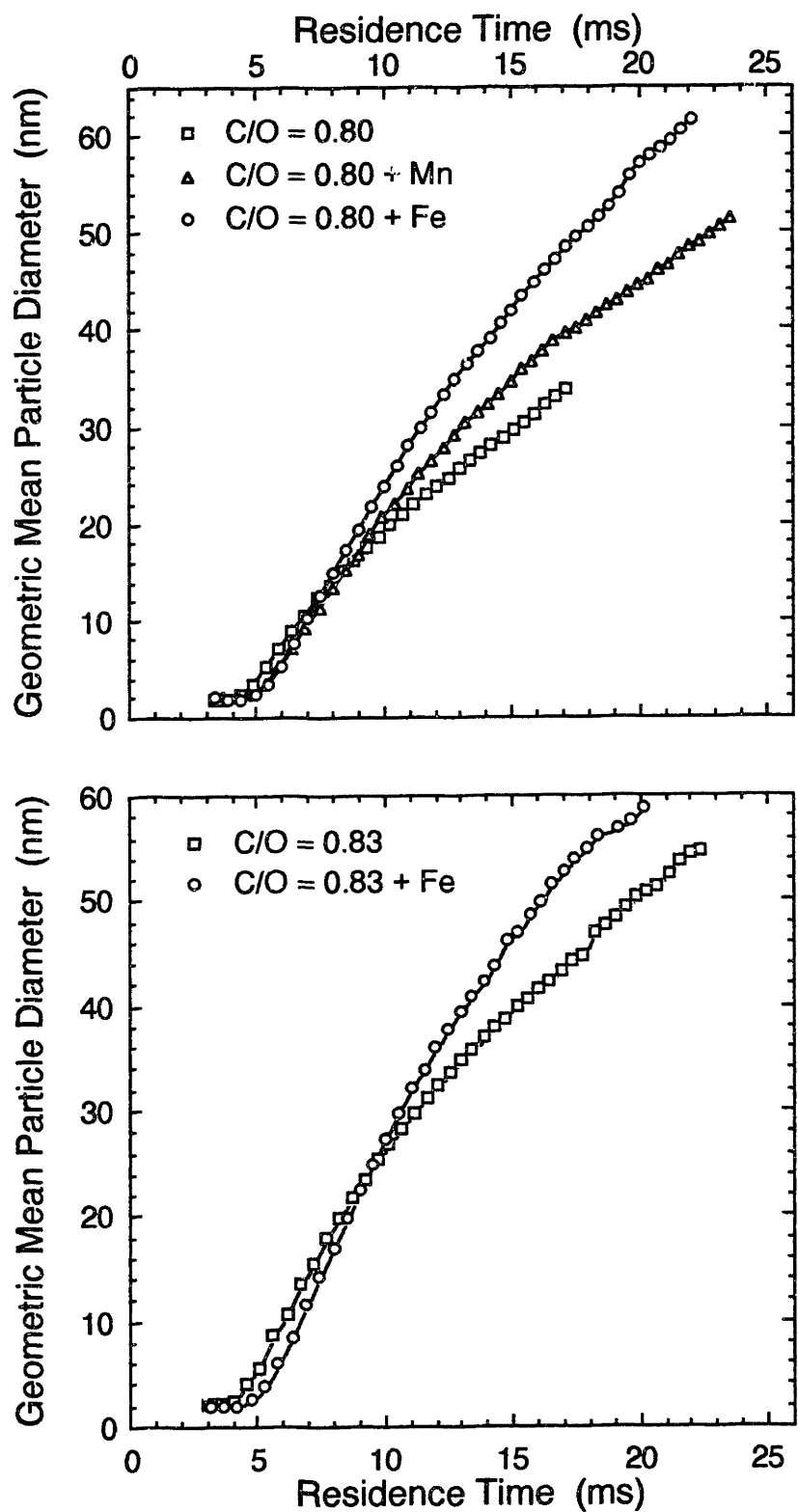


Figure 5.4-2: Optically determined particle diameters in the C/O = 0.80 and C/O = 0.83 flames, both with and without additives.

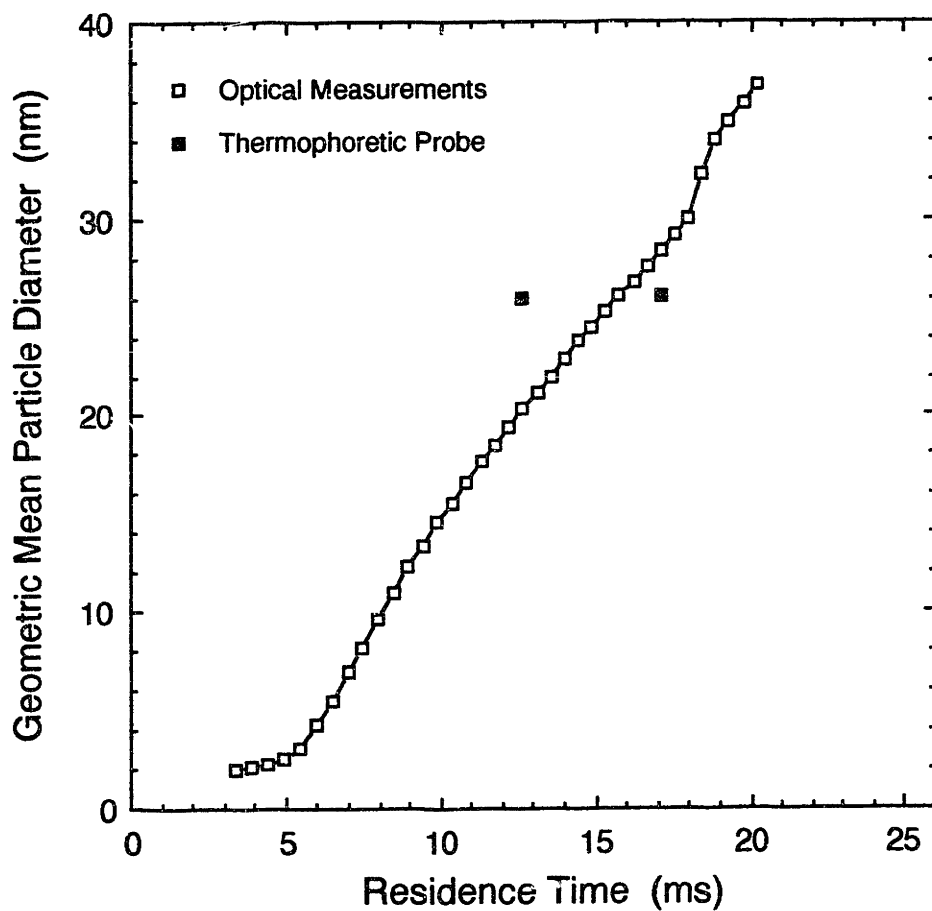


Figure 5.4-3: Comparison of geometric mean particle diameters in the $C/O = 0.77$ flame, as determined by optical measurements and thermophoretic probing and image analysis. The agreement between the two techniques is encouraging.

the thermophoretic probe was approximately 4 ms (see Section 3.5). The visible diameter of the TEM grid itself was 1.5 mm, corresponding to about a 1.5 ms range of residence times. These two factors, combined with positioning errors, may account for some of the differences between the two techniques. Flow disturbances introduced by the motion of the probe may also limit the spatial resolution.

Another possible reason for the differences between the two techniques is that they measure different properties of the particles. Recall that soot particles are not perfect spheres. The thermophoretic probe and subsequent image analysis measured the projected area diameter, d_a (see Section 2.1). In contrast, the light scattering measurements yield an “effective optical diameter,” that is, the diameter of the sphere that scatters the same as the irregularly shaped particle of the same volume. An irregularly shaped small particle absorbs the same but scatters more light than the sphere of the same volume.

5.5 Soot Particle Number Density

Soot particle number densities were calculated from measurements of Q_w and K_{ext} using Equation 2.2.1-9, with $m = 1.6 - 0.59 i$ and $f_N = 2.0788$. Profiles of N in flames with and without additives are shown in Figures 5.5-1 and 5.5-2. The initial number density is high, about 10^{13} particles/cm³ at a residence time of 5 ms, and decreases with increasing residence time. By about 20 ms, the number density has decreased by about 3 orders of magnitude, to less than 10^{10} particles/cm³.

The number density measurements were fit to free-molecule coagulation theory using Equation 2.5.2-4. As shown in Section 2.5.2, a plot of $N^{-5/6}$ versus the integral in Equation 2.5.2-4 should be a straight line, with slope m_{th} given by Equation 2.5.2-5. Taking $\alpha_{sp} = 6.554$, as estimated by Graham and Robinson (1976), and the density of soot as $\rho = 1.8$ g/cm³, Equation 2.5.2-5 gives

$$m_{th} = 4.614 \times 10^{-11} \text{ cm}^{5/2} \text{ K}^{-1/2} \text{ ms}^{-1} \quad (5.5-1)$$

Figure 5.5-3 plots $N^{-5/6}$ versus the integral in Equation 2.5.2-4, using the measurements from the C/O = 0.83 flame. The fit to coagulation theory is very good ($R^2 = 0.993$), but the slope of the best-fit line is 4 times greater than m_{th} . As discussed in Section 2.5.2, a slope greater than m_{th} can be attributed to an increase in the coagulation rate caused by interparticle van der Waals forces.

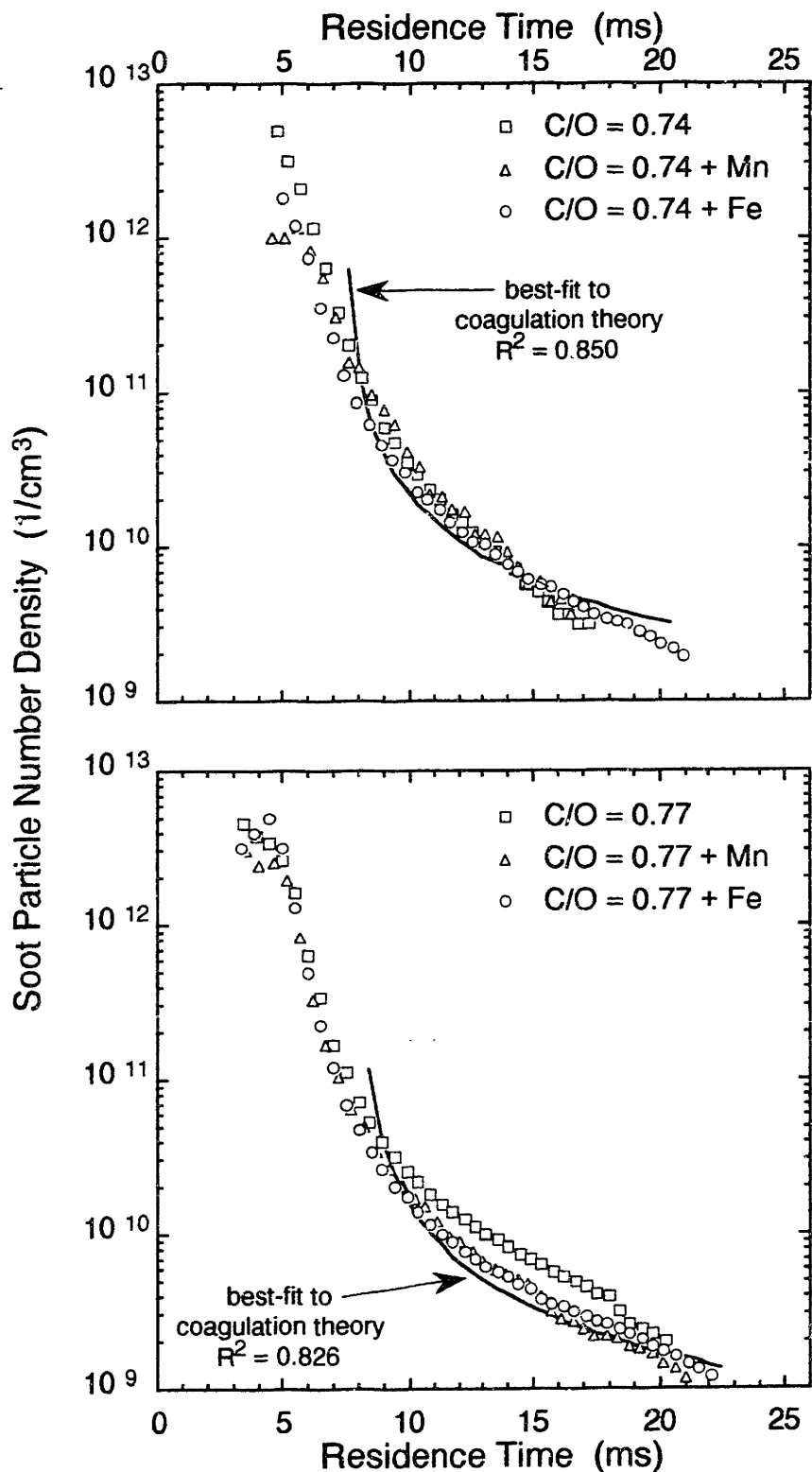


Figure 5.5-1: Soot particle number density profiles in the C/O = 0.74 and C/O = 0.77 flames, both with and without additives. The best-fits to coagulation theory are also shown.

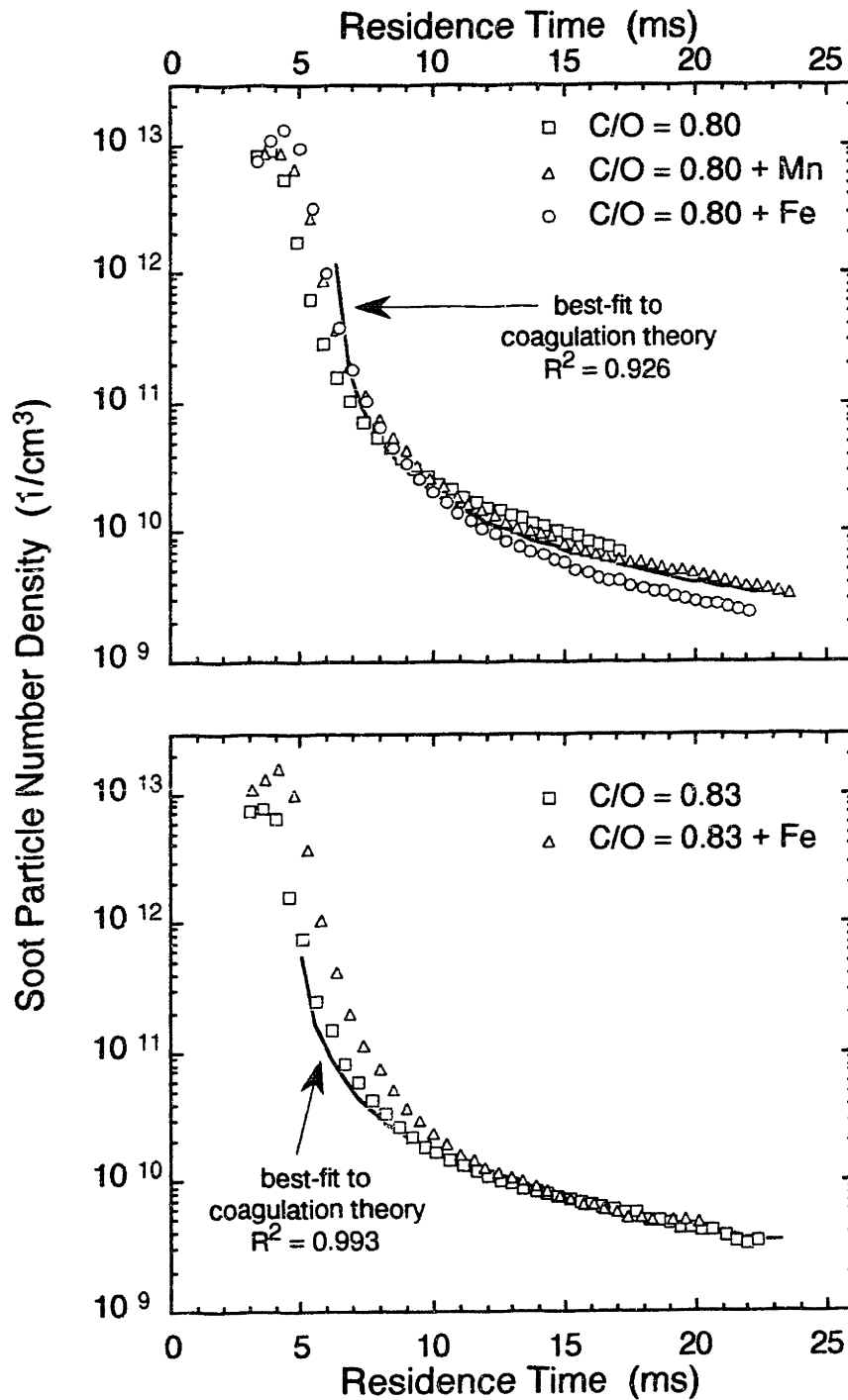


Figure 5.5-2: Soot particle number density profiles in the C/O = 0.80 and C/O = 0.83 flames, both with and without additives. The best-fits to coagulation theory are also shown.

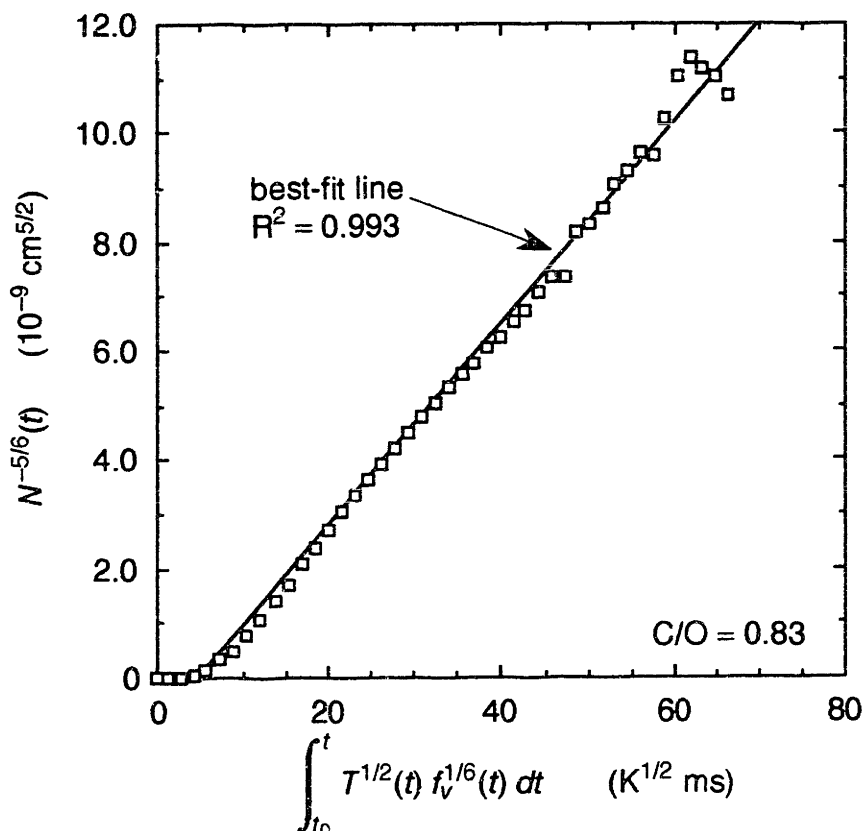


Figure 5.5-3: Demonstration of the method used to determine the best-fit of number density measurements to free-molecule coagulation theory. Shown here is the best-fit of the C/O = 0.83 flame measurements. The integration starts from residence time $t_0 = 3.0$ ms. The slope of the best-fit line shown in this figure is

$$\text{slope} = 1.846 \times 10^{-10} \text{ cm}^{5/2} \text{ K}^{-1/2} \text{ ms}^{-1} = 4.00 m_{th}$$

where m_{th} is given by Equation 2.5.2-5, and was calculated assuming the density of soot was 1.8 g/cm^3 .

Flame(s)	Slope of best-fit line
C/O = 0.74, 0.74 + Mn, and 0.74 + Fe	9.30 m_{th}
C/O = 0.77, 0.77 + Mn, and 0.77 + Fe	13.7 m_{th}
C/O = 0.80, 0.80 + Mn, and 0.80 + Fe	5.05 m_{th}
C/O = 0.83	4.00 m_{th}
C/O = 0.83 + Fe	3.81 m_{th}

Table 5.5-1: Results of coagulation theory best-fit calculations. The last two entries in this table show that the iron additive did not have a significant effect on the best-fit slope. For this reason, the number density measurements from flames with the same C/O ratio were combined and fit to coagulation theory as a group, as indicated in the table.

At short residence times, Figure 5.5-3 shows the fit to coagulation theory is poor. The slope of a smooth curve through the data is less than the slope of the best-fit line, indicating the coagulation rate is lower than expected. One could attempt to attribute the difference between the measurements and theory as an indication of the time required for the self-preserving size distribution to develop. However, as shown in Section 2.5.2, even if the size distribution were monodisperse, the slope of the line would decrease by only 14% (α_{sp} decreases from 6.554 to 5.657). A more plausible explanation is that particle inception is still taking place, and that the change in particle number density is not governed solely by particle collisions and coagulation.

The slopes of the best-fits to coagulation theory for other flames are given in Table 5.5-1. The slopes are expressed as multiples of m_{th} . The last two entries in Table 5.5-1 show that the iron additive had no effect on the coagulation rate. For this reason, the measurements from flames with the same C/O ratio were combined and fit to coagulation theory as a group. The best-fits were then used to calculate the solid lines shown in Figures 5.5-1 and 5.5-2. There is a general decrease in the slope of the best-fit line with increasing C/O ratio (from 9.30 m_{th} in the C/O = 0.74 flames to 3.81 m_{th} in the C/O = 0.83 + Fe flame). The decrease in slope is consistent with an expected decrease in interparticle van der Waals forces as the soot particle diameter increases (Harris and Kennedy, 1988). The geometric mean particle diameter increases with increasing C/O ratio (see Section 5.4).

The results in this section show that the iron and manganese additives had no effect on particle collision and particle inception rates. The initial number density in each flame containing an additive is about the same as the initial number density in the flame of the same C/O ratio without an additive. Therefore, the charge transfer reaction mechanism, proposed by Haynes *et al.* (1979) for alkaline earth metal additives (see Section 2.6.2), does not apply to iron and manganese additives. No evidence has been found to support the hypothesis made by Ritrievi (1984) that iron can increase particle inception.

5.6 Soot Particle Surface Area per Unit Volume

Profiles of the soot particle surface area per unit volume (S) are shown in Figures 5.6-1 and 5.6-2. As in Section 5.3, 5.4, and 5.5, the soot particle surface area was calcu-

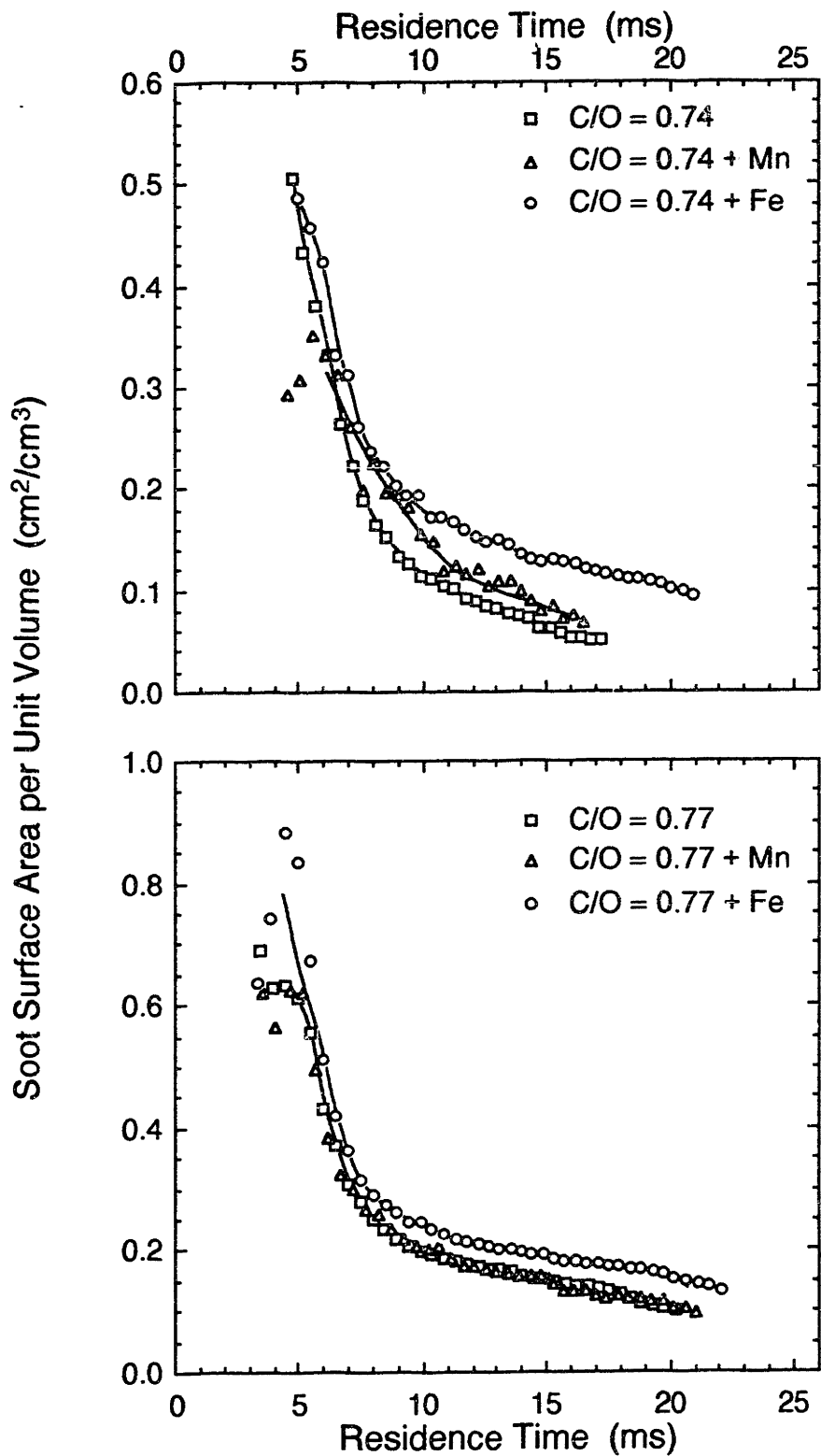


Figure 5.6-1: Soot surface area per unit volume in the C/O = 0.74 and C/O = 0.77 flames, both with and without additives.

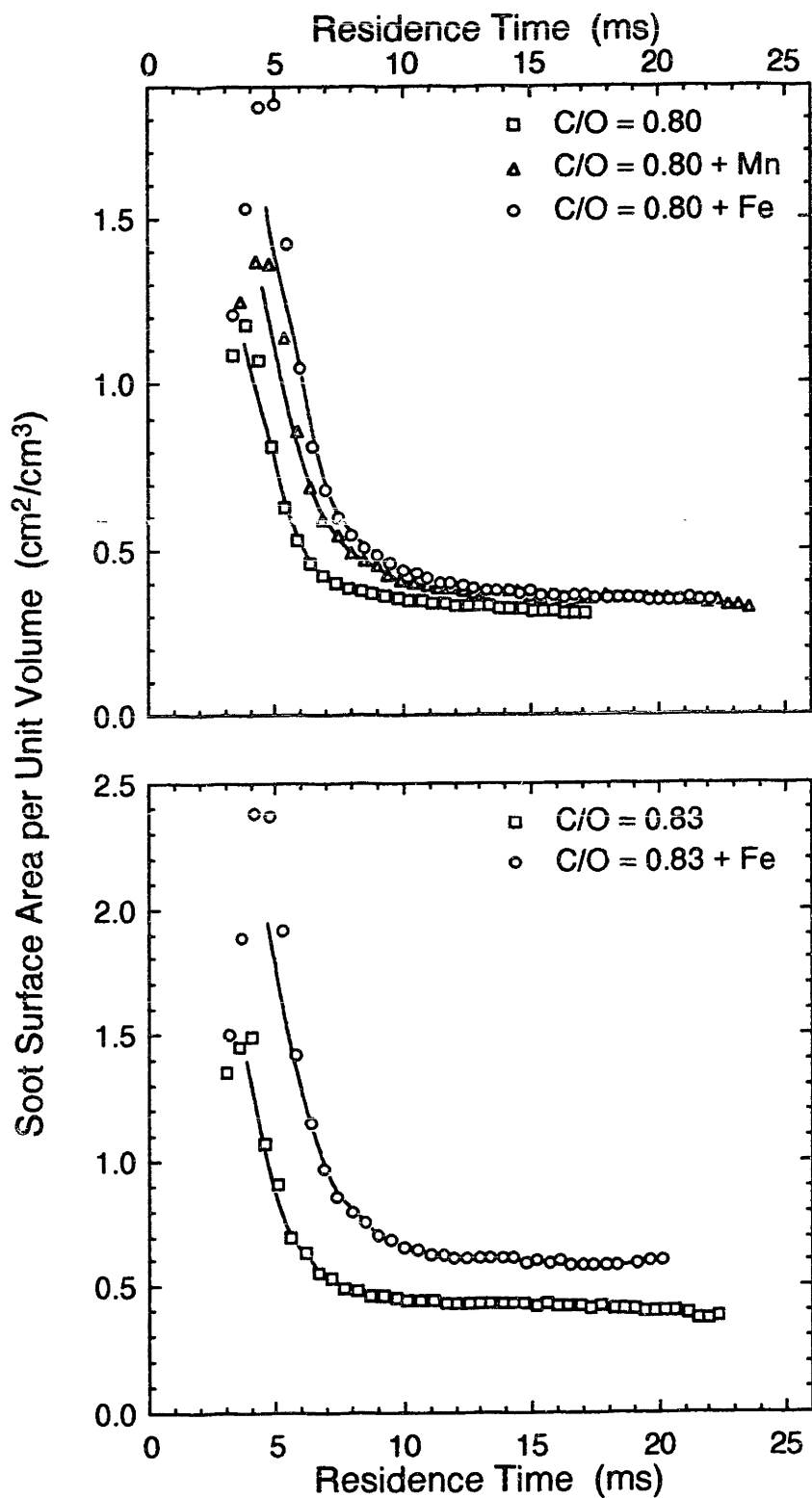


Figure 5.6-2: Soot surface area per unit volume in the C/O = 0.80 and C/O = 0.83 flames, both with and without additives.

lated from Q_{vw} and K_{ext} measurements using Rayleigh light scattering theory for homogeneous spheres (see Equation 2.2.1-15) and assuming $m = 1.6 - 0.59i$ and $\sigma_g = 0.28515$ ($f_N = 2.0788$).

The profiles of S in all of the flames are very similar. Initially, S decreases rapidly, but after about 10 ms S remains approximately constant. Harris and Weiner (1983(a), 1983(b)), in their studies of premixed ethylene flames, also observed that S is approximately constant at residence times greater than 10 ms. The increase in d and the decrease in N with increasing residence time tend to cancel each other, rendering S approximately constant.

The surface areas presented in Figures 5.6-1 and 5.6-2 are calculated from the optical measurements assuming the particles are nonporous spheres. Du (1990) has recently presented measurements that suggest soot particles may be microporous. If the micropores are accessible to the surface growth species, then the nonporous sphere surface area may be a poor approximation to the true surface area. However, there is not enough data to incorporate this suggestion into soot growth models, and the hard sphere surface area will be used here. Additional investigations of the *in situ* porosity of soot would be very useful.

5.7 Soot Mass Addition Rate

The net soot mass addition rate (or net mass growth rate), dm_{soot}/dt , is given by

$$\frac{dm_{soot}}{dt} = \rho_{soot} \frac{df_v}{dt} \quad (5.7-1)$$

Net soot mass addition rates were calculated by numerical differentiation of the volume fraction data shown in Figures 5.3-1 and 5.3-2. This rate is a net rate because pyrolysis and dehydrogenation reactions remove mass while surface growth is adding mass.

Since differentiation is a noise-inducing operation, the derivatives were smoothed using the numerical method of Savitzky and Golay (1964). A sliding 7-point quadratic convolution simultaneously smoothed and differentiated the volume fraction data. The density of soot was assumed to be 1.8 g/cm^3 .

Mass addition rates in the $C/O = 0.74$ and $C/O = 0.77$ flames, both with and without additives, are shown in Figure 5.7-1. Figure 5.7-2 shows the mass addition rates in the

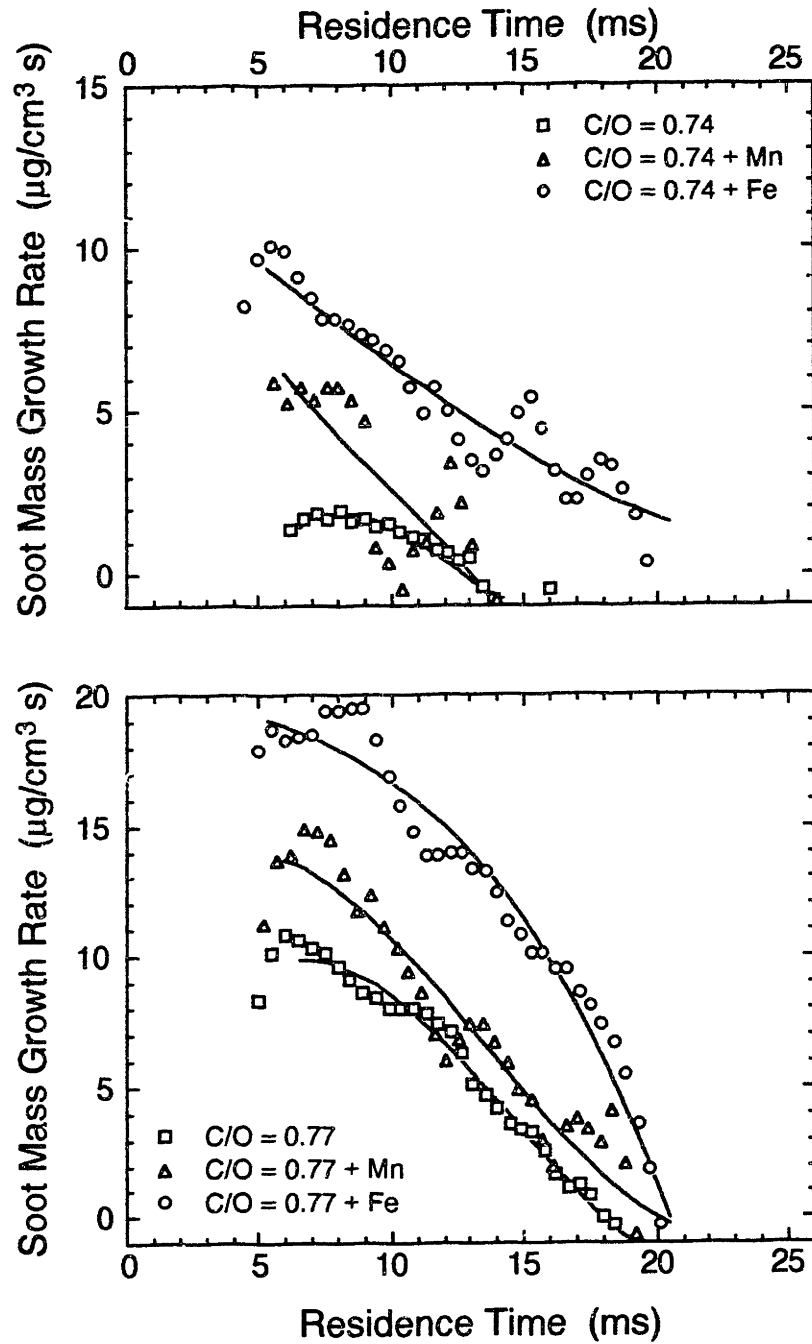


Figure 5.7-1: Soot mass addition rates in the C/O = 0.74 and C/O = 0.77 flames, both with and without additives.

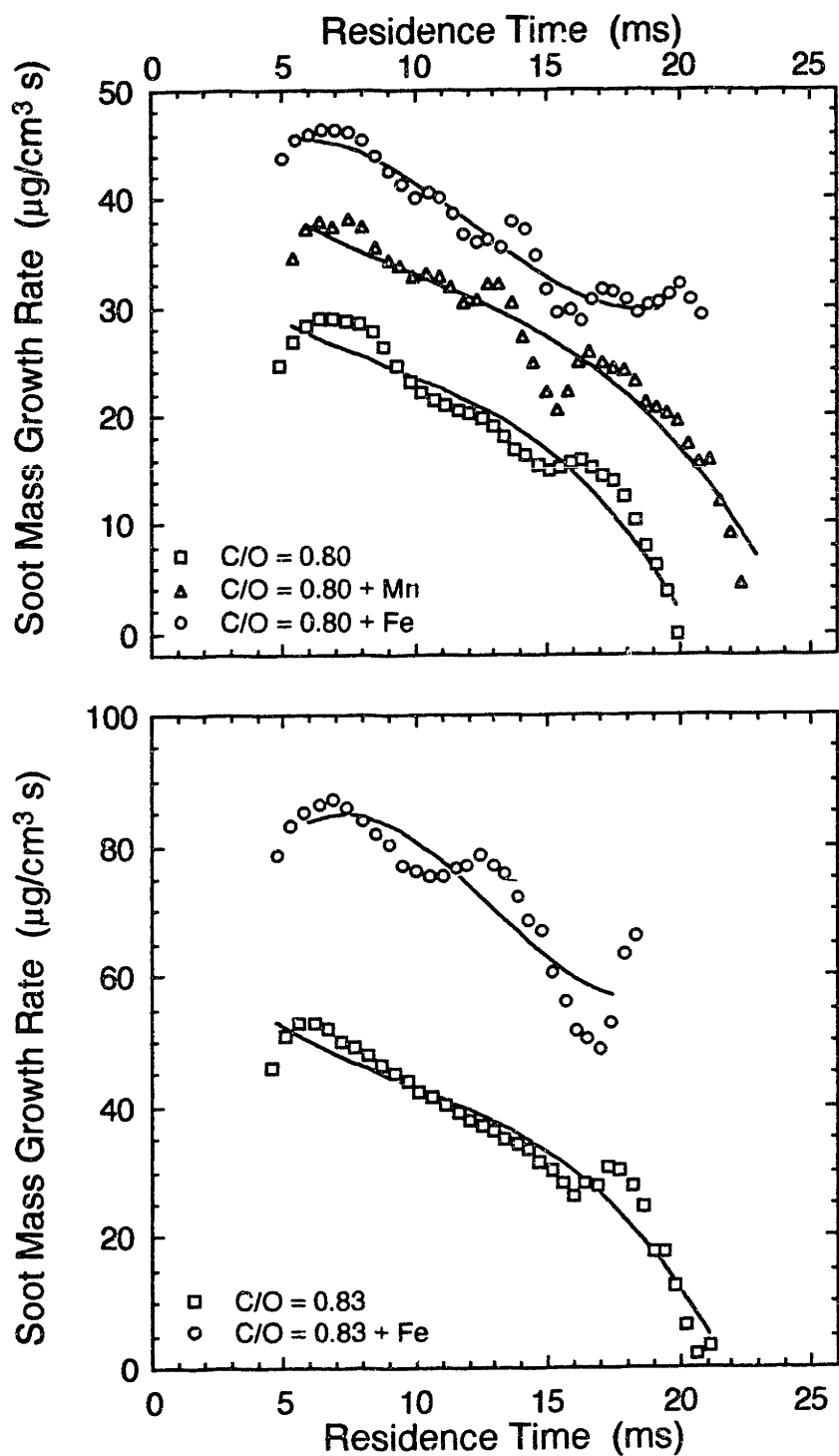


Figure 5.7-2: Soot mass addition rates in the C/O = 0.80 and C/O = 0.83 flames, both with and without additives.

$C/O = 0.80$ and $C/O = 0.83$ flames, both with and without additives. Perhaps the most striking feature in these figures is the rapidly decreasing soot mass growth rate in the flames without additives. In all of the flames without additives the soot mass growth rate decreases to zero (within the precision of the measurements). In the $C/O = 0.74$ flame, the mass addition rate is barely above the measurement limit at $2 \mu\text{g}/\text{cm}^3 \text{ s}$, and then decreases to zero by about 14 ms. As the C/O ratio increases the mass addition rate increases, but dm_{soot}/dt still decreases to zero, although more time is required. In the $C/O = 0.83$ flame, the mass addition rate is initially $50 \mu\text{g}/\text{cm}^3 \text{ s}$, but dm_{soot}/dt decreases to zero by about 22 ms. As shown in Section 2.5.3, the decrease in the soot mass growth rate in premixed flames has been observed by many researchers. Haynes and Wagner (1982) have empirically correlated soot growth rates, and Harris and Weiner (1983(a), 1983(b)) and Woods (1988) have proposed mechanistic explanations of the decrease in the soot particle growth rate.

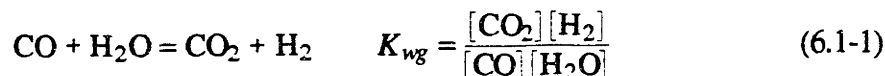
Both the iron additive and the manganese additive increased the soot mass addition rate. The iron additive increased the soot growth rate more than the manganese additive. The initial growth rate increased from about $2 \mu\text{g}/\text{cm}^3 \text{ s}$ in the $C/O = 0.74$ flame to about $5 \mu\text{g}/\text{cm}^3 \text{ s}$ in the $C/O = 0.74 + \text{Mn}$ flame, and about $10 \mu\text{g}/\text{cm}^3 \text{ s}$ in the $C/O = 0.74 + \text{Fe}$ flame. In the $C/O = 0.80$ flame, the initial soot mass growth rate of $28 \mu\text{g}/\text{cm}^3 \text{ s}$ was increased to $37 \mu\text{g}/\text{cm}^3 \text{ s}$ by the manganese additive and $46 \mu\text{g}/\text{cm}^3 \text{ s}$ by the iron additive.

The additives also increased the time required for the soot growth rate to decrease to zero, and in some flames containing additives the soot growth rate did not decrease to zero within the limited residence time range of the measurements. In the $C/O = 0.74 + \text{Fe}$ and $C/O = 0.77 + \text{Fe}$ flames, the soot mass growth rate decreased to zero by about 20 ms. In the $C/O = 0.80 + \text{Fe}$ and $C/O = 0.83 + \text{Fe}$ flames, the soot growth rate did not decrease to zero by the end of the range of measurements. As will be shown in Chapter 6, equilibrium predicts the iron additive is continuously precipitating out of the gas phase as metallic iron. The continuous precipitation of the iron could then create sites at which acetylene decomposition is catalyzed. A model which uses this hypothesis to explain the increase in the soot growth rate is presented in Chapter 7.

6. EQUILIBRIUM CALCULATIONS

6.1 Water-Gas Shift Equilibration

In section 4.6, the temperature in the $C/O = 0.52$ flame was calculated by assuming that the water-gas shift reaction



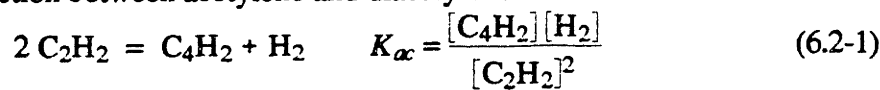
was equilibrated. The composition measurements shown in Section 4.7 were used to investigate the degree of equilibration of this overall reaction in the $C/O = 0.77 + \text{Fe}$ flame.

Figure 6.1-1 compares the experimentally measured value of $[\text{H}_2][\text{CO}_2]/[\text{H}_2\text{O}][\text{CO}]$ to the equilibrium-predicted value of K_{wg} , calculated from the flame temperature. Figure 6.1-1 shows that this reaction was not equilibrated in the $C/O = 0.77$ flame. The concentrations of CO_2 and H_2 were lower than expected, while the concentrations of CO and H_2O were higher than expected. The measured value of K_{wg} was about one-half of the equilibrium value.

Other workers have found similar results. Woods (1988) made concentration measurements in premixed ethylene/air flames with C/O ratios ranging between 0.75 and 0.87. The measured value of K_{wg} was about two-thirds of the equilibrium value. Taylor (1984) made composition measurements in ethylene/air flames with C/O ratios ranging from 0.54 to 0.61. The water-gas shift reaction was near equilibrium in flames with low hydrocarbon concentrations, but the measured value of K_{wg} decreased below equilibrium as the hydrocarbon content of the burned gas increased. This observation indicates that the assumption of water-gas shift equilibration in the $C/O = 0.52$ flame was probably good. Taylor also shows that inadequate sample quenching cannot account for values of K_{wg} below equilibrium.

6.2 Acetylene-Diacetylene Equilibration

The overall reaction between acetylene and diacetylene is



Bittner (1981) found this overall reaction to be near equilibrium in a premixed

benzene/oxygen/argon flame with a fuel equivalence ratio of 1.8.

Figure 6.2-1 compares the measured value of $[C_4H_2][H_2]/[C_2H_2]^2$ to the equilibrium value of K_{ac} (calculated from the flame temperature) in the $C/O = 0.77 + Fe$ flame. This figure shows that the acetylene-diacetylene reaction was not equilibrated; the measured value of $[C_4H_2][H_2]/[C_2H_2]^2$ was about one-fourth of the equilibrium K_{ac} . Woods (1938) found $[C_4H_2][H_2]/[C_2H_2]^2$ was about one-half of the equilibrium K_{ac} in sooting ethylene flames. Lam (1988(b)) also found $[C_4H_2][H_2]/[C_2H_2]^2$ to be below the equilibrium K_{ac} in studies of ethylene combustion in a jet-stirred/plug-flow reactor. These observations may be useful in guiding the development of gas phase kinetic models.

6.3 Chemical State of Iron and Manganese

Computer programs developed by Gordon and McBride (1976) and Reynolds (1987) were used to predict the equilibrium composition and the chemical state of metal additives in these flames. Figure 6.3-1 shows the equilibrium-predicted fraction of the iron in the $C/O = 0.77 + Fe$ flame appearing as $Fe_{(v)}$, $Fe_{(s)}$, and $Fe(OH)_{2(v)}$ as a function of temperature. In the gas phase, iron is predicted to exist predominantly as free metal atoms. Equilibrium predicts iron will begin to precipitate out of this flame in the form of metallic iron at about 1760 K. Contrary to predictions made by Ritrievi (1984), FeO is not expected to form. Equilibrium also predicts that the addition of iron at this concentration will have no effect on the concentration of any of the stable species (e.g., CO and H_2) or any of the radical species (e.g., H , OH , and O).

The curves in Figure 6.3-1 shift slightly as the C/O ratio of the flame and the amount of iron added to the flame change. As the C/O ratio increases, iron is predicted to begin precipitating out of the gas phase at a slightly higher temperature. At a given temperature, the fraction of the iron existing as $Fe_{(s)}$ increases as the C/O ratio increases. A 10-fold increase in the concentration of iron in the flame shifts the curves in Figure 6.3-1 to the right. Some of the iron would be expected to exist in the condensed phase at temperatures as high as 2000 K. Liquid iron would be predicted to exist at temperatures above 1818 K, the melting point of iron.

In one sense, Figure 6.3-1 should be read from right to left, because the temperature in any flame decreases with increasing residence time. In the $C/O = 0.74 + Fe$,

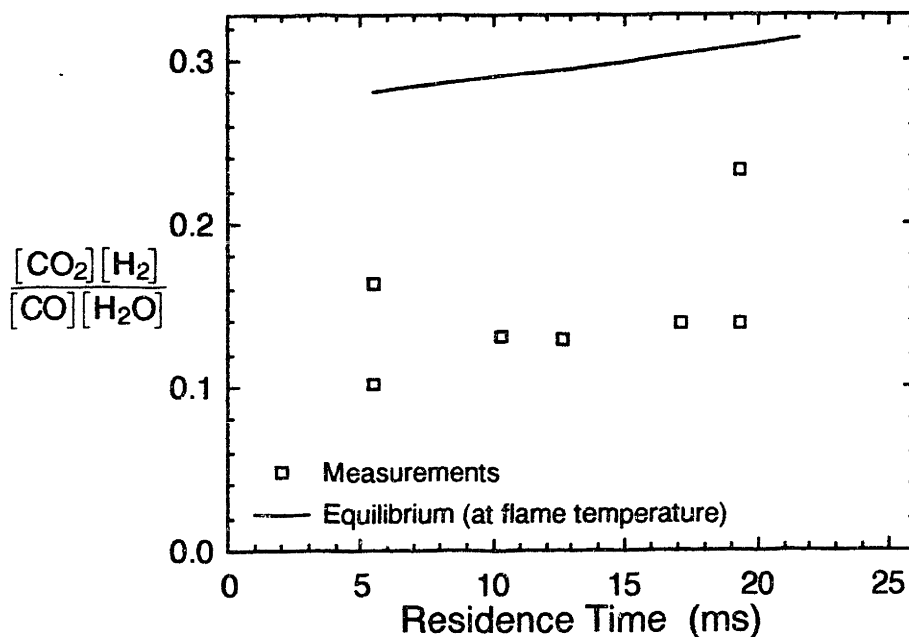


Figure 6.1-1: Comparison of gas phase composition measurements and the water-gas shift reaction equilibrium constant in the $C/O = 0.77 + \text{Fe}$ flame.

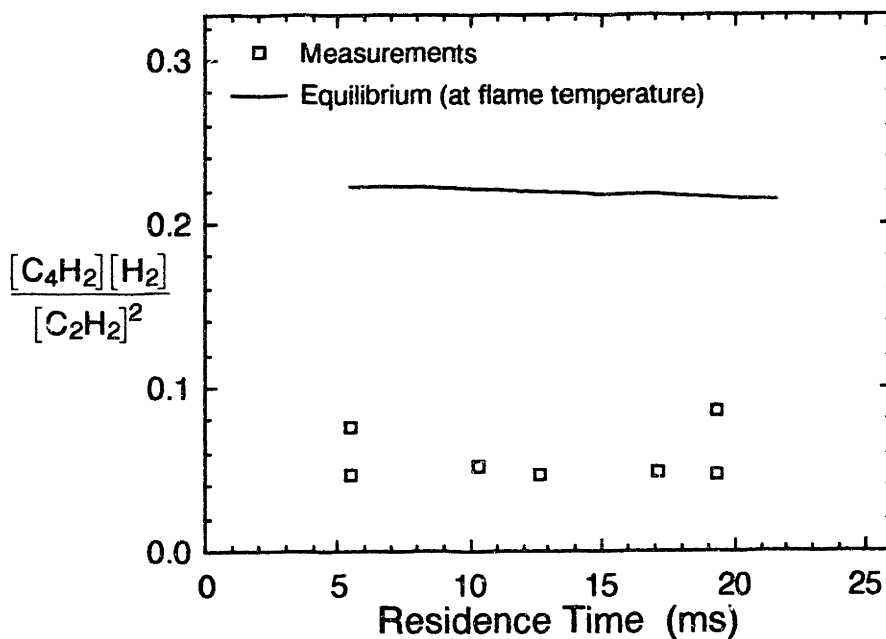


Figure 6.2-1: Comparison of gas phase composition measurements and the acetylene-diacetylene reaction equilibrium constant in the $C/O = 0.77 + \text{Fe}$ flame.

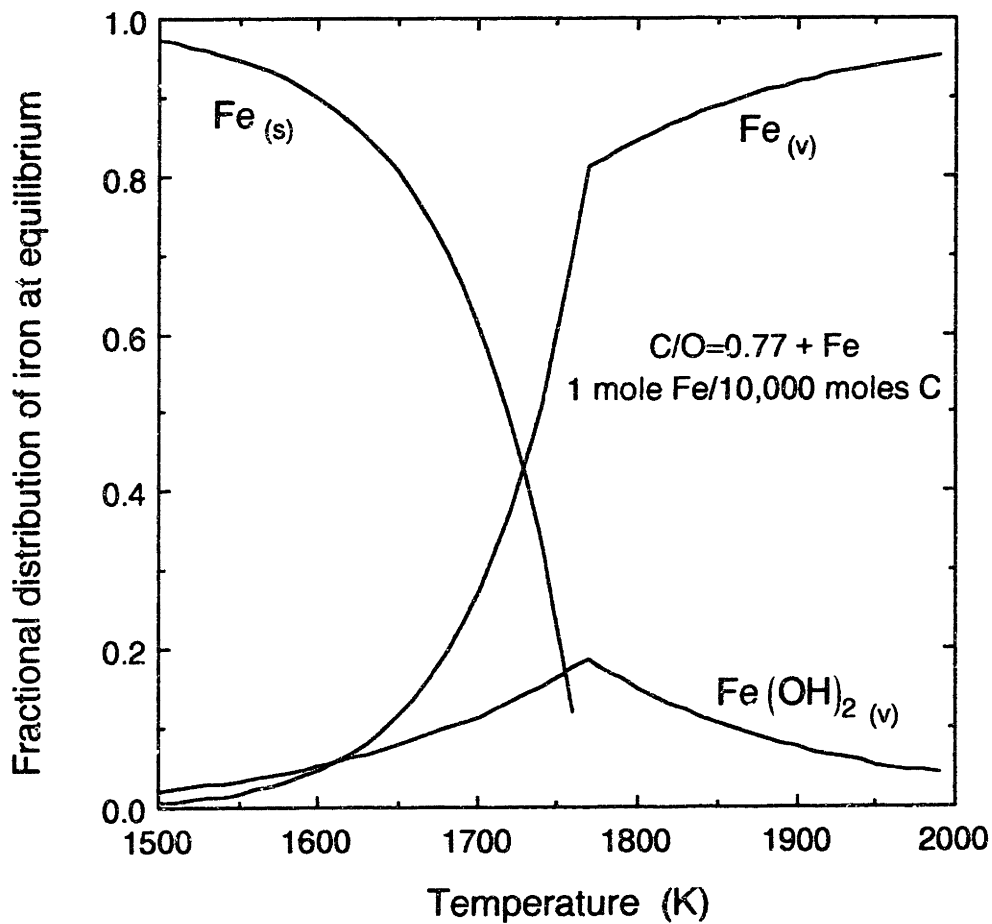


Figure 6.3-1: Equilibrium prediction of the chemical state of iron in the $\text{C/O} = 0.77 + \text{Fe}$ flame. Equilibrium predicts that metallic iron will begin to precipitate out of the vapor phase when the flame temperature drops to about 1760 K. Similar results were found for all of the C/O ratios studied, although the curves shift slightly.

$C/O = 0.77 + Fe$, and $C/O = 0.80 + Fe$ flames, these equilibrium calculations (combined with the temperature measurements in Section 4.6) predict that iron will be in the gas phase at short residence times, and begin to precipitate out as metallic iron at residence times between 3 and 5 ms. Metallic iron is expected to exist at all residence times at which optical measurements were made in the $C/O = 0.83 + Fe$ flame, because the temperature in this flame is lower than the temperature in the other flames.

Similar equilibrium calculations were performed to predict the chemical state of manganese. Equilibrium predicts manganese will exist in the vapor phase predominantly as free Mn atoms (see Figure 6.3-2). Solid MnO will begin to form as the temperature in the $C/O = 0.77 + Mn$ flame drops below 1675 K. These predictions are in qualitative agreement with the observations of Padley and Sugden (1959), who observed the emission spectra of hydrogen flames containing added manganese. The two major species present were free Mn atoms (~75% of the manganese) and MnO (~25%).

These equilibrium calculations must be used with caution, since soot formation is a kinetically-controlled process that is far from equilibrium. For example, equilibrium does not predict the formation of solid carbon in any of the premixed flames. The equilibrium mole fraction of C_2H_2 in the $C/O = 0.77$ flame is about 2×10^{-12} at 1700 K, while the measured mole fraction was about 0.03. On the other hand, metal reactions may be faster than carbonaceous reactions, and equilibrium among the metal species may be obtained rapidly. In the absence of experimental measurements, these equilibrium calculations can be used as a guide.

6.4 Chemical State of Calcium, Barium, and Sodium

Equilibrium calculations can also be performed to predict the chemical states of other metals. Figures 6.4-1, 6.4-2, and 6.4-3 show the results of equilibrium calculations for calcium, barium, and sodium, respectively, using a concentration in the flame of 1 mole metal/10,000 moles C. Predictions for the $C/O = 0.74$ and $C/O = 0.83$ flames are shown in these figures.

Calcium is predicted to exist in the flame primarily as $CaO_{(s)}$, although small amounts of $Ca(OH)_{2(v)}$ and $CaOH_{(v)}$ are expected at high temperatures (the $CaOH_{(v)}$ curve is not shown in Figure 6.4-1). Barium is expected to exist entirely in the vapor

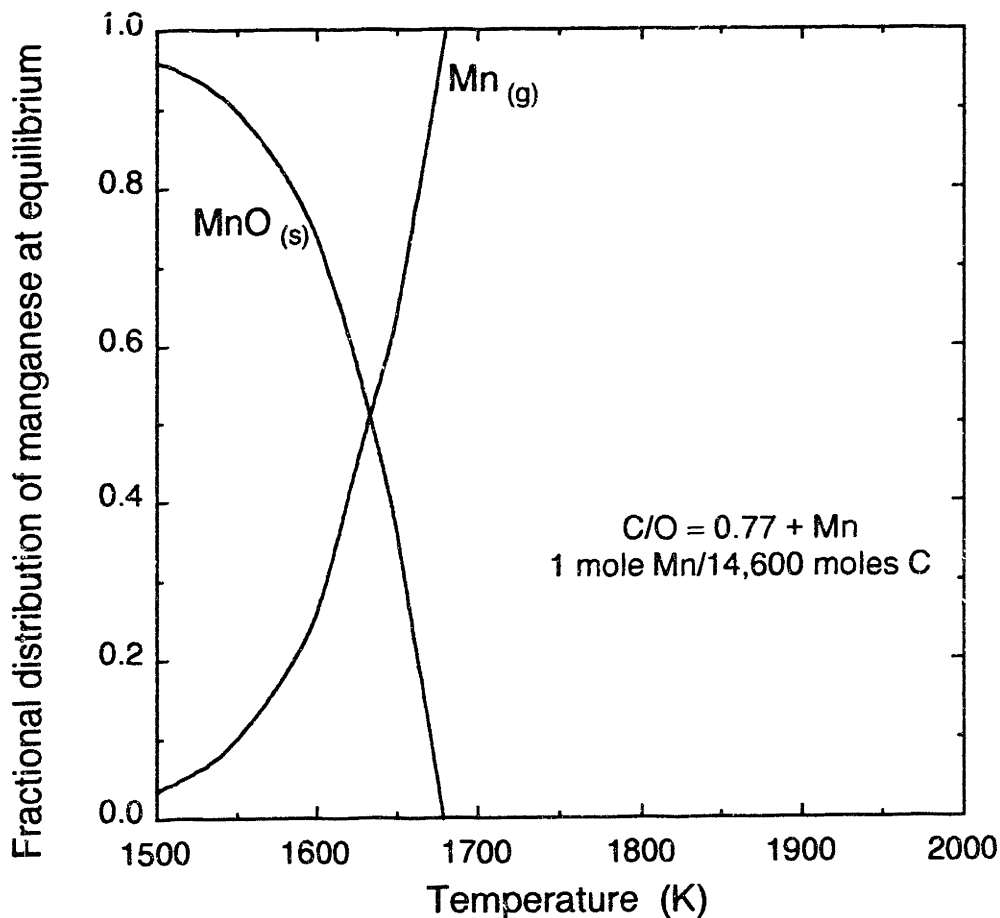


Figure 6.3-2: Equilibrium prediction of the chemical state of manganese in the $C/O = 0.77 + Mn$ flame. Equilibrium predicts that MnO will begin to precipitate out of the flame when the flame temperature drops to about 1675 K. Trace amounts ($\sim 0.1\%$ of the manganese) of liquid Mn metal begin to appear near this temperature as well. Above this temperature, virtually all of the manganese is in the vapor state as free Mn atoms. Similar results are found for all of the C/O ratios studied.

These calculations are in qualitative agreement with the experimental observations of Padley and Sugden (1959), who observed the emission spectra of hydrogen flames containing added manganese. The two major species present were free Mn atoms ($\sim 75\%$ of the manganese) and MnO ($\sim 25\%$).

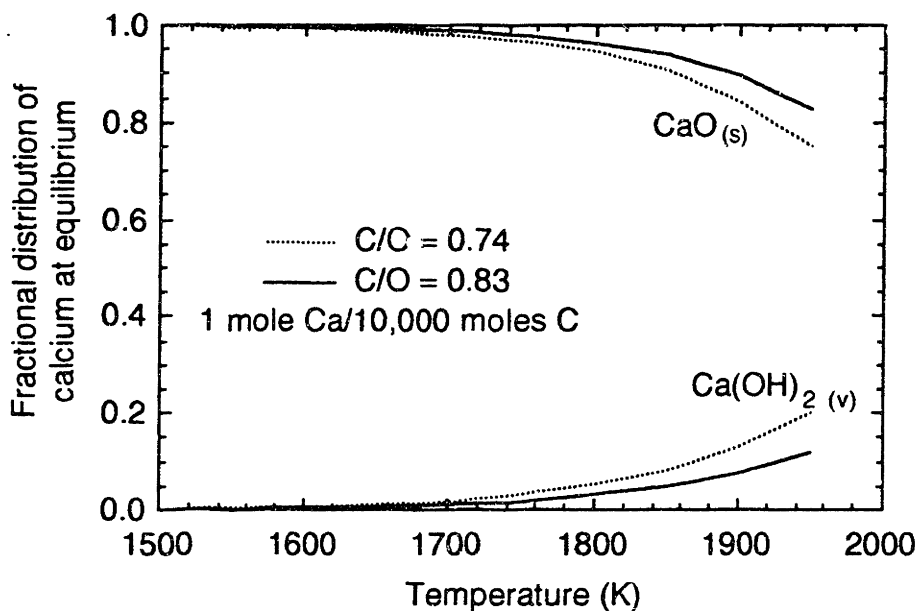


Figure 6.4-1: Equilibrium prediction of the chemical state of calcium added to the $C/O = 0.74$ and $C/O = 0.83$ flames.

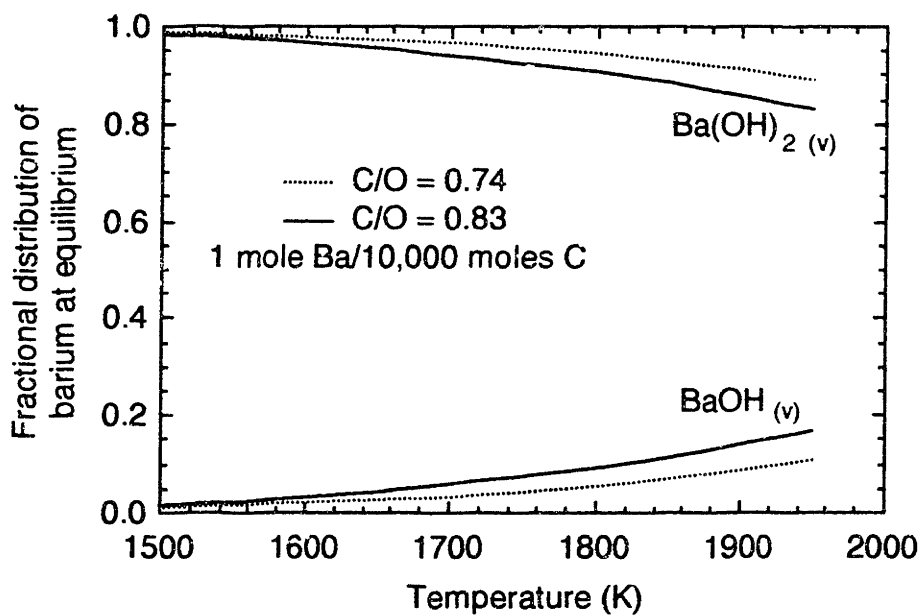


Figure 6.4-2: Equilibrium prediction of the chemical state of barium added to the $C/O = 0.74$ and $C/O = 0.83$ flames.

phase, predominantly as $\text{Ba}(\text{OH})_{2(v)}$. A small amount of $\text{BaOH}_{(v)}$ is expected at high temperatures. Sodium should exist primarily as free metal atoms in the vapor phase, with an increasing amount of $\text{NaOH}_{(v)}$ as the temperature decreases.

These equilibrium calculations can be a useful tool for distinguishing between possible mechanisms of additive action. For a metal to catalyze soot surface growth, as proposed in Chapter 7, a metal must be in a condensed phase. Therefore, catalyzed soot growth is not expected for barium and sodium additives, which are expected to be entirely in the gas phase.

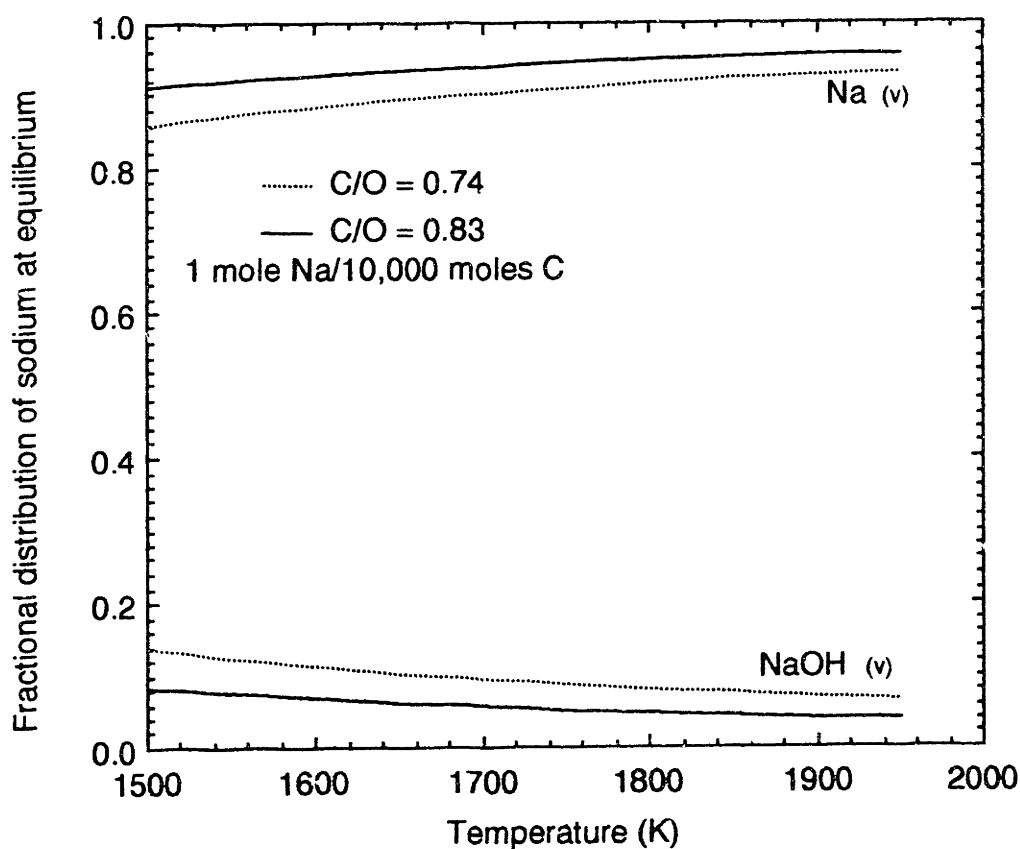


Figure 6.4-3: Equilibrium prediction of the chemical state of Na added to the $C/O = 0.74$ and $C/O = 0.83$ flames.

7. CATALYZED C₂H₂ DEPOSITION MODEL

7.1 Model Assumptions

Several workers (e.g., Baker, 1979) have observed that transition metals in general, and iron in particular, can catalyze the formation of carbon from acetylene. This observation was used to develop a catalyzed acetylene deposition model to explain the increase in the amount of soot caused by the iron additive. Iron atoms on the surface of the soot particles were assumed to be active sites where C₂H₂ reacted with and added to the soot.

The net rate of soot mass growth was expressed as

$$r_{net} = r_{mass\ growth} - r_{oxidation} \quad (7.1-1)$$

The net rate of soot mass growth, $r_{net} = dm_{soot}/dt$, was measured (see Section 5.7). The rate of soot oxidation, $r_{oxidation}$, was estimated from the model developed by Neoh (1980), using a reaction probability between soot and OH of 0.28 and the global equilibrium OH concentration (see Section 2.5.4). The global equilibrium OH mole fraction ranged from a high of about 2.8×10^{-6} in the C/O = 0.74 flame to a low of about 1.7×10^{-7} at large residence times in the C/O = 0.83 flame. The oxidation rate was generally negligible in comparison to the net growth rate.

The rate of soot mass growth, $r_{mass\ growth}$, in flames containing iron was written as

$$r_{mass\ growth} \text{ (with Fe)} = \left[r_{mass\ growth} \text{ (no Fe)} \right] \frac{S_{with\ Fe} + \gamma \Theta z x S_{with\ Fe} M}{S_{no\ Fe}} \quad (7.1-2)$$

where

- γ = reaction probability between a C₂H₂ molecule and an iron site,
- Θ = fraction of total particle surface area covered by iron,
- z = gas kinetic collision rate between gas and soot [moles/(area)(time)],
- x = mole fraction acetylene,
- S = total soot surface area per unit volume [area/volume], and
- M = molecular weight of acetylene.

The notation "with Fe" refers to the soot growth rate or surface area in a flame with an additive. The notation "no Fe" refers to the growth rate or surface area in the flame with the same C/O ratio but no additive.

The model assumes the mass growth reaction is proportional to surface area, and that the additive does not change the concentration of the soot growth species. The model

makes no other assumptions about the mechanism of soot formation in flames without additives. The additional soot formed in flames with additives is modeled as entirely due to the catalyzed addition of acetylene to soot at the iron sites.

To determine the fraction of the surface covered by iron, two limiting cases were considered. The first case assumes the solid-state diffusion of iron through soot is infinitely fast (or fast relative to the surface growth reaction), and the iron is uniformly distributed throughout each particle at all times. With this assumption,

$$\Theta = \frac{f_{v, Fe}}{f_{v, soot}} \quad (7.1-3)$$

The equilibrium calculations described in Section 6.3 were used to determine the amount of iron in the condensed phase at any residence time in the flame. Even if all of the iron were in the solid phase as metallic iron, the soot particles would never be more than 5% iron by volume (see Section 5.2.2).

The second limiting case assumes that the diffusion of iron through carbon is infinitely slow (or slow relative to the surface growth reaction). An iron atom, once precipitated onto the surface of a soot particle, never moves. An iron atom covered by one carbon atom is inactivated. For this case, Θ was calculated by discretizing time into small time intervals Δt . The fraction of the surface covered by iron at time $(t + \Delta t)$ is then

$$\Theta(t + \Delta t) = \frac{A_{Fe}(\Delta t)}{S(t + \Delta t)} + \Theta(t) \left[1 - \frac{A_{Fe}(\Delta t) + A_{soot}(\Delta t)}{S(t + \Delta t)} \right] \quad (7.1-4)$$

$A_{Fe}(\Delta t)$ represents the total area of iron deposited in the time interval Δt ; the area of a single iron site was taken as 0.045 nm^2 , the cross-sectional area of a single iron atom. $A_{soot}(\Delta t)$ represents the total area of soot deposited in the time interval; the area of a soot site was taken to be 0.015 nm^2 , the cross-sectional area of a single carbon atom in soot. The first term on the right hand side of Equation 7.1-4 represents new sites deposited in the time interval Δt . The second term on the right hand side of Equation 7.1-4 represents old sites that were not covered up by the soot and iron deposited in the time interval. The time step size was made small enough to insure that only a fraction of the total surface area was covered in each time interval. Equation 7.1-4 represents random deposition of soot and iron on the particle surface.

Equations 7.1-1, 7.1-2, and either 7.1-3 or 7.1-4 were solved simultaneously to

determine the value of γ that best fit the soot volume fraction measurements in flames with additives. The net soot growth rate was integrated to determine the soot volume fraction. The inputs were the soot mass growth rate, surface area, number density, and acetylene concentration measurements in flames without additives. Also used were the measured flame temperatures in flames with additives and the equilibrium prediction of the amount of iron in the solid phase. The initial f_v in a flame with an additive was assumed to be the same as the initial volume fraction in the flame of the same C/O ratio without an additive.

An iterative solution was required to determine the soot volume fraction, surface area, net soot growth rate, and Θ as a function of residence time in each flame. As shown by Equation 7.4-2, the surface area in a flame with an additive was required to calculate the growth rate. To calculate the surface area, the soot volume fraction was needed (the number density was specified as the number density in the corresponding flame without an additive), and to calculate the soot volume fraction, the growth rate was needed. Therefore, an iterative solution was required. The equations were satisfied by choosing γ , and then iteratively solving the equations in the four flames with additives. The model predictions of f_v were compared to the measurements, γ was adjusted, and the process was repeated. The best-fit value of γ was chosen by eye, by simultaneously comparing the model predictions of f_v to the measurements in all four flames containing additives. A least-squares fit would have biased γ to fit the data at large soot volume fractions better than the data at low soot volume fractions. Recall that the soot volume fraction varies by almost an order of magnitude in some flames.

7.2 Comparison of Measurements and Model Predictions

Figures 7.2-1 and 7.2-2 compare the predictions of f_v in the flames containing iron to the measured f_v , using a value of $\gamma = 0.023$. The measurements tend to fall between the two limiting assumptions, infinitely fast iron diffusion in carbon and infinitely slow iron diffusion in carbon. Also shown for comparison are the volume fraction measurements in the same flames without additives; the model collapses to the no-additive flames if $\gamma = 0$. Figure 7.2-3 shows the predictions of Θ , the fraction of the total particle surface area covered by iron. Θ varies from a maximum value of about 0.03 in the C/O = 0.74 + Fe flame to 0.004 in the C/O = 0.80 flame. The slow diffusion and fast diffusion assumptions

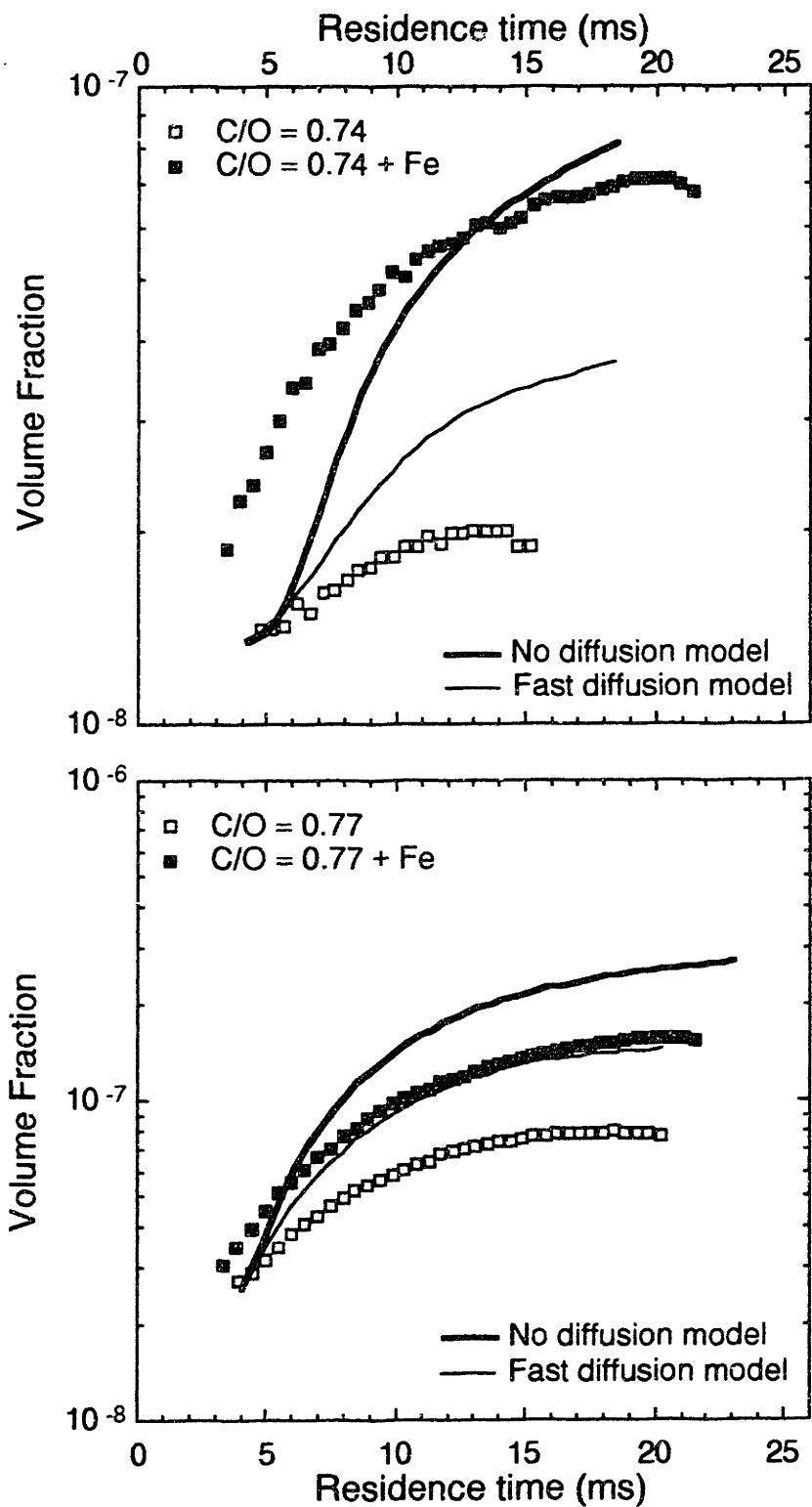


Figure 7.2-1: Comparison of soot volume fraction measurements in flames with iron additives and catalyzed acetylene deposition model. The volume fraction measurements in the flames without additives are also shown.

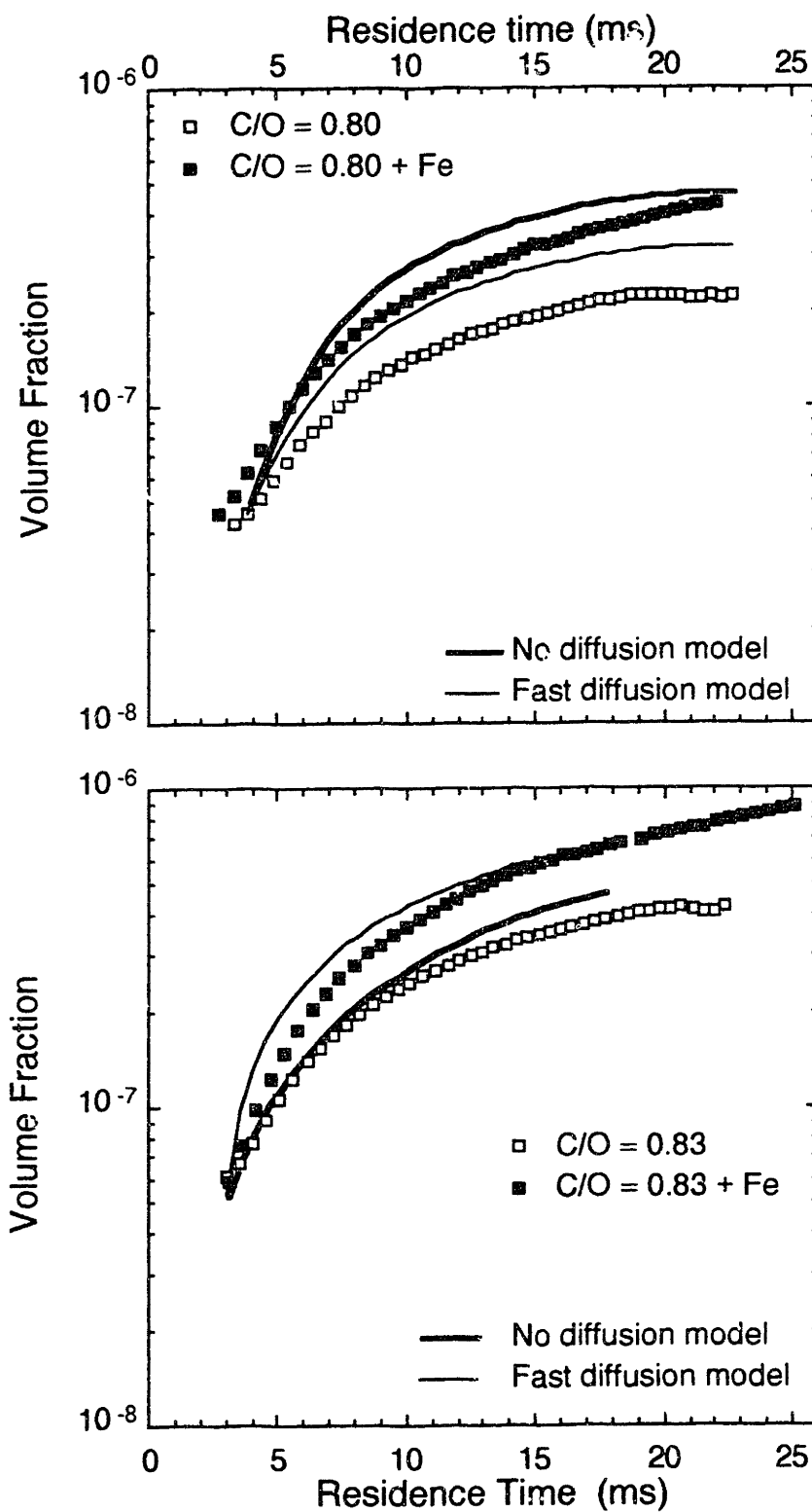


Figure 7.2-2: Comparison of soot volume fraction measurements in flames with iron additives and catalyzed acetylene deposition model. The volume fraction measurements in the flames without additives are also shown.

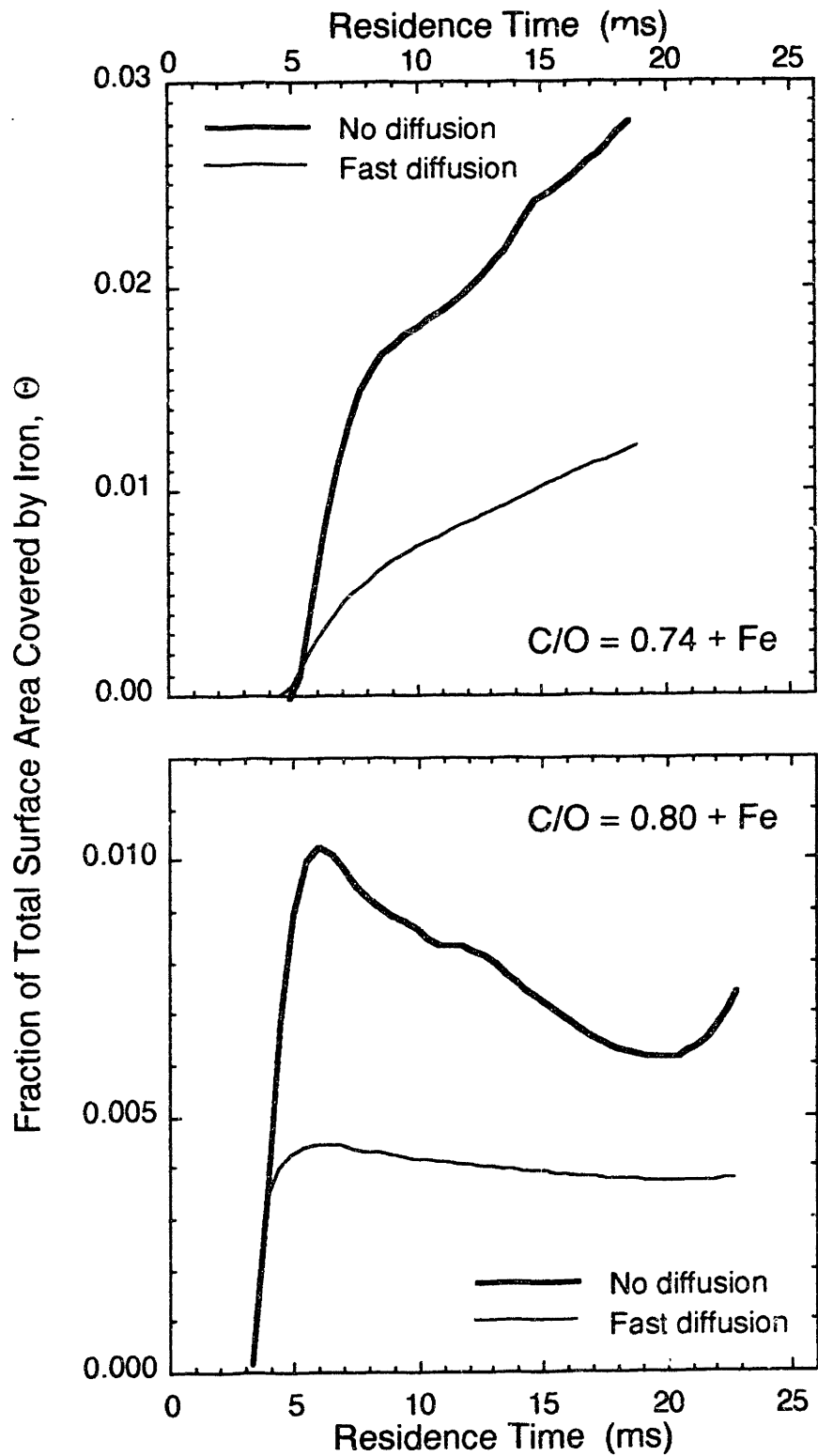


Figure 7.2-3: Model predictions of the fraction of the total soot surface area covered by iron. The particles are never more than 1% iron by volume.

lead to predictions of Θ that differ by up to a factor 3. The particles are never predicted to be more than about 1% iron by volume.

In the $C/O = 0.74 + Fe$, $C/O = 0.77 + Fe$, and $C/O = 0.80 + Fe$ flames, the slow diffusion model predicts larger values of Θ than the fast diffusion model. Θ is lower in the fast diffusion model because iron diffuses inward, towards the center of the particle. In the $C/O = 0.83 + Fe$ flame, the slow diffusion model predicts a smaller values of Θ than the fast diffusion model. The difference is that in the $C/O = 0.83 + Fe$ flame, the temperature is low enough for 60% of the iron to exist as $Fe_{(s)}$ even before the first optical measurements could be made. In the no diffusion model, all of this iron is lost beneath the surface of the particles before the first volume fraction measurement was made. In the fast diffusion model, the iron can diffuse outward to the particle surface, and some of this iron is still available at the surface to catalyze acetylene deposition.

The fit between the model and the data is reasonably good, and adds confidence that the model assumptions are correct. The agreement between the model and the data is weakest in the $C/O = 0.74 + Fe$ flame. Part of the difficulty in this flame lies in the assumption that the initial volume fractions are the same in flames with and without additives. Although this is a good assumption in other flames, this assumption is poor in the $C/O = 0.74 + Fe$ flame. If volume fraction measurements could be taken at earlier residence times in the $C/O = 0.74$ and $C/O = 0.74 + Fe$ flames, the assumption of equal initial volume fraction might improve.

The second major reason for the poor fit in the $C/O = 0.74 + Fe$ flame is that the model does not predict enough iron in the solid phase. The equilibrium-predicted amount of iron in the solid phase is strongly dependent upon the flame temperature. If the actual temperature in this flame is slightly lower than the measured temperature, then the model predictions would be in closer agreement with the data. Temperature measurements were most difficult, and contain the most uncertainty, in flames with low soot volume fractions.

Both the slow diffusion model and the fast diffusion model could be fit to the measurements reasonably well. Fitting just the fast diffusion model to the data, the best-fit value of γ was found to be about 0.03. Fitting just the no diffusion model to the data, the best-fit value of γ was found to be about 0.015. The weak dependence of γ on the diffusion rate of iron in soot shows that modeling the diffusion rate is relatively

unimportant. Estimating the diffusion rate, to determine if the slow diffusion model or the fast diffusion model is a better approximation of physical reality, is difficult. Although diffusion rates of iron in carbon have been measured, they can vary over a wide range, depending on whether diffusion is parallel to or perpendicular to the graphite planes. Although soot is not graphite, soot is generally accepted to contain small, randomly oriented domains that are graphitic in nature.

There are several tests which could be used to critically evaluate this model. Adding iron to flames with temperatures above the precipitation temperature should, according to this model, have no effect on the soot volume fraction. The flame temperature could be changed by using argon as a diluent instead of nitrogen. The concentration of the additive in the flame could also be changed. The model can be used to predict the additive concentration at which iron will not precipitate out. Soot particles could also be collected for burnout studies on a thermogravimetric analyzer. Particles collected from flames with additives should oxidize faster than particles collected from flames without additives. The model also predicts the spatial distribution of iron within the particles. This may prove useful, since a metal must be at the surface to catalyze soot oxidation.

8. SUMMARY AND CONCLUSIONS

1) The iron and manganese additives had no effect on soot particle inception. The initial soot particle diameters, concentrations, and volume fractions were approximately the same in flames with and without additives.

2) The iron and manganese additives did not participate in charge transfer reactions under these conditions. The particle number density followed the predictions of coagulation theory in the free-molecule regime, and the additives had no effect on the soot particle concentration.

3) Iron and manganese had no measurable effect on the concentration of any of the low molecular weight, stable gas phase species, up through the C_4 hydrocarbons and benzene.

4) Iron and manganese did not alter the soot particle shape, at least as could be determined from depolarization ratio measurements.

5) The iron and manganese additives increased the total amount of soot formed in the flames. The manganese additive increased the amount of soot formed by up to 50%, while the iron additive increased the amount of soot formed by up to 300%.

6) The iron additive increased the fluorescence coefficient in the flames studied by up to a factor of 6. The manganese additive had almost no effect on the fluorescence coefficient. The fluorescence coefficient was roughly proportional to the total tar concentration (defined as the CH_2Cl_2 soluble PAH species), given the precision of the measurements.

7) Under the conditions studied, thermodynamic equilibrium predicts that iron and manganese are initially in the gas phase, predominantly as free metal atoms, and enter the condensed phase as the flame temperature decreases. Iron is predicted to precipitate out in the metallic state, while manganese is expected to form solid MnO .

8) Metallic iron on the surface of the growing soot particles may catalyze the addition of acetylene to soot. A model in which the reaction probability between C_2H_2 and an iron site is about 0.023 fits the data reasonably well. The model has a weak dependence on the solid-state diffusion rate of metallic iron in soot. The data tend to fall between the limiting

assumptions of infinitely slow iron/soot diffusion and infinitely fast iron/soot diffusion.

9) Metallic iron on the surface of the soot particles may catalyze PAH formation. This explanation of the observed increase in the PAH concentration seems more likely than assuming a decrease in the OH concentration and, therefore, a decrease in the PAH destruction rate. Measurements of the OH concentration might distinguish between these possibilities.

10) In practical systems, transition metal additives probably reduce soot emissions by catalyzing soot burnout, and not by inhibiting soot particle formation. Soot burnout could not be observed in the premixed flames chosen for this study.

11) The geometric mean soot particle diameters measured with the thermophoretic probe are in reasonable agreement with the *in situ* optical measurements of the particle diameter. However, the width of the particle size distribution, as determined by the thermophoretic probe, is much broader than expected. Additional work is needed before the thermophoretic probe results can be accepted with confidence. Thermophoretic sampling may prove to be a useful tool for studying the evolution of the soot particle size and shape distributions in premixed atmospheric pressure flames.

12) The volume weighted average refractive index of a small coated sphere can be a good approximation for the effective refractive index. A simple, graphical technique has been developed for determining the sensitivity of optically determined particle sizes and concentrations to uncertainties in the structure and composition of a small coated sphere.

APPENDIX A: Calibration of Optical Pyrometer

An optical pyrometer, Pyrometer Instrument Model No. 95, Serial No. M6854, was used to measure the flame brightness temperature (T_{br}). The calibration of this pyrometer was tested by measuring brightness temperatures as a function of the current through a filament lamp (General Electric #20AT24/2) calibrated by the National Bureau of Standards (NBS).

The circuit shown in Figure A-1 was constructed to determine the lamp current, I_c . A highly stable DC source (Hewlett-Packard 6268B) provided power for the lamp. The voltage drop, E , across a resistor, R_e , placed in series with the lamp was measured using a digital multimeter (Keithley 195A). The resistance R_e was 4.835 m Ω . The current through the resistor (and the lamp) was then determined using Ohm's Law, $I_c = E/R_e$. Voltage and brightness temperature measurements were taken over the range 30 mV $< E <$ 48 mV.

The NBS procedure for measuring the lamp T_{br} was followed. The lamp was operated base down, and the portion of the filament at the notch was made vertical. The pyrometer was sighted on the center of the filament at the notch, with the arrow, etched on the back of the glass envelope, appearing at the notch. Room temperature was 25°C.

Figure A-2 plots the measured T_{br} at 655 nm versus the lamp current. Brightness temperature measurements were taken using either filter #1 or filter #2 of the pyrometer. Also shown are the NBS T_{br} measurements of the same lamp (NBS, 1977). The agreement between these measurements and the NBS measurements demonstrates that the pyrometer was calibrated correctly.

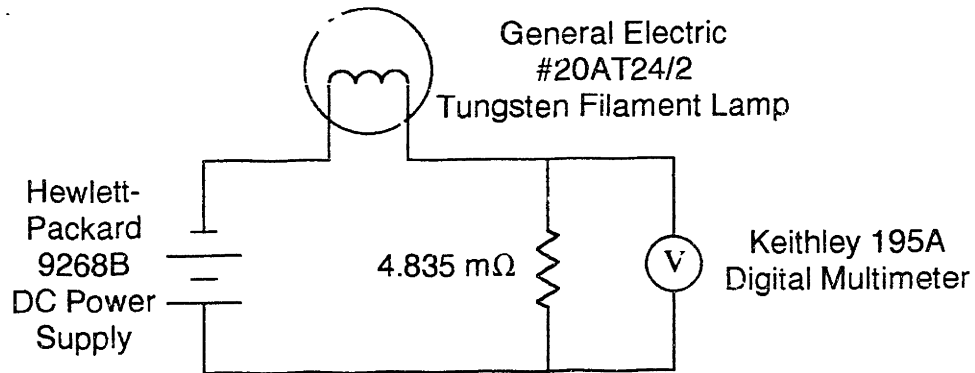


Figure A-1: The circuit used to test the calibration of the optical pyrometer. The filament lamp was calibrated by the National Bureau of Standards.

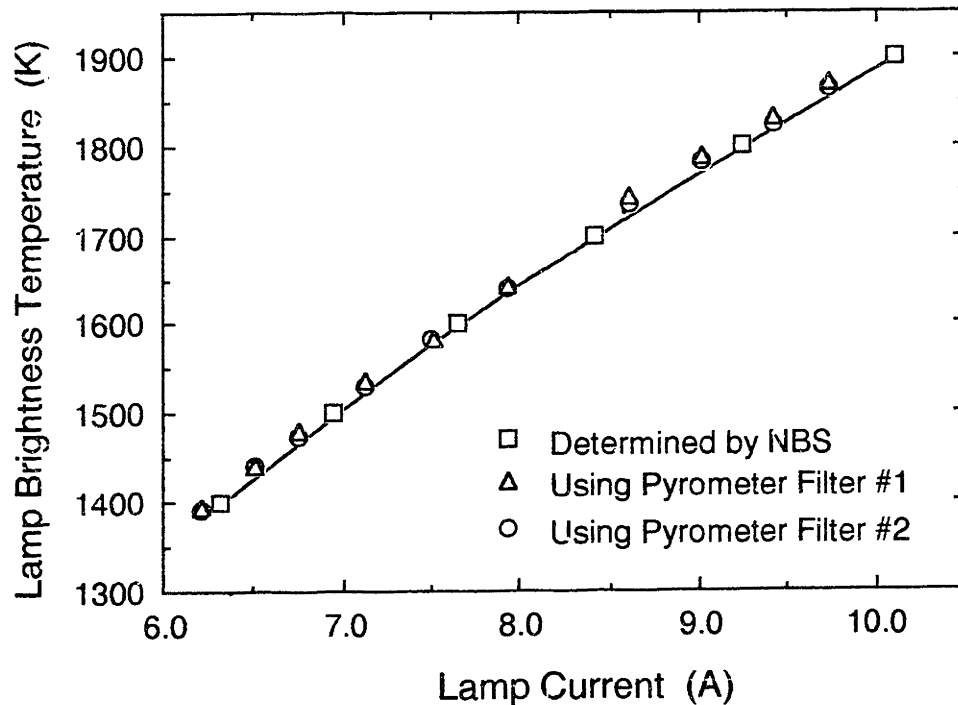


Figure A-2: The variation of lamp brightness temperature with current. The agreement between the NBS measurements and the measurements taken with the pyrometer indicate that the pyrometer was calibrated properly.

APPENDIX B: Calibration and Alignment of Light Scattering Apparatus

The objective of the light scattering measurements was to determine the scattering and fluorescence coefficients (Q_w , Q_{vh} , and $Q_{f\lambda}\Delta\lambda$) of a medium with unknown characteristics. One possible method of determining these coefficients is to measure all of the quantities in Equations 2.2-1 and 2.3-1: the power reaching the detector, the scattering volume, the incident intensity, the solid angles of the incident and detected beams, and the overall efficiency of the detection optics. However, determining some of these quantities with high accuracy is difficult, and uncertainties would combine to give an even larger uncertainty in Q_w , Q_{vh} , and $Q_{f\lambda}\Delta\lambda$. An easier and more accurate method is to calibrate the experimental system by measuring the scattering signal of a known medium, and then to reference the measurements in the unknown medium to the measurements in the known medium. This calibration technique was the method used to determine Q_w , Q_{vh} , and $Q_{f\lambda}\Delta\lambda$.

The “scattering signal” was the current signal produced by the detector; the detected power P_0 given in Equation 2.2-1 was not determined. The detector (a PMT) converts the detected power into a current signal, S , which could not be used to determine P_0 because the detector efficiency, η_e , defined as

$$S = \eta_e P_0 \quad (\text{B-1})$$

was unknown. However, Eq. B-1 can be used to eliminate P_0 from Eq. 2.2-1:

$$S = \eta_e \eta Q V I_0 \Omega_0 \Omega_1 \quad (\text{B-2})$$

The incident laser light was vertically polarized. If the polarizing filter shown in Figure 3.3-2 was oriented to allow only vertically polarized light to reach the PMT, then the signal measured was S_{vv} , corresponding to the component of the scattered light that was vertically polarized. Rotating the filter 90° allowed measurement of S_{vh} , corresponding to the component of the scattered light that was horizontally polarized.

Consider two measurements of the current signal, $S_{vv,1}$ and $S_{vv,2}$, from two media with two different scattering coefficients, $Q_{w,1}$ and $Q_{w,2}$, respectively. If η_e , η , V , I_0 , Ω_0 , and Ω_1 are kept constant for both measurements, then Eq. B-2 leads to

$$Q_{w,2} = \frac{S_{w,2}}{S_{w,1}} Q_{v,1} \quad (\text{B-3})$$

The calibration of the system was achieved by measuring the current signal, $S_{w,1}$, from a medium with a known scattering coefficient, $Q_{v,1}$. Scattering coefficients in the pre-mixed flames were then determined from current signal measurements using Eq. B-3.

For all of the experiments described in this thesis, the calibration of the scattering apparatus was achieved by measuring the scattering signal from nitrogen gas at room temperature and pressure. $Q_{v,1}$ for nitrogen at 514.5 nm is given by Equations 2.2.5-1 through 2.2.5-3, and the data in Table 2.2.5-1. A measurement of $S_{w,Nitrogen}$ was taken before every scattering coefficient profile.

In order to determine $Q_{v,1}$, the polarizing filter shown in Figure 3.3-2 was positioned to allow only the vertically polarized component of the scattered light to reach the detector. To determine Q_{vh} , the filter was rotated 90° to allow only the horizontally polarized component of the scattered light to reach the detector. To measure $Q_{f\lambda}\Delta\lambda$, no polarizing filter was used, while for measurements of $Q_{fv}\Delta\lambda$ and $Q_{fh}\Delta\lambda$ the polarizing filter was inserted and rotated to the appropriate orientation.

The calibration and alignment of the light scattering and absorption apparatus was verified by checking four criteria:

- (1) the incident beams passed over the center of the burner;
- (2) the laser beam was parallel to the plane of the burner surface;
- (3) spurious reflections were eliminated at all scattering angles;
- (4) the plane defined by the intersecting incident and detected beams remained unchanged as the rotating arm moved through scattering angles of 30° to 135°.

Since the laser beam was visible to the unaided eye, criterion (1) was verified easily. The burner could be translated horizontally until the center of the burner was under the laser beam. For absorption measurements, a piece of paper was held over the center of the burner, and the focused image of the filament that appeared on the paper was used to position the burner. Since any horizontal cross-section of the flame was uniform, small errors in positioning the center of the burner were not important.

Criterion (2) was also verified by inspection with the unaided eye. Raising the burner just below the laser beam made it easy to see if the burner and the beam were par-

allel. If the burner was not parallel to the beam, then the burner was made level with the laser beam by inserting shims underneath flanges that attached the burner to the translation stage that moved the burner in the vertical direction. Criteria (1) and (2) were checked whenever the ceramic honeycomb burner was replaced. Criterion (1) was also checked whenever the apparatus was switched between scattering and absorption measurements.

Criteria (3) and (4) were checked as part of the alignment procedure. The alignment of the scattering system was checked every few months. After the system was aligned for the first time, the system was never found to be out of alignment.

The first part of checking criteria (3) and (4) was verifying that the scattering signals from nitrogen and carbon dioxide varied with scattering angle in the expected manner. As shown in Section 2.2, Q_w is independent of scattering angle for small particles. However, the scattering volume varied with $\sin \theta$, as shown in Figure B-1. The scattering volume can be approximated as a cylinder, and the height of the cylinder was determined by a slit mounted in front of the PMT. As the PMT was rotated, the width of the slit did not change, but the height of the slanted cylinder did change. As shown in Figure B-1, the scattering volume V_0 was not constant, but varied with scattering angle:

$$V_0 = \frac{\pi r^2 L}{\sin \theta} \quad (\text{B-4})$$

Substituting Equation B-4 into Equation B-2 shows that although S_{vv} is not independent of scattering angle, the product $(S_{vv} \sin \theta)$ should be independent of scattering angle. Therefore, the first step in the alignment consisted of verifying that $(S_{vv, \text{nitrogen}} \sin \theta)$ was a constant, independent of scattering angle. Figure B-2 shows a typical result of checking the alignment. $(S_{vv, \text{nitrogen}} \sin \theta)$ was a constant, with a standard deviation of just 4% of the average value. Similar results were found using CO_2 , with a standard deviation of just 2% of the average value.

The second part of checking the alignment consisted of measuring the ratio of the scattering signals from CO_2 and N_2 . If both gases are at the same temperature and pressure (room temperature and pressure), then the ratio of the scattering signal from carbon dioxide to the scattering signal of nitrogen is

$$\frac{S_w, \text{CO}_2}{S_w, \text{N}_2} = \frac{Q_w, \text{CO}_2}{Q_w, \text{N}_2} = C_w, \text{rel} \quad (\text{B-5})$$

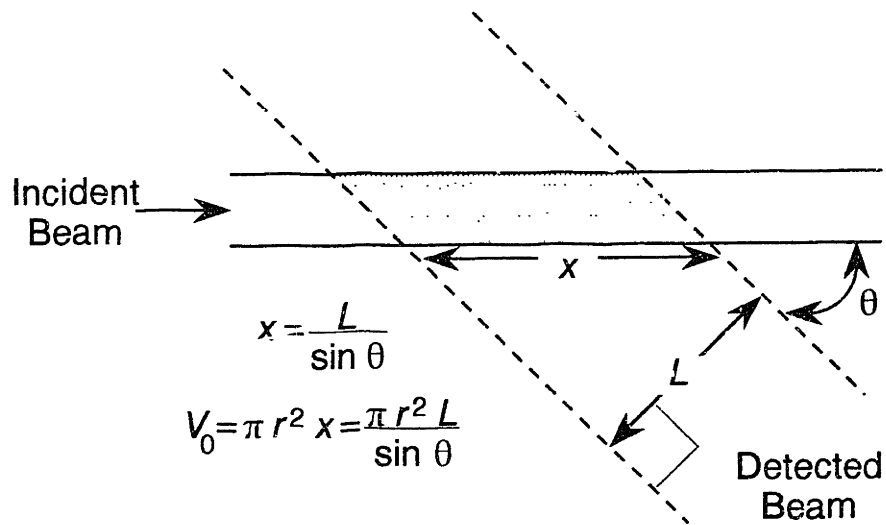
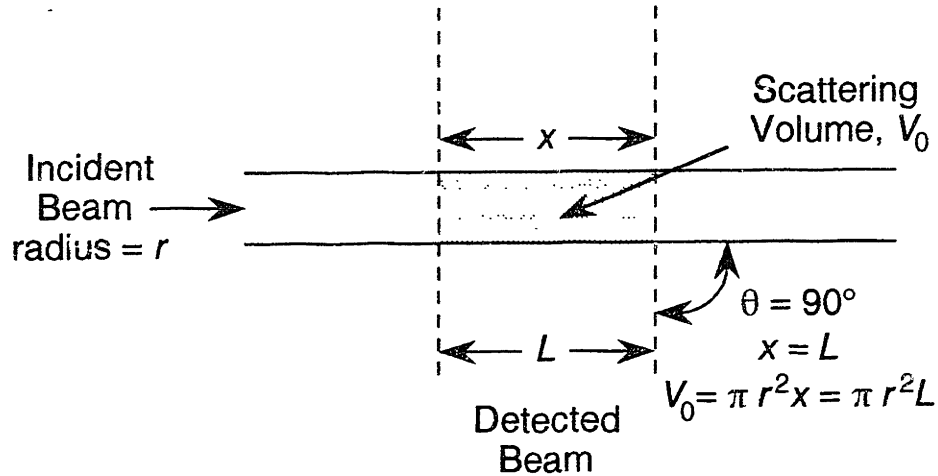


Figure B-1: Geometry of scattering volume. The length L is determined by the slits mounted in front of the PMT and does not change as the scattering angle is varied. However, the scattering volume is a function of the scattering angle. In this illustration, the beams have been idealized as cylinders. This approximation is good as long as the beam divergence is small.

where $C_{vv,rel}$ is independent of θ (see Equation 2.2.5-4). For CO_2 at 514.5 nm, $C_{vv,rel}$ is given in Table 2.2.5-1 as 2.28. Figure B-3 shows that the measured average value of $C_{vv,rel}$ was $2.29 \pm 4\%$. The agreement between the literature value and the measurements indicates that the light scattering apparatus was aligned correctly.

Two tips may be useful for future researchers aligning and calibrating light scattering systems. First, the elimination of spurious reflections (by covering reflective surfaces with black paint or cloth) is very important. In the process of checking the alignment for the first time, the scattering signal was found to increase dramatically at certain angles. The source of the increase was found to be spurious reflections from shiny metal objectives in the field of view of the detector. These surfaces were covered with black cloth, and the scattering signal decreased to the expected value.

The elimination of contaminants from the calibration gas is also important. Dust particles (or other contaminants) that pass through the beam are easily seen by the unaided eye (and, therefore, the detector). As the occasional dust (or other type of contaminant) particle passed through the laser beam, a bright flash was observed. The bright flashes were in sharp contrast to the steady, uniform scattering observed from dust-free nitrogen and carbon dioxide. Filters were placed in all the gas feed lines to remove dust particles. Without the filters, there was a large amount of noise in the scattering signals (due to the random nature of particles passing through the sample volume), and the measured value of $C_{vv,rel}$ was much lower than the literature value.

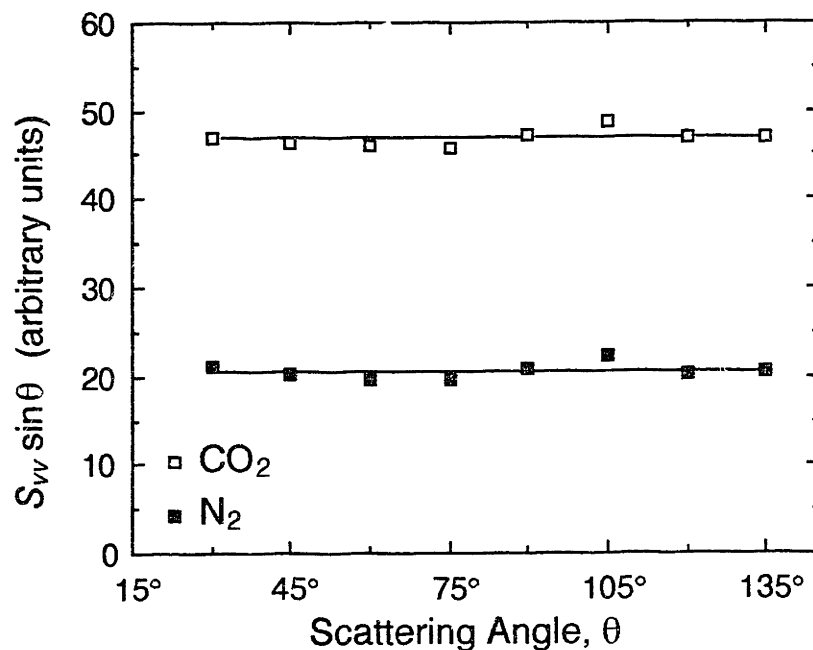


Figure B-2: Demonstration of alignment of the light scattering apparatus. These are typical measurements of the scattering signals from nitrogen and carbon dioxide. The horizontal lines are the average value for each gas.

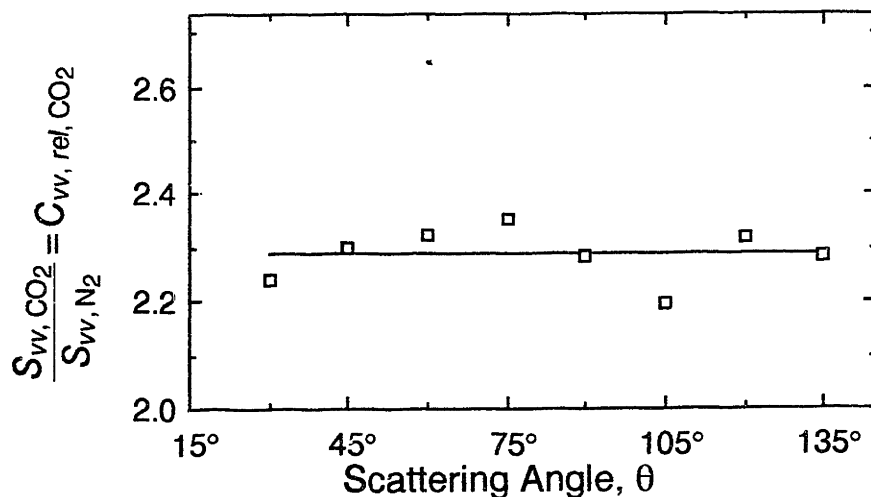


Figure B-3: Demonstration of alignment of the light scattering apparatus. These are typical measurements of the ratio of the scattering signals from nitrogen and carbon dioxide. The average value of the measurements (indicated by the horizontal line) is $2.29 \pm 4\%$. The literature value of this ratio is 2.28 (see Table 2.2.5-1). The good agreement between the measurements and the literature value indicates that the light scattering apparatus was aligned properly.

APPENDIX C: Correction of Mole Fractions to Account for Water Condensation

To correct the measured mole fractions to account for water condensation, a mass balance was performed on the system shown in Figure C-1. The purpose of the mass balance is to determine the total mole change upon reaction and the amount of water lost from the gas sample through condensation in the water cooled probe. This information can then be used to calculate the mole fractions in the flame ($x_i, IN SITU$) from the mole fractions measured in the sample bulb (x_i). The mass balance will show that the *in situ* mole fractions are about 12% less than the measured mole fractions.

The basis for the calculations is one minute of operation of the $C/O = 0.77$ flame. The inlet amounts of N_2 , O_2 , and C_2H_4 are known from the gas feed rates (see Table 3.1-1). The gases react to form a mixture which is assumed to consist of only seven species: N_2 , H_2 , H_2O , C_2H_2 , CO , CO_2 , and CH_4 . All other species have measured mole fractions less than 10^{-3} and can be neglected for these calculations. The total number of moles present after reaction is denoted by n . An unknown fraction of the total gas flow, ϵ , enters the water-cooled quartz probe. Two streams are assumed to leave the probe: the first stream consists only of condensed H_2O ; the second stream consists only of gas, and is assumed to be saturated with H_2O at the cooling water temperature, $16^\circ C$. Therefore, the mole fraction of water in the sample bulb is 0.018.

The values assigned to the streams in Figure C-1 already satisfy the nitrogen balance. In addition, the mass balances around the probe and the branch point labeled B have been satisfied. The next step in solving the mass balance is to take advantage of the composition measurements and the assumption of saturation:

$$\frac{a}{n-d} = x_{H_2} \quad (C-1)$$

$$\frac{b}{n-d} = x_{H_2O(g)} = 0.018 \quad (C-2)$$

$$\frac{e}{n-d} = x_{C_2H_2} \quad (C-3)$$

$$\frac{f}{n-d} = x_{CO} \quad (C-4)$$

$$\frac{g}{n-d} = x_{CO_2} \quad (C-5)$$

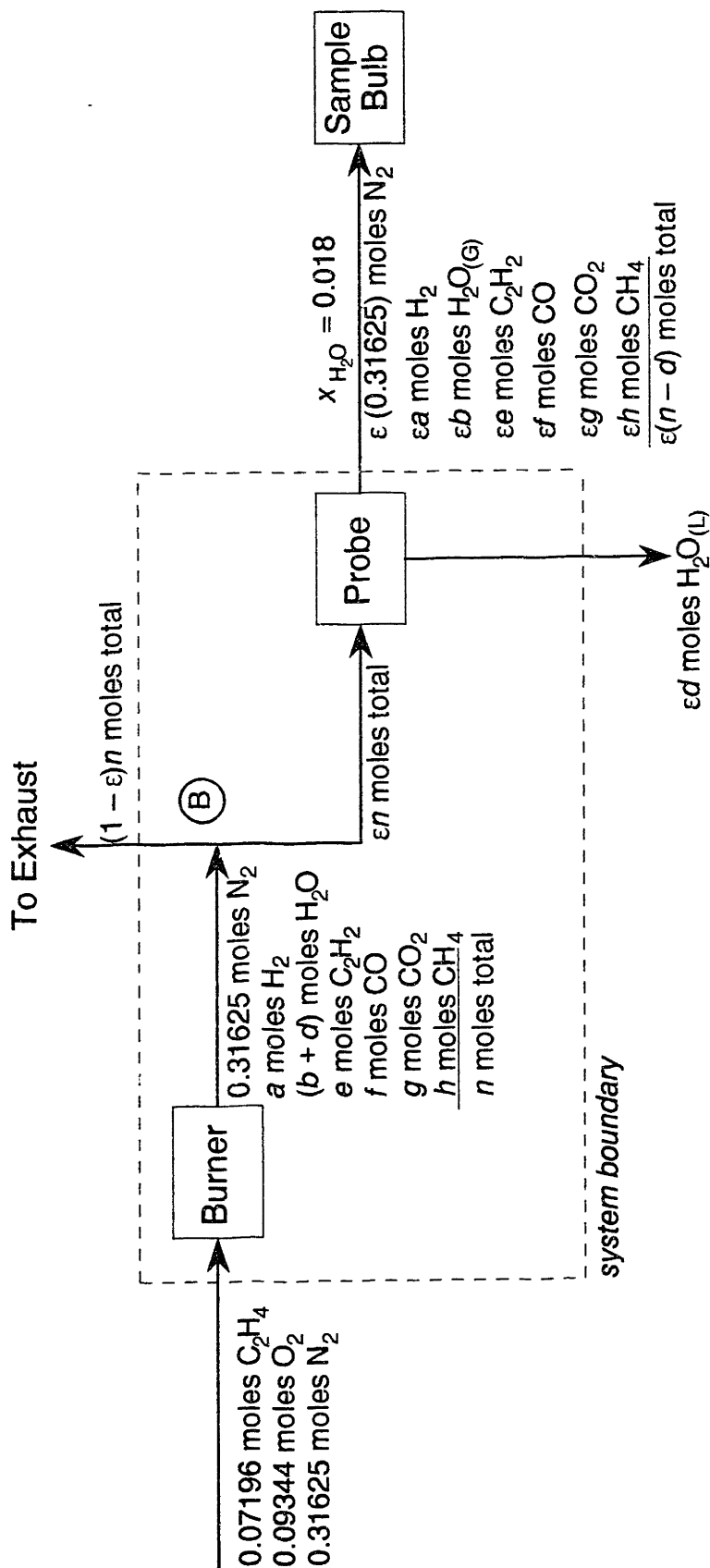


Figure C-1: Diagram of the gas sampling apparatus and the system on which the mass balance is performed. In this Figure, the mass balance on nitrogen has already been satisfied. The mass balances around the probe and the branch point labeled *B* have been satisfied as well. The gas leaving the probe is saturated with water at 16°C. The basis for the calculations is one minute of operation of the C/O = 0.77 flame. The mole fractions of hydrogen, acetylene, carbon monoxide, carbon dioxide, and methane in the sample bulb were measured.

$$\frac{h}{n-d} = x_{\text{CH}_4} \quad (\text{C-6})$$

Performing a carbon balance around the system boundary shown in Figure C-1 yields

$$2 (0.07196) = 2e + f + g + h \quad (\text{C-7})$$

A hydrogen balance around the same system gives

$$4 (0.07196) = 2a + 2b + 2d + 2e + 4h \quad (\text{C-8})$$

and an oxygen balance gives

$$2 (0.09344) = b + d + f + 2g \quad (\text{C-9})$$

Finally, the definition of n gives

$$n = 0.31625 + a + b + d + e + f + g + h \quad (\text{C-10})$$

Thus, there are 10 equations and 8 unknowns: a, b, d, e, f, g, h , and n . Notice that ε cancels out of all of the equations, and cannot be determined. Again, the nitrogen balance around this system has already been used in writing Equations C-1 through C-10.

Since the system is over-determined, Equations C-1 through C-10 cannot be satisfied simultaneously; two equations must be left unsatisfied. There are many possible combinations of equations that could be solved. However, in order to take maximum advantage of the measurements and the assumption of saturation, Equations C-1 through C-6 should always be satisfied. If these 6 equations are substituted into Equations C-7 through C-10, then a, b, e, f, g , and h can be eliminated, leaving a set of 4 equations with 2 unknowns. The carbon balance (Eq. C-7) becomes

$$\frac{2 (0.07196)}{n-d} = 2 x_{\text{C}_2\text{H}_2} + x_{\text{CO}} + x_{\text{CO}_2} + x_{\text{CH}_4} \quad (\text{C-11})$$

The hydrogen balance (Eq. C-8) becomes

$$\frac{4 (0.07196)}{n-d} = 2 x_{\text{C}_2\text{H}_2} + 2 x_{\text{H}_2\text{O}_{(g)}} + 2 x_{\text{H}_2} + 4 x_{\text{CH}_4} + \frac{2d}{n-d} \quad (\text{C-12})$$

and the oxygen balance (Eq. C-9) becomes

$$\frac{2 (0.09344)}{n-d} = x_{\text{H}_2\text{O}_{(g)}} + 2 x_{\text{CO}_2} + x_{\text{CO}} + \frac{d}{n-d} \quad (\text{C-13})$$

The approach used here will be to solve any two of these three equations for n and d . The *in situ* mole fractions of CO , CO_2 , H_2 , C_2H_2 , and CH_4 are found by rearranging Equations C-1 and C-3 through C-6 to give:

$$x_{i, \text{INSITU}} = x_i \frac{n-d}{n} \quad (\text{C-14})$$

The *in situ* mole fraction H_2O is found by rearranging Equation C-2, giving

$$x_{\text{H}_2\text{O}, \text{INSITU}} = x_{\text{H}_2\text{O}(\text{g})} \frac{n-d}{n} + \frac{d}{n} \quad (\text{C-15})$$

and the *in situ* mole fraction N_2 is given by

$$x_{\text{N}_2, \text{INSITU}} = \frac{0.31625}{n} \quad (\text{C-16})$$

The three possible combinations of Equations C-11, C-12, and C-13 will be denoted ‘Method #1,’ ‘Method #2,’ and ‘Method #3’ (see Table C-1). In Method #1, the carbon balance and the hydrogen balance (Eq. C-11 and Eq. C-12) are solved simultaneously to determine n and d . In Method #2, the carbon balance and the oxygen balance (Eq. C-11 and Eq. C-13) are solved to determine n and d . In Method #3, the oxygen balance and the hydrogen balance (Eq. C-12 and Eq. C-13) are solved to determine n and d . In each method, the *in situ* mole fractions are subsequently calculated from Equations C-14, C-15, and C-16.

In the original set of 10 equations (Equations C-1 through C-10), two equations had to be left unsatisfied. In Method #1, Eq. C-9 (the oxygen balance) is not satisfied; in Method #2, Eq. C-8 (the hydrogen balance) is not satisfied; and in Method #3, Eq. C-7 (the carbon balance) is not satisfied. For each method, the second unsatisfied equation is Eq. C-10. This equation will be used as a consistent check on the “goodness” of the mass balance closure. If Eq. C-10 is divided by n , it is equivalent to stating that the sum of the *in situ* mole fractions must be unity:

$$\sum_{i=1}^7 x_{i, \text{INSITU}} = 1.0 \quad (\text{C-17})$$

Therefore, by comparing the left-hand side of Eq. C-17 to 1.0 for each of the three methods, a comparative measure of the “goodness” of the mass balance closure in each of three methods can be obtained.

Figure C-2 compares the sum of the *in situ* mole fractions for each of the three methods. Method #1 and Method #2 give almost identical results. For these two methods, the average sum of the *in situ* mole fractions is 1.05, or in other words, the mass balance closes within 5%. For Method #3, the average sum of the *in situ* mole fractions is 1.51, or the mass balance closes within 51%. The relatively poor closure of the mass balance using Method #3 arises from having to subtract two numbers which are almost equal

Mass Balance Method	Equations Satisfied	Equations Not Satisfied	Average Value of $\sum_{i=1}^7 x_i, IN\ SITU$	Average Value of $\frac{n-d}{n}$
#1	C-11, C-12	C-13, C-17	1.05	0.875
#2	C-11, C-13	C-12, C-17	1.05	0.883
#3	C-12, C-13	C-11, C-17	1.51	0.654

Table C-1: Summary of the mass balance methods and results. Equations C-11, C-12, C-13, and C-17 form an over-determined system of 4 equations with only 2 unknowns, n and d .

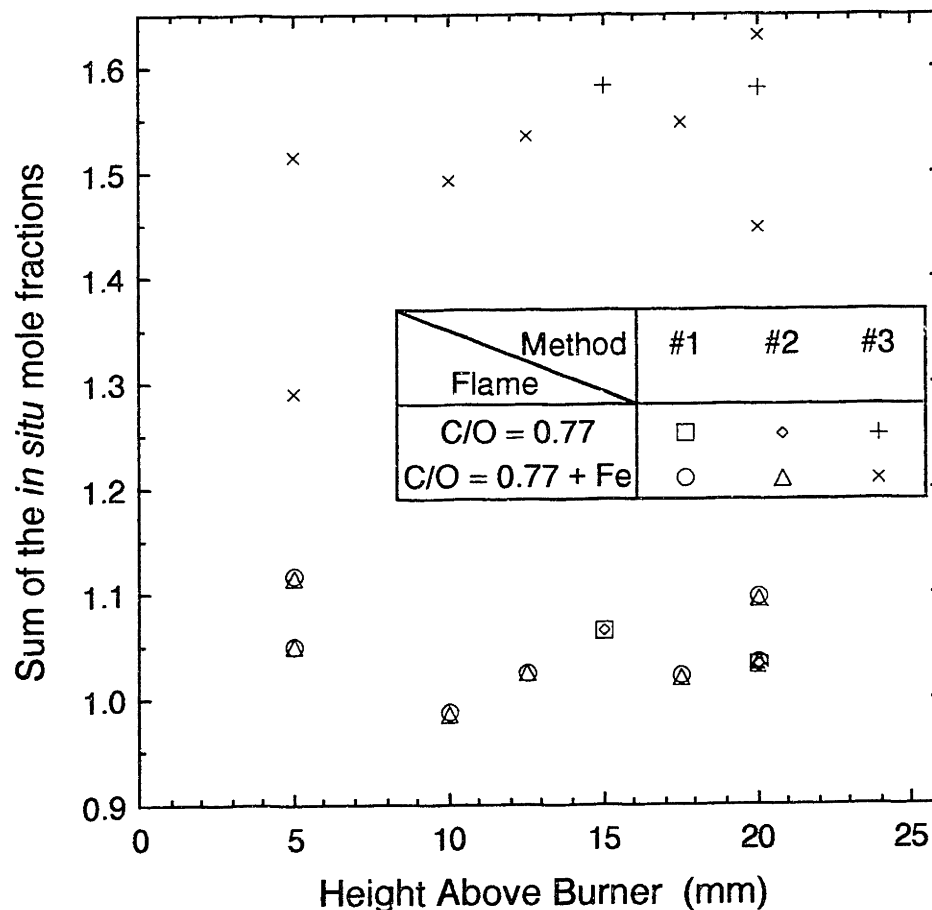


Figure C-2: The sum of the *in situ* mole fractions calculated by three different methods. Methods #1 and 2 yield almost identical results, and close the mass balance within an average of 5%. The closure of the mass balance is not effected by the addition of iron or by changes in the height above burner.

in order to determine n and d . Figure C-2 also shows that the presence or absence of the additive does not effect the sum of the *in situ* mole fractions. In addition, there is no correlation between the height above burner and the sum of the *in situ* mole fractions.

Another parameter of interest is $(n - d)/n$, since this is the factor the measured mole fractions are multiplied by to determine the *in situ* mole fractions. As shown in Table C-1, the average value of $(n - d)/n$ is 0.875 using Method #1 and 0.883 using Method #2. In other words, the *in situ* mole fractions are about 12% less than the measured mole fractions. Like the sum of the *in situ* mole fractions, $(n - d)/n$ does not vary significantly with changes in the height above burner or the addition of iron.

Allowing water to condense in the probe significantly improves the mass balance closure. Although the details will not be presented here, a similar analysis can be conducted without allowing water to condense in the probe, by assuming that all of the water ends up in the gas phase in the bulb. With this assumption, a similar set of equations can be developed, consisting of 9 equations and 7 unknowns (Eq. C-2 is removed from the set, along with the unknown d). The analogs to Methods #1, 2, and 3 can be formulated and the sum of the *in situ* mole fractions can be calculated. For Method #1, the average sum of the *in situ* mole fractions increases from 1.05 to 1.19; for Method #2, it increases from 1.05 to 1.15; and for Method #3, it increases from 1.51 to 1.59. In addition, this approach yields a mole fraction of water in the bulb that is above saturation, and as stated in Section 3.4, water condensation was not observed in the sample bulbs.

For these reasons, measured mole fractions have been converted into *in situ* mole fractions using Method #2. The *in situ* mole fraction H_2O was also calculated using Method #2. Equation C-14 and the correction factor $(n - d)/n$ were applied to all species measured in the gas sample bulbs, not just the species appearing in the mass balance. The choice of Method #2 over Method #1 is arbitrary, since both methods yield equally good closure of the mass balance.

The mole fractions of CO , CO_2 , and H_2 were not measured for some samples because the GC used for these measurements was, at times, not functioning. For these samples, the measured mole fractions were corrected using Eq. C-14 and the average value of $(n - d)/n$ given in Table C-1 for Method #2.

APPENDIX D: Thermophoretic Sampling Probe Timing Circuit

A schematic diagram of the timing circuit that was used to control the motion of the thermophoretic sampling probe is shown in Figure D-1. This circuit is designed to be powered by a 12 V battery, and output a 12 V square pulse when a pushbutton switch is closed. The width of the pulse is determined by the setting of 10-turn, 100 k Ω potentiometer.

The circuit was calibrated by attaching a Tektronix 5223 digitizing oscilloscope across the output terminals with no load attached. The results of the calibration are shown in Figure D-2, which plots the width of the output voltage pulse as a function of the potentiometer dial setting. The width of the pulse is a linear function of the potentiometer setting, with the best-fit line being

$$\text{Pulse Width (ms)} = 206.78 - 0.20444 \times (\text{Setting}) \quad (\text{D-1})$$

Substitution of this equation for pulse width into Eq. 3.5-1 gives

$$\tau_e \text{ (ms)} = 171.1 - 0.1987 \times (\text{Setting}) \quad (\text{D-2})$$

Equation D-2 is the relationship used in practice to set the exposure time.

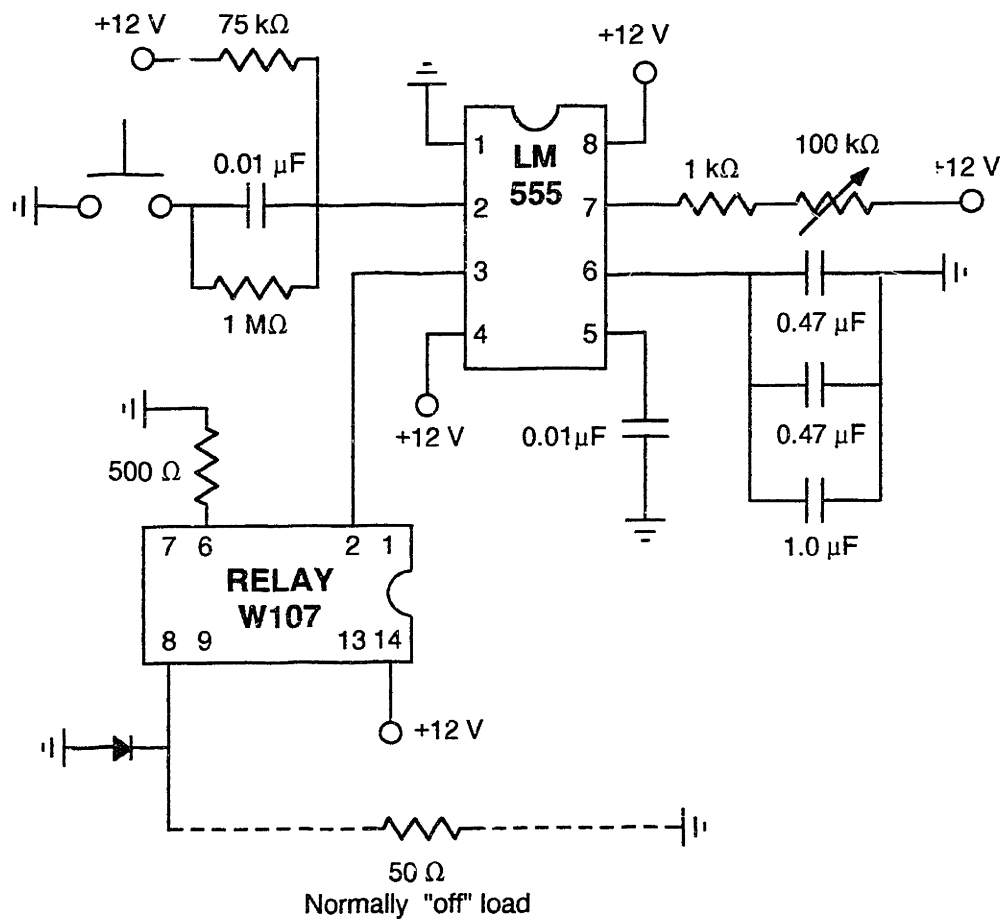


Figure D-1: Schematic diagram of the thermophoretic sampling probe timing circuit. The normally "off" load is a 4-way valve. Ground is the negative pole of a 12 V battery.

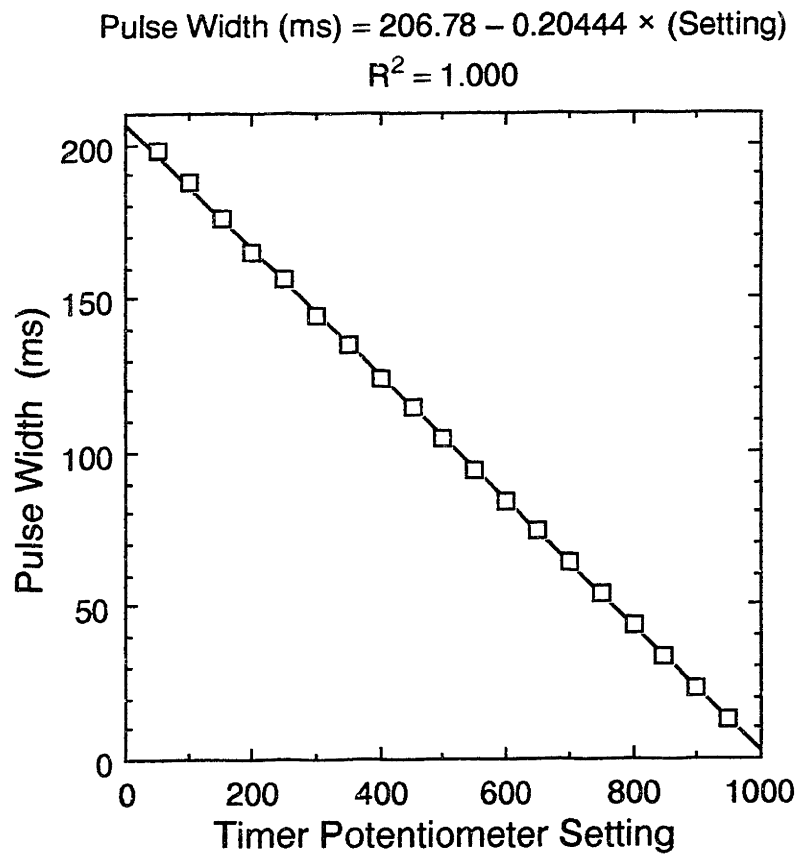


Figure D-2: Calibration of the thermophoretic sampling probe timing circuit.

APPENDIX E: Validity of Light Scattering Assumptions

In Section 2.2, three assumptions were made to simplify the interpretation of light scattering and absorption measurements. The purpose of this appendix is to show that these three assumptions were valid for the measurements made in this thesis.

The first assumption was that the optical sample volume contained a statistically large number of particles. The scattering volume can be approximated as a cylinder, with its axis parallel to the burner. The diameter of the cylinder was about 250 μm , and the height of the cylinder was about 2 mm, giving a total volume of about $9.8 \times 10^{-5} \text{ cm}^3$. Since the minimum number density in any of the flames was about 10^9 particles/ cm^3 , the scattering sample volume contained a minimum of about 10^5 particles. The maximum number density was about 10^{13} particles/ cm^3 , so the scattering sample volume contained as many as 10^9 particles at short residence times. The sample volume for K_{ext} measurements was larger than the scattering sample volume. Therefore, the assumption of a statistically large number of particles in the optical sample volume was good.

The second assumption was that each particle scatters as a separate entity, which is a good assumption provided that the separation distance between particles is greater than 3 particle radii (Kerker, 1969). For 100 nm particles, this constraint translates into a maximum number density of 10^{13} particles/ cm^3 ; the maximum permitted number density increases as the particle diameter decreases. Examination of the diameter and number density profiles in Sections 5.4 and 5.5 shows that the number density was always far below the limit, and the assumption that each particle scatters as a separate entity is valid.

The third assumption was that multiple scattering is negligible, or that the optical mean free path was greater than the physical dimension of the system. This assumption is equivalent to assuming $1/K_{ext} \gg L$, or $(K_{ext} L) \ll 1$. The product $(K_{ext} L)$ reached its maximum values at large residence times in flames with the largest soot volume fractions. In the C/O = 0.77 + Fe flame, the maximum value of $(K_{ext} L)$ was 0.063. In the C/O = 0.83 + Fe flame, the maximum value of $(K_{ext} L)$ was 0.31. This assumption was very good in most flames at all residence times, but not as good in the heavily sooting flames at large residence times.

REFERENCES

- Andrews, J. T. S. and E. F. Westrum, Jr., "Vapor Pressure and Third-Law Entropy of Ferrocene," *Journal of Organometallic Chemistry*, **17**: 349-352 (1969).
- Baker, R. T. K., "In Situ Electron Microscopy Studies of Catalyst Particle Behavior," *Catal. Rev.-Sci. Eng.*, **19** (2): 161-209 (1979).
- Barbella, R., F. Beretta, A. Ciajolo, A. D'Alessio, M. V. Prati, and A. Tregrossi, "Optical and Chemical Characterization of Carbon Polymorphs Formed During Spray Combustion of Hydrocarbons," *Combustion Science and Technology*, to appear (1990).
- Bartholomé, E. and H. Sachsse, "Katalytische Erscheinungen an Aerosolen," *Zeitschrift für Elektrochemie*, **53** (5): 326 (1949).
- Baum, R. M., "Ideas on Soot Formation Spark Controversy," *Chemical and Engineering News*, pp. 30-32, February 5, 1990.
- Baumgärtner, L., D. Hesse, H. Jander, and H. Gg. Wagner, "Rate of Soot Growth in Atmospheric Premixed Laminar Flames," *Twentieth Symposium (International) on Combustion*, Pittsburgh: The Combustion Institute, 959-967 (1984).
- Berlman, I. B., *Handbook of Fluorescence Spectra of Aromatic Molecules*, Second Edition, New York: Academic Press (1971).
- Bittner, J. B., "A Molecular Beam Mass Spectrometer Study of Fuel-Rich and Sooting Benzene-Oxygen Flames," Ph. D. Thesis, Department of Chemical Engineering, Massachusetts Institute of Technology (1981).
- Bockhorn, H., F. Fetting, A. Heddrich, and G. Wannemacher, "Investigation of the Surface Growth of Soot in Flat Low Pressure Hydrocarbon Oxygen Flames," *Twentieth Symposium (International) on Combustion*, Pittsburgh: The Combustion Institute, 979-988 (1984).
- Bockhorn, H., F. Fetting, G. Wannemacher, and H. W. Wenz, "Optical Studies of Soot Particle Growth in Hydrocarbon Oxygen Flames," *Nineteenth Symposium (International) on Combustion*, Pittsburgh: The Combustion Institute, 1413-1420 (1982).

- Bockhorn, H., F. Fetting, U. Meyer, R. Reck, and G. Wannemacher, "Measurements of the Soot Concentration and Soot Particle Sizes in Propane Oxygen Flames," *Eighteenth Symposium (International) on Combustion*, Pittsburgh: The Combustion Institute, 1131-1147 (1981).
- Bohren, C. F. and D. R. Huffman, *Absorption and Scattering of Light by Small Particles*, New York: Wiley and Sons (1983).
- Bonczyk, P. A., "In-Situ Optical Measurement of Additive Effects on Particulates in a Sooting Diffusion Flame," *Combustion and Flame*, **51**: 219-229 (1983).
- Bonczyk, P. A., "Suppression of Soot in Flames by Alkaline-Earth and Other Metal Additives," *Combustion Science and Technology*, **59**: 143-163 (1988).
- Bonczyk, P. A., "The Influence of Alkaline-Earth Additives on Soot and Hydroxyl Radicals in Diffusion Flames," *Combustion and Flame*, **67**: 179 (1987).
- Bonne, U., K. H. Homann, and H. Gg. Wagner, "Carbon Formation in Premixed Flames," *Tenth Symposium (International) on Combustion*, Philadelphia: The Combustion Institute, 503-512 (1965).
- Bridge, N. J. and A. D. Buckingham, "The Polarization of Laser Light Scattered by Gases," *Proc. Roy. Soc.*, **A295**: 334-349 (1966).
- Bulewicz, E. M., D. G. Evans, and P. J. Padley, "Effect of Metallic Additives on Soot Formation Processes in Flames," *Fifteenth Symposium (International) on Combustion*, Pittsburgh: The Combustion Institute, 1461-1470 (1975).
- Calcote, H. F., "Ions in Flames," in *Ion-Molecule Reactions*, J. L. Franklin, ed., New York: Plenum Press (1972).
- Calcote, H. F. and D. G. Keil, "Ion Molecule Reactions in Sooting Acetylene-Oxygen Flames," *Combustion and Flame*, **74**: 131-146 (1988).
- Charalampopoulos, T. T. and J. D. Felske, "Refractive Indices of Soot Particles Deduced from In-Situ Laser Light Scattering Measurements," *Combustion and Flame*, **68**: 283-294 (1987).

- Coe, D. S., B. S. Haynes, and J. I. Steinfeld, "Identification of a Source of Argon-Ion-Laser Excited Fluorescence in Sooting Flames," *Combustion and Flame*, **43**: 211-214 (1981).
- Cordes, Von J. F. and S. Schreiner, "Dampfdruckmessungen bei einigen Aromatenkomplexen," *Zeitschrift für anorganische und allgemeine Chemie*, Band 299, 87-91 (1959).
- Cotton, D. H., N. J. Friswell, and D. R. Jenkins, *Combustion and Flame*, **17**: 87 (1971).
- Curtis, H., *Biology*, New York: Worth Publishers (1979).
- D'Alessio, A., "Laser Light Scattering and Fluorescence Diagnostics of Rich Flames Produced by Gaseous and Liquid Fuels," in *Particulate Carbon: Formation During Combustion*, D. C. Siegla and G. W. Smith, eds., New York: Plenum Press (1981).
- D'Alessio, A., A. Di Lorenzo, A. Borghese, F. Beretta and S. Masi, "Study of the Soot Nucleation Zone of Rich Methane-Oxygen Flames," *Sixteenth Symposium (International) on Combustion*, Pittsburgh: The Combustion Institute, 695-708 (1977).
- D'Alessio, A., A. Di Lorenzo, A. F. Sarofim, F. Beretta, S. Masi, and C. Venitozzo, "Soot Formation in Methane-Oxygen Flames," *Fifteenth Symposium (International) on Combustion*, Pittsburgh: The Combustion Institute, 1427-1438 (1975).
- D'Alessio, A., A. Di Lorenzo, F. Beretta, and C. Venitozzi, "Optical and Chemical Investigations on Fuel-Rich Methane-Oxygen Flames at Atmospheric Pressure," *Fourteenth Symposium (International) on Combustion*, Pittsburgh: The Combustion Institute, 941-953 (1973).
- Dalzell, W. H. and A. F. Sarofim, "Optical Constants of Soot and Their Application to Heat-Flux Calculations," *Journal of Heat Transfer*, **91** (1): 100-104 (1969).
- Dasch, C. J., "The Decay of Soot Surface Growth Reactivity and Its Importance in Total Soot Formation," *Combustion and Flame*, **61**: 219-225 (1985).

- Di Lorenzo, A., A. D'Alessio, V. Cincotti, S. Masi, P. Menna, and C. Venitozzi, "UV Absorption, Laser Excited Fluorescence and Direct Sampling in the Study of the Formation of Polycyclic Aromatic Hydrocarbons in Rich CH₄/O₂ Flames," *Eighteenth Symposium (International) on Combustion*, Pittsburgh: The Combustion Institute (1981).
- Dobbins, R. A. and C. M. Megaridis, "Absorption and Scattering of Light by Fractal Aggregates," presented at the Second International Congress on Optical Particle Sizing, Tempe, Arizona (1990).
- Dobbins, R. A. and C. M. Megaridis, "Morphology of Flame-Generated Soot as Determined by Thermophoretic Sampling," *Langmuir*, **3**: 254 (1987).
- Dobbins, R. A., Santoro, and Semerjian, "Interpretation of Optical Measurements of Soot in Flames," in *Combustion Diagnostics by Nonintrusive Methods*, T. D. McCay and J. A. Roux, eds., New York: American Institute of Aeronautics and Astronautics (1983).
- Du, Z., "Kinetic Modeling of Carbon Oxidation," Sc. D. Thesis, Department of Mechanical Engineering, Massachusetts Institute of Technology (1990).
- Eckert, E. R. G. and R. M. Drake, Jr., *Heat and Mass Transfer*, New York: McGraw-Hill (1959).
- Edwards, J. W. and G. L. Kington, "Thermodynamic Properties of Ferrocene; Part 2.— Vapor Pressure and Latent Heat of Sublimation at 25°C by the Effusion and Thermistor and Manometer Methods," *Trans. Faraday Soc.*, **58**: 1323-1333 (1962).
- Felske, J. D., P. F. Hsu, and J. C. Ku, "The Effect of Soot Particle Optical Inhomogeneity and Agglomeration on the Analysis of Light Scattering Measurements in Flames," *J. Quant. Spectrosc. Radiat. Transfer*, **35** (6): 447-465 (1986).
- Felske, J. D., T. T. Charalampopoulos, and H. S. Hura, "Determination of the Refractive Index of Soot Particles from the Reflectivities of Compressed Soot Pellets," *Combustion Science and Technology*, **37**: 263-284 (1984).
- Fenimore, C. P. and G. W. Jones, "Oxidation of Soot by Hydroxyl Radicals," *J. Phys. Chem.*, **71** (3): 593-597 (1967).
- Feugier, A., *Adv. Chem.*, **166**: 178 (1978).

- Feugier, A., *Combustion Institute European Symposium*, F. J. Weinberg, ed., London: Academic Press, 406 (1973).
- Figueiredo, J. L., J. Rivera-Utrilla, and M. A. Ferro-Garcia, "Gasification of Active Carbons of Different Textures Impregnated with Nickel, Cobalt and Iron," *Carbon*, **25** (5): 703-708 (1987).
- Floess, J. K., "The Effects of Calcium on the Gasification Reactions of Carbon," Ph. D. Thesis, Department of Chemical Engineering, Massachusetts Institute of Technology (1985).
- Frenklach, M., D. W. Clary, W. C. Gardiner, and S. E. Stein, *Twentieth Symposium (International) on Combustion*, Pittsburgh: The Combustion Institute, 887 (1984).
- Friedlander, S. K., *Smoke, Dust and Haze: Fundamentals of Aerosol Behavior*, New York: John Wiley & Sons (1977).
- Friswell, N. J., "Emissions from Gas-Turbine-Type Combustors," in *Emissions from Continuous Combustion Systems*, W. Cornelius and W. G. Agnew, eds., New York: Plenum Press, p. 161 (1972).
- Giovanni, D. V., P. J. Pagni, R. F. Sawyer, and L. Hughes, *Comb. Sci. Tech.*, **6**: 107 (1972).
- Golothan, D. W., "Diesel Engine Exhaust Smoke: The Influence of Fuel Properties and the Effects of Using a Barium Containing Fuel Additive," SAE Paper 670092, January (1967).
- Gomez, A., M. G. Littman, and I. Glassman, "Comparative Study of Soot Formation on the Centerline of Axisymmetric Laminar Diffusion Flames: Fuel and Temperature Effects," *Combustion and Flame*, **70**: 225-241 (1987).
- Gordon, S. and McBride, "Computer Program for Calculation of Complex Chemical Equilibrium Compositions, Rocket Performance, Incident and Reflected Shocks, and Chapman-Jouget Detonations," NASA-SP-273, March (1976).
- Graham, S. C., A. J. Grant, and J. M. Jones, *AIAA Journal*, **12**: 1140 (1974).

- Graham, S. C. and A. Robinson, "A Comparison of Numerical Solutions to the Self-Preserving Size Distribution for Aerosol Coagulation in the Free-Molecule Regime," *J. Aerosol Sci.*, **7**: 261-273 (1976).
- Graham, S. C., "The Collisional Growth of Soot Particles at High Temperatures," *Sixteenth Symposium (International) on Combustion*, Pittsburgh: The Combustion Institute, 663-669 (1977).
- Gray, D. E., ed., *American Institute of Physics Handbook*, 3rd edition, New York: McGraw-Hill, p. 6-118 (1972).
- Güttler, Von. A., "Die Miesche Theorie der Beugung durch dielektrische Kugeln mit absorbierendem Kern und ihre Bedeutung für Probleme der interstellaren Materie und des atmosphärischen Aerosols," *Annalen der Physik*, 6. Folge, Band 11, 65-98 (1952).
- Habib, Z. and P. Vervisch, "Optical Constants of Soot by Means of the H/C Ratio in Hydrocarbon Flames," *Joint Meeting of the French and Italian Sections of the Combustion Institute*, Naples: CUEN (1987).
- Harris, S. J. and A. M. Weiner, "Surface Growth of Soot Particles in Premixed Ethylene/Air Flames," *Combustion Science and Technology*, **31**: 155-167 (1983(a)).
- Harris, S. J. and A. M. Weiner, "Determination of the Rate Constant for Soot Surface Growth," *Combustion Science and Technology*, **32**:, 267-275 (1983(b)).
- Harris, S. J. and A. M. Weiner, "Soot Particle Growth in Premixed Toluene/Ethylene Flames," *Combustion Science and Technology*, **33**: 75-87 (1984(a)).
- Harris, S. J. and A. M. Weiner, "Some Constraints on Soot Particle Inception in Premixed Ethylene Flames," *Twentieth Symposium (International) on Combustion*, Pittsburgh: The Combustion Institute, 969-878 (1984(b)).
- Harris, S. J., A. M. Weiner, and C. C. Ashcraft, "Soot Particle Inception Kinetics in a Premixed Ethylene Flame," *Combustion and Flame*, **64**: 65-81 (1986).
- Harris, S. J. and I. M. Kennedy, "The Coagulation of Soot Particles with van der Waals Forces," *Combustion Science and Technology*, **59**: 443-454 (1988).

- Hayhurst, A. N. and H. R. N. Jones, "The Effect of Metallic Additives on Ionization and Soot Formation in Oxy-Acetylene Flames," *Combustion and Flame*, **78**: 339-356 (1989).
- Haynes, B. S. and H. Gg. Wagner, "Soot Formation," *Progress in Energy and Combustion Science*, **7**: 229-273 (1980).
- Haynes, B. S. and H. Gg. Wagner, "The Surface Growth Phenomenon in Soot Formation," *Zeitschrift für Physikalische Chemie, Neue Folge*, **133**: 201-213 (1982).
- Haynes, B. S., H. Jander, and H. Gg. Wagner, "Optical Studies of Soot Formation Processes in Premixed Flames," *Berichte der Bunsen Gesellschaft für Physikalische Chemie*, **84**: 585 (1980).
- Haynes, B. S., H. Jander, and H. Gg. Wagner, "The Effect of Metal Additives on the Formation of Soot in Premixed Flames," *Seventeenth Symposium (International) on Combustion*, Pittsburgh: The Combustion Institute, 1365-1374 (1979).
- Haynes, B. S., H. Jander, H. Mätzing, and H. Gg. Wagner, "The Influence of Gaseous Additives on the Formation of Soot in Premixed Flames," *Nineteenth Symposium (International) on Combustion*, Pittsburgh: The Combustion Institute, 1379-1385 (1982).
- Homann, K. H. and H. G. Wagner, "Some New Aspects of the Mechanism of Carbon Formation in Premixed Flames," *Eleventh Symposium (International) on Combustion*, Philadelphia: The Combustion Institute, 371-379 (1967).
- Howard, J. B. and W. J. Kausch, Jr., "Soot Control by Fuel Additives," *Prog. Energy Comb. Sci.*, **6**: 263-276 (1980).
- Howard, J. B. and J. P. Longwell, "Formation Mechanisms of PAH and Soot in Flames," in *Polynuclear Aromatic Hydrocarbons: Formation, Metabolism, and Measurement*, M. Cooke and A. J. Dennis, Columbus: Battelle Press, 27 (1983).
- Hughes, R., "An Unfamiliar Michelangelo," *Time*, February 11, 1985.
- Hughes, R., "Out of Grime, a Domain of Light," *Time*, April 27, 1987.

- Jenkins, D. R., "Proposed Mode of Action of Alkaline Earth Metals in Suppressing Soot," *Combustion Science and Technology*, **5**: 245-249 (1972).
- Jones, A. R. and W. Wong, "Direct Optical Evidence for the Presence of Sooty Agglomerates in Flames," *Combustion and Flame*, **24**: 139-140 (1975).
- Kennedy, I. M., "Soot Aerosol Dynamics in a Stagnation Point Diffusion Flame," *Twentieth Symposium (International) on Combustion*, Pittsburgh: The Combustion Institute, 1095 (1984).
- Kerker, M., *The Scattering of Light and other Electromagnetic Radiation*, New York: Academic Press (1969).
- Kettlewell, H. B. D., "Phenomenon of Industrial Melanism in Lepidoptera," *Annual Review of Entomology*, **6**: 245 (1961).
- Krishnan, R. S., *Kolloid-Z.*, **84**: 2 (1938).
- Kukin, I., *Environ. Sci. Tech.*, **7** (7): 606 (1973).
- Kumar, S. and C. L. Tien, "Effective Diameter of Agglomerates for Radiative Extinction and Scattering," *Combustion Science and Technology*, **66**: 199-216 (1989).
- Lafleur, A. L., personal communication, May, 1990.
- Lafleur, A. L., P. A. Monchamp, E. F. Plummer, and E. L. Kruzel, *Analytical Letters*, **19**: 2013 (1986).
- Lam, F. W., J. B. Howard, and J. P. Longwell, "The Behavior of Polycyclic Aromatic Hydrocarbons During the Early Stages of Soot Formation," *Twenty-Second Symposium (International) on Combustion*, Pittsburgh: The Combustion Institute, 323-332 (1988).
- Lam, F. W., personal communication, November, 1988(a).
- Lam, F. W., "The Formation of Polycyclic Aromatic Hydrocarbons and Soot in a Jet-Stirred/Plug-Flow Reactor," Ph. D. Thesis, Department of Chemical Engineering, Massachusetts Institute of Technology (1988(b)).

- Landolt-Börnstein, ed., *Zahlenwerte und Funktionen aus Physik, Chemie, Astronomie, Geophysik, und Technik*, II. Band, Eigenschaften der Materie in Ihren Aggregatzuständen, 8. Teil, Optische Konstanten, Berlin: Springer-verlag (1962).
- Lee, S. C. and C. L. Tien, "Optical Constants of Soot in Hydrocarbon Flames," *Eighteenth Symposium (International) on Combustion*, Pittsburgh: The Combustion Institute, 1159-1166 (1981).
- Lorenz, L., *Oeuvres Scientifiques*, Vol. 1, p. 301, Copenhagen (1898).
- Marinescu, M. and A. Danescu, *Rev. Roum. Sci. Tech. Electrochem. Ener.*, **21**: 617 (1976).
- Marlow, W. H. and L. A. Slatest, "Intermolecular Forces in the Collision Rates of Small Molecular Clusters," in *Aerosols: Science, Technology, and Industrial Applications of Airborne Particles*, B. Y. H. Liu, D. Y. H. Pui, and H. J. Fissan, eds., New York: Elsevier (1984).
- Martin, G. B., D. W. Pershing, and E. E. Berkau, U. S. EPA, Office of Air Programs, RTP, Pub. No. AP-87, June (1971).
- McKee, D. W., in *Chemistry and Physics of Carbon*, Vol. 16, P. L. Walker Jr., and P. A. Throver, eds., New York: Marcel Dekker (1980).
- McKinnon, J. T. Jr., "Chemical and Physical Mechanisms of Soot Formation," Ph. D. Thesis, Department of Chemical Engineering, Massachusetts Institute of Technology (1989).
- McMurray, P. H. and S. K. Friedlander, "Aerosol Formation in Reacting Gases: Relation of Surface Area to Rate of Gas-to-Particle Conversion," *J. Coll. Inter. Sci.*, **64**: 248 (1978).
- Megaridis, C. M., "Thermophoretic Sampling and Soot Aerosol Dynamics of an Ethene Diffusion Flame," Ph. D. Thesis, Brown University (1987).
- Mie, G., "Considerations on the optics of turbid media, especially colloidal metal sols," *Ann. Physik.*, **25**: 377 (1908).
- Millikan, R. C., "Non-Equilibrium Soot Formation in Premixed Flames," *J. Phys. Chem.*, **66**: 794 (1962).

- Müller-Dethlefs, K., "Optical Studies of Soot Formation and the Addition of Organic Peroxides to Flames," Ph. D. Thesis, Department of Chemical Engineering and Chemical Technology, Imperial College, London (1979).
- Müller-Dethlefs, K. and F. J. Weinberg, "Burning Velocity Measurement Based on Laser Rayleigh Scattering," *Seventeenth Symposium (International) on Combustion*, Pittsburgh: The Combustion Institute, 985-992 (1979).
- Nagle, J. and R. F. Strickland-Constable, "Oxidation of Carbon between 1000-2000°C," in *Proceedings of the Fifth Conference on Carbon*, London: Pergamon Press, 154-164 (1962).
- National Bureau of Standards, "Report of Calibration: Ribbon Filament Lamp," Test No. 217191, private communication, November 25, 1977.
- National Cancer Institute, *Survey of Compounds which have been Tested for Carcinogenic Activity, Sections I and II*, NIH Publication No. 85-2774, November, 1985.
- Nenniger, R. D., "Aerosols Produced from Coal Pyrolysis," Ph. D. Thesis, Department of Chemical Engineering, Massachusetts Institute of Technology (1986).
- Neoh, K. G., "Soot Burnout in Flames," Sc. D. Thesis, Department of Chemical Engineering, Massachusetts Institute of Technology (1980).
- Padley, P. J. and T. M. Sugden, *Trans. Farad. Soc.*, **55**: 2054 (1959).
- Page, F. M. and F. Ates, "Oxidation of Soot in Fuel-Rich Flames," *Evaporation-Combustion of Fuels*, in ACS Advances in Chemistry Series, J. T. Zang, ed., No. 166, pp. 190-197, Washington: ACS (1978).
- Palmer, H. B. and C. F. Cullis, "The Formation of Carbon from Gases," in *Chemistry and Physics of Carbon*, Vol. 1, P. L. Walker, ed., New York: Marcel Dekker (1965).
- Pelino, M., M. Tomassetti, V. Piacente, and G. D'Ascenzo, "Vapor Pressure Measurements of Ferrocene, Mono- and 1,1'-diacetylferrocene," *Thermochim. Acta* **44** (1): 89-99 (1981).

- Perrin, F., *J. Chem. Phys.*, **10**: 415 (1942).
- Perry, R. H. and C. H. Chilton, eds., *Chemical Engineers' Handbook*, Fifth Edition, New York: McGraw-Hill (1973).
- Petarca, L. and F. Marconi, "Fluorescence Spectra and Polycyclic Aromatic Species in a *N*-Heptane Diffusion Flame," *Combustion and Flame*, **78**: 308-325 (1989).
- Prado, G., A. Garo, A. Ko, and A. Sarofim, "Polycyclic Aromatic Hydrocarbons Formation and Destruction in a Laminar Diffusion Flame," *Twentieth Symposium (International) on Combustion*, Pittsburgh: The Combustion Institute, 989-996 (1984).
- Prado, G., J. Jagoda, K. Neoh, and J. Lahaye, "A Study of Soot Formation in Premixed Propane/Oxygen Flames by In-situ Optical Techniques and Sampling Probes," *Eighteenth Symposium (International) on Combustion*, Pittsburgh: The Combustion Institute, 1127-1136 (1981).
- Prado, G. and J. Lahaye, "Physical Aspects of Nucleation and Growth of Soot Particles," in *Particulate Carbon: Formation During Combustion*, D. C. Siegla and G. W. Smith, eds., New York: Plenum Press (1981).
- Ramer, E. R., J. F. Merklin, C. M. Sorensen, and T. W. Taylor, "Chemical and Optical Probing of Premixed Methane/Oxygen Flames," *Combustion Science and Technology*, **48**: 241 (1986).
- Rayleigh, Lord, *Phil. Mag.*, **49** (1900).
- Reynolds, W. C., STANJAN chemical equilibrium solver, v 3.60, available on disk (1987).
- Ritrievi, K. E., "The Effects of Iron on Soot Particle Formation and Growth," Sc. D. Thesis, Department of Chemical Engineering, Massachusetts Institute of Technology (1984).
- Rowell, R. L., G. M. Aval, and J. J. Barrett, "Rayleigh-Raman Depolarization of Laser Light Scattered by Gases," *The Journal of Chemical Physics*, **54** (5): 1960-1964 (1971).

- Rudder, R. R. and D. R. Bach, "Rayleigh Scattering of Ruby-Laser Light by Neutral Gases," *Journal of the Optical Society of America*, **58** (9): 1260-1266 (1968).
- Savitzky, A. and M. J. E. Golay, "Smoothing and Differentiation of Data by Simplified Least Squares Procedures," *Analytical Chemistry*, **36** (8): 1627-1639 (1964).
- Sax, N. I., *Dangerous Properties of Industrial Materials*, 6th ed., New York: Van Nostrand (1984).
- Smith, G. W., "Kinetic Aspects of Diesel Soot Coagulation," SAE Technical Paper 820466 (1982).
- Street, J. C. and A. Thomas. "Carbon Formation in Premixed Flames," *Fuel*, **34**: 4 (1955).
- Swift, D. L. and S. K. Friedlander, "The Coagulation of Hydrosols by Brownian Motion and Laminar Shear Flow," *Journal of Colloid Science*, **19**: 621 (1964).
- Taylor, B. R., "Reactions of Fixed Nitrogen Species in Fuel-Rich Flames," Sc. D. Thesis, Department of Chemical Engineering, Massachusetts Institute of Technology (1984).
- Toone, B., "A Review of Aero Engine Smoke Emission," *Cranfield International Symposium Series*, Vol. 10, *Combustion in Advanced Gas Turbine Systems*, I. E. Smith, ed., London: Pergamon Press (1968).
- Vaerman, J., "Problems of Soot Emissions and Low Temperature Corrosion in Domestic Oil-Fired Boilers," *Journal of the Institute of Petroleum*, **50** (487): 155 (1964).
- Vaughn, C. B., "Formation of Soot and Polycyclic Aromatic Hydrocarbons in a Jet-Stirred Reactor," Ph. D. Thesis, Department of Chemical Engineering, Massachusetts Institute of Technology (1988).
- Volk, W., *Applied Statistics for Engineers*, 2nd ed., New York: Robert E. Krieger Publishing Company (1980).
- Wang, C. S. and S. K. Friedlander, "The Self-Preserving Particle Size Distribution for Coagulation by Brownian Motion," *Journal of Colloid and Interface Science*, **24**: 170 (1967).

- Weeks, R. L., W. L. Clinkerbeard, and J. D. Solties, *Proc. Fifth World Petroleum Congress*, Section VI, 381 (1959).
- Wersborg, B. L., A. C. Yeung, and J. B. Howard, "Concentration and Mass Distribution of Charged Species in Sooting Flames," *Fifteenth Symposium (International) on Combustion*, Pittsburgh: The Combustion Institute, 1439-1448 (1975).
- Wersborg, B. L., J. B. Howard, and G. C. Williams, "Physical Mechanisms in Carbon Formation in Flames," *Fourteenth Symposium (International) on Combustion*, Pittsburgh: The Combustion Institute, 929-940 (1973).
- Wersborg, B. L., L. K. Fox, and J. B. Howard, "Soot Concentration and Absorption Coefficient in a Low-Pressure Flame," *Combustion Science and Technology*, **24**: 1-10 (1975).
- Westmoreland, P. R., J. B. Howard, and J. P. Longwell, "Tests of Published Mechanisms by Comparison with Measured Flame Structure in Fuel-Rich Acetylene Combustion," *Twenty-first Symposium (International) on Combustion*, Pittsburgh: The Combustion Institute, 773-782 (1986).
- Woods, I. T., "Hydrocarbon Reactions and Soot Growth in Fuel-Rich Flames," Ph. D. Thesis, Department of Chemical Engineering, University of Sydney (1988).
- Wornat, M. J., "Pyrolysis-Induced Changes in the Composition of Polycyclic Aromatic Compounds from a Bituminous Coal," Sc. D. Thesis, Department of Chemical Engineering, Massachusetts Institute of Technology (1988).
- Wright, F. J., "The Oxidation of Soot by O Atoms," *Fifteenth Symposium (International) on Combustion*, Pittsburgh: The Combustion Institute, 1449-1460 (1975).
- Zhang, Q. L., S. C. O'Brien, J. R. Heath, Y. Liu, R. F. Curl, H. W. Kroto, and R. E. Smalley, "Reactivity of Large Carbon Clusters: Spheroidal Carbon Shells and Their Possible Relevance to the Formation and Morphology of Soot," *The Journal of Physical Chemistry*, **90** (4): 525-528 (1986).

PRODUCTION NOTE

This thesis was written and printed, in its entirety, with an Apple Macintosh II computer and a Hewlett-Packard DeskWriter printer. The text was composed in MacWrite II Release 1.1v1 and equations were formatted with Expressionist 2.07. Graphs, figures, and illustrations were prepared using MacDraw II Release 1.1v2, Cricket Graph 1.3.2, and Theorist 1.01.